



AD-A274 692



JOINT SERVICES ELECTRONICS PROGRAM

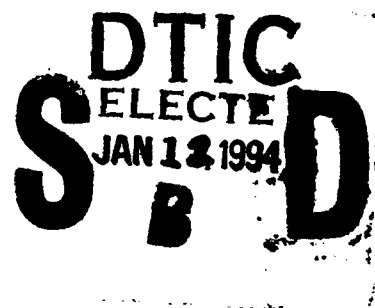
Sixteenth Annual Report Appendix

The Ohio State University

ElectroScience Laboratory

Department of Electrical Engineering
Columbus, Ohio 43212

Annual Report Appendix 721563-6
Contract No. N00014-89-J-1007
October 1993



Department of the Navy
Office of Naval Research
800 North Quincy Street
Arlington, Virginia 22217

94 1 10 171

94-01203



NOTICES

When Government drawings, specifications, or other data are used for any purpose other than in connection with a definitely related Government procurement operation, the United States Government thereby incurs no responsibility nor any obligation whatsoever, and the fact that the Government may have formulated, furnished, or in any way supplied the said drawings, specifications, or other data, is not to be regarded by implication or otherwise as in any manner licensing the holder or any other person or corporation, or conveying any rights or permission to manufacture, use, or sell any patented invention that may in any way be related thereto.

Contents

SECTION	PAGE
INTRODUCTION	1
JSEP REFEREED JOURNAL PAPERS PUBLISHED SEPTEMBER 1992 TO SEPTEMBER 1993	2
JSEP RELATED REFEREED JOURNAL PAPERS ACCEPTED FOR PUBLICATION SEPTEMBER 1992 TO SEPTEMBER 1993	3
JSEP RELATED PAPERS SUBMITTED FOR PUBLICATION SEPTEMBER 1992 TO SEPTEMBER 1993	4
JSEP RELATED PAPERS IN PREPARATION FOR PUBLICATION SEPTEMBER 1992 TO SEPTEMBER 1993	5
JSEP RELATED CONFERENCES/ORAL PRESENTATIONS SEPTEMBER 1992 TO SEPTEMBER 1993	7
JSEP RELATED AWARDS, PH.D. DISSERTATIONS AND M.SC THESES SEPTEMBER 1992 TO SEPTEMBER 1993	9
REPRINTS JSEP REFEREED JOURNAL PAPERS PUBLISHED SEPTEMBER 1992 TO SEPTEMBER 1993	11

DTIC QUALITY INSPECTED 8

Accession For	
NTIS GRA&I	<input checked="" type="checkbox"/>
DTIC TAB	<input type="checkbox"/>
Unannounced	<input type="checkbox"/>
Justification	
By _____	
Distribution/	
Availability Codes	
Dist	Avail and/or Special
A-1	

INTRODUCTION

This Appendix contains the reprints published under JSEP in the time September 1992 to September 1993.

In addition to the 10 reprints contained herein, there are 6 papers already accepted for publication during the next contract period, 11 papers submitted and 16 papers in preparation.

**JSEP REFEREED JOURNAL PAPERS
PUBLISHED SEPTEMBER 1992 TO SEPTEMBER 1993**

1. M. A. Marin and P.H. Pathak, "An Asymptotic Closed-Form Representation for the Grounded Double-Layer Surface Green's Function," *IEEE Transactions on Antennas and Propagation*, Vol. 40, No. 11, pp. 1357-1366, November 1992.
2. J. Ward and R.T. Compton, Jr., "High Throughput Slotted ALOHA Packet Radio Networks with Adaptive Arrays," *IEEE Trans. on Communications*, Vol. 41, No. 3, pp. 460-470, March 1993.
3. P.H. Pathak and R.J. Burkholder, "A Reciprocity Formulation for the EM Scattering by an Obstacle Within a Large Open Cavity," *IEEE Transactions on Microwave Theory and Techniques*, Vol. 41, No. 4, pp. 702-707, April 1993.
4. H.C. Ly, R.G. Rojas and P.H. Pathak, "EM Plane Wave Diffraction by a Planar Junction of Two Thin Material Half-Planes — Oblique Incidence," *IEEE Transactions on Antennas and Propagation*, Vol. 41, No. 4, pp. 429-441, April 1993.
5. N. Wang and L. Peters, Jr., "Scattering by Thin Wire Loaded with a Ferrite Ring," *IEEE Transactions on Antennas and Propagation*, Vol. 41, No. 5, pp. 694-697, May 1993.
6. H.C. Ly and R.G. Rojas, "Analysis of Diffraction by Material Discontinuities in Thin Material Coated Planar Surfaces based on Maliuzhnets' Method," *Radio Science*, Vol. 28, pp. 281-297, May-June 1993.
7. J. Li and R.T. Compton, Jr., "Angle and Polarization Estimation in a Coherent Signal Environment," *IEEE Trans. on Aerospace and Electronic Systems*, Vol. 29, No. 3, pp. 706-716, July 1993.
8. G.A. Somers, "A Proof of the Woodward-Lawson Sampling Method for a Finite Linear Array," *Radio Science*, pp. 481-485, July-August 1993.
9. J. Li and R.T. Compton, Jr., "Maximum Likelihood Angle Estimation for Signals with Known Waveforms," *IEEE Trans. on Signal Proc.*, Vol. 41, No. 9, pp. 2850-2862, September 1993.
10. R.G. Rojas and M. Otero, "Scattering by a Resistive Strip Attached to an Impedance Wedge," *Journal of Electromagnetic Waves and Applications (JEWA)*, Vol. 7, No. 3, pp. 373-402, 1993.

**JSEP RELATED REFEREED JOURNAL PAPERS
ACCEPTED FOR PUBLICATION
SEPTEMBER 1992 TO SEPTEMBER 1993**

1. J.L. Blanchard, E.H. Newman and M.E. Peters, "Integral Equation Analysis of Artificial Media," *IEEE Transactions on Antennas and Propagation*.
2. L.M. Chou, R.G. Rojas and P.H. Pathak, "WH/GSMT Based Full-Wave Analysis of Planar Transmission Lines Embedded in Multilayered Dielectric Substrates," *IEEE Trans. on Microwave Theory and Techniques*.
3. R. Lee and T.T. Chia, "Analysis of Electromagnetic Scattering from a Cavity with a Complex Termination by Means of a Hybrid Ray-FDTD Method," *IEEE Transactions on Antennas and Propagation*.
4. U. Pekel and R. Lee, "An A Posteriori Error Reduction Scheme for the Three Dimensional Finite Element Solution of Maxwell's Equations," *IEEE Trans. Microwave Theory and Techniques*.
5. G.A. Somers and P.H. Pathak, "Efficient Numerical and Closed Form Asymptotic Representations of the Dyadic Aperture Green's Function for Material Coated Ground Planes," *Radio Science*.
6. R. Torres and E.H. Newman, "Integral Equation Analysis of a Sheet Impedance Coated Window Slot Antenna," *IEEE Transactions on Antennas and Propagation*.

**JSEP RELATED PAPERS
SUBMITTED FOR PUBLICATION
SEPTEMBER 1992 TO SEPTEMBER 1993**

1. H.T. Anastassiou and P.H. Pathak, "High Frequency Analysis of Gaussian Beam Scattering by a Two-Dimensional Parabolic Contour of Finite Width," *Radio Science*.
2. T.T. Chia, R. Lee and R.C. Chou, "Comparison of Waveguide Fields Obtained via SBR and GRE," *IEEE Microwave and Guided Wave Letters*.
3. L.M. Chou and R.G. Rojas, "Dispersion and Lateral Leakage of Conductor Backed Coplanar Waveguides with Layered Substrate and Finite-Extent Lateral Ground Planes," *IEEE Transactions on Microwave Theory and Techniques*.
4. J.O. Jevtic and R. Lee, "A Theoretical and Numerical Analysis of the Measured Equation of Invariance," *IEEE Transactions on Antennas and Propagation*.
5. R. Lee and V. Chupongstimun, "A Partitioning Technique for the Finite Element Solution of Electromagnetic Scattering from Electrically Large Dielectric Cylinders," *IEEE Transactions on Antennas and Propagation*.
6. H.C. Ly and R.G. Rojas, "EM Plane Wave Diffraction by a Material Coated Perfectly Conducting Half-Plane—Oblique Incidence," *IEE Proceedings-H*.
7. P. Munk and P.H. Pathak, "EM Scattering by a Dielectric Filled Rectangular Antenna Cavity Recessed in a Ground Plane and Backed with an Array of Loaded Dominant Mode Waveguides," *IEEE Transactions on Antennas and Propagation*.
8. P. Munk and P.H. Pathak, "A Useful Approximate Analysis of the EM Scattering by a Rectangular Antenna Cavity containing an Array of Dominant Mode Waveguide Loaded Slots," *Journal of EM Waves and Applications*, (special issue on EM Scattering).
9. M.E. Peters and E.H. Newman, "Analysis of an Artificial Dielectric Composed of Small Dielectric Spheres," *IEEE Transactions on Antennas and Propagation*.
10. W.P. Pinello, R. Lee and A.C. Cangellaris, "Finite Element Modeling of Electromagnetic Wave Interactions with Periodic Structures," *IEEE Trans. Microwave Theory and Techniques*.
11. R.G. Rojas, "Integral Equations for the EM Scattering by Homogeneous/Inhomogeneous Two Dimensional Chiral Bodies," *IEE Proceedings-H*.

**JSEP RELATED PAPERS
IN PREPARATION FOR PUBLICATION
SEPTEMBER 1992 TO SEPTEMBER 1993**

1. T.L. Barkdoll and R. Lee, "Application of the Measured Equation of Invariance to Bodies of Revolution."
2. R.J. Burkholder and P.H. Pathak, "A Generalized Ray Expansion for Computing the EM Fields Radiated by an Antenna in a Complex Environment."
3. T.T. Chia, R. Lee and R.J. Burkholder, "A Three-Dimensional Implementation of the Hybrid Ray-FDTD Method for Modeling Electromagnetic Scattering from Electrically Large Cavities."
4. Y.S. Choi-Grogan, R. Lee, K. Eswar and P. Sadayappan, "A Parallel Implementation of a Partitioning Technique for the Finite Element Method."
5. M. Hsu, P.H. Pathak and C.W. Chuang, "Analysis of the Asymptotic HF EM Coupling Between Sources Anywhere in the Vicinity of a Circular Cylinder."
6. J.O. Jevtic and R. Lee, "On the Choice of Metrons for the Measured Equation of Invariance."
7. M.R. Kragalott and E.H. Newman, "Low Frequency Shielding of Electromagnetic Waves."
8. M.F. Otero and R.G. Rojas, "Synthesis of the Frequency Response of an Inhomogeneous Resistive Strip."
9. P.H. Pathak, R.J. Burkholder and P. Rousseau, "On the Question of Causality Associated with the Inversion into Time Domain of Ray Fields that Pass Through Caustics."
10. P.H. Pathak, H.T. Chou and R.J. Burkholder, "Ray Like Gaussian Basis Functions for Analyzing Propagation into and Scattering from Large Open Cavities with the GRE."
11. P.H. Pathak, A. Nagamune and R.G. Kouyoumjian, "An Analysis of Compact Range Measurements."
12. U. Pekel and R. Lee, "A Three-Dimensional Finite Element Method for Electromagnetic Scattering from Objects in an Unbounded Region."
13. R.G. Rojas, "Generalized Impedance/Resistive Boundary Conditions for a Planar Homogeneous Chiral Slab."
14. P. Rousseau and R.J. Burkholder, "A Hybrid Approach for Calculating the Scattering from Obstacles within Large Open Cavities."

15. P. Rousseau and P.H. Pathak, "A Time-Domain UTD for a Perfectly-Conducting Edge in a Curved Screen."
16. G. Zogbi, R.J. Burkholder and P.H. Pathak, "An Efficient Planar Antenna Near and Far Field Analysis using Gaussian Aperture Elements."

**JSEP RELATED CONFERENCES/ORAL PRESENTATIONS
SEPTEMBER 1992 TO SEPTEMBER 1993**

1. **SHORT COURSE:** R.G. Rojas, "Prediction of Mounted Antenna's Radiation Pattern using the GTD/UTD Approach," invited short course at PT. Industri Peswat Terbang Nusantara (IPTN), Banbung, Indonesia, November 1992.
2. P.H. Pathak, "A Review of Some Asymptotic HF Methods with Applications to Electromagnetic Radiation and Scattering," invited IEEE AP-S distinguished lecture, IEEE AP-S/MTT chapter in Atlanta, Georgia, January 27, 1993.
3. R. Lee and T.T. Chia, "A Hybrid Ray/FDTD Method for Computing Electromagnetic Scattering from an Engine Cavity with a Complex Termination," 9th Annual Review of Progress in Applied Computational Electromagnetics, Monterey, California, March 1993.
4. Y.S. Choi-Grogan and R. Lee, "A Sequential and Parallel Implementation of a Partitioning Finite Element Technique for Electromagnetic Scattering," International IEEE AP-S Symposium and URSI Radio Science Meeting, Ann Arbor, Michigan, June 28-July 2, 1993.
5. T.L. Barkdoll and R. Lee, "Finite Element Analysis of Bodies of Revolution using the Measured Equation of Invariance," International IEEE AP-S Symposium and URSI Radio Science Meeting, Ann Arbor, Michigan, June 28-July 2, 1993.
6. J. Jevtic and R. Lee, "Higher Order Divergenceless Edge Elements," International IEEE AP-S Symposium and URSI Radio Science Meeting, Ann Arbor, Michigan, June 28-July 2, 1993.
7. J. Jevtic and R. Lee, "An Analysis of the Measured Equation of Invariance," International IEEE AP-S Symposium and URSI Radio Science Meeting, Ann Arbor, Michigan, June 28-July 2, 1993.
8. M.F. Otero and R.G. Rojas, "Scattering and Radiation in the Presence of a Material Loaded Impedance Wedge," International IEEE AP-S Symposium and URSI Radio Science Meeting, Ann Arbor, Michigan, June 28-July 2, 1993.
9. H.T. Anastassiou and P.H. Pathak, "High Frequency Analysis of Gaussian Beam Scattering by a Parabolic Surface Containing an Edge," International IEEE AP-S and National URSI meeting in Ann Arbor, Michigan, June 28-July 2, 1993.
10. G.A. Somers and P.H. Pathak, "An Asymptotic Closed Form Aperture Green's Function with Applications to Radiation and Scattering by Slots in Material Coated Ground Planes," International IEEE AP-S and National URSI meeting in Ann Arbor, Michigan, June 28-July 2, 1993.

11. R.J. Burkholder and P.H. Pathak, "A Generalized Ray Expansion for Computing the EM Fields Radiated by an Antenna in a Complex Environment," International IEEE AP-S and National URSI meeting in Ann Arbor, Michigan, June 28-July 2, 1993.
12. H.T. Anastassiou and P.H. Pathak, "A Simple Gaussian Beam Analysis of the Fields Radiated by Two-Dimensional Paraboloid Reflector Antennas Illuminated by a Feed Array," International IEEE AP-S and National URSI meeting in Ann Arbor, Michigan, June 28-July 2, 1993.
13. P.H. Pathak, "EM Analysis of HF Scattering by and Coupling into Open Cavities," invited lecture, 11th Annual IEEE Benjamin Franklin Symposium in Philadelphia, Pennsylvania, May 1, 1993.
14. P.H. Pathak, "Some Recent Accomplishments and Future Directions in the Area of High Frequency Techniques," invited lecture, XXIVth General Assembly of URSI, Kyoto, JAPAN, August 25-September 3, 1993.
15. P.H. Pathak, "Asymptotic HF Techniques for EM Antenna and Scattering Analysis," invited lecture, Symposium on Mathematical Methods in Wave Scattering Theory, Faculty of Science and Engineering, Chuo University, Tokyo, JAPAN, September 3, 1993.

The following conference paper was not included in the 1992 Annual Appendix.

1. S. Ozeki and R.G. Rojas, "Symmetry Analysis of Chiro-Dielectric Waveguides," Conference on Microwave Circuits and Devices, Inst. of Electronic, Information and Communication Engineers, Tokyo, Japan, June 1992.

JSEP RELATED AWARDS, PH.D. DISSERTATIONS AND M.SC. THESES SEPTEMBER 1992 TO SEPTEMBER 1993

Awards:

1. Dr. Rojas has received the 1993 Lumley Research Award from the College of Engineering at The Ohio State University. This award is based on the previous four years of work.
2. H.T. Anastassiou received the second IEEE AP-S student prize awarded for the paper entitled "A Simple Gaussian Beam Analysis of the Fields Radiated by Two Dimensional Parabolic Reflector Antennas Illuminated by a Feed Array," (co-author, P.H. Pathak), presented at the International IEEE AP-S and National URSI meeting in Ann Arbor, Michigan, June 28-July 2, 1993.

Dissertations:

1. Ling-Miao Chou, "A Novel Hybrid Full-Wave Analysis Method for Planar Transmission Lines Embedded in Multilayered Dielectrics — The WH/GSMT," Ph.D. dissertation, Department of Electrical Engineering, The Ohio State University, Columbus, Ohio, December 1992.
2. Gary A. Somers, "Efficient Numerical and Asymptotic Analyses of the Dyadic Aperture Green's Function for a Grounded Material Slab and Its Application to Slot Arrays," Ph.D. dissertation, Department of Electrical Engineering, The Ohio State University, Columbus, Ohio, March 1993.

Thesis:

1. H.T. Chou, "Development of Gaussian Ray Basis Elements for Efficient GRE Analysis of EM Backscatter from Open Cavities," M.Sc. thesis, Department of Electrical Engineering, The Ohio State University, Columbus, Ohio, September 1993.

REPRINTS
JSEP REFEREED JOURNAL PAPERS
SEPTEMBER 1992 TO SEPTEMBER 1993

An Asymptotic Closed-Form Representation for the Grounded Double-Layer Surface Green's Function

M. A. Marin, *Member, IEEE*, and Prabhakar H. Pathak, *Fellow, IEEE*

Abstract—In this paper, an efficient closed-form asymptotic representation for the grounded double-layer (substrate-superstrate) Green's function is presented. The formulation is valid for both source (a horizontal electric dipole) and observation points anywhere inside the superstrate or at the interfaces. The asymptotic expressions are developed via a steepest descent evaluation of the original Sommerfeld-type integral representation of the Green's function, and the large parameter in this asymptotic development is proportional to the lateral separation between source and observation points. The asymptotic solution is shown to agree with the exact Green's function for lateral distances even as small as a few tenths of the free-space wavelength, thus constituting a very efficient tool for analyzing printed circuits/antennas. Also, since the asymptotic approximation gives separate contributions pertaining to the different wave phenomena, it thus provides physical insight into the field behavior, as shown through the examples.

I. INTRODUCTION

THE grounded double-layer (substrate-superstrate) configuration is of increasing interest in printed circuit/antenna technology. It has been demonstrated in [1] and [2] that, by properly choosing the layer thicknesses and material parameters, significant improvements can be achieved in the performance of the printed antennas, including the reduction or elimination of surface waves, which is a subject of primary concern when dealing with large arrays of printed elements. Also, a double-layer structure allows for the separation of active circuitry and radiating patches in hybrid or monolithic integrated circuit technologies. These potential advantages lead to the need for accurate, "full-wave" analysis of such structures.

So far, the most commonly used approach to solve these problems (in single or double layers) has been the solution of the corresponding electric field or mixed potential integral equation (EFIE or MPIE), via the method of moments [3]–[8]. However, two different techniques have been applied to evaluate the elements of the mo-

ment method (MM) mutual impedance matrices. One of these is the spectral domain approach [4], [6], [7], which has the advantage of using simple formulas for the spectral representation of the Green's function, but requires numerical integration over the entire spectral plane. On the other hand, for the spatial domain method [3], [5], [8] the range of integration is restricted to the area of each subdomain or basis function, but the Green's function is expressed in terms of Sommerfeld-type integrals, which must be numerically evaluated at each spatial point. It is clear that both methods require a fairly large amount of computer time. Moreover, since both spectral and spatial integrands contain terms that oscillate faster for increasing separation between subdomains, the numerical integrations become very inefficient when computing the MM mutual coupling between widely separated basis functions. Also, if the spatial size of the basis functions is small, their transforms extend farther in the spectral domain, thus adding inefficiency to the numerical integration when the spectral domain approach is employed.

To overcome these limitations, we propose the use of an asymptotic closed-form representation of the Green's function, which makes the mutual coupling computation in the spatial domain extremely efficient. Such an asymptotic representation has already been obtained for the single-layer case [9]–[11], and was found to provide excellent results even for very small distances between source and observation points (usually down to a few tenths of the free-space wavelength). As an extension to the above work, the purpose of this paper is to develop an accurate asymptotic closed-form representation for the Green's function of a grounded double layer planar structure, as well as to show some of its advantages.

A further extension to include multilayers does not appear straightforward. The development of the closed form asymptotic result requires one to evaluate certain derivatives of the integrand present in the Green's function integral; such an evaluation becomes complicated for multilayers because in this case the integrand itself becomes rather complicated. It is for this reason that an asymptotic treatment of the more general, grounded multilayer Green's function has not been attempted here; only the special double layer case, which is of sufficient practical interest, is considered in this paper.

This paper is organized as follows. Section II presents the formulation of the substrate-superstrate Green's func-

Manuscript received October 28, 1988; revised September 26, 1991. This work was supported in part by Joint Services Electronics Program under Contract N00014-88-K-0004 and The Ohio State University Research Foundation.

M. A. Marin is currently with Ingenieria de Radiofrecuencias, 28035 Madrid, Spain; he was with the Ohio State University, Electroscience Laboratory, Columbus, OH 43212.

P. H. Pathak is with The Ohio State University, Electroscience Laboratory, Columbus, OH 43212.

IEEE Log Number 9204904.

tion in terms of Sommerfeld-type integrals for a horizontal Hertzian dipole embedded in the superstrate. Section III discusses the number and location of the relevant poles of the structure. The asymptotic evaluation of the original Sommerfeld integrals is carried out in Section IV. Finally, Section V presents numerical results showing the accuracy of the new asymptotic representation. It will be shown how the asymptotic formulas provide not only computational efficiency, but also physical insight into the field behavior. An $e^{+j\omega t}$ time dependence for the fields and sources is assumed and suppressed in the following analysis.

II. FORMULATION

Consider an infinitesimal \hat{x} -directed electric dipole at (x', y', z') embedded in the superstrate of a planar grounded double-layer configuration, as shown in Fig. 1. We are interested in calculating the \hat{x} - and \hat{y} -direction electric fields at any observation point (x, y, z) in the superstrate including the interfaces ($0 \leq z, z' \leq d_2$). These fields can be written as follows:

$$E_{xx} = \frac{-1}{2\pi\omega\epsilon_2} \left\{ k_2^2 U + \frac{\partial^2}{\partial x^2} [U - W] \right\} \quad (1)$$

$$E_{yx} = \frac{-1}{2\pi\omega\epsilon_2} \left\{ \frac{\partial^2}{\partial x \partial y} [U - W] \right\} \quad (2)$$

where

$$U = \int_0^\infty F^U(\xi) J_0(\rho\xi) d\xi \quad (3)$$

$$W = \int_0^\infty F^W(\xi) J_0(\rho\xi) d\xi \quad (4)$$

J_0 being the zeroth-order Bessel function

$$\rho = \sqrt{(x - x')^2 + (y - y')^2} \quad (5)$$

the lateral separation between source and field points. The wavenumbers in media 1 and 2 are defined as $k_1 = k_0\sqrt{\mu_1\epsilon_1}$ and $k_2 = k_0\sqrt{\mu_2\epsilon_2}$, respectively, where k_0 is the wavenumber of the semiinfinite medium above the superstrate (this semiinfinite region is usually free-space), and μ_{ri}, ϵ_{ri} are the relative permeability and permittivity referred to that medium so that $\mu_i = \mu_0\mu_{ri}$ and $\epsilon_i = \epsilon_0\epsilon_{ri}$. The functions $F^{U,W}$ in (3) and (4) can be determined by solving the boundary-value problem in the spectral domain, yielding (for $0 \leq z, z' \leq d_2$):

$$F^U(\xi) = \frac{\xi}{2k_{2z}} \left\{ \frac{T_1^s\beta_1 + T_2^s\beta_2 + T_3^s\beta_3}{D_e} \right\} \quad (6)$$

where the T^s terms are given by:

$$T_1^s = D_{e1}^-(1 + \alpha_e) - D_{e1}^+(1 - \alpha_e)e^{-2jk_{1z}d_2} \quad (7)$$

$$T_2^s = D_{e1}^+ \{1 + \alpha_e + (1 - \alpha_e)e^{-2jk_{1z}(d_2 - z')}\} \quad (8)$$

$$T_3^s = \{D_{e1}^- + D_{e1}^+e^{-2jk_{1z}z'}\}(1 - \alpha_e)e^{-2jk_{1z}d_2} \quad (9)$$

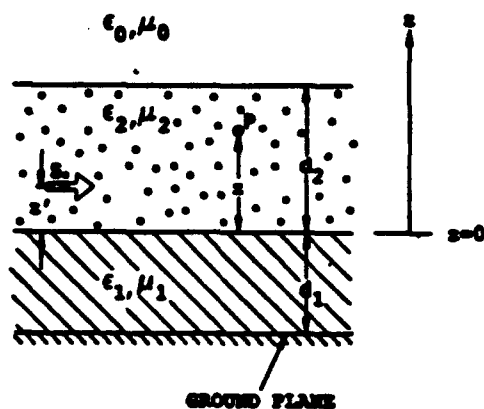


Fig. 1. Grounded double-layer configuration with source S (a horizontal electric dipole) and observation point P embedded in the superstrate.

and

$$D_{e1}^\pm = \frac{k_{2z}}{\mu_2} \pm j \frac{k_{1z}}{\mu_1} \cot[k_{1z}d_1] \quad (10)$$

$$\alpha_e = \frac{k_{0z}/\mu_0}{k_{2z}/\mu_2} \quad (11)$$

$$\beta_1 = e^{-jk_{1z}(z-z')}; \quad \delta_z = \begin{cases} 1 & z > z' \\ -1 & z < z' \end{cases} \quad (12)$$

$$\beta_2 = e^{-jk_{1z}(z+z')}; \quad \beta_3 = e^{+jk_{1z}(z+z')} \quad (13)$$

being

$$k_{0z} = \sqrt{k_0^2 - \xi^2}; \quad k_{1z} = \sqrt{k_1^2 - \xi^2}; \quad k_{2z} = \sqrt{k_2^2 - \xi^2}. \quad (14)$$

It is noted that to be consistent with the Sommerfeld radiation condition the choice of the branch in (14) must be such that

$$\text{Im}\{k_{0z}\} < 0. \quad (15)$$

Finally, the denominator in (6) is given by

$$D_e = \left\{ \left(\frac{k_{2z}}{\mu_2} \right)^2 - j \frac{k_{0z}k_{1z}}{\mu_0\mu_1} \cot[k_{1z}d_1] \right\} \left\{ \frac{1 - e^{-2jk_{1z}d_2}}{k_{2z}/\mu_2} \right\} + \left\{ \frac{k_{0z}}{\mu_0} - j \frac{k_{1z}}{\mu_1} \cot[k_{1z}d_1] \right\} (1 + e^{-2jk_{1z}d_2}). \quad (16)$$

Similarly, F^W can be written as

$$F^W(\xi) = \frac{k_{2z}}{2\xi} \left\{ \frac{T_1^m\beta_1 + T_2^m\beta_2 - T_3^m\beta_3}{D_m} - \frac{T_1^s\beta_1 + T_2^s\beta_2 + T_3^s\beta_3}{D_e} \right\} \quad (17)$$

with

$$T_1^m = D_{m1}^+(1 + \alpha_m) - D_{m1}^-(1 - \alpha_m)e^{-2jk_{1z}d_2} \quad (18)$$

$$T_2^m = D_{m1}^- \{-(1 + \alpha_m) + (1 - \alpha_m)e^{-2jk_{1z}(d_2 - z')}\} \quad (19)$$

$$T_3^m = [D_{m1}^+ - D_{m1}^-e^{-2jk_{1z}z'}](1 - \alpha_m)e^{-2jk_{1z}d_2} \quad (20)$$

and

$$D_{m1}^{\pm} = \frac{k_{2z}}{\epsilon_2} \pm \frac{k_{1z}}{\epsilon_1} j \tan[k_{1z} d_1] \quad (21)$$

$$\alpha_m = \frac{k_{0z}/\epsilon_0}{k_{2z}/\epsilon_2} \quad (22)$$

The denominator D_m in (17) is now

$$D_m = \left\{ \left(\frac{k_{2z}}{\epsilon_2} \right)^2 + j \frac{k_{0z} k_{1z}}{\epsilon_0 \epsilon_1} \tan[k_{1z} d_1] \right\} \frac{(1 - e^{-2j k_{1z} d_1})}{k_{2z}/\epsilon_2} + \left\{ \frac{k_{0z}}{\epsilon_0} + j \frac{k_{1z}}{\epsilon_1} \tan[k_{1z} d_1] \right\} (1 + e^{-2j k_{1z} d_1}). \quad (23)$$

The above expressions for the fields have been checked to reduce to the single-layer case when μ_2, ϵ_2 tend to μ_0, ϵ_0 and/or d_2 tends to zero. Also, the denominators (16) and (23) agree with those given in [2], except for a multiplicative factor.

III. POLE STRUCTURE

The zeros of D_e, D_m in (6) and (17) constitute the poles of the composite (double) layer. Their number and location depend on the layer thicknesses and material constants, as well as the wavenumber k_0 . Restricting our attention to the lossless case, it is well known that D_e, D_m exhibit a certain number of zeros on the real axis of the ξ -plane, in the interval $[k_0, \max(k_1, k_2)]$. These poles describe the surface waves guided by the structure, and therefore appear on the proper Riemann sheet (consistent with the radiation condition) of the ξ -plane, as defined in (15). But there are also poles on the improper Riemann sheet of the ξ -plane, known as leaky wave poles. Although there are in general an infinite number of them [12], it was found in [10] and [13] for the single-layer case that the inclusion of only a particular set of these poles produced a significant improvement in the asymptotic solution, for nearby source and observation points on the surface of the slab. This set of poles is located on the real axis of the improper Riemann sheet of the ξ -plane for the lossless case, and therefore they will be referred to as improper surface wave poles. It was also found that proper and improper surface wave poles are closely related. In fact, surface wave poles (except for the first TM surface wave pole, which is always above cutoff) are originally improper poles that move towards the branch cut at k_0 along the real axis of the improper Riemann sheet as the layer thickness increases, and finally "jump" into the proper plane, then moving away from k_0 along the proper real axis. In the same way, improper surface wave poles are originally improper complex (or leaky wave) poles that move onto the improper real axis when the appropriate conditions are met. In this section, we will investigate the number of TE and TM poles on the real axes of both, the proper and improper sheets (ξ -plane) for a general double layer structure, as a function of its constitutive parameters. Also, a simple procedure to locate the first TE and TM proper and/or improper surface wave poles will be outlined.

cate the first TE and TM proper and/or improper surface wave poles will be outlined.

A. Zeros of D_e

As mentioned before, a new TE surface wave pole will always appear initially at $\xi = k_0$ on the proper Riemann sheet, so the following condition must be met:

$$D_e(\xi = k_0) = 0 \quad (24)$$

which can be written using (16) as

$$\frac{\sqrt{n_2 - 1}}{\mu_{r2}} \tan[k_0 d_2 \sqrt{n_2 - 1}] = \frac{\sqrt{n_1 - 1}}{\mu_{r1}} \cot[k_0 d_1 \sqrt{n_1 - 1}] \quad (25)$$

where $n_1 = \epsilon_{r1} \mu_{r1}$; $n_2 = \epsilon_{r2} \mu_{r2}$. Defining, in a way similar to [12], the parameters $L_1 = k_0 d_1 \sqrt{n_1 - 1}$, $L_2 = k_0 d_2 \sqrt{n_2 - 1}$, (25) can be expressed more compactly as

$$\frac{\sqrt{n_2 - 1}}{\mu_{r2}} \tan(L_2) = \frac{\sqrt{n_1 - 1}}{\mu_{r1}} \cot(L_1). \quad (26)$$

It is noted that this equation was already given by Jackson and Alexopoulos [1, eq. (37)], and it represents the condition for any TE surface wave mode to turn on. For example, for a given $\epsilon_{r2}, \mu_{r2}, d_2$ such that $L_2 < \pi/2$, (26) will be satisfied at infinite points, each one for a certain L_1 such that $N\pi < L_1 < (N+1)\pi$ with $(N = 0, 1, 2, \dots)$. If we plot the condition (26) in a two-dimensional L_1, L_2 plane for a given set of ϵ_{r1}, μ_{r1} , we get a plot like in Fig. 2(a). In the regions between two consecutive curves, the number of surface waves is constant. However, the number of improper surface wave poles (lwp in Fig. 2) is not. As discussed before, two leaky wave poles move onto the improper real axis when the point defined by (L_1, L_2) in Fig. 2(a) moves close enough to the curve defining the order of the next region. As L_1 or L_2 increases, one of these poles begins moving towards the branch cut and finally "jumps" onto the proper Riemann sheet, thus constituting a new surface wave pole.

Note in Fig. 2(a) that, if $\epsilon_{r2} = \mu_{r2} = 1$ (no second layer present), $L_2 = 0$ and the L_1, L_2 plane reduces to the L_1 axis, yielding the results already reported in [12] for the single-layer case. It is also noted that the curved segments between dots in Fig. 2 can be convex or concave, depending on the particular values of ϵ_{r1}, μ_{r1} in (26).

In most practical configurations, there is only one proper or improper TE surface wave pole, and it can be easily found as follows. The pole will be located on the real axis of the proper (improper) sheet if the left-hand side of (26) is greater (smaller) than the right-hand side. In either case, a Newton-Raphson searching procedure implemented in (16) with $\xi_{i1} = 0.99k_0\sqrt{n_2}$ (for a swp) or $\xi_{i1} = k_0$ (for a lwp) as initial value has been found to provide the actual location of the pole in only a few iterations. Note that the subscript i on ξ_{i1} above refers to the value of

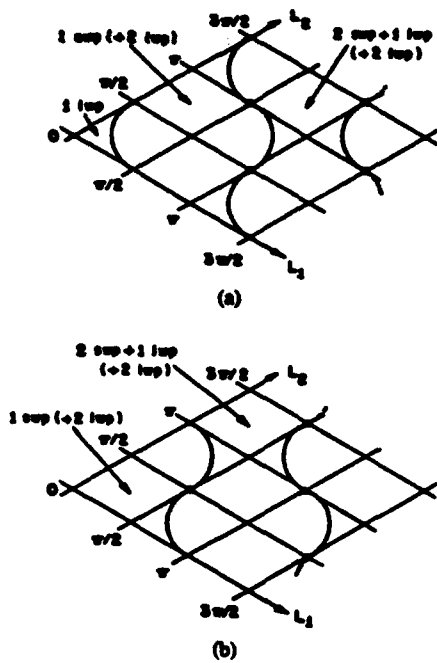


Fig. 2. Number of proper (swp) and improper (lwp) surface wave poles for given materials (ϵ_{ri} , μ_{ri}), as a function of layer thicknesses: (a) TE case, and (b) TM case ($L_1 = k_0 d_1 \sqrt{\epsilon_{r1} \mu_{r1} - 1}$, $L_2 = k_0 d_2 \sqrt{\epsilon_{r2} \mu_{r2} - 1}$). The number of lwp indicated within the brackets are additional improper surface wave poles that can exist in each region.

the initial guess for the location (in the ξ plane) of the proper surface wave pole, and likewise the subscript il on ξ_{il} refers to the initial value of ξ pertaining to the improper surface wave pole.

B. Zeros of D_m

Similar considerations to those discussed in the previous case lead now to the following condition, for a TM pole to arise on the proper Riemann sheet

$$\frac{\sqrt{n_2 - 1}}{\epsilon_{r2}} \tan(L_2) = -\frac{\sqrt{n_1 - 1}}{\epsilon_{r1}} \tan(L_1) \quad (27)$$

We can again plot the condition (27) in an L_1, L_2 plane, as we did for D_e . The result for a given set of ϵ_{ri}, μ_{ri} is shown in Fig. 2(b). The same general considerations discussed above for D_e are applicable here. It is also seen that, for $L_2 = 0$ (single layer case), the plane in Fig. 2(a) reduces to the L_1 axis, with the result already given in [12].

In most practical double layer structures, there is only one TM surface wave pole, although two leaky wave poles may also exist on the improper real ξ -axis. This situation corresponds to the first region in Fig. 2(b). The surface wave pole can be found by implementing a Newton-Raphson search procedure in (23) with $\xi_{i1} = 0.99k_0\sqrt{n_2}$ as a starting value. The improper surface wave poles (if any) can be located in a similar manner, now starting the search at both $\xi_{i1} = k_0$ and $\xi_{i2} = 0.99k_0\sqrt{n_2}$. The ξ_{i1} and ξ_{i2} above represent the values of the initial guesses for the location in the ξ plane of the first and second

improper surface wave poles, respectively. When $L_1 > \pi/2$, D_m presents a singularity at $d_1\sqrt{k_1^2 - \xi_i^2} = \pi/2$. In this case special care must be taken with the starting value of the searching algorithm in both Riemann sheets, because the searching procedure cannot "cross" a singularity. These situations can be easily handled by plotting D_m along both (proper and improper) real ξ -axes to determine appropriate starting values.

IV. ASYMPTOTIC EVALUATION OF THE SOMMERFELD INTEGRALS

Conventional numerical evaluation of the Sommerfeld-type integrals (3), (4) presents two main difficulties. First, the integrands exhibit a certain number of poles that have to be extracted in order to obtain a relatively smooth function suitable for numerical integration. Second, the oscillatory, slowly decaying behavior of the Bessel function results in a poor convergence of the integrals, particularly when the lateral separation between source and observation points is large in terms of the wavelength.

To overcome these limitations, asymptotic closed-form expressions for U and W in (3) and (4) will be developed in this section. To carry out the asymptotic evaluation we first write integrals (3) and (4), due to the oddness of $F^{U,W}$ with respect to ξ , as:

$$U = \frac{1}{2} \int_{C_s} F^U(\xi) H_0^{(2)}(\rho\xi) d\xi \quad (28)$$

$$W = \frac{1}{2} \int_{C_s} F^W(\xi) H_0^{(2)}(\rho\xi) d\xi \quad (29)$$

where C_s is the Sommerfeld path, as shown in Fig. 3. This path can be deformed to give the sum of the enclosed residues plus the integral around the branch cut (contour C_B in Fig. 3):

$$U = -\frac{1}{2} \sum_i 2\pi j R^U(\xi_i) H_0^{(2)}(\rho\xi_i) + \frac{1}{2} \int_{C_B} F^U(\xi) H_0^{(2)}(\rho\xi) d\xi \quad (30)$$

$$W = -\frac{1}{2} \sum_i 2\pi j R^W(\xi_i) H_0^{(2)}(\rho\xi_i) + \frac{1}{2} \int_{C_B} F^W(\xi) H_0^{(2)}(\rho\xi) d\xi \quad (31)$$

Here, $R^{U,W}$ are the residues of $F^{U,W}$ at $\xi = \xi_i$ (proper surface wave poles), and can be calculated as follows:

$$R^U(\xi_i) = \lim_{\xi \rightarrow \xi_i} (\xi - \xi_i) F^U(\xi) = \frac{N^U(\xi_i)}{D'_i(\xi_i)} \quad (32)$$

$$R^W(\xi_i) = \lim_{\xi \rightarrow \xi_i} (\xi - \xi_i) F^W(\xi) = \frac{N^W(\xi_i)}{D_{n2}(\xi_i) \cdot D'_i(\xi_i)} \quad (33)$$

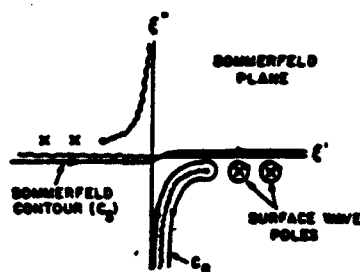


Fig. 3. Original Sommerfeld contour (C_S), and the deformation to give the sum of the enclosed residues plus the integral around the branch cut (C_B). Here, $\xi = \xi' + j\xi''$.

where $N^{U,W}$ represent the numerators of F^U and F^W in (6) and (17) and D_s, D_{ns} stand for the singular and non-singular denominators in (17). The minus sign of the residues in (30) and (31) comes from clockwise integration around the poles.

The above result, (30), (31), allows for the interpretation of the solution in terms of two contributions: a discrete number of surface waves, whose strengths are given by the corresponding residues at the poles, plus a continuous spectrum of waves, represented by the integral around the branch cut. The purpose of the asymptotic evaluation is to obtain the dominant terms in the latter.

With the above view in mind, the following changes of variable can be used [9]–[11]:

$$\tau = \sqrt{k_0^2 - \xi^2} \quad (34)$$

$$\cos \gamma = \frac{\tau}{k_0} \quad (35)$$

$$\sin \gamma = 1 - js^2. \quad (36)$$

The first one transforms the integral around the branch cut into a real-axis integral in the τ plane. The second performs the angular spectrum mapping, and the third transforms the steepest descent path (SDP) in the γ plane onto the real axis of the s -plane. The three planes, as well as the paths of integration and the location of proper and improper surface wave poles (lossless case) are shown in Fig. 4.

Since the above transformations have been discussed in more detail in [9]–[11], it will thus suffice for our purposes to consider the direct transformation from the ξ -plane to the s -plane:

$$\xi = k_0(1 - js^2). \quad (37)$$

Introducing the above transformation in a general integral of the form

$$I_B = \frac{1}{2} \int_{C_B} F(\xi) H_0^{(2)}(\rho \xi) d\xi \quad (38)$$

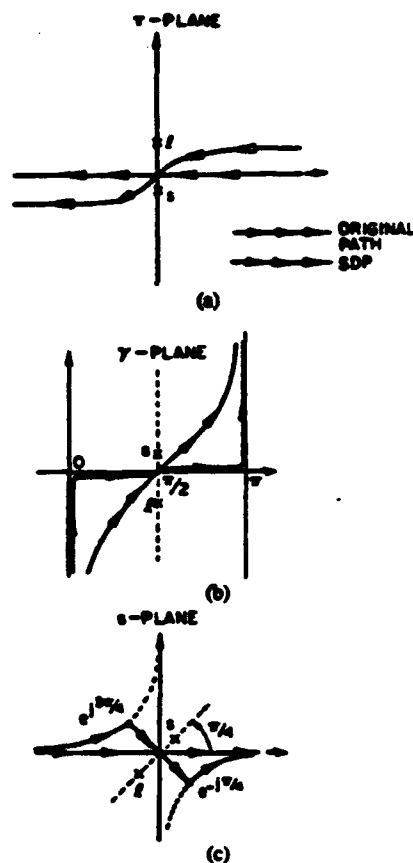


Fig. 4. Original and steepest descent (SDP) paths of integration in the (a) τ -plane; (b) γ -plane; and (c) s -plane. The location of proper (s) and improper (l) surface wave poles is also shown.

where C_B is the contour shown in Fig. 2, one gets

$$I_B = \frac{1}{2} \int_{\Gamma'_0} F[k_0(1 - js^2)] H_0^{(2)}[k_0 \rho(1 - js^2)] (-2jk_0 s) ds \quad (39)$$

where Γ'_0 is the resulting contour of integration in the s -plane, as shown in Fig. 4(c). Now, if $k_0 \rho$ is assumed to be large, we can use the large-argument form of the Hankel function in (39), yielding

$$I_B \sim \frac{1}{2} \sqrt{\frac{2k_0}{\pi \rho}} e^{K\pi/4} e^{-jk_0 \rho} \int_{\Gamma'_0} G(s) e^{-k_0 \rho s^2} ds \quad (40)$$

where

$$G(s) = F[k_0(1 - js^2)] \frac{-2js}{\sqrt{1 - js^2}} \quad (41)$$

By deforming the original contour Γ'_0 into Γ'_{SDP} , extracting the singularities and approximating the resulting regular function by the first two nonvanishing terms of its Taylor series expansion around $s = 0$ [14], [15], one gets the following result:

$$I_B \sim \frac{e^{K\pi/4}}{\sqrt{2}} \frac{e^{-jk_0 \rho}}{\rho} \left[\sum_i \frac{R(b_i)}{b_i} [1 - \bar{F}(jk_0 \rho b_i^2)] + \frac{1}{2k_0 \rho} \left\{ \frac{G''(0)}{2} + \sum_i \frac{R(b_i)}{b_i^3} \right\} \right] \quad (42)$$

where $R(b_i)$ are the residues of $G(s)$ at $s = b_i$ (singularities in the s -plane), $G''(0)$ is the second-order derivative of (41) evaluated at $s = 0$ and $\tilde{F}(x)$ is the transition function (as defined in [11]).

It can be easily shown that the residues of $G(s)$ at $s = b_i$ are related to those of $F(\xi)$ at $\xi = \xi_i$ by

$$R(b_i) = \frac{R(\xi_i)}{\sqrt{k_0 \xi_i}} \quad (43)$$

where $R(\xi_i)$ is defined in (32) and (33), and

$$b_i = e^{K(\pi/4)} \sqrt{\xi_i/k_0 - 1} \quad (44)$$

where the principal branch of the above square root ($\text{Re}(b_i) > 0$) corresponds to surface wave poles, and the other branch to leaky wave poles.

It can be seen that the solution given in (42) is in a very amenable format, involving only simple algebraic operations and the well-known transition function \tilde{F} , which contains simple Fresnel integrals in the lossless case [11]. Also, the summations in (42) involve only one or two poles in most practical cases (which typically involve only moderately thin layers). The evaluation of the second derivative of (41) at $s = 0$ is also simplified by noting that:

$$G''(s = 0) = -4jF'(s = 0) \quad (45)$$

where F is $F^{U,W}(\xi)$ in (6) or (17) evaluated at $\xi = k_0(1 - js^2)$. Although somewhat cumbersome due to the relatively functions involved, the evaluation of $F'(s = 0)$ in (45) is straightforward, and the results for three different situations (source and observation points both along the first or second interface and along different interfaces) are given in Appendix A.

It must be mentioned at this point that a complex leaky wave pole existing on the improper sheet of the original ξ -plane may contribute to the solution if it is captured in the path deformation (Γ_0' into Γ_{SDP}'), or it may still influence the solution if it appears close enough to the saddle point. In these cases, the asymptotic solution including only the real ξ -axis proper and improper surface wave poles will be seen to lose accuracy in the neighborhood of the source. However, this can be regarded as a second-order effect, since the complex leaky wave poles cannot appear arbitrarily close to the saddle point, while real-axis poles do. Nevertheless, these situations are rarely found in practice.

Finally, when the observation point is very close to the source, the asymptotic solution will fail, and a numerical integration procedure (see e.g., [11]) or alternative integral representations [16] must be used.

V. NUMERICAL RESULTS AND CONCLUSIONS

In this section we will first examine the accuracy of the asymptotic approximation in the three cases considered in the Appendix. The examples have been selected to show the validity of the closed-form expressions for different combinations of low and high dielectric constants, as well as thin and thick dielectric slabs (lossless case). Although

magnetic materials will not be used throughout these examples, it must be mentioned that there is no essential difference in the treatment of the magnetic material and the dielectric material from a purely numerical point of view, and the asymptotic solution is equally valid for both.

In the examples shown below, one TM surface wave pole (plus two improper surface wave poles when necessary) and one TE proper or improper surface wave pole have been included in the asymptotic solution. Thus, Fig. 5 shows a comparison between the numerical evaluation of the exact W (4) and its asymptotic approximation [(31) and (42)], versus lateral separation between source and observation points. The "exact" value of the function U and W is always calculated by a numerical (Gaussian) integration of (3) and (4), once the limiting behavior and singularities of the integrand have been extracted [11]. In this case, the source and observation points are located on the interface between the two dielectric layers. As can be seen, the asymptotic closed-form expression remains valid for lateral distances as small as two tenths of the free-space wavelength λ_0 . Also, Table I shows a CPU time comparison between the calculation based on the numerical integration procedure and the asymptotic closed-form expressions. It is apparent that the use of the closed-form result in conjunction with any spatial-domain formulation will result in a substantial savings of computer time. It must also be mentioned that, in all the cases studied here, the accuracy of the asymptotic approximation for U is at least as good as it is for W .

Another example is shown in Fig. 6 in which a thin, low dielectric constant slab is placed on top of a moderately thick, high dielectric constant layer. In this case, the source and observation points are along different interfaces. Again, the asymptotic solution remains valid for lateral distances of the order of $0.4\lambda_0$, although probably $0.2\lambda_0$ could be used for most practical purposes. In this case, there is no singularity when $\rho \rightarrow 0$, because the source and observation points are at least separated by the thickness of the second (superstrate) layer.

One more representative case is shown in Fig. 7, where a thick layer is now placed on top of a thin one, both with high dielectric constants. Source and observation points are here along the dielectric-air interface. As can be seen, the asymptotic solution can be used in this case almost down to one tenth of the free-space wavelength.

In general it can be said that the asymptotic closed-form expressions for U and W can be used down to a few tenths of the free-space wavelength, for source and observation points along the same or different interfaces. This also applies if source and/or observation points are embedded somewhere inside the layers. However, as it was mentioned before, in those particular situations in which a complex leaky wave pole contributes significantly to the asymptotic solution, the above expressions for U and W converge at large lateral distances from the source, of the order of one free-space wavelength. However, this restriction in the asymptotic solution can be eliminated even in the latter case if the effect of such complex leaky wave

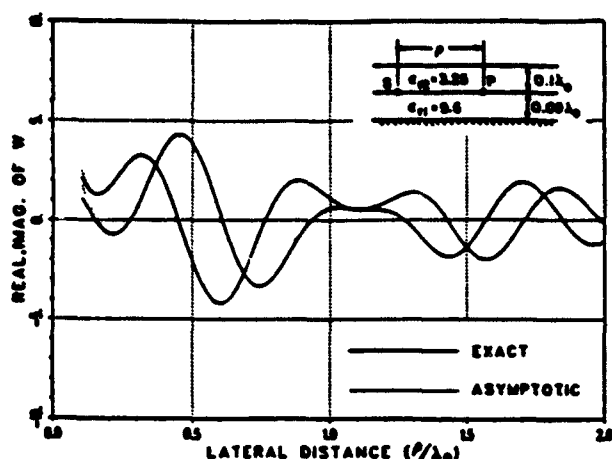


Fig. 5. Comparison between the exact W and its asymptotic approximation, for source and observation points both along the first interface.

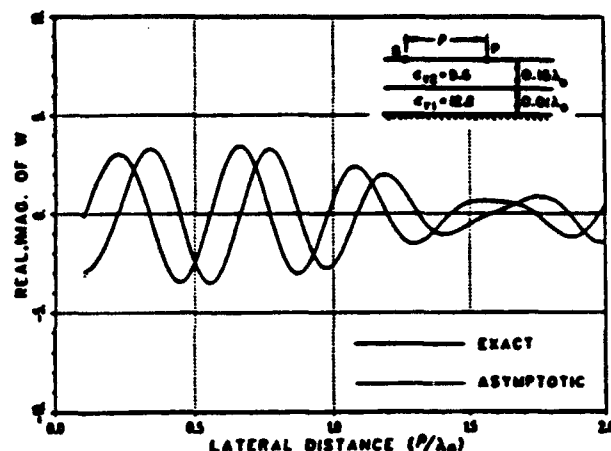


Fig. 7. Exact and asymptotic W for a case in which both source and observation points are along the dielectric-air interface.

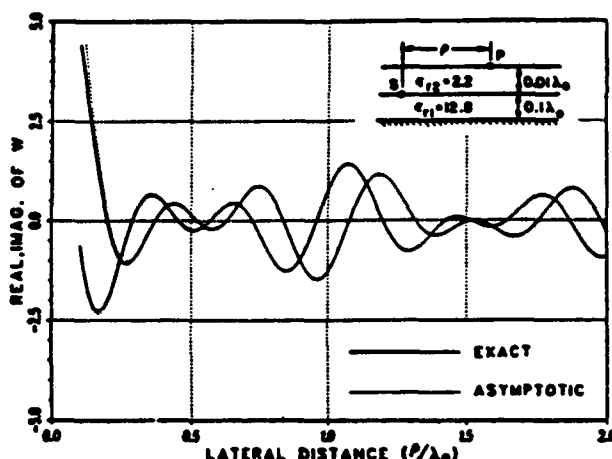


Fig. 6. Comparison between exact and asymptotic W in another example. In this case, source and observation points are along different interfaces.

TABLE I
CPU TIME (MILLISECONDS IN A VAX 8550) TO CALCULATE BOTH U AND W AT SEVERAL DISTANCES FROM THE SOURCE IN THE EXAMPLE OF FIG. 5

Lateral distance (ρ/λ_0)	CPU time numerical integration	CPU time asymptotic closed-form
0.5	84	4
1.0	145	4
2.0	176	4

poles is incorporated into the solution in a manner similar to that done for the improper surface wave poles.

On the other hand, computational efficiency is not the only advantage of an asymptotic solution. It also provides physical insight into the field behavior, giving separate contributions that vividly highlight the different wave phenomena. Thus, the interference between the space wave and the pole wave transition effects is contained in (42), whereas the effect of proper surface wave poles is explicitly represented by the residue terms in (30) and (31). As

an example, it is known that a TM surface wave can be eliminated by using a superstrate (cover) under certain conditions [1]. It turns out that for nonmagnetic superstrates, the surface wave elimination is only possible when the substrate is very thin, whereas the use of a magnetic second layer allows for much thicker substrates. These facts can be easily shown by plotting the residue (33) at the first TM surface wave pole. This residue actually represents the "strength" with which the TM surface wave is excited, and therefore will vanish when the appropriate conditions are met. Fig. 8 shows an example in which the absolute value of the TM residue (case 1 of the Appendix) is plotted versus superstrate thickness, for both a magnetic and a non-magnetic superstrate. As can be seen, the surface wave residue for the magnetic superstrate¹ exhibits a zero at $d_2 = 0.02\lambda_0$, while in the nonmagnetic case there is no such phenomena. It is noted that both residues reduce to the single-layer case when $d_2 \rightarrow 0$. It must also be mentioned that, for the nonmagnetic superstrate, the next (TE) surface wave arises at $d_2 = 0.033\lambda_0$, while for the magnetic case this occurs at $d_2 = 0.07\lambda_0$.

Also, by using the asymptotic closed-form expressions, we can easily plot the fields produced by an elementary source. Let us imagine an \hat{x} -directed elementary electric dipole in a double-layer structure. If the observation point moves around the source in a circumference of radius R (in the plane of the source), using (1) and (2) we can calculate the E_{xx} and E_{yx} "planar" radiation patterns, as a function of the aspect angle ϕ with the \hat{x} -axis. Fig. 9 shows the results for a structure that supports only one TM surface wave, which produces a lobe of E_{xx} in the endfire direction (note that in free space such a lobe will appear in the broadside direction). However, when another (now TE) surface wave is present, a second lobe appears around $\phi = 90^\circ$, as shown in Fig. 10. In these examples the derivatives in (1) and (2) were evaluated numerically, but for R large enough to where only the

¹Results for the mutual impedance between two printed dipoles in this particular case are presented in [7], Fig. 8.

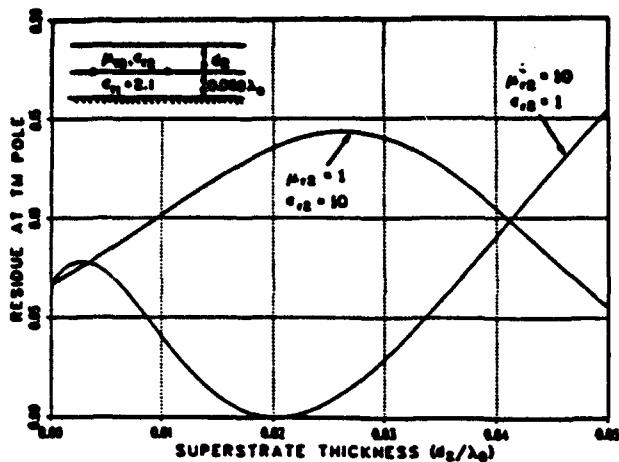


Fig. 8. Residue at the TM surface wave pole for a magnetic ($\mu_{r2} = 10$, $\epsilon_{r2} = 1$) and a non-magnetic ($\epsilon_{r2} = 10$, $\mu_{r2} = 1$) superstrate, versus superstrate thickness.

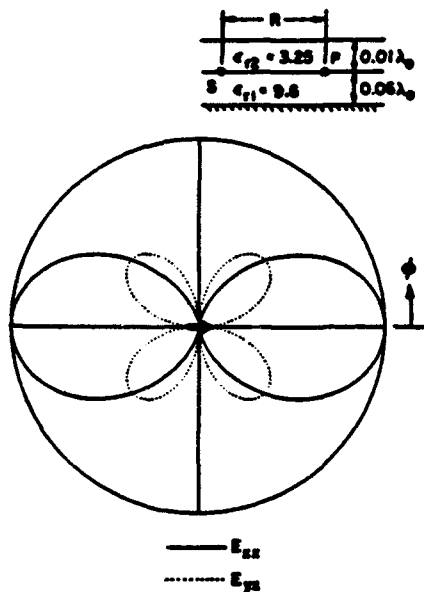


Fig. 9. Normalized surface fields E_{xx} , E_{yx} produced by an elementary electric dipole at a distance R , versus ϕ ($R = 5\lambda_0$). In this case, only a TM surface wave exists.

surface waves [first terms in (30) and (31)] need to be considered. It can be done analytically, yielding $\sin^2 \phi$ or $\cos^2 \phi$ type patterns corresponding to the TE or TM surface wave poles, respectively.

Finally, since the calculation of the field produced by an elementary source is extremely efficient in terms of computer time, it allows for parametric studies, like the one shown in Fig. 11. In this example, the E_{xx} field produced by an elementary source at $R = 5\lambda_0$, $\phi = 0$ is plotted as a function of both the relative permeability and thickness of the superstrate. The line shown in the figure represents the locus of the combinations (μ_{r2}, d_2) that eliminate the first TM surface wave. As can be seen, the "cut" of the above figure defined by $\mu_{r2} = 10$ is the one already shown in Fig. 8.

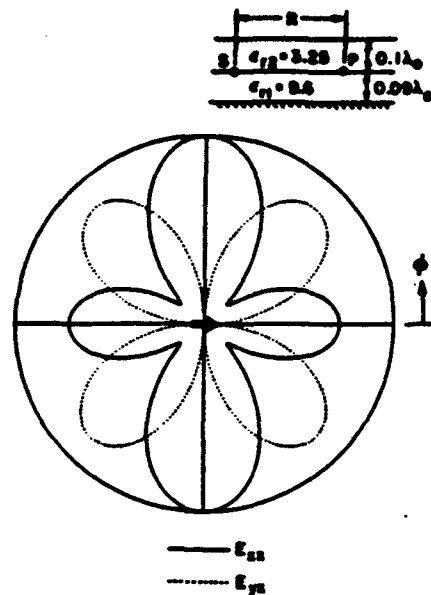


Fig. 10. Normalized surface fields produced by an elementary electric dipole at an observation point (R, ϕ) versus ϕ ($R = 5\lambda_0$). In this case both a TE and a TM surface wave exist.

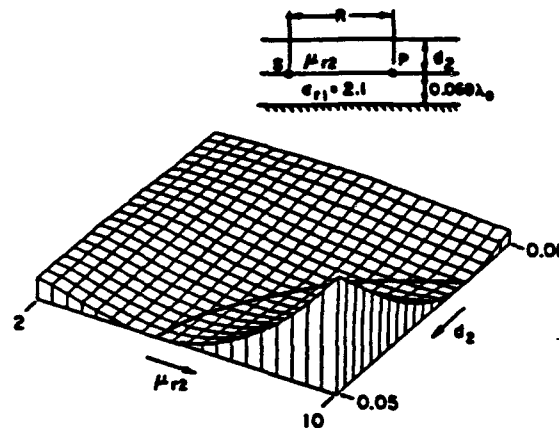


Fig. 11. Magnitude of the E_{xx} field produced by an elementary electric dipole at $R = 5\lambda_0$, $\phi = 0$ as a function of both superstrate permeability and thickness. The solid line shows the locus of the combinations μ_{r2}, d_2 that eliminate the first TM surface wave ($\epsilon_{r2} = 1$).

In conclusion, an asymptotic closed-form approximation for the Green's function of a horizontal electric dipole in a grounded double-layer configuration has been derived. This representation is valid for source and observation points anywhere in the superstrate (including interfaces), although it can be easily extended to cases in which source and/or observation points are in the substrate. The large parameter in the asymptotic approximation is the lateral separation between source and observation points, and the asymptotic solution has been checked to agree with the exact Green's function for lateral separations down to a few tenths of the free-space wavelength. Also, the usefulness of the asymptotic expressions has been demonstrated with illustrative examples. It is noted that the present asymptotic procedure can, in principle, be generalized to n layers; however, the n layer case would

require one to perform certain differentiations in the s plane (as in the Appendix for $n = 2$ case), which can become far more cumbersome than for the $n = 2$ case, if done analytically. At present, we are looking at efficient numerical procedures to overcome this difficult problem in the generalization to n layers. It is believed that these asymptotic closed-form expressions can greatly improve the efficiency of the present methods of analyzing printed circuits/antennas, as well as contribute to a better understanding of the related phenomena.

APPENDIX. DERIVATIVES IN THE S -PLANE

The calculation of derivatives in the s -plane can be done in the general case as follows. We first write $F^{U,W}$ in (6) and (17) using (37) as

$$F^U[\xi = k_0(1 - js^2)] = \frac{N^U(s)}{D_e(s)} \quad (A.1)$$

$$F^W[\xi = k_0(1 - js^2)] = \frac{N_m^W(s)}{D_m(s)} - \frac{N_e^W(s)}{D_e(s)} \quad (A.2)$$

where $D_e(\xi), D_m(\xi)$ are given in (16) and (23); and N^U, N_e^W, N_m^W are simply found by comparing (A.1) and (A.2) with (6) and (17). Now the problem has been reduced to compute derivatives of the form:

$$F'(s) = \frac{\partial}{\partial s} \frac{N(s)}{D(s)} = \frac{N'(s) \cdot D(s) - N(s) D'(s)}{D^2(s)} \quad (A.3)$$

Since we are only interested in the derivatives at $s = 0$ (i.e., $\xi = k_0$), the above formula simplified to:

$$F'(s=0) = \frac{N'(s=0) \cdot D(\xi = k_0) - N(\xi = k_0) \cdot D'(s=0)}{D^2(\xi = k_0)} \quad (A.4)$$

Using the formulas in Section II, N^U, N_e^W, N_m^W and $D_{e,m}$ at $\xi = k_0$ are easily found. The only remaining quantities to evaluate in (A.4) are the first derivatives of N^U, N_e^W, N_m^W and $D_{e,m}$ at $s = 0$. These are given by:

$$D_e'(s=0) = (-k_0\sqrt{2}e^{j\pi/4}) \left[-\frac{j}{\mu_1} \left\{ \frac{\sqrt{n_1-1}}{\tan(k_0 d_1 \sqrt{n_1-1})} \right\} \frac{\mu_2}{\sqrt{n_2-1}} \cdot (1 - e^{-2jk_0 d_2 \sqrt{n_2-1}}) + 1 + e^{-2jk_0 d_2 \sqrt{n_2-1}} \right] \quad (A.5)$$

$$D_m'(s=0) = (-k_0\sqrt{2}e^{j\pi/4}) \left[\frac{j}{\epsilon_1} \left\{ \sqrt{n_1-1} \tan(k_0 d_1 \sqrt{n_1-1}) \right\} \cdot \frac{\epsilon_2}{\sqrt{n_2-1}} (1 - e^{-2jk_0 d_2 \sqrt{n_2-1}}) + 1 + e^{-2jk_0 d_2 \sqrt{n_2-1}} \right] \quad (A.6)$$

Note that D_e, D_m do not depend on the position of source and/or observation point, so their values at $\xi = k_0$ and their derivatives at $s = 0$ do not need to be changed in the cases described below.

Case 1. Source and Observation Points Both Along the First Interface ($z' = 0, z = 0$):

$$N^U(s=0) = -k_0\sqrt{2}e^{j\pi/4} \frac{1 - e^{-2jk_0 d_2 \sqrt{n_2-1}}}{\sqrt{n_2-1}} \quad (A.7a)$$

$$N_e^W(s=0) = -k_0\sqrt{2}e^{j\pi/4} \sqrt{n_2-1} (1 - e^{-2jk_0 d_2 \sqrt{n_2-1}}) \quad (A.7b)$$

$$N_m^W(s=0) = -jk_0\sqrt{2}e^{j\pi/4} \sqrt{n_1-1} \frac{\epsilon_2}{\epsilon_1} \tan(k_0 d_1 \sqrt{n_1-1}) \cdot [1 + e^{-2jk_0 d_2 \sqrt{n_2-1}}] \quad (A.7c)$$

Case 2. Source and Observation Points Along Different Interfaces ($z' = 0, z = d_2$):

$$N^U(s=0) = 0 \quad (A.8a)$$

$$N_e^W(s=0) = 0 \quad (A.8b)$$

$$N_m^W(s=0) = -jk_0\sqrt{2}e^{j\pi/4} \frac{\epsilon_2}{\epsilon_1} \sqrt{n_1-1} \tan(k_0 d_1 \sqrt{n_1-1}) \cdot 2e^{-jk_0 d_2 \sqrt{n_2-1}} \quad (A.8c)$$

Case 3. Source and Observation Points Both Along the Second Interface ($z' = d_2, z = d_2$):

$$N^U(s=0) = 0 \quad (A.9a)$$

$$N_e^W(s=0) = 0 \quad (A.9b)$$

$$N_m^W(s=0) = -k_0\sqrt{2}e^{j\pi/4} \left\{ \sqrt{n_2-1} (1 - e^{-2jk_0 d_2 \sqrt{n_2-1}}) + j\sqrt{n_1-1} \frac{\epsilon_2}{\epsilon_1} \tan(k_0 d_1 \sqrt{n_1-1}) \cdot (1 + e^{-2jk_0 d_2 \sqrt{n_2-1}}) \right\} \quad (A.9c)$$

ACKNOWLEDGMENT

The authors gratefully acknowledge Sina Barkeshli for numerous helpful and stimulating discussions.

REFERENCES

- [1] N. G. Alexopoulos and D. R. Jackson, "Fundamental superstrate (cover) effects on printed circuit antennas," *IEEE Trans. Antennas Propagat.*, vol. AP-32, pp. 807-816, Aug. 1984.
- [2] D. R. Jackson and N. G. Alexopoulos, "Gain enhancement methods for printed circuit antennas," *IEEE Trans. Antennas Propagat.*, vol. AP-33, pp. 976-987, Sept. 1985.
- [3] I. E. Rana and N. G. Alexopoulos, "Current distribution and input impedance of printed dipoles," *IEEE Trans. Antennas Propagat.*, vol. AP-29, pp. 99-106, Jan. 1981.

- [4] D. M. Pozar, "Input impedance and mutual coupling of rectangular microstrip antennas," *IEEE Trans. Antennas Propagat.*, vol. AP-30, pp. 1191-1196, Nov. 1982.
- [5] P. B. Ketehe and N. G. Alexopoulos, "Frequency-dependent characteristics of microstrip discontinuities in millimeter-wave integrated circuits," *IEEE Trans. Microwave Theory Tech.*, vol. MTT-33, pp. 1029-1035, Oct. 1985.
- [6] R. W. Jackson and D. M. Pozar, "Full-wave analysis of microstrip open-end and gap discontinuities," *IEEE Trans. Microwave Theory Tech.*, vol. MTT-33, pp. 1036-1042, Oct. 1985.
- [7] D. R. Jackson and N. G. Alexopoulos, "Analysis of planar strip geometries in a substrate-superstrate configuration," *IEEE Trans. Antennas Propagat.*, vol. AP-34, pp. 1430-1438, Dec. 1986.
- [8] J. R. Monig, "Arbitrarily shaped microstrip structures and their analysis with a mixed potential integral equation," *IEEE Trans. Antennas Propagat.*, vol. AP-36, pp. 314-323, Feb. 1988.
- [9] S. Barkeshli, "An efficient approach for evaluating the planar microstrip Green's function and its applications to the analysis of microstrip antennas and arrays," Ph.D. dissertation, The Ohio State Univ., Dept. of Elect. Eng., Columbus, OH, 1988.
- [10] S. Barkeshli, P. H. Pathak, and M. Marin, "An asymptotic closed form microstrip surface Green's function for the efficient moment method analysis of mutual coupling in microstrip antenna arrays," *IEEE Trans. Antennas Propagat.*, vol. AP-38, no. 9, pp. 1374-1383, Sept. 1990.
- [11] M. Marin, S. Barkeshli, and P. H. Pathak, "Efficient analysis of planar microstrip geometries using an asymptotic closed-form of the grounded dielectric slab Green's function," *IEEE Trans. Microwave Theory Tech.*, vol. MTT-37, no. 4, pp. 669-678, Apr. 1989.
- [12] R. E. Collin, *Field Theory of Guided Waves*. New York: McGraw-Hill, 1960.
- [13] M. Marin, S. Barkeshli, and P. H. Pathak, "On the location of surface and leaky wave poles for the grounded dielectric slab," *IEEE Trans. Antennas Propagat.*, vol. AP-38, pp. 570-573, Apr. 1990.
- [14] L. B. Felsen and N. Marcuvitz, *Radiation and Scattering of Waves*. Englewood Cliffs, NJ: Prentice-Hall, 1973.
- [15] R. G. Rojas, "Comparison between two asymptotic methods," *IEEE Trans. Antennas Propagat.*, vol. AP-35, pp. 1489-1492, Dec. 1987.
- [16] S. Barkeshli and P. H. Pathak, "Radially propagating and steepest descent path integral representations of the planar microstrip dyadic Green's function," *Radio Sci.*, vol. 25, no. 2, pp. 161-174, Mar.-Apr. 1990.

M. A. Marin (M'87) for a photograph and biography please see page 1383 of the September 1990 issue of this TRANSACTIONS.

Prabhakar H. Pathak (M'76-SM'81-F'86), for photograph and biography, please see page 4 of the January 1988 issue of this TRANSACTIONS.

High Throughput Slotted ALOHA Packet Radio Networks with Adaptive Arrays

James Ward, *Member, IEEE*, and R. Ted Compton, Jr.

Abstract—We consider the use of a *multiple beam adaptive array* (MBAA) in a packet radio system. In a multiple beam adaptive array, a given set of antenna elements is used to form several antenna patterns simultaneously. When used in a packet radio system, an MBAA can successfully receive two or more overlapping packets at the same time. Each beam captures a different packet by automatically pointing its pattern toward one packet while nulling other contending packets. This paper describes how an MBAA can be integrated into a single-hop slotted ALOHA packet radio system and analyzes the resulting throughput for both finite and infinite user populations.

I. INTRODUCTION

IN an ALOHA packet radio system, radio terminals transmit packets to each other in a common channel. In the original ALOHA system, packet collisions limit channel throughput to 18% for unslotted ALOHA and 36% for slotted ALOHA [1]. This low throughput has motivated much research on collision resolution algorithms and better protocols to obtain higher throughputs while still permitting random access [2], [3].

Underlying most work on improved protocols is the assumption that a packet terminal can receive only one packet successfully at a time. It is assumed that when two or more packets collide, none is received correctly. In some systems a capture effect [4]–[8] may allow one packet to be received correctly during a collision. However, even with capture, it is still usually assumed that a terminal can receive only one packet at a time.

The main exception to this assumption occurs in spread spectrum systems. Spread spectrum packet systems allow

reception of more than one packet in the same slot [10], [11]. However, spread spectrum systems require much wider bandwidths than conventional ALOHA systems for the same information rate.

Recently, Ghez *et al.* [12], [13] proposed a general “Multipacket ALOHA” model in which multiple packets may be successful in each slot. Their work mainly addresses the stability and optimal control of a general multiple capture system, with the emphasis on spread-spectrum slotted ALOHA systems.

In this paper we present a new method for achieving multiple captures in a slot: the use of an adaptive array [14] as the receiving antenna at a packet radio terminal. We propose a system where the signals from a set of array elements are combined with more than one set of weights to form several simultaneous receiving patterns. We call such an array a *multiple-beam adaptive array* (MBAA). Each beam has its maximum response in the direction of one of the arriving packets and has nulls on the other packets. Such an MBAA allows a terminal to receive several packets successfully in each slot. Moreover, it provides this capability without any need for additional bandwidth as in a spread spectrum system.

In a previous paper [15], the authors showed how a single-beam adaptive array could be used in a slotted ALOHA system to receive one packet correctly in the presence of interfering packets. The performance improvement obtained with a single beam adaptive array is similar to that obtained with Carrier Sense Multiple access (CSMA) [16]. However, the adaptive array technique has the advantage over CSMA that it does not require all terminals in the network be able to hear each other.

With an MBAA, however, a much more substantial improvement can be obtained than with a single-beam adaptive array. In this paper, we describe how an MBAA can be used in a slotted packet system, and we evaluate the performance of a single-hop ALOHA network with an MBAA. We obtain results for a finite population system by using a Markov chain model for the system backlog similar to that in [12]. We also obtain results for an infinite population system by applying a theorem due to Ghez *et al.* [13]. Our results show that a very significant improvement in both throughput and delay can be achieved with only modest MBAA capabilities.

Paper approved by the Editor for Mobile Communications of the IEEE Communications Society. Manuscript received July 13, 1990; revised April 17, 1991.

This work was supported in part by the U.S. Army Research Office, Research Triangle Park, NC, and by the Office of Naval Research, Arlington, VA, under contracts DAAL03-89-K-0073 and N00014-89-J-1007 with The Ohio State University Research Foundation, Columbus, OH. This paper was presented in part at the 25th Annual Asilomar Conference on Signals, Systems, and Computers, Pacific Grove, CA, November 1991.

J. Ward was with the ElectroScience Laboratory, The Ohio State University, Columbus, OH 43212. He is now with M.I.T. Lincoln Laboratory, P.O. Box 73, Lexington, MA, 02173.

R. T. Compton, Jr. was with the ElectroScience Laboratory, The Ohio State University, Columbus, OH 43212. He is now with Compton Research, Inc., Worthington, OH 43085.

IEEE Log Number 9208046.

The MBAA technique described here should not be confused with the use of multiple beam antennas in satellite communications. Satellite multiple beam antennas consist of a number of fixed beams, which divide the coverage area into spatially disjoint geographical regions. Several authors [17]–[20] have considered systems where users in a particular region (beam) access the satellite according to an ALOHA protocol. In this case, each beam represents an independent ALOHA process. The use of multiple uplink beams reduces the overall contention by allowing users from different regions simultaneous access to the satellite. However, collisions still result for users within the same region. Satellite systems with scanned beams have also been proposed [21]. In these systems, users in a given region can access the satellite only during the time when their region is covered by the satellite beam.

For the MBAA concept presented here, however, any beam can receive a packet from any user. Each beam responds adaptively to all the packets transmitted in each slot. Each packet is captured by a separate beam that nulls other contending packets. This technique allows multiple packets to be received successfully in the same slot without requiring any scheduling or reservation-based protocols. Such a system appears to be equally applicable to terrestrial or satellite packet radio systems.

The organization of the paper is as follows. Section II provides a short discussion of multiple-beam adaptive arrays and describes certain of their characteristics that are important for packet radio applications. Section III describes how an MBAA can be used in a packet radio system. In Section IV the throughput and delay performance of a slotted ALOHA system with an MBAA is calculated. Section V presents numerical results, and Section VI contains our conclusions.

II. MULTIPLE-BEAM ADAPTIVE ARRAYS

An adaptive array is an antenna that controls its own pattern, by means of feedback, while it operates [14], [22]. Fig. 1 shows an adaptive array with N_e elements. The complex signal $x_j(t)$ from element j is multiplied by a complex weight w_j and then summed to produce the array output signal $s(t)$. The weights are controlled by a feedback system that maximizes the signal-to-interference-plus-noise ratio (SINR) at the array output. Maximizing the output SINR typically causes the array to steer a beam toward the desired signal and to null other incident signals.

In an adaptive array, the optimal array weights, which maximize the output SINR, are given by [14]

$$W = \Phi^{-1} S, \quad (1)$$

where W is the weight vector,

$$W = [w_1, w_2, \dots, w_{N_e}]^T, \quad (2)$$

Φ is the covariance matrix,

$$\Phi = E[X^* X^T], \quad (3)$$

and S is the steering vector,

$$S = E[X^* \tilde{r}(t)]. \quad (4)$$

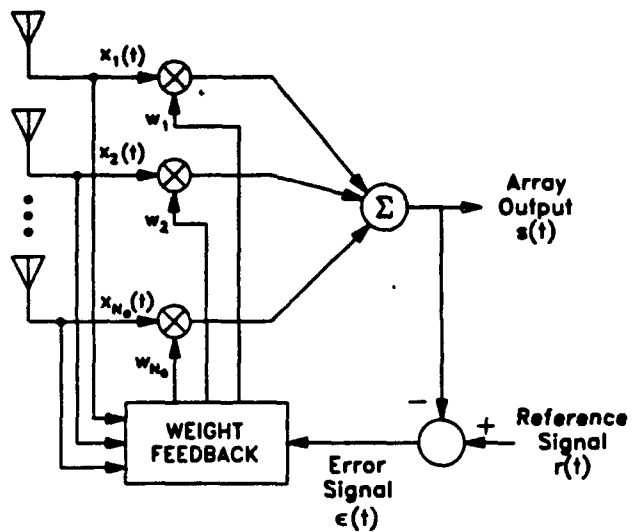


Fig. 1 An adaptive antenna array.

In these equations, X is the signal vector,

$$X = [x_1(t), x_2(t), \dots, x_{N_e}(t)]^T, \quad (5)$$

and $\tilde{r}(t)$ is a locally generated reference signal, usually derived from the array output [14]. (T denotes transpose and $*$ complex conjugate.)

Several algorithms can be used to control the weights in an adaptive array to make them approach the optimal weights in (1) [14]. The Sample Matrix Inverse (SMI) algorithm of Reed *et al.* [23], for example, is a popular technique. In the SMI algorithm, the array signals are sampled, the covariance matrix and steering vector are estimated from these samples, and the weights are obtained by solving a linear system of equations. The sample covariance matrix is calculated from

$$\hat{\Phi} = \frac{1}{N_s} \sum_{k=1}^{N_s} X^*(k) X^T(k), \quad (6)$$

and the sample steering vector from

$$\hat{S} = \frac{1}{N_s} \sum_{k=1}^{N_s} X^*(k) \tilde{r}(k), \quad (7)$$

where $X(k)$ and $\tilde{r}(k)$ denote the k th samples of the signal vector X and the reference signal $\tilde{r}(t)$, and N_s is the number of samples. The array weights are then obtained by solving

$$\hat{\Phi} W = \hat{S} \quad (8)$$

for W . Reed *et al.* [23] have shown that approximately $N_s = 2N_e$ samples are needed to achieve an average SINR within 3 dB of the optimal SINR. For the system described below, we assume the SMI algorithm is used.

The simple adaptive array shown in Fig. 1 has a single output signal. However, an adaptive array need not be limited to one output signal. One can obtain multiple output signals from the same set of elements by applying multiple sets of weights to the same element signals. Each set of weights yields a different array output, representing a different array pattern, or beam. It is possible to choose the weights so each pattern

has its maximum on a different incoming packet and also has nulls on all the other packets. We shall call such an adaptive array with multiple sets of weights a *multiple-beam adaptive array* (MBAA). By using an MBAA as the receiving antenna at a packet radio terminal, it is possible for that terminal to receive more than one packet successfully at a time.

An MBAA with K beams is essentially K simple adaptive arrays operating in parallel with the same antenna elements. Each beam requires a steering vector chosen for a different incoming packet. (The next section explains how the required steering vectors may be obtained.)

Two factors limit the performance of an adaptive array: the number of degrees of freedom it has and its angular resolution. An adaptive array with N_e elements has only $N_e - 1$ degrees of freedom in its pattern [14]. Each null or beam maximum formed by the array requires one degree of freedom. For this application, each MBAA beam must use one degree of freedom to form a pattern maximum on one of the packets. Thus, each beam can null up to $N = N_e - 2$ interfering packets. If there are more than N interfering packets, the output SINR from the array will usually be too low for successful reception.

The resolution capability of an array depends primarily on the array aperture size but also to a lesser extent on the element patterns and the number of elements. Array resolution is important in a packet system because if the arrival angles of an interfering packet and the desired packet are too close, the array cannot simultaneously null the interference and form a pattern maximum on the desired packet. In this case, the output SINR from the array will again be too low for the reception of the desired packet. We shall characterize the resolution capability of an adaptive antenna by its *resolution width* θ_r . We define θ_r to be the minimum angular separation between a desired and interfering packet at which the array can maintain an output SINR as large as the output SNR for a packet received by an omnidirectional antenna. In general, θ_r is much less than the beamwidth between first nulls of the array, because of the array gain. Since each beam in an MBAA uses the same antenna elements, the resolution width and the number of available adaptive array nulls are the same for each beam.

With this background, we now describe the use of an MBAA in a packet radio network.

III. A PACKET RADIO-MBAA SYSTEM

Consider a packet radio system in which multiple terminals send packets to a base station, as shown in Figs. 2 and 3. Assume the network uses a slotted ALOHA protocol. Each packet received at the base station is demodulated and checked for errors using an error detection code on the packet. If no errors are detected, the packet is successful. If errors are found, the packet is unsuccessful and is simply discarded. For each successful packet, an acknowledgment is sent from the base station back to the network. Acknowledgments are done on a different frequency than incoming packets, so the base station and the terminals can transmit and receive at the same time. Unacknowledged packets are retransmitted after a delay.

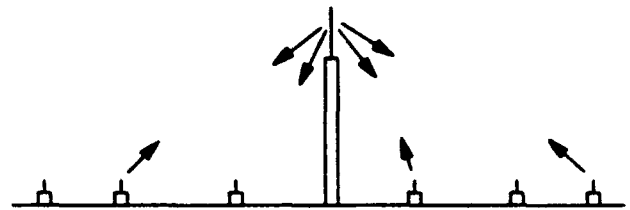


Fig. 2. A single-hop packet radio network with a central base station.

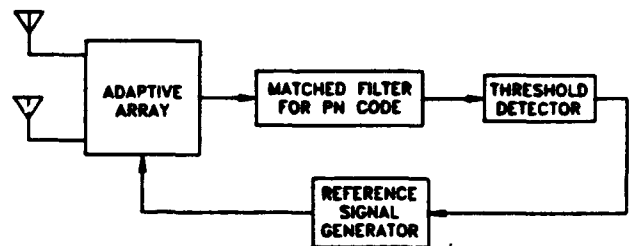


Fig. 3. Block diagram of the acquisition circuitry for a single-beam adaptive array.

To improve the throughput into the base station, an MBAA is used as the receiving antenna at the base station. The patterns of the MBAA beams will be adapted to the incoming packets in each slot.

The main problem in using an MBAA in a packet radio network is the *acquisition problem*, i.e., the problem of locking each beam onto a different packet while nulling all other packets in the slot. We use the following technique for acquisition.

First, we add a special preamble to the beginning of each packet. This preamble consists of three periods of a known pseudonoise (PN) sequence [25]. Second, we make the width of the slot slightly larger than the packet width by an *uncertainty interval*. Packet transmission times from each user are then randomized over this interval in each slot, so each packet arrives at a slightly different time.

Packets are then acquired as follows. Suppose first that only one beam is to be formed. The goal is to point the beam toward the first packet to arrive in each slot with nulls on any other packets in that slot. For packet acquisition, a single array element with an omnidirectional pattern will be used as the receiving antenna, so any packet can access the system. The omnidirectional element output is passed through a matched filter, as shown in Fig. 4. This filter is matched to one period of the preamble PN code. At the filter output, a timing spike occurs after each period of the preamble code for each packet. The filter output is compared to a threshold, and the first threshold crossing in the slot triggers calculation of the array weights for that packet. The weights are calculated over one period of the PN code. The element signals $x_i(t)$ in Fig. 1 are sampled in baseband I and Q samples during the entire slot. $\hat{\Phi}$ in (6) and \hat{S} in (7) are computed over one period of the preamble code by using the received samples and a stored replica of the preamble PN code. The threshold crossing is used to determine the correct timing of the N_s samples used in (6) and (7). The weights are then obtained by solving (8). These weights are used for the rest of the slot.

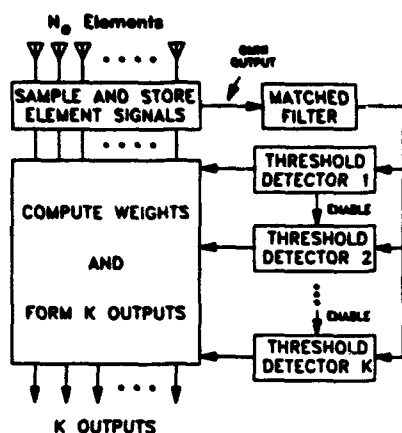


Fig. 4. Block diagram of a multiple-beam adaptive array and the acquisition signal processing.

If a second packet arrives in the same slot, the first packet will still be received successfully as long as the second packet arrives at least one bit later than the first. There are three reasons why this is so.

First, the threshold detection logic will be designed so that the weight calculation process begins only once per slot.¹ Even though later packets in the same slot cause additional timing spikes at the matched filter output, the threshold detector will not respond to these later spikes.

Second, the length of the uncertainty interval will be chosen just less than one period of the preamble PN sequence. Consequently, all interfering packets in a given slot will be present during the second period of the first packet preamble, when the weights are calculated. Thus the interfering packets will be included in the calculation of $\hat{\Phi}$. The presence of interfering packets in $\hat{\Phi}$ causes the array to null the interfering packets.

Finally, when the second packet is at least one bit later than the first, it will be essentially uncorrelated with the stored code replica $r(t)$. (The cross-correlation of two PN codes is small as long as they are displaced at least one bit from one another.) Hence the second packet will have little effect on the computed value of \hat{S} .

However, if a second packet arrives less than one bit after the first packet, the calculated value of \hat{S} will be in error because of the correlation between the two packets. In this case it is assumed the array will lose both packets.

Now consider packet acquisition for an MBAA that can receive multiple packets per slot. To acquire multiple packets, the signal processing in Fig. 4 will be used. Each adaptive array beam will have a separate threshold detector and weight calculation module. The first packet in a slot will trigger threshold detector 1 (TD1). When TD1 is triggered, it will enable TD2, whose function is to acquire the next packet, if another one arrives. (TD2 will not operate until after TD1 has been triggered.) Similarly, TD3, whose job is to acquire a third packet, will be enabled once TD2 is triggered, and so on. When the threshold detector for each beam is triggered, a

separate weight calculation will be done to obtain the weights for that beam, in the same manner as described above.

In the next section, we analyze the performance of a packet radio system using this technique.

IV. PERFORMANCE ANALYSIS FOR A K-BEAM MBAA

In this section we model the operation of a single-hop slotted ALOHA system using an MBAA at the base station. For a finite population system, we extend the Markov chain model of Namislo [5] to include the effect of the MBAA. For an infinite population system, we make use of a theorem due to Ghez *et al.* [13]. In both cases the effect of the MBAA appears only through the success probabilities $P_s(i|j, K)$, where $P_s(i|j, K)$ is the probability that i packets are successful in a slot, given that j packets were transmitted in the slot and given that the base station MBAA has K beams. We begin by obtaining these success probabilities.

A. MBAA Success Probabilities

To understand how the adaptive array affects performance, it is necessary to distinguish between *acquired* packets and *successful* packets. An acquired packet is one that trips the threshold detector and causes weight calculations to begin for that packet. Acquisition depends on the relative arrival times of the incoming packets, the length of the PN code in the acquisition preamble, and the threshold level. However, packet acquisition does not by itself guarantee successful reception. For success, the adaptive array must also be able to null other packets that arrive in the same slot. After a packet is acquired, success still depends on: 1) the arrival angles of any interfering packets in that slot (because of array resolution), 2) the number of available beams (because a packet can be acquired only when a beam is available), and 3) the total number of packets in the slot (because of the finite number of nulls available in the array). Only successful packets contribute to the system throughput.

We assume that each beam of the K -beam MBAA can form N nulls and has a resolution width of θ_r . In a given slot, we characterize each packet by an arrival time and an arrival angle. We assume that packet arrival times are random variables uniformly distributed on the interval $[0, T_u]$ within each slot, where T_u is length of the uncertainty interval in each slot. We set $T_u = (\tau - 1)T_b$, where τ is the period of the preamble PN code in bits and T_b is the bit duration. We assume packet arrival angles are random variables independent of the arrival times and uniformly distributed in azimuth $[0, 2\pi]$ about the MBAA.

For the acquisition scheme described in Section III, a packet arriving at time t_1 is acquired if one of the beams begins weight calculation for that packet and no interfering packets arrive within $\pm T_b$ of time t_1 . We define $P_a(l|j, K)$ to be the probability that l packets are acquired given that j packets are transmitted in the slot and there are K beams. We also define $P_{sa}(i|l, j, K)$ to be the probability that i packets are successful given that l packets are acquired, j packets are transmitted, and there are K beams. Because each beam has N nulls, we assume that no acquired packets are successful

¹In this discussion we are still considering the case of a single-beam array.

if $j > N + 1$. For $j \leq N + 1$, an acquired packet will be successful as long as no interfering packet arrives from an angle within θ_r of the acquired packet arrival angle.

Let $P(l, i | j, K)$ be the joint probability that l packets are acquired and i of them are successful, given that j packets are transmitted in the slot. Then

$$P(l, i | j, K) = P_a(l | j, K) P_{s|a}(i | l, j, K). \quad (9)$$

$P(l, i | j, K)$ is nonzero only for $i \leq l$, because a packet must first be acquired before it can be successful, and for $l < K$, since we can acquire at most one packet for each beam.

Finally, the success probabilities $P_s(i | j, K)$ are given by

$$\begin{aligned} P_s(i | j, K) &= \sum_{l=i}^{\min(j, K)} P(l, i | j, K) \\ &= \sum_{l=i}^{\min(j, K)} P_a(l | j, K) P_{s|a}(i | l, j, K), \end{aligned} \quad (10)$$

since there cannot be more acquired or successful packets than the number of packets transmitted. Under the above assumptions, the success probabilities for a single-beam adaptive array were found in [26] to be

$$P_s(1 | j, 1) = \begin{cases} 0, & j = 0 \\ 1, & j = 1 \\ \left(1 - \frac{1}{r-1}\right)^j \left(1 - \frac{\theta_r}{\pi}\right)^{j-1}, & 2 \leq j \leq N+1 \\ 0, & j > N+1 \end{cases} \quad (11)$$

and

$$P_s(0 | j, 1) = 1 - P_s(1 | j, 1). \quad (12)$$

For a two beam MBAA, the derivation of the success probabilities is straightforward but tedious. Obtaining general expressions for both $P_a(l | j, 2)$ and $P_{s|a}(i | l, j, 2)$ involves an induction process with iterated integrals. Because of space limitations, we shall simply state the results here. The complete derivations of these results may be found in [24]. First, the two-beam acquisition probabilities are given by

$$P_a(0 | j, 2) = 1 - P_a(1 | j, 2) - P_a(2 | j, 2), \quad j = 0, 1, 2, \dots, \quad (13)$$

$$P_a(1 | j, 2) = \begin{cases} 0, & j = 0, 2 \\ 1, & j = 1 \\ \left(1 - \frac{1}{r-1}\right)^j - \left(1 - \frac{2}{r-1}\right)^j + \sum_{i=3}^j Q(i | j, 2), & j > 2 \end{cases} \quad (14)$$

$$P_a(2 | j, 2) = \begin{cases} 0, & j < 2 \\ \left(1 - \frac{1}{r-1}\right)^2, & j = 2 \\ \left(1 - \frac{2}{r-1}\right)^j, & j > 2 \end{cases} \quad (15)$$

where

$$Q(i | j, 2) = \left(1 - \frac{2}{r-1}\right)^j - \sum_{k=0}^{i-3} \binom{j}{k} \left(\frac{1}{r-1}\right)^k \left(1 - \frac{3}{r-1}\right)^{j-k}, \quad i = 3, \dots, j-1, \quad (16)$$

and

$$Q(j | j, 2) = \left(1 - \frac{1}{r-1}\right)^j - \sum_{k=0}^{j-3} \binom{j}{k} \left(\frac{1}{r-1}\right)^k \left(1 - \frac{2}{r-1}\right)^{j-k}, \quad j \geq 3. \quad (17)$$

The $P_{s|a}(i | l, j, 2)$ are found [24] to be

$$P_{s|a}(1 | 1, j, 2) = \left(1 - \frac{\theta_r}{\pi}\right)^{j-1}, \quad j \geq 1 \quad (18)$$

$$P_{s|a}(1 | 2, j, 2) = \begin{cases} 0, & j \leq 2 \\ \frac{2}{j-1} \left(1 - \frac{3\theta_r}{2\pi}\right)^{j-1} + \frac{j-3}{j-1} \left(1 - \frac{2\theta_r}{\pi}\right)^{j-1}, & j > 2 \end{cases} \quad (19)$$

$$P_{s|a}(2 | 2, j, 2) = \begin{cases} 0, & j < 2 \\ \left(1 - \frac{\theta_r}{\pi}\right), & j = 2 \\ 2 \sum_{k=1}^{j-2} \binom{j-2}{k} F_r(k, j), & j > 2 \end{cases} \quad (20)$$

where the $F_r(k, j)$ are given by

$$F_r(k, j) = \frac{2}{(2\pi)^{j-1}} \int_{\theta_r}^{2\theta_r} (2\pi - 2\theta_r - \phi)^{j-2-k} \phi^k d\phi + \left(\frac{\theta_r}{\pi}\right)^k \left(1 - \frac{2\theta_r}{\pi}\right)^{j-1-k}, \quad (21)$$

for $k = 1, \dots, j-2$. The two-beam success probabilities can now be found from (10).

In the numerical results below, the success probabilities for the one and two-beam cases were obtained from the above expressions. For $K > 2$, however, deriving general expressions for $P_a(l | j, K)$ and $P_{s|a}(i | l, j, K)$ becomes intractable. Instead, we obtained the success probabilities for $K > 2$ from Monte Carlo simulations. For example, Fig. 5 shows the results of a Monte-Carlo simulation to find the success probabilities $P_s(i | j, 2)$ for the case $N = 8$, $\theta_r = 5^\circ$. The figure shows the estimated success probabilities obtained from the Monte Carlo simulation and the actual success probabilities computed from (15)–(21). Note the excellent agreement between the two.

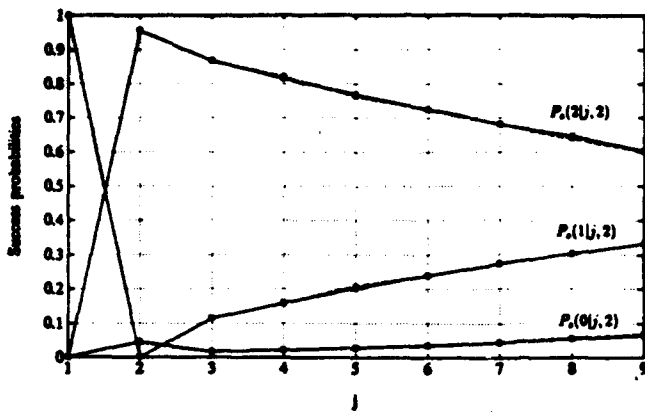


Fig. 5. Comparison of $P_e(i|j, 2)$ obtained analytically with those estimated from a Monte-Carlo simulation. The MBAA parameters are $r = 63$, $\theta_r = 5^\circ$, $N = 8$. The simulation consists of 25 000 trials. (Solid line: theory; dashed line: simulation results.)

B. Finite Population

We assume a finite population of M terminals that send packets to the MBAA. At the beginning of each time slot, each terminal is either *unblocked* or *blocked*, depending on whether its last transmitted packet was successful or not. We assume that at the end of each slot, all terminals receive immediate feedback as to the fate of their packets. We also make the single packet buffer assumption, where blocked terminals are prevented from generating new packets until their backlogged packet is successfully retransmitted. Unblocked terminals transmit a new packet with a probability p_n in each slot. A blocked terminal retransmits its backlogged packet with probability p_r in each slot until successful, at which time it becomes unblocked again. We assume that p_r is constant and that $p_r \geq p_n$ so backlogged packets are quickly cleared.

Given the above assumptions, a sufficient state description for the system at slot k is the number of blocked terminals X_k at the beginning of slot k . Since the number of blocked terminals at the beginning of slot $k+1$ depends only on the number blocked at slot k and the number of successful packets during slot k , the process X_k is a Markov chain. The state space of this Markov chain is $E_X = \{0, \dots, M\}$, where M is the number of terminals in the network.

Let $n_t = n_n + n_r$ be the number of packets transmitted in a given slot, where n_n is the number of new packets and n_r the number of backlogged packets transmitted. Given that the system is in state $i \in E_X$, the number of blocked terminals retransmitting backlogged packets is a Bernoulli random variable with distribution

$$Q_r(l|i) = \Pr\{n_r = l | X_k = i\} = \binom{i}{l} p_r^l (1-p_r)^{i-l}. \quad (22)$$

Similarly, n_n has distribution

$$Q_n(l|i) = \Pr\{n_n = l | X_k = i\} = \binom{M-i}{l} p_n^l (1-p_n)^{M-i-l}. \quad (23)$$

Thus the total number of packets is distributed according to

$$Q_t(l|i) = \Pr\{n_t = l | X_k = i\} = \sum_{s=0}^l Q_n(s|i) Q_r(l-s|i). \quad (24)$$

To find the transition probabilities of the Markov chain, we consider the operation of the MBAA and enumerate the ways that each possible transition can occur. For an MBAA with K beams, at most K packets can be successful in a slot, so the state can decrease by at most K terminals in a slot. Given that the system is in state i at the beginning of a slot, the possible system transitions during the slot are to states $j = i - \min(i, K), \dots, i, \dots, M$. Listed below are the ways that each possible transition may occur.

- $j < i - K$: Not possible, since at most K packets can be successful in a given slot.
- $j = i - t$, $t = 0, 1, \dots, \min(i, K)$:
 - 1) $n_n = 0$, $n_r \geq t$, and t packets are successful.
 - 2) $n_n = 1$, $n_r \geq t$, and $t+1$ packets are successful.
 - 3) $n_n = 2$, $n_r \geq t$, and $t+2$ packets are successful.
 - ⋮
 - 4) $n_n = K - t$, $n_r \geq t$, and K packets are successful.
- $j = i + t$, $t = 0, 1, \dots, M - i$:
 - 1) $n_n = t$, $n_r \geq 0$, and no packets are successful; all new arrivals become backlogged.
 - 2) $n_n = t + 1$, $n_r \geq 0$, and 1 packet is successful.
 - 3) $n_n = t + 2$, $n_r \geq 0$, and 2 packets are successful.
 - ⋮
 - 4) $n_n = t + K$, $n_r \geq 0$, and K packets are successful.

From the information above and the success probabilities, the transition probabilities $P_{i,j} = \Pr\{X_{k+1} = j | X_k = i\}$ can be written as

$$P_{i,j} = 0; \quad i = K+1, \dots, M, \quad j < i - K, \quad (25)$$

$$P_{i,i-t} = \sum_{m=0}^{K-t} Q_n(m|i) \sum_{l=t}^i Q_r(l|i) P_s(m+t|l+m, K); \quad i = 1, \dots, M, \quad t = 1, \dots, \min(i, K), \quad (26)$$

$$P_{i,i+t} = \sum_{m=t}^{K+t} Q_n(m|i) \sum_{l=0}^i Q_r(l|i) P_s(m-t|l+m, K); \quad i = 0, \dots, M, \quad t = 0, 1, \dots, M - i. \quad (27)$$

We denote the transition probability matrix as $P = [P_{i,j}]$.

This Markov chain is irreducible, aperiodic, and ergodic, since the number of states is finite. Consequently, there exists

a limiting probability distribution $\pi = [\pi(0), \pi(1), \dots, \pi(M)]$ given by the solution to the linear system of equations [27]

$$\pi = \pi P \quad (28)$$

subject to the constraint

$$\sum_{i=0}^M \pi(i) = 1. \quad (29)$$

Once the $\pi(i)$ are found, we can determine the average (long run) throughput, delay, and backlog of the system.

In any slot, the throughput can be from 0 to K packets. We define the conditional throughput $S(i)$ to be the average number of successful packets in a slot given that i terminals are blocked at the beginning of the slot.

$$\begin{aligned} S(i) &= \sum_{m=1}^K m \Pr\{m \text{ packets are successful} \mid X_k = i\} \\ &= \sum_{m=1}^K m \sum_{l=m}^M Q_t(l|i) P_s(m|l, K). \end{aligned} \quad (30)$$

The average throughput is then

$$\bar{S} = \sum_{i=0}^M S(i) \pi(i). \quad (31)$$

The average backlog \bar{B} is the average number of blocked terminals,

$$\bar{B} = \sum_{i=0}^M i \pi(i). \quad (32)$$

The new packet input rate in state i is

$$S_{in}(i) = (M - i) p_n. \quad (33)$$

In the steady state, the average input rate equals the average throughput, so

$$\bar{S}_{in} = S_{in}(\bar{B}) = \bar{S}. \quad (34)$$

We use Little's theorem [28] to express the average delay \bar{D} experienced by a new packet as

$$\bar{D} = \frac{\bar{B}}{\bar{S}_{in}} = \frac{\bar{B}}{\bar{S}}. \quad (35)$$

Due to the single packet buffer assumption, the delay results obtained here are a lower bound on the delay in any system with queues at the terminals. The quantities \bar{S} , \bar{B} , and \bar{D} will be used to compare the performance of the system with different MBAA capabilities.

C. Infinite Population

Ghez *et al.* [12], [13] have recently studied the stability and control of a general multiple capture slotted ALOHA system with an infinite population of users. An infinite population slotted ALOHA system is said to be stable if the backlog Markov chain is ergodic; it is unstable otherwise [29], [30]. Without dynamic control of p_r , the infinite population system with an MBAA is always unstable unless the number of nulls is infinite. However, slotted ALOHA with an MBAA can be stabilized in the same manner as other ALOHA systems [2]. Ghez *et al.* [13] have proven a useful theorem that gives the maximum achievable throughput under optimal control of p_r for a general multiple capture system. We state the theorem below and apply it to our MBAA system. The resulting curves (described in Section V) provide insight as to the effects of the MBAA parameters. The reader is referred to [13] for the proof and for details on the control scheme.

Theorem 1 ([13]): *If new packet arrivals are Poisson distributed, the maximum throughput S_o achievable in a multiple capture channel with optimal control is*

$$S_o = \sup_{x \geq 0} t(x), \quad (36)$$

where

$$t(x) = e^{-x} \sum_{n=1}^{\infty} \frac{x^n}{n!} C_n, \quad (37)$$

and

$$C_n = \sum_{k=1}^n k P_s(k|n). \quad (38)$$

C_n is the average number of successes given that n packets are transmitted.

To apply the above theorem to the case of a K -beam MBAA, we replace the $P_s(k|n)$ in (38) with our K -beam success probabilities $P_s(k|n, K)$ from (10). Recall that $P_s(k|n, K) = 0$ for $n > N + 1$, so that

$$t(x) = e^{-x} \sum_{n=1}^{N+1} \frac{x^n}{n!} C_n. \quad (39)$$

Since $t(x)$ is nonnegative and continuous with $t(0) = t(\infty) = 0$,

$$\sup_{x \geq 0} t(x) = \max_{x \geq 0} t(x). \quad (40)$$

Thus S_o is given as the maximum of (39).

V. NUMERICAL RESULTS

In this Section we present typical performance results for a network equipped with an MBAA. First we examine a finite population of $M = 50$ terminals using the results of Section IV-B.

Fig. 6 shows the conditional throughput $S(i)$ as a function of the number of blocked users for several cases when $p_r = 0.2$ and $p_n = 0.02$ so that, on average, more than one packet

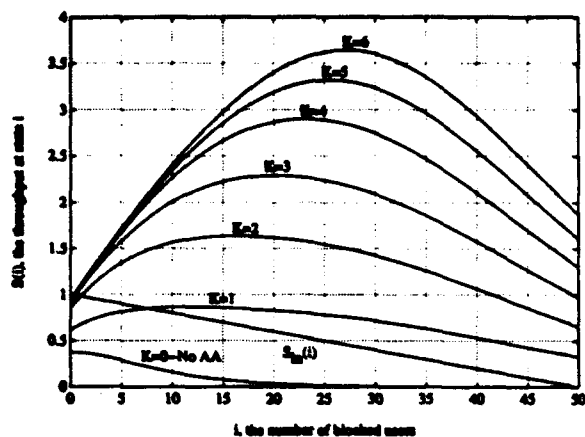


Fig. 6. $S(i)$ and $S_{in}(i)$ for an $M = 50$ terminal system as the number of MBAA beams is increased. $p_n = 0.02$, $p_r = 0.2$, $N = 8$, $\theta_r = 5^\circ$, $r = 63$.

per slot is arriving at the base station. $S(i)$ and $S_{in}(i)$ (the load line) are plotted for MBAA's with $K = 1$ to 6 beams. These curves are for $N = 8$ nulls and $\theta_r = 5^\circ$, corresponding to a 10-element antenna array. The period of the preamble PN code is $r = 63$. Fig. 6 also shows the $S(i)$ that results for slotted ALOHA without an adaptive array. It may be seen that the conditional throughput increases significantly as the adaptive array is added and the number of beams is increased. Conditional throughput levels of nearly 4 packets per slot are possible with a 6-beam MBAA.

Fig. 6 also provides insight into the stability and average performance of the system. Although the Markov chain describing the finite population slotted ALOHA system is always ergodic, we can discuss the stability in the sense of [1], [31]. The finite population ALOHA model is said to be stable if there is a single intersection point of the $S(i)$ and $S_{in}(i)$ curves. Ideally, this intersection point should occur in a region of high throughput and low delay. If there is one intersection point in a region of very low throughput and high delay, the system is said to be saturated, and if more than one intersection point exists, the system operates in a bistable mode, in which case the average performance is typically poor. When there is only one intersection point, the average performance is approximated by the performance level at the intersection point. We see that without an adaptive array, performance is very poor, with essentially zero throughput and all terminals blocked. This is to be expected, since the total traffic is more than one packet per slot. All the MBAA cases are stable. In general, increasing any of the MBAA capabilities has a stabilizing effect on the system. As K is increased the average throughput increases from 0.83 packets/slot with $K = 1$ to 0.994 packets/slot for $K > 3$ beams.

For larger K , the input traffic (p_n and M) or the retransmission probability (p_r) can also be increased substantially while still maintaining "stability." In Fig. 6, near optimal throughput of $Mp_n = 1.0$ packets per slot is achieved with only 2 beams, and the performance for 3 or more beams is essentially the same as for the 2-beam case. For $K \geq 2$, we could improve the delay performance slightly by increasing p_r , but the average throughput will not increase noticeably since

the 2-beam throughput is already very close to the maximum. However, for $K \geq 2$, Mp_n is much less than the maximum value of the conditional throughput, so there is room for the average throughput to be significantly increased by increasing the input traffic.

Fig. 7 shows the average performance as a function of p_n . The retransmission probability is 0.2 for all cases. Fig. 7(a) shows the average throughput. For low traffic, the rise in average throughput is approximately linear with p_n . In this region there is essentially no backlog and the maximum average throughput of $\bar{S} = Mp_n$ is very nearly attained. The length of this linear region increases with the number of beams until the total traffic on average exceeds the adaptive array capabilities. As p_n increases, more collisions are destructive (no captures) due to either poor acquisition (a collision in time), insufficient array resolution (a collision in angle), or not enough nulls per beam. Thus, the average throughput peaks and begins to decrease. Increasing p_n further drives the system toward saturation where nearly all terminals are blocked.

Fig. 7(b) shows \bar{D} versus \bar{S} for the same cases. These curves exhibit the typical bistable ALOHA behavior. Any throughput less than the maximum can be achieved at a desirable low delay point or at an undesirable high delay point. Fig. 7(c) shows the average delay versus p_n . When the input traffic is high, the delay improvement provided by additional beams can be quite large. The increased capacity provided by the multiple beams reduces the delay experienced when the system is highly backlogged. Fig. 7(d) shows the average backlog.

We now show results for an infinite population form Section IV-C. For a particular choice of MBAA parameters, we compute $t(x)$ from (39) and find its maximum numerically. This maximum value is S_0 . Fig. 8 shows S_0 as the number of beams and nulls per beam are increased. Note that when $N = 0$, we get the standard slotted ALOHA (no MBAA) maximum throughput² of e^{-1} . Several important points are evident. For a given number of beams there is a minimum number of nulls above which no further improvement in throughput is obtained. As the number of beams increases, one needs more nulls/beam in order to attain the maximum S_0 (for that K). Also, the improvement gained by adding beams becomes larger as the number of nulls increases, until the maximum S_0 is attained. However, this increase in throughput becomes smaller with each additional beam.

Fig. 9 shows how S_0 depends on the resolution width θ_r for a 3-beam adaptive array. As expected, the maximum S_0 increases as the resolution of the array improves (as θ_r decreases). More nulls/beam are required to achieve the maximum S_0 for an array with good resolution than for one with poor resolution.

Fig. 10 shows how S_0 decreases for a 3-beam array as the period r of the preamble code, and thus the length of the uncertainty interval T_u , decreases. The reduction in S_0 is due to the reduced probability of acquiring packets. In general, S_0 drops less as r is reduced from the ideal case of $r = \infty$

²Actually, one should not choose $N < K - 1$ because then some beams will never successfully receive a packet.

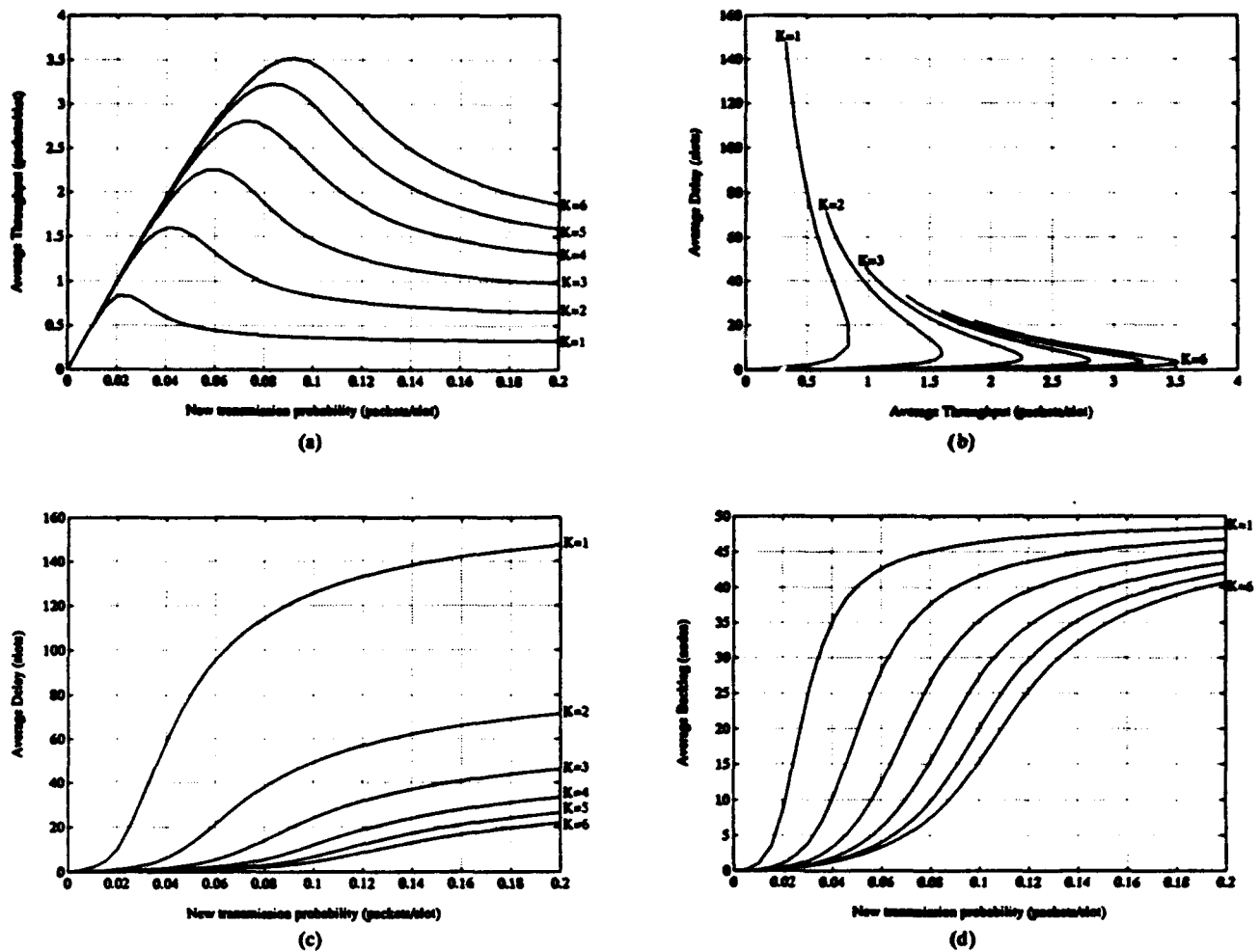


Fig. 7. Average performance. $M = 50$, $p_r = 0.2$, $N = 8$, $\theta_r = 5^\circ$, $r = 63$. (a) \bar{S} versus p_n . (b) \bar{D} versus \bar{S} . (c) \bar{D} versus p_n . (d) \bar{B} versus p_n .

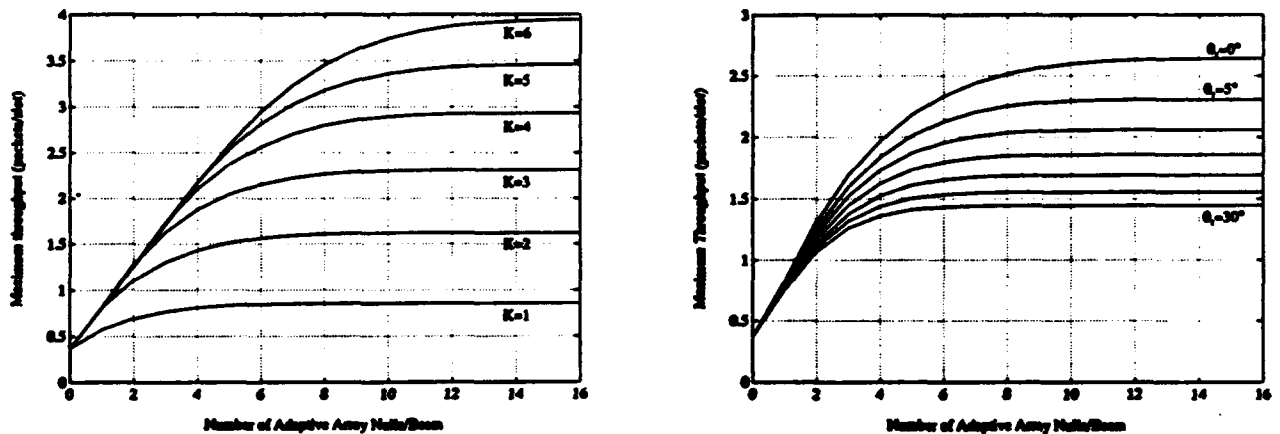


Fig. 8. Maximum throughput S_0 with optimal control as a function of the number of nulls/beam N and the number of beams K . $r = 63$, $\theta_r = 5^\circ$.

Fig. 9. Maximum throughput S_0 with optimal control as a function of the number of nulls/beam N and the resolution width θ_r . $r = 63$, $K = 3$ beams.

than when θ_r is increased from the ideal case of $\theta_r = 0^\circ$. Furthermore, the drop in S_0 with either θ_r or r becomes more severe as the number of beams is increased. In other words, very good acquisition and resolution performance is necessary to obtain the full benefit of a large multiple beam capability. In the ideal case of $\theta_r = 0$, $r = \infty$, the maximum throughput

approaches K as N is increased for a K -beam MBAA.

It should also be noted that the maximum throughput in an infinite population model is always less than that of any finite population model. However, we have observed that the infinite population results closely match those for finite population systems of $M \geq 20$ terminals.

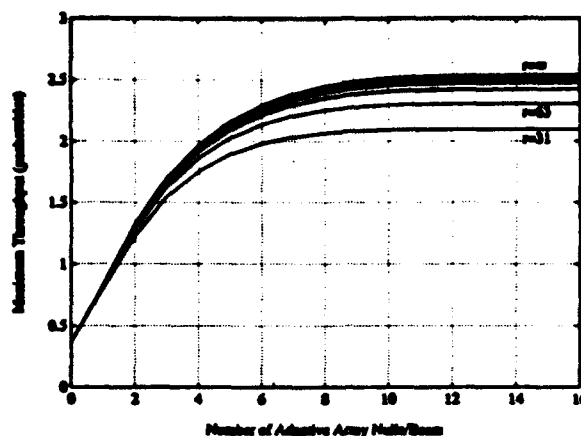


Fig. 10. Maximum throughput S_0 with optimal control as a function of the number of nulls/beam N and the period r of the preamble PN code ($T_n = (r-1)T_b$). $K = 3$ beams, $\theta_r = 5^\circ$.

VI. CONCLUSIONS

In this paper we have proposed the use of a multiple-beam adaptive array to improve the performance of a slotted ALOHA packet radio network. Each beam captures a different packet by automatically pointing its maximum at one packet in each slot and adaptively nulling other packets in that slot. We presented a procedure for packet acquisition and analyzed the performance of a packet system with an MBAA. It was shown that throughput levels between 2 and 4 packets per slot are possible with only modest MBAA capabilities. Even higher throughputs are possible with increased MBAA capabilities. Because this MBAA technique can be used with narrowband packets, it is an attractive alternative to spread-spectrum multiple access techniques.

ACKNOWLEDGMENT

The authors gratefully acknowledge the helpful suggestions of Dr. R. L. Hamilton.

REFERENCES

- [1] A. B. Carlisle and M. E. Hellman, "Bistable behavior of ALOHA-type systems," *IEEE Trans. Commun.*, vol. COM-23, pp. 410-414, Apr. 1975.
- [2] D. Bertsekas and R. Gallager, *Data Networks*, Englewood Cliffs, NJ: Prentice-Hall, 1987.
- [3] A. S. Tanenbaum, *Computer Networks*, Englewood Cliffs, NJ: Prentice-Hall, 1981.
- [4] N. Abramson, "The throughput of packet broadcasting channels," *IEEE Trans. Commun.*, vol. COM-25, pp. 117-128, Jan. 1977.
- [5] C. Namislo, "Analysis of mobile radio slotted ALOHA networks," *IEEE Trans. Vehic. Technol.*, vol. VT-33, pp. 199-204, Aug. 1984.
- [6] C. C. Lee, "Random signal levels for channel access in packet broadcast networks," *IEEE J. Select. Areas Commun.*, vol. SAC-5, pp. 1026-1034, July 1987.
- [7] B. Ramamurthi, A. Saleh, and D. J. Goodman, "Perfect-capture ALOHA for local radio communications," *IEEE J. Select. Areas Commun.*, vol. SAC-5, pp. 806-813, June 1987.
- [8] D. G. Goodman and A. Saleh, "The near/far effect in local ALOHA radio communications," *IEEE Trans. Vehic. Technol.*, vol. VT-36, pp. 19-27, Feb. 1987.
- [9] D. A. Davis and S. A. Gronemeyer, "Performance of slotted ALOHA random access with delay capture and randomized time of arrival," *IEEE Trans. Commun.*, vol. COM-28, pp. 703-710, May 1980.
- [10] M. B. Pursley, "The role of spread spectrum in packet radio networks," *Proc. IEEE*, vol. 75, pp. 116-134, Jan. 1987.
- [11] J. S. Storey and F. A. Tobagi, "Throughput performance of an unslotted directsequence SSMA packet radio network," *IEEE Trans. Commun.*, vol. 37, pp. 814-823, Aug. 1989.
- [12] S. Ghez, S. Verdu, and S. C. Schwartz, "Stability properties of slotted ALOHA with multipacket reception capability," *IEEE Trans. Automat. Contr.*, vol. 33, pp. 640-649, July 1988.
- [13] ———, "Optimal decentralized control in the random access multipacket channel," *IEEE Trans. Automat. Contr.*, vol. 34, pp. 1153-1163, Nov. 1989.
- [14] R. T. Compton, Jr., *Adaptive Antennas—Concepts and Performance*, Englewood Cliffs, NJ: Prentice-Hall, 1988.
- [15] J. Ward and R. T. Compton, Jr., "Improving the performance of a slotted ALOHA packet radio network with an adaptive array," *IEEE Trans. Commun.*, vol. 40, pp. 292-300, Feb. 1992.
- [16] L. Kleinrock, *Queueing Systems, vol. II: Computer Applications*, New York: Wiley, 1976.
- [17] J. K. DeRosa, L. H. Orazow, and L. N. Weiner, "Efficient packet satellite communications," *IEEE Trans. Commun.*, vol. COM-27, pp. 1416-1422, Oct. 1979.
- [18] J. Chang, "Packet satellite system with multiuplinks and priority discipline," *IEEE Trans. Commun.*, vol. COM-30, pp. 1143-1152, May 1982.
- [19] ———, "A multibeam packet satellite using random access techniques," *IEEE Trans. Commun.*, vol. COM-31, pp. 1143-1152, Oct. 1983.
- [20] I. Chlamtasc and O. Ganz, "Performance of multibeam packet satellite systems with conflict free scheduling," *IEEE Trans. Commun.*, vol. COM-34, pp. 1016-1023, Oct. 1986.
- [21] W. W. Wu, *Elements of Digital Satellite Communications*, vol. 1, Rockville, MD: Computer Science Press, 1984.
- [22] R. A. Monzingo and T. W. Miller, *Introduction of Adaptive Arrays*, New York: Wiley, 1980.
- [23] I. S. Reed, J. D. Mallett, and L. E. Brennan, "Rapid convergence rate in adaptive arrays," *IEEE Trans. Aerosp. Electron. Syst.*, vol. AES-10, p. 853, Nov. 1974.
- [24] J. Ward, "Improving the performance of packet radio networks with adaptive arrays," Ph.D. dissertation, Ohio State Univ., Columbus, OH, 1990.
- [25] R. E. Ziemer and R. L. Peterson, *Digital Communications and Spread Spectrum Systems*, New York: Macmillan, 1985.
- [26] J. Ward and R. T. Compton, Jr., "Sidelobe level performance of adaptive sidelobe canceller arrays with element reuse," *IEEE Trans. Antennas Propagat.*, vol. 38, pp. 1684-1693, Oct. 1990.
- [27] Çinar, *Introduction of Stochastic Processes*, Englewood Cliffs, NJ: Prentice-Hall, 1975.
- [28] J. D. C. Little, "A proof for the queueing formula $l = \lambda w$," *Oper. Res.*, vol. 9, pp. 383-387, May 1961.
- [29] G. Fayolle, E. Gelenbe, and J. Labatouille, "Stability and optimal flow control of the packet switching broadcast channel," *J. ACM*, vol. 24, pp. 375-386, July 1977.
- [30] M. Kaplan, "A sufficient condition for the nonergodicity of a Markov chain," *IEEE Trans. Inform. Theory*, vol. IT-25, pp. 470-471, July 1979.
- [31] L. Kleinrock and S. S. Lam, "Packet switching in a multiaccess broadcast channel: Performance evaluation," *IEEE Trans. Commun.*, vol. COM-23, pp. 410-422, Apr. 1975.



James Ward (S'84-M'91) was born in Belleville, NJ, on July 11, 1964. He received the B.E.E. degree from the University of Dayton, Dayton, OH, in 1985, and the M.S.E.E. and Ph.D. degrees in electrical engineering from The Ohio State University, Columbus, in 1987 and 1990, respectively.

From 1985 to 1990 he worked as a Graduate Research Associate at The Ohio State University ElectroScience Laboratory. He is now a Staff Member of the Radar Systems Group at M.I.T. Lincoln Laboratory, Lexington, MA. His current research

interests include radar signal processing, adaptive antenna systems, and packet radio networks.

Dr. Ward is a member of Tau Beta Pi, Sigma Xi, and Phi Kappa Phi.



Ted Compton, Jr., was born in St. Louis, MO, in 1935. He received the S.B. degree from the Massachusetts Institute of Technology, Cambridge, in 1958 and the M.Sc. and Ph.D. degrees from The Ohio State University, Columbus, in 1961 and 1964, respectively, all in electrical engineering.

From 1958 to 1959 he worked at DECO Electronics, Inc. Leesburg, VA, and from 1959 to 1962 he was with Battelle Memorial Institute in Columbus, OH. During 1962-1965, he was a staff member at the Antenna Laboratory (now the Electro-Science

Laboratory) at The Ohio State University. From 1965 to 1967, he was an Assistant Professor of Engineering at Case Institute of Technology Cleveland, OH. He spent the academic year 1967-1968 as a Guest Professor at the Technische Hochschule, Munich, German. In 1968 he returned to the Department of Electrical Engineering at Ohio State University, where he was Associate Professor from 1968 to 1980, Professor from 1980 to 1991, and a member of the staff at the ElectroScience Laboratory. Since 1992, he has been a private consultant. He has worked in a number of areas, including antennas, radar communications, signal processing, and adaptive antennas. He is the author of *Adaptive Antennas—Concepts and Performance* (Prentice-Hall, 1988). His recent work has been in high resolution angle and polarization estimation techniques and in high throughput packet radio networks.

Dr. Compton is a member of Sigma Xi and Pi Mu Epsilon. He has been a Battelle Memorial Institute Graduate Fellow and a National Science Foundation Postdoctoral Fellow. He received the M. Barry Carlton award from the IEEE Aerospace and Electronic Systems Society for best paper in 1983.

A Reciprocity Formulation for the EM Scattering by an Obstacle Within a Large Open Cavity

Prabhakar H. Pathak, *Fellow, IEEE*, and Robert J. Burkholder, *Member, IEEE*

Abstract—A formulation based on a generalized reciprocity theorem is developed for analyzing the external high frequency EM scattering by a complex obstacle inside a relatively arbitrary open-ended waveguide cavity when it is illuminated by an external source. This formulation is also extended to include EM fields whose time dependence may be non-periodic. A significant advantage of this formulation is that it allows one to break up the analysis into two independent parts; one deals with the waveguide cavity shape alone and the other with the obstacle alone. Thus, it is useful for independently estimating the scattering effects due to modifications in the waveguide cavity shape for a given type of large complex obstacle, and due to different types of complex obstacles for a given type of large open waveguide cavity shape, respectively, without requiring one to treat the entire configuration each time one of these is changed. The external scattered field produced by the obstacle (in the presence of the waveguide cavity structure) is given in terms of a generalized reciprocity integral over a surface S_T corresponding to the interior waveguide cavity cross-section located conveniently but sufficiently close to the obstacle. Furthermore, the fields coupled into the cavity from the source in the exterior region generally need to propagate only one-way via the open front end (which is directly illuminated) to the interior surface S_T in this approach, and not back, in order to find the external field scattered by the obstacle.

I. INTRODUCTION

A FORMULATION based on a generalized reciprocity theorem is developed for analyzing the high frequency electromagnetic (EM) scattering by relatively arbitrary open-ended waveguide cavities containing a large complex interior obstacle or termination. An extension of this formulation to include EM fields with non-periodic or arbitrary time dependence is also presented. These results are of significant interest in scattered field and EM coupling predictions. An important advantage of the formulation developed here is that it allows one to independently estimate the effects on the overall cavity-obstacle scattering due to modifications in the waveguide cavity shape for a given interior obstacle, and due to different obstacles for a given open waveguide cavity shape, respectively, without having to analyze the entire cavity-obstacle configuration each time one of them (i.e., the cavity shape or the obstacle) is changed. The latter aspect will be discussed in more detail in a separate paper.

Manuscript received September 26, 1991; revised July 7, 1992. This work was supported in part under Grant NAG3-476 from NASA Lewis Research Center, Cleveland, Ohio, and in part by the Joint Services Electronics Program under Contract No. N00014-89-J-1007.

The authors are with The Ohio State University ElectroScience Laboratory, 1320 Kinnear Road, Columbus, OH 43212.

IEEE Log Number 9206296.

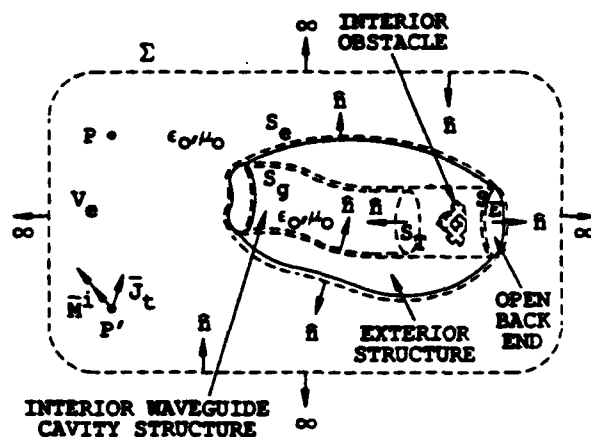


Fig. 1. Original problem configuration.

A typical geometry of the general problem under consideration is depicted in Fig. 1. The geometry is illuminated by an external current source (at P'), and the observer is also assumed to be in the external region (at P). It is primarily of interest in this study to be able to analyze the external scattering from a geometry of the type in Fig. 1 for cases where the open front end of the cavity is directly illuminated by the source, and for observation points which are also in direct view of the open front end, as shown in the figure. Furthermore, the medium surrounding the cavity structure is taken to be free space and the external surface as well as the interior cavity walls are assumed to be impenetrable (e.g. perfectly conducting walls with or without material coating). S_T is an arbitrary surface which either encloses the interior obstacle or partitions the obstacle/termination region from the rest of the open-ended waveguide region (as in Fig. 1), and S_E is the surface defined by the open back end of the cavity beyond the obstacle. It is noted that as a special case, the back end of the cavity (at S_E) could be closed, or the obstacle itself could form a termination which completely closes the back end of the cavity. Furthermore, the waveguide region beyond the obstacle could also, as a special case, be made semi-infinite. These latter special cases of the more general situation depicted in Fig. 1 are discussed in Section II.

The formulation for the field scattered into the exterior region by just the interior obstacle is based on a generalized reciprocity integral which requires a knowledge of the fields on the surfaces S_T and S_E due to the illumination from the original current source (at P') with the obstacle present, and it also requires a knowledge of the fields on S_T and S_E due to a conveniently chosen impressed test current source placed at the

observer location (at P) but in the absence of the obstacle and with the original source turned off. This reciprocity integral which exists over S_T and S_E is shown in the next section to furnish the field scattered into the exterior by the obstacle in the presence of the waveguide cavity structure. Such a formulation has the additional advantage that, in most cases of practical interest, the fields coupled into the cavity from the sources in the exterior region need to propagate only one-way (in the forward direction) via the open front end to the interior surface S_T , and not back (in the reverse direction), in order to find the external field scattered by the obstacle. More will be said about this property later.

The development of the generalized reciprocity integral is given in Section II, and Section III discusses some methods for finding the relevant field quantities which appear within this integral. Section IV presents some numerical results based on this development, and compares them with the corresponding solutions obtained without the use of the generalized reciprocity integral for the sake of establishing an independent check. An $e^{j\omega t}$ time convention for the fields and sources is assumed and suppressed for the periodic or time harmonic case. Also, the cavity-obstacle configuration is assumed to be embedded in free space.

II. GENERALIZED RECIPROCITY INTEGRAL FOR TIME HARMONIC INTERIOR OBSTACLE SCATTERED FIELDS

Consider the open-ended waveguide cavity configuration illustrated in Fig. 1 which is illuminated by an external impressed electric current source $\vec{J}^i(P')$ and a magnetic current source $\vec{M}^i(P')$ at P' . Let (\vec{E}_c, \vec{H}_c) denote the (electric, magnetic) fields which are produced by these sinusoidally time varying impressed sources $\vec{J}^i(P')$ and $\vec{M}^i(P')$ when the cavity structure is present but with the interior obstacle absent. The $\vec{J}^i(P')$ and $\vec{M}^i(P')$ radiating in the presence of the cavity structure and the obstacle produce the fields (\vec{E}, \vec{H}) where

$$\vec{E} = \vec{E}_c + \vec{E}_s \quad (1)$$

$$\vec{H} = \vec{H}_c + \vec{H}_s \quad (2)$$

and (\vec{E}_s, \vec{H}_s) therefore denote the fields scattered by just the interior obstacle but in the presence of the cavity walls. Note that the above fields satisfy the following Maxwell's Curl equations:

$$\begin{cases} \nabla \times \vec{E} = -j\omega\mu_0\vec{H} - \vec{M}^i(P') \\ \nabla \times \vec{H} = \vec{J}^i(P') + j\omega\epsilon_0\vec{E} \end{cases} \quad (3)$$

$$\begin{cases} \nabla \times \vec{E}_c = -j\omega\mu_0\vec{H}_c - \vec{M}^i(P') \\ \nabla \times \vec{H}_c = \vec{J}^i(P') + j\omega\epsilon_0\vec{E}_c \end{cases} \quad (4)$$

and hence,

$$\begin{cases} \nabla \times \vec{E}_s = -j\omega\mu_0\vec{H}_s \\ \nabla \times \vec{H}_s = j\omega\epsilon_0\vec{E}_s \end{cases} \quad (5)$$

It is of primary interest to find (\vec{E}_c, \vec{H}_c) at any external point P when P is on the same side of the cavity as the original source at P' . The fields (\vec{E}_c, \vec{H}_c) can be found in terms of a set of equivalent sources on S_T and S_E (of Fig. 1) along with

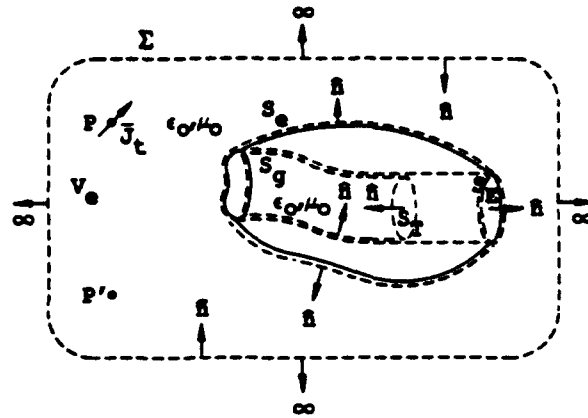


Fig. 2. Related test problem configuration.

a set of test fields, (\vec{E}_t, \vec{H}_t) , which are produced by an electric current test source $\vec{J}_t(P)$ at P that has the same frequency as (\vec{J}^i, \vec{M}^i) when it radiates with the cavity structure present but with the interior obstacle absent, as illustrated in Fig. 2. The fields (\vec{E}_t, \vec{H}_t) satisfy the following Maxwell's Curl equations:

$$\begin{cases} \nabla \times \vec{E}_t = -j\omega\mu_0\vec{H}_t \\ \nabla \times \vec{H}_t = \vec{J}_t(P) + j\omega\epsilon_0\vec{E}_t \end{cases} \quad (6)$$

The fields (\vec{E}_c, \vec{H}_c) can be related to the fields (\vec{E}_t, \vec{H}_t) via the divergence theorem applied to the quantity $\vec{E}_c \times \vec{H}_t - \vec{E}_t \times \vec{H}_c$ within the volume V_e which is bounded by the surfaces $[S_T + S_E + S_g + S_s + \Sigma]$ as shown in Figs. 1 and 2. Thus,

$$\begin{aligned} \int_{V_e} \nabla \cdot (\vec{E}_c \times \vec{H}_t - \vec{E}_t \times \vec{H}_c) dv \\ = - \oint_{\Sigma + S_g + S_s + S_T + S_E} (\vec{E}_c \times \vec{H}_t - \vec{E}_t \times \vec{H}_c) \cdot \hat{n} ds \end{aligned} \quad (7)$$

where \hat{n} is the unit normal vector which points into the region V_e . Using (5) and (6), the L.H.S. of (7) reduces, via the radiation and boundary conditions together with some vector algebra, to

$$\int_{V_e} \vec{J}_t(P) \cdot \vec{E}_c dv = \int_{S_T + S_E} (\vec{E}_c \times \vec{H}_t - \vec{E}_t \times \vec{H}_c) \cdot \hat{n} ds. \quad (8)$$

It is noted that the fields satisfy the radiation condition on Σ as $\Sigma \rightarrow \infty$, hence the integral on Σ vanishes in (7). For perfectly conducting walls, both $\hat{n} \times \vec{E}_c$ as well as $\hat{n} \times \vec{E}_t$ vanish on $S_g + S_s$, so that the integrals on those boundaries also vanish in (7); on the other hand if these walls are coated with absorbing layers, then $S_g + S_s$ is taken to be on the conducting walls, whereas, if the walls are impenetrable then S_g and S_s can be made to lie just within the impenetrable wall of some thickness (however small), so that the integrals on S_g and S_s can be made to vanish again in (7). This leaves one with integrals only over S_T and S_E on the R.H.S. of (7), thereby leading directly to the expression on the R.H.S.

of (8). The result in (8) constitutes a generalized reciprocity relationship because (\vec{E}_c, \vec{H}_c) and (\vec{E}_t, \vec{H}_t) are evaluated in different environments, i.e., (\vec{E}_c, \vec{H}_c) are found with the interior obstacle present while (\vec{E}_t, \vec{H}_t) are found with the interior obstacle absent. In contrast, the standard reciprocity theorem [1] relates a pair of fields (due to a pair of sources) in the same environment.

Let the test current $\vec{J}_t(P)$ be a point source of strength \vec{P}_t ; thus,

$$\vec{J}_t(P) = \vec{P}_t \delta(\vec{r}'' - \vec{r}) \quad (9)$$

where \vec{r} is the position vector of the observation point at P and \vec{r}'' is the variable of integration (in V_c) on the L.H.S. of (8). Now, from (8) and (9) one obtains,

$$\vec{P}_t \cdot \vec{E}_c(\vec{r}) = \int_{S_T + S_E} (\vec{E}_c \times \vec{H}_t - \vec{E}_t \times \vec{H}_c) \cdot \hat{n} ds. \quad (10)$$

When the source and observer are in direct view of the open front end, as in the case shown in Fig. 1, then the contribution to $\vec{E}_c(\vec{r})$ at P from the integration over S_E in (10) is, in general, sufficiently small in comparison to that from the integration over S_T for a relatively large obstacle, as is assumed to be the case here. Therefore, (10) can be approximated in this case by:

$$\vec{P}_t \cdot \vec{E}_c(\vec{r}) \cong \int_{S_T} (\vec{E}_c \times \vec{H}_t - \vec{E}_t \times \vec{H}_c) \cdot \hat{n} ds. \quad (11)$$

It is noted that (11) is obtained exactly if the cavity is closed at the end S_E , or if the obstacle is assumed to totally block S_E from S_T . One can also arrive at (11) exactly if the surface S_E is allowed to recede to infinity so that the open-ended cavity configuration in Fig. 1 becomes semi-infinite (as S_E recedes to ∞). In the latter case, one must impose a physical requirement that there are only outgoing waves crossing S_E and no waves incoming (or reflected back) into the cavity from S_E as $S_E \rightarrow \infty$. This in turn implies that the waveguide cavity region near and at S_T must be assumed to be uniform (i.e., with a constant cross section) if $S_E \rightarrow \infty$; one can then define an orthogonal set of waveguide modes at S_E and express (\vec{E}_c, \vec{H}_c) as well as (\vec{E}_t, \vec{H}_t) in terms of these modes within the uniform waveguide region. It follows from modal orthogonality that the integral over S_E (as $S_E \rightarrow \infty$) vanishes in (10) for the latter case thereby leading to the desired result in (11). On the other hand, if the waveguide cavity is made lossy (or even slightly lossy) as $S_E \rightarrow \infty$, then the integral over S_E in (10) vanishes once more thereby leading again to (11). Furthermore, if it is assumed that the interior reflection of the waves back into the cavity from the electrically large open front end is small, then (\vec{E}_c, \vec{H}_c) at S_T may be approximated simply by the fields denoted by (\vec{E}_o, \vec{H}_o) within the cavity which are scattered by the obstacle, but which exclude the effects of all multiple wave interactions between the obstacle and the open front end. Likewise, one may approximate (\vec{E}_t, \vec{H}_t) at S_T in (11) by the fields denoted as $(\vec{E}_t^i, \vec{H}_t^i)$ which arrive directly at S_T from $\vec{J}_t(P)$ via the open front end, but which exclude any contributions arriving from $\vec{J}_t(P)$ via the open end at S_E in Fig. 2 and which also exclude any effects of multiple wave interactions between the

open front end and the back end S_E ; therefore, $(\vec{E}_t^i, \vec{H}_t^i)$ are found by tracking the fields one way from $\vec{J}_t(P)$ at P to S_T via the open front end. Finally, under the above approximations which are assumed to hold true, (11) leads to the following desired result for the field $\vec{E}_c(P)$ scattered at P by the interior obstacle when the cavity-obstacle configuration of Fig. 1 is illuminated externally by $\vec{J}(P')$; namely,

$$\vec{E}_c(P) \cdot \vec{P}_t \approx \int_{S_T} (\vec{E}_o \times \vec{H}_t^i - \vec{E}_t^i \times \vec{H}_o) \cdot \hat{n} dS. \quad (12)$$

It is noted that the $\vec{E}_c(P)$ on the L.H.S. of (12) can be found via the R.H.S. of (12) in terms of (\vec{E}_o, \vec{H}_o) and $(\vec{E}_t^i, \vec{H}_t^i)$, both of which need to be evaluated only over the interior surface S_T near the obstacle. An alternative form of (12) can be expressed as:

$$\vec{E}_c(P) \cdot \vec{P}_t \approx \oint_{S_o} (\vec{E}_o \times \vec{H}_t^i - \vec{E}_t^i \times \vec{H}_o) \cdot \hat{n} dS \quad (13)$$

where the integration is over a closed surface S_o which encapsulates the obstacle.

III. ON THE EVALUATION OF $(\vec{E}_t^i, \vec{H}_t^i)$ AND (\vec{E}_o, \vec{H}_o) AT S_T FOR THE TIME-HARMONIC CASE

For relatively arbitrary cavities and for high frequencies, $(\vec{E}_t^i, \vec{H}_t^i)$ in (12) can be evaluated, for example, by the shooting and bouncing ray (SBR) technique [2]–[5], the Gaussian beam (GB) shooting method [4], [5] or the generalized ray expansion (GRE) technique [5], [6]. As mentioned in the introduction, the use of (12) requires that the fields from the exterior sources at P and P' need to propagate only one-way via the open front end to S_T and not back. Furthermore, the GB/GRE methods require shooting a set of beams/rays only once from the open front end since the launching directions of these beams/rays and hence the propagation paths within the cavity are independent of the source location (i.e., whether the excitation be at the original source at P' or be at the observation point P for generating $(\vec{E}_t^i, \vec{H}_t^i)$); only the initial beam/ray amplitudes depend on the excitation. The fields (\vec{E}_o, \vec{H}_o) can be found by first obtaining (\vec{E}^i, \vec{H}^i) at S_T , which are the fields incident from the original source $\vec{J}_t(P')$ at P' in the absence of the interior cavity obstacle; (\vec{E}^i, \vec{H}^i) are found in exactly the same manner as $(\vec{E}_t^i, \vec{H}_t^i)$ and are thus based on the same assumptions and approximations as those required to find $(\vec{E}_t^i, \vec{H}_t^i)$. It may be possible that the interior reflection from some types of obstacles can be analyzed using ray methods, in which case the ray fields (\vec{E}^i, \vec{H}^i) enter the cavity after being excited by the original source $\vec{J}_t(P')$ and continue beyond S_T into the obstacle-cavity region to subsequently reflect back from the obstacle to S_T as (\vec{E}_o, \vec{H}_o) . In the event that an analytical approach based on ray methods either cannot be used or does not easily lend itself to find (\vec{E}_o, \vec{H}_o) , it may be possible to employ a numerical approach to accomplish this task. Such a numerical approach may be based on a partial differential equation solution of the wave problem using the finite element

or finite difference methods, or the integral equation solution based on the method of moments, or a hybrid combination of both methods to provide $(\vec{E}_o^s, \vec{H}_o^s)$ once $(\vec{E}^{ig}, \vec{H}^{ig})$ is given. In these numerical methods, it would be worth employing the "Green's function" for the cavity without the obstacle in the region beyond S_T which would otherwise contain the obstacle, so that only the fields (or currents) induced in/on the obstacle would need be found, because the presence of the cavity walls is automatically accounted for by this Green's function. Furthermore, the Green's function for the cavity without the obstacle can be represented locally by an eigenfunction expansion for waveguide cavities with, for example, a circular cross section in the region where the obstacle would otherwise be present, or be approximated via ray methods in the case of arbitrary cavities for which modes cannot be defined in the usual manner. If neither the analytical nor the numerical methods can be employed effectively to find $(\vec{E}_o^s, \vec{H}_o^s)$, as may be the case for highly complex and electrically large obstacles, then alternative (e.g. experimental) methods must be employed.

It is noted that the $(\vec{E}_o^s, \vec{H}_o^s)$ can also be found, in principle, via a different approach which employs any of the aforementioned techniques such as the ray methods, numerical methods or other alternative (e.g. experimental) techniques to develop a local Green's function for the obstacle-cavity region contained between S_T and S_E with the obstacle present. This local obstacle-cavity Green's function would provide the response at S_T , due to a point source also located in the same plane S_T and with the obstacle present. Such a Green's function can be constructed approximately, but with sufficient accuracy, to emphasize only the local cavity-obstacle region between S_T and S_E ; it would then also furnish the obstacle response $(\vec{E}_o^s, \vec{H}_o^s)$ at S_T due to an excitation $(\vec{E}^{ig}, \vec{H}^{ig})$ at S_T due to the original source \vec{J}_i at P' . The evaluation of $(\vec{E}^{ig}, \vec{H}^{ig})$ and $(\vec{E}_t^{ig}, \vec{H}_t^{ig})$ on S_T are totally dependent on the long waveguide cavity shape from the open front end (directly illuminated by $\vec{J}_i(P')$ and $\vec{J}_t(P)$, respectively) to the fictitious plane S_T ; whereas, the local cavity-obstacle Green's function alluded to above (and which plays a role in furnishing $(\vec{E}_o^s, \vec{H}_o^s)$) depends primarily on the short cavity section between S_T and S_E containing the obstacle. Thus, one can separate the effects of the short obstacle region of the cavity from the rest of the cavity, and indeed very effectively ascertain how a given obstacle affects a variety of long waveguide cavity shapes connected to the short part of the cavity containing the obstacle, and vice versa. Yet another different, but related, approach which separates the analysis of the shape dependent cavity region from the obstacle region is described in [7]-[9].

IV. GENERALIZED RECIPROCTY INTEGRAL FOR INTERIOR OBSTACLE SCATTERED FIELDS FOR ARBITRARY TIME DEPENDENT EXCITATION

The general result obtained in (8) of Section II for sinusoidally time varying (or time harmonic) fields can be extended directly to fields whose time dependence is arbitrary, as will be shown below. Indeed, a procedure for extending the frequency

domain (or time harmonic) form of a reciprocity theorem as originally developed by Lorentz into a form valid for fields with non-periodic time dependence has been presented by Goubau [10]. The present procedure for the development of the time dependent form of (8) follows essentially from [10]. Since (8) represents a result which is valid for all frequencies (ω) , it can be converted as usual into the time domain via the inverse Fourier transform defined by

$$f(t) = \frac{1}{2\pi} \int_{-\infty}^{\infty} F(\omega) e^{j\omega t} d\omega \quad (14a)$$

where $f(t)$ is an arbitrary time dependent function synthesized from the frequency domain spectrum function $F(\omega)$. The $F(\omega)$ can be found from the direct Fourier transform of $f(t)$

$$F(\omega) = \int_{-\infty}^{\infty} f(T) e^{-j\omega T} dT. \quad (14b)$$

The relationship in (14a) and (14b), between the transform pair $f(t)$ and $F(\omega)$, is commonly denoted by:

$$f(t) \leftrightarrow F(\omega). \quad (14c)$$

Next, employing the spectral inversion of (14a) to (8) yields

$$\begin{aligned} & \frac{1}{2\pi} \int_{V_c} dv'' \int_{-\infty}^{\infty} d\omega e^{j\omega t} \vec{E}_c^s(\vec{r}''; \omega) \cdot \vec{J}_t(\vec{r}, \vec{r}''; \omega) \\ &= \frac{1}{2\pi} \iint_{S_T + S_E} ds \int_{-\infty}^{\infty} d\omega e^{j\omega t} \hat{n} \cdot \left[\vec{E}_c^s(\vec{r}; \omega) \times \vec{H}_t(\vec{r}; \omega) \right. \\ & \quad \left. + \vec{H}_c^s(\vec{r}; \omega) \times \vec{E}_t(\vec{r}; \omega) \right]_{\vec{r} \text{ on } S_T + S_E} \quad (15) \end{aligned}$$

The orders of integration have been interchanged in (15). Following the notation in (14c), one may introduce the necessary time domain field quantities via the relations:

$$\vec{e}_c^s(\vec{r}; t) \leftrightarrow \vec{E}_c^s(\vec{r}; \omega); \quad (16a)$$

$$\vec{h}_c^s(\vec{r}; t) \leftrightarrow \vec{H}_c^s(\vec{r}; \omega); \quad (16b)$$

$$\vec{e}_t(\vec{r}; t) \leftrightarrow \vec{E}_t(\vec{r}; \omega); \quad (17a)$$

$$\vec{h}_t(\vec{r}; t) \leftrightarrow \vec{H}_t(\vec{r}; \omega). \quad (17b)$$

$$\vec{j}_t(\vec{r}, \vec{r}''; t) \leftrightarrow \vec{J}_t(\vec{r}, \vec{r}''; \omega). \quad (18)$$

At this juncture, it is useful to represent the $(\vec{E}_c^s, \vec{H}_c^s)$ spectral (frequency domain) values in (15) by the arbitrary time domain functions $(\vec{e}_c^s, \vec{h}_c^s)$ which they synthesize:

$$\begin{aligned} & \int_{V_c} dv'' \int_{-\infty}^{\infty} d\omega e^{j\omega t} \int_{-\infty}^{\infty} d\tau e^{-j\omega \tau} \vec{e}_c^s(\vec{r}''; \tau) \cdot \vec{J}_t(\vec{r}, \vec{r}''; \omega) \\ &= \iint_{S_T + S_E} ds \int_{-\infty}^{\infty} d\omega e^{j\omega t} \int_{-\infty}^{\infty} d\tau e^{-j\omega \tau} \hat{n} \\ & \quad \cdot \left[\vec{e}_c^s(\vec{r}; \tau) \times \vec{h}_t(\vec{r}; \omega) \right. \\ & \quad \left. + \vec{h}_c^s(\vec{r}; \tau) \times \vec{e}_t(\vec{r}; \omega) \right]_{\vec{r} \text{ on } S_T + S_E} \quad (19a) \end{aligned}$$

Performing the integration on ω in (19a) yields

$$\begin{aligned} \int_{V_c} dv \int_{-\infty}^{\infty} d\tau \bar{\mathbf{e}}_c^s(\bar{\mathbf{r}}; \tau) \cdot \bar{\mathbf{j}}_t(\bar{\mathbf{r}}, \bar{\mathbf{r}}; t - \tau) \\ = \iint_{S_T + S_E} ds \int_{-\infty}^{\infty} d\tau \hat{n} \cdot [\bar{\mathbf{e}}_c^s(\bar{\mathbf{r}}; \tau) \times \bar{\mathbf{h}}_t(\bar{\mathbf{r}}; t - \tau) \\ + \bar{\mathbf{h}}_c^s(\bar{\mathbf{r}}; \tau) \times \bar{\mathbf{e}}_t(\bar{\mathbf{r}}; t - \tau)]_{\bar{\mathbf{r}}_{\text{on}} S_T + S_E} \quad (19b) \end{aligned}$$

If one assumes an impulsive behavior for $\bar{\mathbf{j}}_t$ in both space and time, then:

$$\bar{\mathbf{j}}_t(\bar{\mathbf{r}}, \bar{\mathbf{r}}''; t) = \bar{\mathbf{P}}_t \delta(\bar{\mathbf{r}} - \bar{\mathbf{r}}'') \delta(t). \quad (20)$$

It follows from (20) that $\bar{\mathbf{j}}_t(\bar{\mathbf{r}}, \bar{\mathbf{r}}''; t - \tau) = \bar{\mathbf{P}}_t \delta(\bar{\mathbf{r}} - \bar{\mathbf{r}}) \delta(t - \tau)$; incorporating this information into (19b) yields

$$\begin{aligned} \bar{\mathbf{e}}_c^s(\bar{\mathbf{r}}; t) \cdot \bar{\mathbf{P}}_t = \iint_{S_T + S_E} ds \int_{-\infty}^{\infty} d\tau \hat{n} \\ \cdot [\bar{\mathbf{e}}_c^s(\bar{\mathbf{r}}; \tau) \times \bar{\mathbf{h}}_t(\bar{\mathbf{r}}; t - \tau) \\ + \bar{\mathbf{h}}_c^s(\bar{\mathbf{r}}; \tau) \times \bar{\mathbf{e}}_t(\bar{\mathbf{r}}; t - \tau)]_{\bar{\mathbf{r}}_{\text{on}} S_T + S_E} \quad (21) \end{aligned}$$

The above result in (21), which is in the time domain, is the counterpart of (8) for the frequency domain. The L.H.S. of (21) can be found via a time convolution of the fields of the original arbitrarily time varying source located at P' , in the presence of the cavity and obstacle, with the fields of a time impulsive point test source at P , in the presence of the cavity but in the absence of the obstacle. It is noted that the time convolutions are performed at each point in $S_T + S_E$; these are then superposed as evident from the integral over $S_T + S_E$ on the R.H.S. of (21).

If one makes the approximations leading from (8) to (12), then one can likewise obtain a time-dependent form of (12) using the same procedure as above; thus:

$$\begin{aligned} \bar{\mathbf{e}}_c^s(\bar{\mathbf{r}}; t) \cdot \bar{\mathbf{P}}_t \approx \iint_{S_T} ds \int_{-\infty}^{\infty} d\tau \hat{n} \cdot [\bar{\mathbf{e}}_o^s(\bar{\mathbf{r}}; \tau) \times \bar{\mathbf{h}}_t^{ig}(\bar{\mathbf{r}}; t - \tau) \\ + \bar{\mathbf{h}}_o^s(\bar{\mathbf{r}}; \tau) \times \bar{\mathbf{e}}_t^{ig}(\bar{\mathbf{r}}; t - \tau)]_{\bar{\mathbf{r}}_{\text{on}} S_T} \quad (22a) \end{aligned}$$

where

$$\bar{\mathbf{e}}_o^s(\bar{\mathbf{r}}; t) \leftrightarrow \bar{\mathbf{E}}_o^s(\bar{\mathbf{r}}; \omega); \quad \bar{\mathbf{h}}_o^s(\bar{\mathbf{r}}; t) \leftrightarrow \bar{\mathbf{H}}_o^s(\bar{\mathbf{r}}; \omega) \quad (22b)$$

$$\bar{\mathbf{e}}_t^{ig}(\bar{\mathbf{r}}; t) \leftrightarrow \bar{\mathbf{E}}_t^{ig}(\bar{\mathbf{r}}; \omega); \quad \bar{\mathbf{h}}_t^{ig}(\bar{\mathbf{r}}; t) \leftrightarrow \bar{\mathbf{H}}_t^{ig}(\bar{\mathbf{r}}; \omega) \quad (22c)$$

Since the result in (12) is obtained from (8) after using high frequency approximations, it is thus reasonable to expect that the time domain result for $\bar{\mathbf{e}}_c^s(\bar{\mathbf{r}}, t)$ in (22a) (obtained from (12)) will provide a useful approximation to the time domain result for $\bar{\mathbf{e}}_c^s(\bar{\mathbf{r}}, t)$ in (21) (obtained from (8)) only during the early to intermediate times of arrival of the signal $\bar{\mathbf{e}}_c^s(\bar{\mathbf{r}}, t)$ which is observed at the point P . The quantities on the right side of (22a) may be found by transforming the corresponding frequency domain fields (see (22b) and (22c)) into the time domain; alternatively, they could be found directly in the time domain. The latter aspect will be discussed in more detail in a separate paper.

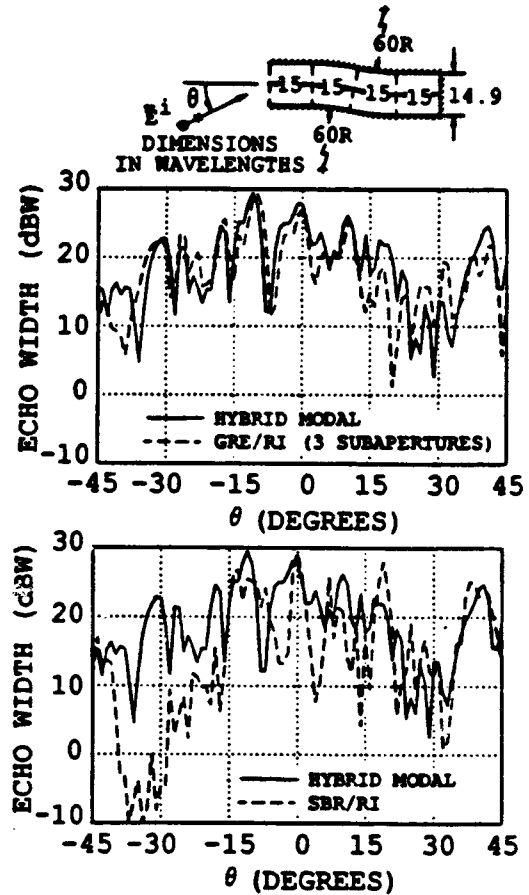


Fig. 3. Echo width versus aspect angle for a 2-D S-shaped open-ended cavity with a planar termination found using the reciprocity integral (RI) with the GRE and SBR methods.

V. NUMERICAL RESULTS

Figs. 3 and 4 show the EM echo width vs. aspect angle patterns of a perfectly conducting 2-D S-shaped open-ended waveguide cavity with a planar interior termination. The 2-D echo width σ is defined by

$$\sigma = \lim_{\rho \rightarrow \infty} 2\pi\rho \frac{|\bar{\mathbf{E}}_c^s(\bar{\rho})|^2}{|\bar{\mathbf{E}}^i|^2}, \quad (23)$$

where $\bar{\rho}$ is the vector to the far field observer (at P), $\bar{\mathbf{E}}_c^s(\bar{\rho})$ is the field at $\bar{\rho}$ scattered by the interior termination of the cavity, as given by (12), and $|\bar{\mathbf{E}}^i|$ is the magnitude of the plane wave field incident on the open front end (P' is located at infinity to create an incident plane wave). In Figs. 3 and 4, the echo width is given in decibels relative to a wavelength (DBW) (i.e., as $10 \log \sigma$ with σ in free space wavelengths), and the incident electric field is polarized perpendicular to the plane of the geometry. It is noted that only the first order scattering from the interior of the cavity is shown in these figures. No external scattering or multiple wave interaction effects are included.

The solid line in the plots of Figs. 3 and 4 is calculated using the hybrid asymptotic-modal method [4], [5] and is used as a reference solution. The dashed lines are solutions based on the SBR [2]–[5] and GRE [5], [6] methods; in Fig. 3, the one-way tracking procedure of the generalized reciprocity integral of

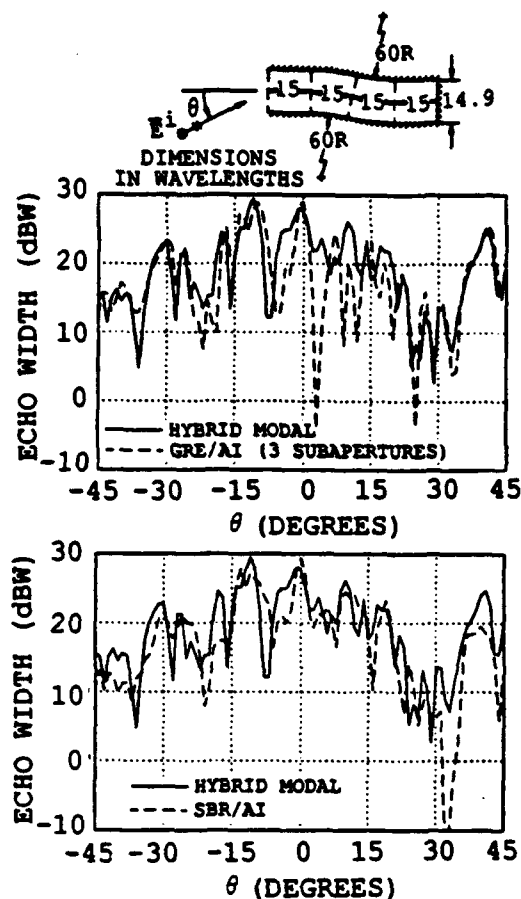


Fig. 4. Echo width versus aspect angle for a 2-D S-shaped open-ended cavity with a planar termination found using aperture integration (AI) with the GRE and SBR methods.

(12) is used, and in Fig. 4, the two-way tracking procedure of the aperture integration method is used. The numerical results in Fig. 3 which are based on the one way ray tracking that makes use of the reciprocity integral can be obtained almost twice as fast as the ones in Fig. 4 that require a two-way tracking. To compute the generalized reciprocity results of Fig. 3, the ray fields at the termination plane are converted into parallel plate waveguide modes and the orthogonality property of the modes is used to easily evaluate (12). Generally, the type of results in Fig. 3 can be obtained in less than a couple of minutes on, for example, a VAX 8550 computer.

This method can also be employed with the same degree of success for 3-D problems which are currently under study; the solutions to these will be reported later along with results for fields with non-periodic or arbitrary time dependence.

REFERENCES

- [1] R. F. Harrington, *Time-Harmonic Electromagnetic Fields*. New York: McGraw-Hill, 1961.
- [2] H. Ling, R. Chou, and S. W. Lee, "Shooting and bouncing rays: Calculating RCS of an arbitrary cavity," *IEEE Trans. Antennas Propagat.*, vol. 37, no. 2, pp. 194-205, Feb. 1989.
- [3] H. Ling, S. W. Lee, and R. C. Chou, "High-frequency RCS of open cavities with rectangular and circular cross sections," *IEEE Trans. Antennas Propagat.*, vol. 37, no. 5, pp. 648-654, May 1989.

- [4] P. H. Pathak and R. J. Burkholder, "Modal, ray and beam techniques for analyzing the EM scattering by open-ended waveguide cavities," *IEEE Transactions Antennas Propagat.*, vol. 37, no. 5, pp. 635-647, May 1989.
- [5] R. J. Burkholder, "High-frequency asymptotic methods for analyzing the EM scattering by open-ended waveguide cavities," Ph.D. dissertation, The Ohio State University, June 1989.
- [6] P. H. Pathak and R. J. Burkholder, "High frequency EM scattering by open-ended waveguide cavities," *Radio Science*, vol. 26, no. 1, pp. 211-218, Jan.-Feb. 1991.
- [7] P. H. Pathak, P. H. Law, G. Crabtree, and D. Foreman, "High frequency electromagnetic scattering by open-ended waveguide cavities with a complex interior termination," presented at the 1990 *IEEE AP-S Int. Symposium and URSI National Radio Science Meeting*, Dallas, TX, May 6-11.
- [8] P. H. Pathak, P. H. Law, and R. J. Burkholder, "Analysis of high frequency EM scattering by open-ended waveguide cavities containing a complex interior obstacle," Technical Report 722592-1, The Ohio State University Electro-Science Laboratory, prepared for General Electric Co., Cincinnati, OH, under Contract 14U11685, Mar. 1990.
- [9] P. Law, "Analysis of EM scattering by open-ended waveguides containing complex obstacles," Ph.D. dissertation, The Ohio State University, Dept. of Electrical Engineering, 1990.
- [10] G. Goubau, "A reciprocity theorem for nonperiodic fields," *IEEE Trans. Antennas Propagat.*, vol. AP-8, no. 3, pp. 339-342, May 1960.



Prabhakar H. Pathak (M'76-SM'81-F'86) received the B.Sc. degree in physics from the University of Bombay, India, in 1962, the B.S. degree in electrical engineering from the Louisiana State University, Baton Rouge, in 1965, and the M.S. and Ph.D. degrees from The Ohio State University (OSU), Columbus, in 1970 and 1973, respectively.

From 1965 to 1966 he was an Instructor in the Department of Electrical Engineering at the University of Mississippi, Oxford. During the summer of 1966 he worked as an electronics engineer with Boeing Company, Renton, WA. Since 1968 he has been with the OSU ElectroScience Laboratory. His research interests are in mathematical methods, electromagnetics, and uniform ray techniques. In 1983, he joined the faculty of the Department of Electrical Engineering, The Ohio State University, where he is currently a Professor. He has contributed to the development of the uniform geometrical theory of diffraction (UTD), which can be applied to analyze a variety of practical electromagnetic antenna and scattering problems. His work continues to be in the UTD and other high-frequency techniques, as well as in the analysis of guided waves, and microstrip and reflector antennas using high-frequency asymptotic procedures. He has presented invited lectures, and several short courses on the UTD, both in the U.S. and abroad. He has also authored and coauthored chapters on ray methods for five books. He has served as Associate Editor for the *IEEE TRANSACTIONS ON ANTENNAS AND PROPAGATION* for about five years. Currently, he is serving as an IEEE AP-S distinguished lecturer.

Dr. Pathak is a member of Commission B of the International Scientific Radio Union (URSI) and Sigma Xi.



Robert J. Burkholder (M'89) received the B.S., M.S. and Ph.D. degrees in electrical engineering from The Ohio State University, Columbus, in 1984, 1985, and 1989, respectively. As an undergraduate he worked as a co-op student for General Electric in East Cleveland, Ohio.

He is currently with The Ohio State University ElectroScience Laboratory as a Postdoctoral Research Associate. In his dissertation, he contributed to the development of modal, ray and beam approaches for analyzing the electromagnetic (EM) fields scattered from and coupled into electrically large, non-uniform open-ended waveguide cavities. His research interests are in the areas of high frequency, modal and hybrid techniques for solving EM antenna and scattering problems. Currently, he is working on the analysis of the EM scattering by open cavities and antenna radiation and coupling in complex environments.

EM Plane Wave Diffraction by a Planar Junction of Two Thin Material Half-Planes – Oblique Incidence

H. C. Ly, *Student Member, IEEE*, R. G. Rojas, *Senior Member, IEEE*, and P. H. Pathak, *Fellow, IEEE*

Abstract—A uniform geometrical theory of diffraction (UTD) solution is developed for analyzing the phenomenon of high-frequency diffraction of an obliquely incident plane wave by a two-part thin, planar transparent material slab. The solution is obtained by appropriately combining two solutions for the two related configurations involving perfectly conducting electric and magnetic ground plane bisections of the original slab. The analysis is based on the Wiener-Hopf technique, and each of the grounded material half-planes is assumed to be electrically thin so that it can be modeled by a generalized impedance boundary condition of $0(t)$, where t is the corresponding slab thickness. It is shown that to solve the boundary value problem completely, an additional condition related to the field behavior at the junction of the two material half-planes needs to be imposed besides the boundary and radiation conditions as well as the usual edge condition. This junction condition is determined by matching an approximate quasi-static solution, which is developed in the proximity of the discontinuity, with the corresponding external Wiener-Hopf solution in the common region of overlap. The solution thus obtained automatically satisfies reciprocity. It is shown that the new UTD solution obtained here reduces to known results and the numerical results based on it agree very well with a corresponding independent moment method solution.

I. INTRODUCTION

THE canonical problem to be studied in this paper is the analysis of the high-frequency electromagnetic (EM) diffraction at a planar junction formed by connecting two thin dielectric/magnetic half-planes. The geometrical configuration pertaining to this canonical problem is depicted in Fig. 1. The incident field is assumed to be a plane wave of arbitrary polarization obliquely incident to the z axis with an angle θ' ($0 < \theta' < \pi$) as shown in Fig. 1. The two-part planar material slab is composed of two dissimilar, semi-infinite homogeneous and isotropic thin dielectric/magnetic half-planes. One half-plane is characterized by relative permittivity ϵ_{r1} , relative permeability μ_{r1} , and thickness t_1 , for $x > 0$, and is connected to the other material half-plane characterized by $(\epsilon_{r2}, \mu_{r2}, t_2)$ in the region $x < 0$. The present study is an extension of a previous investigation [1] for a normally incident ($\theta' = 90^\circ$) plane wave. Note that the uniform geometrical theory of diffraction (UTD) solution for the two-part transparent slab problem can be obtained by superposing the UTD solutions to the two related problems of diffraction by perfectly electric conducting (PEC) and magnetic conducting (PMC) ground

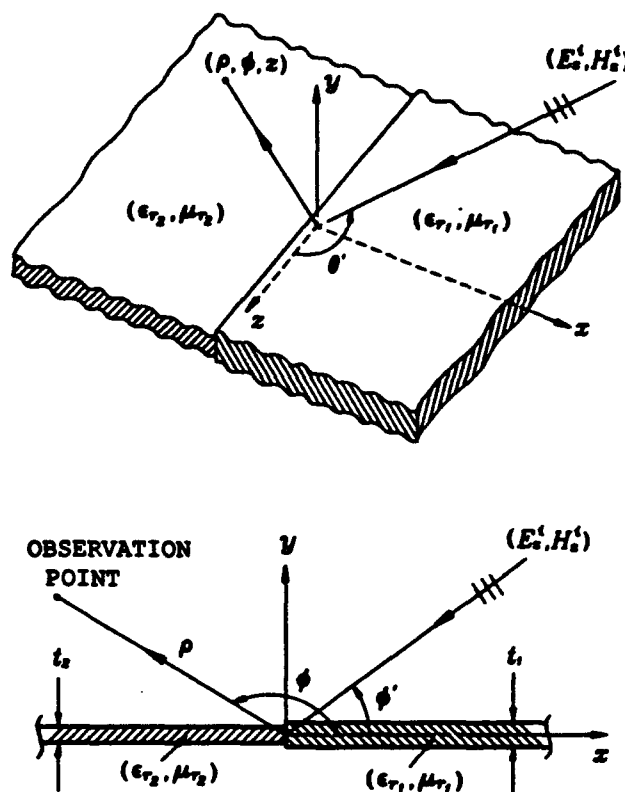


Fig. 1. Two-part dielectric/magnetic slab geometry with obliquely incident plane wave excitation.

plane bisections of the original slab. Fig. 2 shows the geometries of these two bisection problems and how they are equivalent to the original problem. It is important to note that in contrast to the case of normal incidence considered in [1], the fields E_z and H_z are coupled in the present case and obey the symmetry relations depicted in Fig. 2.

The material half-planes in Figs. 1 and 2 are assumed to be electrically thin; in other words, the parameters (ϵ_r, μ_r, t) characterizing each of the material half-planes are restricted so that one can approximately replace the grounded material half-planes by generalized impedance boundary conditions (GIBC) of $0(t)$ [2] in a sufficiently accurate manner. By numerical experimentation, it can be shown that when the thickness, t , of a thin dielectric/magnetic slab satisfies the condition $\text{Re}(\sqrt{\mu_r \epsilon_r})t/2 < 0.1\lambda$, where λ is the free-space wavelength, the use of the GIBC of $0(t)$ to represent the effect of the material half-planes is quite adequate. The PEC/PMC bisection problems modeled by the GIBC of $0(t)$ can be

Manuscript received May 1, 1992; revised December 15, 1992. This work was supported by the Joint Services Electronics Program (contract N00014-89-J-1007).

The authors are with the ElectroScience Laboratory, Department of Electrical Engineering, Ohio State University, Columbus, OH 43212.

IEEE Log Number 9208145.

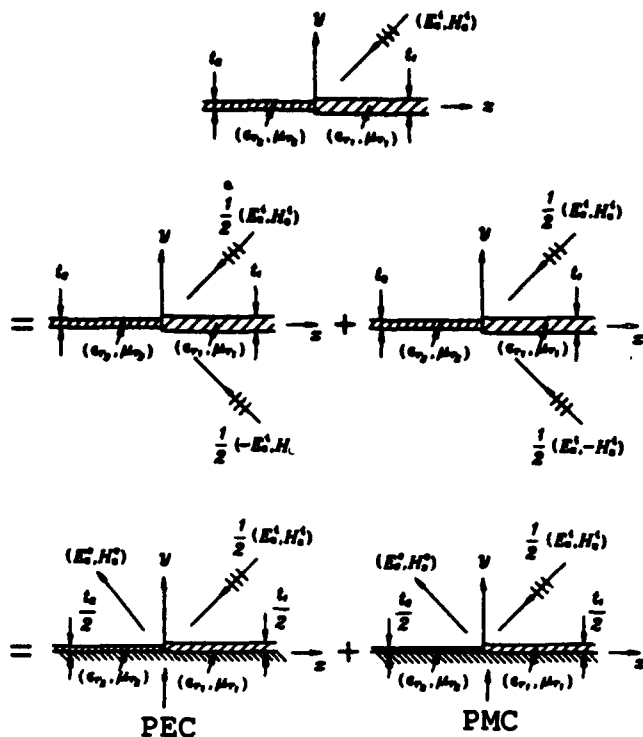


Fig. 2. Two-part dielectric/magnetic slab bisected by a PEC or a PMC ground plane.

solved by the Wiener-Hopf technique [3], [4]. Nevertheless, it is noted that for these problems, the Wiener-Hopf analysis alone does not yield unique solutions because the Wiener-Hopf-based solution contains unknown constants even after the radiation and the usual edge conditions have been applied. This nonuniqueness arises because the GIBC does not model the material discontinuity in the transverse direction. Therefore, to completely solve the boundary value problems, an additional condition is obtained at the junction of the two material half-planes. This junction condition is developed if the field in close proximity to the junction is modeled by a quasi-static solution, which is matched with the corresponding Wiener-Hopf-based solution expanded in the common region of overlap. The approximate quasi-static analysis was first introduced by Leppington [5] and then used by Rojas *et al.* [1]. Unfortunately, it appears that there are some errors in [5], as discussed in [1]. Both works deal with the case of a normally incident field. In this analysis, a similar quasi-static approximation is extended to cover the case of oblique incidence. In contrast to certain solutions found in the literature, where the reciprocity condition must be imposed explicitly, the additional junction condition developed here yields a unique solution which automatically satisfies reciprocity. The term *uniqueness* is used in this paper to state the fact that the solution for the slab geometry obtained here contains no unknown constants provided the following conditions are satisfied: (1) the GIBC of $O(t)$ is an accurate model for the thin grounded slabs; (2) the quasi-static solution is valid near the junction.

The high-frequency EM scattering by nonmetallic objects has been studied in a more limited sense than the EM scattering by metallic or PEC objects. Most earlier studies on the scatter-

ing by nonconducting objects employed impedance/resistive boundary conditions to model a thin dielectric slab. For instance, Anderson [6] solved the diffraction problem of a thin dielectric half-plane by replacing it with an equivalent current sheet (resistive boundary condition). However, in recent years, the GIBC has been used frequently to treat material scatterers such as a dielectric/magnetic half-plane [7]–[10] and a dielectric-coated metallic wedge [11] and half-plane [12], [13]. In particular, boundary conditions similar to the GIBC of $O(t)$ developed by Weinstein were used by Chakrabarti [9] and Volakis and Senior [10] to study the scattering by a dielectric half-plane for the case of normal incidence. Rojas *et al.* [7], [8] employed the GIBC of infinite order [14], [15] to investigate the EM scattering by a dielectric/magnetic half-plane. A special case of the boundary condition used in [7], [8] is the one of $O(t)$ originally developed by Weinstein [2]. Both TM_z and TE_z plane wave excitations were included in [7], [8] as well as the case of oblique incidence with respect to the axis of the half-plane [8]; however, their solutions were obtained by enforcing reciprocity without considering the problem of uniqueness. The approach of imposing reciprocity was also used in [13] to yield the solution for a coated half-plane. Bernard [11] applied a GIBC of $O(t^n)$, where n is arbitrarily large, to treat a dielectric-coated metallic wedge; but it is noted by Senior [12] that Bernard's solution violates reciprocity. In his study on a coated half-plane [12], Senior also explicitly enforces reciprocity, and his final solution contains an unknown constant related to the value of the field at the edge. A diffraction problem similar to the two-part slab problem with oblique incidence given in this study was discussed by Buyukaksoy *et al.* [16]; but their solution, like the one in [10], was limited to a pure dielectric where $\mu_r = 1$. A special case of the two-part problem in [16] is considered in [17], namely, a dielectric half-plane.

Since the two-part slab configurations shown in Figs. 1 and 2 are two-dimensional geometries, all the fields have the same z dependence as the incident field. Therefore, all the field components can be expressed in terms of E_z and H_z . As mentioned before, instead of solving the original boundary value problem depicted in Fig. 1, the solutions to the PEC and PMC bisection problems depicted in Fig. 2 are obtained first. The configuration with PEC bisection gives rise to the field (E_z^o, H_z^o) in the upper half-space $y > 0$, while the one with PMC bisection yields the field (E_z^e, H_z^e) for $y > 0$, where

$$E_z^o(y) = \frac{E_z(y) - E_z(-y)}{2}, \quad H_z^o(y) = \frac{H_z(y) - H_z(-y)}{2}, \quad (1a)$$

$$E_z^e(y) = \frac{E_z(y) + E_z(-y)}{2}, \quad H_z^e(y) = \frac{H_z(y) + H_z(-y)}{2}. \quad (1b)$$

Note that E_z^o and H_z^o are odd functions of y , with $E_z^o(y = 0) = H_z^o(y = 0) = 0$, whereas E_z^e and H_z^e are even functions of y , with $\partial E_z^e / \partial y|_{y=0} = \partial H_z^e / \partial y|_{y=0} = 0$. In the following analysis, the PMC bisection problem involving (E_z^e, H_z^e) is modeled by the GIBC of $O(t)$ [2] and then solved by means of the Wiener-Hopf method to derive the scattered field in the form of an integral, where the Wiener-

Hopf factors in the integrand are expressed in a relatively simple form based on Weinstein's procedure [2]. Next, an additional junction condition which is used to completely solve the problem is developed by matching an approximate quasi-static solution with the corresponding external Wiener-Hopf solution. The complete unique solution for (E_z^e, H_z^o) in integral form is asymptotically evaluated by the steepest descent method to obtain expressions in the format of UTD. The solution to the field (E_z^e, H_z^o) is then obtained from the result for (E_z^e, H_z^o) by employing the concept of duality. A superposition of these even and odd fields produces the result for the original problem. Finally, several numerical examples based on this solution are presented and compared with corresponding moment method (MM) results [18]. It is noted that an $e^{-i\omega t}$ time dependence for all the fields is assumed and suppressed in the following discussion.

II. ANALYSIS

The canonical problem to be considered is the PMC bisection configuration depicted in Fig. 2. The field (E_z^e, H_z^o) satisfies the Helmholtz differential equation, the radiation and edge conditions, and the GIBC of $0(t)$, which can be expressed as follows:

$$\left\{ \frac{\partial^2}{\partial x^2} - iK a_2^e \frac{\partial}{\partial y} + K^2(1 + b_2^e \sin^2 \theta') \right\} E_z^e|_{y=0} - \cos \theta' \frac{\partial}{\partial x} \left(\frac{\partial}{\partial y} + iK a_2^e \right) Z_0 H_z^o|_{y=0} = 0, \quad x \geq 0; \quad (2a)$$

$$\left\{ \frac{\partial}{\partial y} + iK \sin \zeta_2^h - \cos^2 \theta' \frac{\sin \zeta_1^h}{a_2^e} \left(\frac{\partial}{\partial y} + iK a_2^e \right) \right\} Z_0 H_z^o|_{y=0} - \cos \theta' \left(1 - \frac{\sin \zeta_1^h}{a_2^e} \right) \frac{\partial E_z^e}{\partial x}|_{y=0} = 0, \quad x \geq 0; \quad (2b)$$

where

$$K = K_1 + iK_2 = k \sin \theta', \quad K_1, K_2 > 0, \quad K_2 \ll K_1; \quad (3a)$$

$$\sin \zeta_2^h = \frac{i}{K(\epsilon_{r_2} - 1)t_2/2}, \quad (3b)$$

$$a_2^e = \sin \nu_{a_2}^e + \sin \nu_{b_2}^e = -\frac{i\mu_{r_1}}{K(\mu_{r_1} - 1)t_1/2}, \quad (3c)$$

$$b_2^e = \sin \nu_{a_2}^e \sin \nu_{b_2}^e = \frac{1}{\sin^2 \theta'} \left(\frac{a_2^e}{\sin \zeta_1^h} - 1 \right), \quad (3d)$$

$$\sin \nu_{b_1,2}^e = \frac{a_{1,2}^e}{2} \mp \sqrt{\left(\frac{a_{1,2}^e}{2} \right)^2 - b_{1,2}^e}. \quad (3e)$$

Note that k is the free-space wave number, and K is temporarily allowed to have a small imaginary part for purposes of analysis. Once the analysis is completed, the imaginary part

can be set equal to zero. Also, it is convenient to express the solution for (E_z^e, H_z^o) as

$$\tilde{f}_{1z} = \tilde{f}_{1z}^u + \tilde{f}_{1z}^s, \quad y > 0, \quad \tilde{f}_{1z} = \left[\frac{E_z^e}{Z_0 H_z^o} \right]; \quad (4)$$

where \tilde{f}_{1z}^u , which is referred to as the unperturbed field, is the field that would exist if the whole plane $\{y = 0\}$ in Fig. 2 were occupied by a grounded homogeneous thin material slab with parameters $(\epsilon_{r_1}, \mu_{r_1}, t_1/2)$. Hence, \tilde{f}_{1z}^s represents the effect of the material discontinuity resulting from the fact that the actual material layer for $\{y = 0, x < 0\}$ is characterized by $(\epsilon_{r_2}, \mu_{r_2}, t_2/2)$ instead of $(\epsilon_{r_1}, \mu_{r_1}, t_1/2)$.

Since all the field components of \tilde{E}^e and \tilde{H}^o can be determined from \tilde{f}_{1z} , the obliquely incident plane wave field can be completely defined in terms of \tilde{f}_{1z} , namely,

$$\tilde{f}_{1z} = \tilde{F}_{0z} e^{-iK(x \cos \phi' + y \sin \phi') - ikz \cos \theta'}, \quad \tilde{F}_{0z} = \left[\frac{E_{0z}}{Z_0 H_{0z}} \right], \quad 0 < \phi' < \pi, \quad (5)$$

where E_{0z} and H_{0z} are the magnitudes of the incident fields E_z^{ei} and H_z^{oi} , respectively, at the origin $(x, y, z) = (0, 0, 0)$; that is, $E_{0z} = \frac{1}{2} E_z^i(0, 0, 0)$, $H_{0z} = \frac{1}{2} H_z^i(0, 0, 0)$, where E_z^i and H_z^i are incident plane wave fields in the original problem shown in Fig. 1. It follows from the definition of \tilde{f}_{1z}^u that

$$\tilde{f}_{1z}^u = \tilde{f}_{1z}^s + \tilde{C}^{-1}(\pi - \phi') \tilde{A}_1^{(1)} \tilde{C}(\pi + \phi') \tilde{F}_{0z} e^{-iK(x \cos \phi' - y \sin \phi') - ikz \cos \theta'}, \quad (6a)$$

where

$$\tilde{C}(w) = \frac{1}{\Delta(w)} \begin{bmatrix} -\cos w & \sin w \cos \theta' \\ \sin w \cos \theta' & \cos w \end{bmatrix}, \quad \tilde{A}_1^{(1)} = \begin{bmatrix} \mathcal{R}_{e_1}^e & 0 \\ 0 & \mathcal{R}_{h_1}^o \end{bmatrix}, \quad (6b)$$

$$\Delta(w) = \cos^2 \theta' + \cos^2 w \sin^2 \theta', \quad (6c)$$

$$\mathcal{R}_{e_1}^e = -\frac{(\sin \phi' - \sin \nu_{a_1}^e)(\sin \phi' - \sin \nu_{b_1}^e)}{(\sin \phi' + \sin \nu_{a_1}^e)(\sin \phi' + \sin \nu_{b_1}^e)}, \quad (6d)$$

$$\mathcal{R}_{h_1}^o = \frac{(\sin \phi' - \sin \zeta_1^h)}{(\sin \phi' + \sin \zeta_1^h)}. \quad (6e)$$

The next step is to solve for the field \tilde{f}_{1z}^s by means of the Wiener-Hopf technique. At this stage of analysis, the factor $e^{-ikz \cos \theta'}$ is dropped to simplify the notation, and it will be reintroduced after the analysis is completed. Note that the boundary conditions satisfied by the field \tilde{f}_{1z}^s can be obtained easily by substituting the definition of \tilde{f}_{1z}^s in (4) and the solution of the unperturbed field \tilde{f}_{1z}^u given in (6a) into the GIBC of $0(t)$ given in (2). Taking the one-sided Fourier transforms, which were defined and discussed in [1], of the new set of boundary conditions for \tilde{f}_{1z}^s , one obtains the boundary conditions in the spectral s domain which couple $\tilde{E}_{z\pm}^{es}(s, 0)$ and $\tilde{H}_{z\pm}^{os}(s, 0)$. Here, $\tilde{E}_{z\pm}^{es}(s, y)$ and $\tilde{H}_{z\pm}^{os}(s, y)$ are the one-sided Fourier transforms of $E_z^{es}(x, y)$ and $H_z^{os}(x, y)$, respectively, with the subscript $+$ denoting a function regular in the upper half s plane defined by $\text{Im } s = \tau > \tau_- = -K_2$.

and the subscript $-$ denoting a function regular in the lower half s plane $\tau < \tau_+ = K_2 \cos \phi'$. It is noted that the GIBC of $0(z)$ in the spatial domain becomes uncoupled if it is expressed in terms of the normal components (y components in this case) of the fields. Thus, one may also decouple the boundary conditions for the spectral fields in the s domain by introducing the following auxiliary functions:

$$\mathcal{X}_{\pm}(s, y) = -\frac{1}{K \sin \theta'} \left[s Z_0 \hat{H}_{\pm}^{oo}(s, y) + i \cos \theta' \frac{\partial}{\partial y} \hat{E}_{\pm}^{oo}(s, y) \right], \quad (7a)$$

$$Z_{\pm}(s, y) = \frac{1}{K \sin \theta'} \left[s \hat{E}_{\pm}^{oo}(s, y) - i \cos \theta' \frac{\partial}{\partial y} Z_0 \hat{H}_{\pm}^{oo}(s, y) \right], \quad (7b)$$

and

$$\begin{aligned} \mathcal{X}(s, y) &= \mathcal{X}_+(s, y) + \mathcal{X}_-(s, y), \\ Z(s, y) &= Z_+(s, y) + Z_-(s, y). \end{aligned} \quad (7c)$$

The boundary conditions in the s domain can now be expressed via (7a) and (7b) in terms of the unknown functions $\mathcal{X}_{\pm}(s, 0)$ and $Z_{\pm}(s, 0)$ instead of $\hat{E}_{\pm}^{oo}(s, 0)$ and $\hat{H}_{\pm}^{oo}(s, 0)$. Following the Wiener-Hopf procedure (Jones's method) as in [1], one finally obtains two Wiener-Hopf equations which hold in the strip $\tau_- < \tau < \tau_+$ for the unknown functions $\mathcal{X}_{\pm}(s, 0)$ and $Z_{\pm}(s, 0)$ as follows:

$$\begin{aligned} D_-^o(s) - \frac{G_-(s, \zeta_1^*)}{G_-(s, \zeta_2^*)} \mathcal{X}_-(s, 0) \\ = \frac{G_+(s, \zeta_2^*)}{G_+(s, \zeta_1^*)} \mathcal{X}_+(s, 0) - D_+^o(s), \quad \tau_- < \tau < \tau_+, \end{aligned} \quad (8a)$$

$$\begin{aligned} D_-^e(s) - \frac{G_-(s, \nu_{a1}^e) G_-(s, \nu_{b1}^e)}{G_-(s, \nu_{a2}^e) G_-(s, \nu_{b2}^e)} Z_-(s, 0) \\ = \frac{a_2^e G_+(s, \nu_{a2}^e) G_+(s, \nu_{b2}^e)}{a_1^e G_+(s, \nu_{a1}^e) G_+(s, \nu_{b1}^e)} Z_+(s, 0) - D_+^e(s), \\ \tau_- < \tau < \tau_+, \end{aligned} \quad (8b)$$

in which

$$G(s, v) = G_+(s, v) G_-(s, v) = \frac{K}{\beta + K \sin v}, \quad (9a)$$

$$\beta = \sqrt{K^2 - s^2}, \quad \text{Im}(\beta) > 0; \quad (9b)$$

the functions $D_{\pm}^{e,o}$ are defined in Appendix I, and the expressions for $G_{\pm}(s, v)$, which are obtained using Weinstein's procedure [2], are summarized in [7] and are not repeated here. The intermediate steps that lead to the Wiener-Hopf equations in (8) were discussed in detail in [19]. Note that the functional forms of $D_{\pm}^{e,o}$ are known; however, it is seen from the expressions of $D_{\pm}^{e,o}$ in Appendix I that they contain some unknown constants related to the surface values of the fields at the junction, namely, $E_x^{oo}(0^{\pm}, 0)$, $H_x^{oo}(0^{\pm}, 0)$, and $H_y^{oo}(0^{\pm}, 0)$. These constants arise from the one-sided Fourier transforms of the terms involving derivatives with respect to x in the original boundary conditions.

Equations (8a) and (8b) have a common overlapping region $\tau_- < \tau < \tau_+$ in which the functions on the left- and right-hand sides are regular. Hence, by analytic continuation [3], [4] the two sides of (8a) define an entire function denoted by $P^o(s)$, and the two sides of (8b) define another entire function, $P^e(s)$. Since the edge condition allows only algebraic growth of the fields in the neighborhood of singularities [3], it follows from the extended form of Liouville's theorem [3], [4] that $P^o(s)$ and $P^e(s)$ can be expressed as polynomials determined from the behavior of (8a) and (8b) as $|s| \rightarrow \infty$. Applying the edge condition, which is related to finite energy near the discontinuity and thus implies that the components of the fields parallel to the edge are bounded, one can expand both sides of (8) in series up to the terms of $O(s^{-1})$ as $|s| \rightarrow \infty$. Note that the asymptotic expansions of the ratios involving the G_{\pm} functions presented in (8) were given in [1]. Thus, comparing the coefficients of the corresponding terms in the expansions of both sides of (8), one obtains three independent equations for the unknown constants $E_x^{oo}(0^{\pm}, 0)$, $H_x^{oo}(0^{\pm}, 0)$, and $H_y^{oo}(0^{\pm}, 0)$ as follows:

$$H_x^{oo}(0^+, 0) = H_x^{oo}(0^-, 0), \quad (10a)$$

$$E_x^{oo}(0^+, 0) = E_x^{oo}(0^-, 0), \quad (10b)$$

$$\begin{aligned} Z_0 H_y^{oo}(0^-, 0) = \frac{Z_0 [a_2^e H_y^{oo}(0^+, 0) - a_1^e H_y^{oo}(0^-, 0)]}{a_2^e - a_1^e} \left(1 + \frac{\delta}{a_1^e} \right) \\ + \frac{K E_x^{oo}(0^+, 0)}{a_1^e \sin \theta'} \left[1 + \frac{a_2^e b_1^e - a_1^e b_2^e}{a_2^e - a_1^e} \sin^2 \theta' \right] \alpha \\ + i \sqrt{2\pi} \left[\tilde{A}_u^e T_+(K \cos \phi') + \frac{\tilde{C}_u^e \alpha}{a_2^e - a_1^e} \right], \end{aligned} \quad (10c)$$

where \tilde{A}_u^e , \tilde{C}_u^e , $T_+(s)$, α , and δ are defined in Appendix I. The y components of the fields are given by

$$E_y = -\frac{i}{K \sin \theta'} \left[\frac{\partial}{\partial x} Z_0 H_x + \cos \theta' \frac{\partial}{\partial y} E_x \right], \quad (10d)$$

$$Z_0 H_y = \frac{i}{K \sin \theta'} \left[\frac{\partial}{\partial x} E_x - \cos \theta' \frac{\partial}{\partial y} Z_0 H_x \right]. \quad (10e)$$

Furthermore, it follows from the asymptotic expansions of (8) as $|s| \rightarrow \infty$ that the polynomial $P^o(s)$ is a constant given by

$$\begin{aligned} P^o(s) = -\frac{i}{K} \left\{ \frac{\tilde{C}_u^o}{\sin \zeta_2^* - \sin \zeta_1^*} + \frac{\sin \theta'}{\sqrt{2\pi}} Z_0 H_x^{oo}(0, 0) \right. \\ \left. + \frac{\cos \theta' Z_0}{\sqrt{2\pi} (\sin \zeta_2^* - \sin \zeta_1^*)} \left[\frac{H_y^{oo}(0^+, 0)}{1 + b_1^e \sin^2 \theta'} - \frac{H_y^{oo}(0^-, 0)}{1 + b_2^e \sin^2 \theta'} \right] \right\}, \end{aligned} \quad (11a)$$

where \tilde{C}_u^o is given in (40b); and $P^e(s)$ is a linear function of s , namely,

$$P^e(s) = ms + n, \quad (11b)$$

$$m = -\frac{i\alpha}{\sqrt{2\pi}a_1^e K \sin \theta'} E_z^{eo}(0,0), \quad (11c)$$

$$n = -\frac{i}{\sqrt{2\pi}} \left[\frac{\delta E_z^{eo}(0,0)}{a_1^e K \sin \theta'} + \frac{\alpha Z_0 \{a_2^e H_y^{eo}(0^+,0) - a_1^e H_y^{eo}(0^-,0)\}}{a_1^e(a_2^e - a_1^e)} \right]. \quad (11d)$$

Since the three independent equations in (10) are not enough to determine the six unknown constants, some other considerations are needed to determine the final three pieces of information so that a unique solution is obtained for the problem at hand. It is noted that the fields \hat{E}_z^{eo} and \hat{H}_z^{eo} , which are solutions to the Helmholtz differential equation together with the radiation condition in the s domain, are given by

$$\begin{aligned} \hat{E}_z^{eo}(s,y) &= \hat{E}_z^{eo}(s,0)e^{i\beta y}, \\ \hat{H}_z^{eo}(s,y) &= \hat{H}_z^{eo}(s,0)e^{i\beta y}, \quad y \geq 0. \end{aligned} \quad (12)$$

Hence, it follows from (7) and (12) that

$$\hat{E}_z^{eo}(s,y) = \frac{k[sZ(s,0) + \beta \cos \theta' X(s,0)]}{s^2 + k^2 \cos^2 \theta'} e^{i\beta y}, \quad y \geq 0, \quad (13a)$$

$$Z_0 \hat{H}_z^{eo}(s,y) = \frac{k[-sX(s,0) + \beta \cos \theta' Z(s,0)]}{s^2 + k^2 \cos^2 \theta'} e^{i\beta y}, \quad y \geq 0. \quad (13b)$$

The expressions above determine the spectral z -component fields from $X(s,0)$ and $Z(s,0)$. However, in both of (13a) and (13b), there are two poles at $s = \pm ik \cos \theta'$ whose residues introduce nonphysical (exponentially growing) fields in the spatial domain [20]. Therefore, these two nonphysical poles must be suppressed by setting the residues of \hat{E}_z^{eo} and \hat{H}_z^{eo} to zero at $s = \pm ik \cos \theta'$; in other words, two more independent equations are obtained as follows:

$$\pm iZ(\pm ik \cos \theta', 0) + X(\pm ik \cos \theta', 0) = 0. \quad (14)$$

At this point, it remains to impose one more constraint to completely determine all the unknown constants in the expressions for $X_{\pm}(s,0)$ and $Z_{\pm}(s,0)$; this in turn will lead to unique solutions for \hat{E}_z^{eo} and \hat{H}_z^{eo} by means of (7c) and (13). The additional constraint, which may be called a junction condition, is found in this study by following a procedure similar to those used in [5] and [1], where an approximate quasi-static solution for the total even field, $E_z^e(x,y)$, is obtained in the neighborhood of the junction. Note that this quasi-static solution is valid outside and inside the material layers of the material coated PMC ground plane (refer to Fig. 2).

III. DETERMINATION OF JUNCTION CONDITION

Let $E_z^e(x,y)$ denote the total even z -component quasi-static field outside the material region. Also, let $E_{z1}^e(x,y)$ and $E_{z2}^e(x,y)$ be the total z -component fields inside material medium 1 ($x > 0$) and material medium 2 ($x < 0$), respectively. Note that the superscript q is used to denote a quasi-static field. The fields $E_{z1,2}^e$ satisfy Laplace's equation in the region $K\rho = K\sqrt{x^2 + y^2} \ll 1$ along with the boundary

conditions which state that the tangential fields are continuous across the free space-material and material-material interfaces. Note that the z -dependent factor $e^{-ikz \cos \theta'}$ has been suppressed to simplify the notation.

Following the same discussion as in [5] and [1], the quasi-static field $E_{z1,2}^e$ within the region of interest $t_1 < \rho < K^{-1}$ may be expressed as

$$E_{z1,2}^e \approx A_q + \Phi_q, \quad (15a)$$

$$\Phi_q \sim B_q x + C_q \ln \rho, \quad \text{as } \rho/t_1 \rightarrow \infty, \quad (15b)$$

where A_q , B_q , and C_q are constants independent of x and y . In other words, $E_{z1,2}^e$ exhibits logarithmic as well as algebraic growth as $\rho/t_1 \rightarrow \infty$. The key step in this section is to determine the relationship between the logarithmic growth and the algebraic growth (or the relationship between C_q and B_q), which can be accomplished by using the integral form of Laplace's equation, namely,

$$\oint_L \nabla E_{z1,2}^e \cdot \hat{n} dl = \oint_L \frac{\partial}{\partial n} E_{z1,2}^e dl = 0, \quad (16)$$

where \hat{n} is the outer normal of a closed contour L . Applying (16) inside material medium 1 with the contour of integration as follows:

$$(x=0, y=0) \xrightarrow{y=0} (x_0, 0) \xrightarrow{x=x_0} (x_0, \frac{t_1}{2}) \xrightarrow{\text{interfaces}} (0, 0),$$

where $x_0/t_1 \rightarrow \infty$ and the labels above the arrows denote the paths of integration, one obtains

$$B_q \frac{t_1}{2} + \lim_{x_0/t_1 \rightarrow \infty} \int_{(x_0, t_1/2) \text{ interfaces}}^{(0,0)} \frac{\partial E_{z1}^e}{\partial n} dl = 0. \quad (17a)$$

Integrating along a similar contour, but in dielectric medium 2 yields (as $x_0/t_2 \rightarrow \infty$)

$$-B_q \frac{t_2}{2} + \lim_{x_0/t_2 \rightarrow \infty} \int_{(0,0) \text{ interfaces}}^{(-x_0, t_2/2)} \frac{\partial E_{z2}^e}{\partial n} dl = 0. \quad (17b)$$

Likewise, integrating (16) along the following contour in free space (assuming $t_1 > t_2$):

$$(-x_0, \frac{t_2}{2}) \xrightarrow{\text{interfaces}} (x_0, \frac{t_1}{2}) \xrightarrow{x=x_0} (-x_0, \frac{t_1}{2}) \xrightarrow{x=-x_0} (-x_0, \frac{t_2}{2}),$$

one obtains (as $x_0/t_1 \rightarrow \infty$)

$$B_q \frac{t_2 - t_1}{2} + C_q \pi + \lim_{x_0/t_1 \rightarrow \infty} \int_{(-x_0, t_2/2) \text{ interfaces}}^{(x_0, t_1/2)} \frac{\partial E_{z2}^e}{\partial n} dl = 0. \quad (17c)$$

Note that the same equation as in (17c) is obtained if it is assumed that $t_2 > t_1$. To find the relationship between C_q and B_q from (17), one must first find the relationship among the derivatives $\partial E_{z1,2}^e / \partial n$. It is noted that $\partial E_{z1,2}^e / \partial n$ can be expressed in terms of the tangential H field as

$$\frac{\partial E_{z1,2}^e}{\partial n} = Z_0 \left[-ikH_{t1,2}^e + \cos \theta' \left(\frac{\partial H_{t1,2}^e}{\partial l} + ik \cos \theta' H_{t1,2}^e \right) \right], \quad (18a)$$

$$\frac{\partial E_{z1,2}^q}{\partial n} = Z_0 \left[-ik\mu_{r1,2} H_{l1,2}^q + \frac{\cos \theta'}{\epsilon_{r1,2}} \left(\frac{\partial H_{z1,2}^q}{\partial l} + ik \cos \theta' H_{l1,2}^q \right) \right], \quad (18b)$$

where $H_{l1,2}^q = \hat{l} \cdot \vec{H}_{0,1,2}^q$ and \hat{l} is the direction of the integration paths along the interfaces. Thus, substituting (18) into (17) and applying the boundary conditions which require $H_{l1}^q = H_{l2}^q$ and $\partial H_{z1}^q / \partial l = \partial H_{z2}^q / \partial l$ at the material-free space interface, $H_{l1}^q = H_{l2}^q$ and $\partial H_{z1}^q / \partial l = \partial H_{z2}^q / \partial l$ at the material-material interface, one obtains

$$B_q \frac{t_1}{2} + \mu_{r1}(\tilde{q}_1^{(1)} + \tilde{q}_1^{(3)}) + \frac{\cos \theta'}{\epsilon_{r1}}(\tilde{q}_2^{(1)} + \tilde{q}_2^{(3)}) = 0, \quad (19a)$$

$$-B_q \frac{t_2}{2} + \mu_{r2}(\tilde{q}_1^{(2)} - \tilde{q}_1^{(3)}) + \frac{\cos \theta'}{\epsilon_{r2}}(\tilde{q}_2^{(2)} - \tilde{q}_2^{(3)}) = 0, \quad (19b)$$

$$B_q \left(\frac{t_2 - t_1}{2} \right) + C_q \pi - (\tilde{q}_1^{(1)} + \tilde{q}_1^{(2)}) - \cos \theta'(\tilde{q}_2^{(1)} + \tilde{q}_2^{(2)}) = 0; \quad (19c)$$

in which

$$\tilde{q}_1^{(1),(2),(3)} = -ikZ_0 \int_{\text{interface}} H_l^q dl, \quad (20a)$$

$$\tilde{q}_2^{(1),(2),(3)} = Z_0 \int_{\text{interface}} \left(ik \cos \theta' H_l^q + \frac{\partial H_z^q}{\partial l} \right) dl, \quad (20b)$$

where $\tilde{q}_1^{(1)}$, $\tilde{q}_1^{(2)}$, and $\tilde{q}_1^{(3)}$ are, respectively, the integrals along the free space-medium 1, free space-medium 2, and medium 1-medium 2 interfaces in the directions of $-\hat{x}$ and $-\hat{y}$. Eliminating $\tilde{q}_1^{(1),(2),(3)}$ in (19) yields

$$C_q - Q_1 B_q + \cos \theta' \tilde{D}_{q2} = 0, \quad (21a)$$

$$Q_1 = \frac{i}{K\pi} \left(\frac{1}{a_2^e} - \frac{1}{a_1^e} \right), \quad (21b)$$

$$\tilde{D}_{q2} = \frac{1}{\pi} \left[\left(\frac{1}{\mu_{r1}\epsilon_{r1}} - 1 \right) \tilde{q}_2^{(1)} + \left(\frac{1}{\mu_{r2}\epsilon_{r2}} - 1 \right) \tilde{q}_2^{(2)} + \left(\frac{1}{\mu_{r1}\epsilon_{r1}} - \frac{1}{\mu_{r2}\epsilon_{r2}} \right) \tilde{q}_2^{(3)} \right]. \quad (21c)$$

Note that \tilde{D}_{q2} given in (21c) is a constant because the definite integrals $\tilde{q}_2^{(1),(2),(3)}$ evaluated along the horizontal or vertical interfaces between the different media yield constants independent of x and y . Similarly, eliminating $\tilde{q}_1^{(1),(2),(3)}$ in (19), one obtains

$$C_q - Q_2 B_q + \tilde{D}_{q1} = 0, \quad (22a)$$

$$Q_2 = \frac{i}{K\pi} \left(\frac{1}{\sin \zeta_2^\lambda} - \frac{1}{\sin \zeta_1^\lambda} \right), \quad (22b)$$

$$\tilde{D}_{q1} = \frac{1}{\pi} \left[(\mu_{r1}\epsilon_{r1} - 1) \tilde{q}_1^{(1)} + (\mu_{r2}\epsilon_{r2} - 1) \tilde{q}_1^{(2)} + (\mu_{r1}\epsilon_{r1} - \mu_{r2}\epsilon_{r2}) \tilde{q}_1^{(3)} \right]. \quad (22c)$$

\tilde{D}_{q1} is also a constant as a consequence of $\tilde{q}_1^{(1),(2),(3)}$ being constants. By solving B_q and C_q in terms of \tilde{D}_{q1} and \tilde{D}_{q2}

from (21a) and (22a), one may rewrite the expression for Φ_q given in (15b) as follows:

$$\Phi_q \sim \frac{\tilde{D}_{q1}}{Q_2 - Q_1} (x + Q_1 \ln \rho) - \cos \theta' \frac{\tilde{D}_{q2}}{Q_2 - Q_1} (x + Q_2 \ln \rho), \quad (23)$$

as $\rho/t_1 \rightarrow \infty$.

Since the quasi-static solution is used only for matching, no further analysis is required.

A junction condition can be obtained by matching the quasi-static solution developed above with the corresponding Wiener-Hopf solution within the region of overlap $t_1 \ll \rho \ll K^{-1}$. Note that the region $t_1 \ll x \ll K^{-1}$ in the spatial domain transforms into the region $K \ll |s| \ll t_1^{-1}$ in the spectral s domain. Thus, the approximation of the even scattered field $E_z^{es}(x, 0)$ in the region $t_1 \ll x \ll K^{-1}$ can be found by taking the inverse Fourier transform of the function $\tilde{E}_z^{es}(s, 0)$ expanded in a series of s in the region $K \ll |s| \ll t_1^{-1}$. $\tilde{E}_z^{es}(s, 0)$ can be obtained via (13a), and it can then be decomposed into a sum of $\tilde{E}_{z+}^{es}(s, 0)$ and $\tilde{E}_{z-}^{es}(s, 0)$. Without going over the details, the asymptotic form for $\tilde{E}_{z+}^{es}(s, 0)$ in the region $K \ll |s| \ll t_1^{-1}$ is given by

$$\begin{aligned} \tilde{E}_{z+}^{es}(s, 0) \sim & \frac{\text{const}}{s} + \frac{ik}{s^2} \\ & \cdot \left[\frac{Z_0 \{ a_2^e H_y^{es}(0^+, 0) - a_1^e H_y^{es}(0^-, 0) \} c_1}{\sqrt{2\pi}} - \frac{\cos \theta' \sin \zeta_1^\lambda \tilde{C}_u^o}{\sin \zeta_2^\lambda - \sin \zeta_1^\lambda} \right] \\ & - \frac{ik \cos \theta' \sqrt{\sin \zeta_1^\lambda \sin \zeta_2^\lambda} \{ E_z^{es}(0^+, 0) - E_z^{es}(0^-, 0) \}}{\sqrt{2\pi}(\sin \zeta_2^\lambda - \sin \zeta_1^\lambda)} \\ & \cdot \left[\frac{1}{s^2} + \frac{iQ_2}{s} \ln_+ s \right] \\ & - \frac{ik \sqrt{a_1^e a_2^e} Z_0 \{ H_y^{es}(0^+, 0) - H_y^{es}(0^-, 0) \}}{\sqrt{2\pi}(a_2^e - a_1^e)} \\ & \cdot \left[\frac{1}{s^2} + \frac{iQ_1}{s} \ln_+ s \right], \end{aligned} \quad (24a)$$

$$c_1 = \frac{1}{a_2^e - a_1^e} - \frac{\cos^2 \theta' \sin \zeta_1^\lambda \sin \zeta_2^\lambda}{a_1^e a_2^e (\sin \zeta_2^\lambda - \sin \zeta_1^\lambda)}. \quad (24b)$$

The asymptotic expansions of the ratios involving the G_\pm functions in the region $K \ll |s| \ll t_1^{-1}$ were given in [1]. Taking the inverse Fourier transform of (24a) and then adding to the unperturbed even field $E_z^{eu}(x, 0)$, which is expanded in Maclaurin series of x up to the term of $0(x)$, one obtains the behavior of the total even field $E_z^e(x, 0)$ (after some simplification) in the region of interest $t_1 \ll x \ll K^{-1}$ as

$$\begin{aligned} E_z^e(x, 0) \sim & \text{constant} + c_0 x \\ & + \frac{ik \sqrt{a_1^e a_2^e} Z_0 \{ H_y^{es}(0^+, 0) - H_y^{es}(0^-, 0) \}}{(a_2^e - a_1^e)} \\ & \cdot (x + Q_1 \ln x) \\ & + \frac{ik \cos \theta' \sqrt{\sin \zeta_1^\lambda \sin \zeta_2^\lambda} \{ E_z^{es}(0^+, 0) - E_z^{es}(0^-, 0) \}}{(\sin \zeta_2^\lambda - \sin \zeta_1^\lambda)} \\ & \cdot (x + Q_2 \ln x), \end{aligned} \quad (25a)$$

$$c_0 = -\frac{iK \sin \theta' s_z^2 Z_0}{s_z^2 \sin^2 \theta' + K^2 \cos^2 \theta'} \left[\frac{a_2^e H_y^e(0^+, 0) - a_1^e H_y^e(0^-, 0)}{a_2^e - a_1^e} \right], \quad (25b)$$

where s_z^2 is defined in (42b) and H_y^e is the total normal field. Comparing (25a) with (15a) and (23), and noting that $\ln \rho \sim \ln x$ in (23) along the free space-material interface, it is seen that (25a) and (15a) are only matched when the coefficient c_0 in (25a) is identically zero, that is,

$$\frac{1}{a_1^e} H_y^e(0^+, 0) = \frac{1}{a_2^e} H_y^e(0^-, 0). \quad (26)$$

The condition above, which is called the junction condition, together with (10) and (14) determines all of the unknown constants, and complete solutions for \hat{E}_z^{ee} and \hat{H}_z^{ee} can now be obtained by means of (8) and (11)-(13).

IV. UTD SOLUTIONS

At this point, the field \hat{f}_{1z}^e is readily obtained by taking the inverse Fourier transform of $(\hat{E}_z^{ee}, \hat{H}_z^{ee})$ and reintroducing the factor $e^{-ikz \cos \theta'}$ suppressed earlier, namely,

$$\begin{aligned} \hat{f}_{1z}^e &= \left[\frac{E_z^{ee}}{Z_0 H_z^{ee}} \right] \\ &= \frac{e^{-ikz \cos \theta'}}{\sqrt{2\pi}} \int_{-\infty}^{\infty} \left[\frac{\hat{E}_z^{ee}(s, y)}{Z_0 \hat{H}_z^{ee}(s, y)} \right] e^{-isz} ds, \quad y \geq 0. \end{aligned} \quad (27a)$$

Since one is interested in finding a high-frequency UTD solution for \hat{f}_{1z}^e when $K\rho \rightarrow \infty$ instead of numerically integrating (27a), it is convenient to employ polar transformations to the variables in (27a). The transformations are

$$s = -K \cos w, \quad \beta = K \sin w, \quad x = \rho \cos \phi, \quad y = \rho \sin \phi, \quad (27b)$$

where w is a complex variable. The field \hat{f}_{1z}^e can then be expressed as follows:

$$\begin{aligned} \hat{f}_{1z}^e(\rho, \phi, z) &= \frac{e^{-ikz \cos \theta'}}{2\pi i} \int_{\Gamma} \hat{f}_{1z}(w, \phi'; \theta') e^{iK\rho \cos(w-\phi)} dw, \\ \rho &\geq 0, \quad 0 < \phi' < \pi; \end{aligned} \quad (28a)$$

where the integration path Γ in the w plane is the same as the one in [1, fig. 3]. Without going over the details, the spectral function $\hat{f}_{1z}(w, \phi'; \theta')$ is given by

$$\begin{aligned} \hat{f}_{1z}(w, \phi'; \theta') &= \bar{C}(w) \bar{\Psi}(w) \sin w \left[\frac{\bar{A}(w, \phi'; \theta')}{\cos w + \cos \phi'} + \bar{B}(w, \phi'; \theta') \right] \\ &\quad \cdot \sin \phi' \bar{\Psi}(\phi') \bar{Z}(\nu^e, \zeta^e) \bar{C}(\phi') \bar{F}_{0z}; \end{aligned} \quad (28b)$$

where the matrix \bar{C} was defined earlier in (6b), and

$$\bar{Z}(\nu^e, \zeta^e) = 2 \begin{bmatrix} a_2^e - a_1^e & 0 \\ 0 & \sin \zeta_2^e - \sin \zeta_1^e \end{bmatrix}, \quad (29a)$$

$$\bar{\Psi}(w) = \begin{bmatrix} g_+(w, \nu_{a_1}^e) g_+(w, \nu_{b_1}^e) g_-(w, \nu_{a_2}^e) g_-(w, \nu_{b_2}^e) & 0 \\ 0 & g_+(w, \zeta_1^e) g_-(w, \zeta_2^e) \end{bmatrix}. \quad (29b)$$

$$\begin{aligned} \bar{A}(w, \phi'; \theta') &= \begin{bmatrix} A_{11} & 0 \\ 0 & A_{22} \end{bmatrix}, \\ A_{22} &= \sin^2 \theta' \cos w \cos \phi' - \cos^2 \theta', \end{aligned} \quad (29c)$$

$$\begin{aligned} A_{11} &= -A_{22}(\cos w \cos \phi' + \cos^2 w_e) + (\cos w + \cos \phi') \\ &\quad \cdot \left[A_{22} \frac{\cos w_e}{h(w_e)} + \cos^2 \theta' \left(\frac{\cos w \cos \phi' + \cos^2 w_e}{h(w_e) \cos w_e} - \cos w - \cos \phi' \right) \right], \end{aligned} \quad (29d)$$

$$\bar{B}(w, \phi'; \theta') = \cot \theta' \bar{N}^{-1}(w, \theta') \bar{M}(\phi', \theta'), \quad (29e)$$

$$\begin{aligned} \bar{M}(\phi', \theta') &= \begin{bmatrix} \bar{V}_1^-(\phi', \theta') \bar{\Psi}(w_e^-) \\ \bar{V}_1^+(\phi', \theta') \bar{\Psi}(w_e^+) \end{bmatrix}, \\ \bar{N}(w, \theta') &= \begin{bmatrix} \bar{V}_2^-(w, \theta') \bar{\Psi}(w_e^-) \\ \bar{V}_2^+(w, \theta') \bar{\Psi}(w_e^+) \end{bmatrix}, \end{aligned} \quad (29f)$$

$$\bar{V}_1^\pm(\phi', \theta') = \left[\frac{\{h(w_e) \cos w_e - \cos \phi'\} \Delta(w_e)}{h(w_e) \cos w_e}, \pm i \sin^2 \theta' \right], \quad (29g)$$

$$\bar{V}_2^\pm(w, \theta') = \left[\frac{-\cot \theta' \pm i h(w_e) \cos w_e}{h(w_e) \cos w_e - \cos w}, 1 \right]; \quad (29h)$$

in which $\bar{V}_{1,2}^\pm$ are row vectors and

$$g_\pm(w, v) = G_\pm(-k \cos w, v), \quad (30a)$$

$$\begin{aligned} h(w_e) &= \frac{a_1^e g_+^2(w_e, \nu_{a_1}^e) g_+^2(w_e, \nu_{b_1}^e) + a_2^e g_+^2(w_e, \nu_{a_2}^e) g_+^2(w_e, \nu_{b_2}^e)}{a_1^e g_+^2(w_e, \nu_{a_1}^e) g_+^2(w_e, \nu_{b_1}^e) - a_2^e g_+^2(w_e, \nu_{a_2}^e) g_+^2(w_e, \nu_{b_2}^e)}, \end{aligned} \quad (30b)$$

$$w_\theta^\pm = \frac{\pi}{2} \pm i \ln \left(\frac{1 + \cos \theta'}{\sin \theta'} \right), \quad \cos w_e = -\frac{s_e}{K}, \quad (30c)$$

$\Delta(w)$ and s_e are defined in (6c) and (42b), respectively. Note that when $\theta' = \pi/2$, the matrix \bar{B} becomes a zero matrix, $\bar{C}(w)$ becomes diagonal, and the spectral function $\hat{f}_{1z}(w, \phi'; \theta')$ in (28b) reduces to the corresponding solution found by Rojas *et al.* [1] for the case of normal incidence.

Evaluating (28a) using the steepest descent method as in [1] and adding the unperturbed field \hat{f}_{1z}^u yields the total field \hat{f}_{1z} , which is given by

$$\begin{aligned} \hat{f}_{1z}(\rho, \phi, z) &= \left[\frac{E_z^e}{Z_0 H_z^e} \right] = \hat{f}_{1z}^u + \hat{f}_{1z}^r + \hat{f}_{1z}^{sw} + \hat{f}_{1z}^d, \\ 0 &< \phi, \phi' < \pi. \end{aligned} \quad (31)$$

The first term, \hat{f}_{1z}^u , in (31) is the incident field defined in (5). The second term is the reflected field given by

$$\begin{aligned} \hat{f}_{1z}^r &= \bar{C}^{-1}(\pi - \phi') \left[\bar{A}_1^{(1)} U(\pi - \phi - \phi') + \bar{A}_2^{(1)} U(\phi + \phi' - \pi) \right] \\ &\quad \cdot \bar{C}(\pi + \phi') \bar{F}_{0z} e^{-iK\rho \cos(\phi + \phi')} - ikz \cos \theta', \end{aligned} \quad (32)$$

where U is the unit step function and $\bar{A}_i^{(1)}$ are the reflection coefficient matrices defined in (6b). The third term, \bar{f}_{1z}^{sw} , in (31) is the surface wave field expressed as

$$\bar{f}_{1z}^{sw} = \{-\bar{r}_{sw}(w_{s_{b1}}^e) e^{iK\rho \cos(\nu_{b1}^e + \phi)} U(\phi_{s_1} - \phi) + \bar{r}_{sw}(w_{s_{b2}}^e) e^{iK\rho \cos(\nu_{b2}^e - \phi)} U(\phi - \phi_{s_2})\} e^{-ikz \cos \theta'}, \quad (33a)$$

$$\phi_{s_i} = \left[\frac{-\text{Re } \nu_{b_i}^e}{\pi + \text{Re } \nu_{b_i}^e} \right] \pm \arccos \left[\frac{1}{\cosh(\text{Im } \nu_{b_i}^e)} \right], \quad (33b)$$

$\bar{r}_{sw}(w_{s_{b1}}^e)$ and $\bar{r}_{sw}(w_{s_{b2}}^e)$ are the residues of \bar{f}_{1z} at the surface wave poles $w_{s_{b1}}^e = -\nu_{b1}^e$ and $w_{s_{b2}}^e = \pi + \nu_{b2}^e$, respectively, that is,

$$\begin{aligned} \bar{r}_{sw}(w_{s_{bi}}^e) &= \bar{C}(w_{s_{bi}}^e) \bar{P}_i^e(w_{s_{bi}}^e) \\ &\cdot \left[\frac{\bar{A}(w_{s_{bi}}^e, \phi'; \theta')}{\cos w_{s_{bi}}^e + \cos \phi'} + \bar{B}(w_{s_{bi}}^e, \phi'; \theta') \right] \\ &\cdot \sin \phi' \bar{\Psi}(\phi') \bar{Z}(\nu^e, \zeta^e) \bar{C}'(\phi') \bar{F}_{0z}; \end{aligned} \quad (33c)$$

$i = 1, 2$

with $\bar{P}_i^e(w_{s_{bi}}^e)$, $i = 1, 2$, being the residues of $\sin w \bar{\Psi}(w)$ at $w_{s_{bi}}^e$. The last term, \bar{f}_{1z}^d , in (31) is the edge-diffracted field given by

$$\bar{f}_{1z}^d(\rho, \phi, z) \sim \frac{e^{iK\rho - ikz \cos \theta'}}{\sqrt{\rho}} \bar{D}_1(\phi, \phi'; \theta') \bar{F}_{0z}, \quad 0 < \phi, \phi' < \pi, \quad (34a)$$

where $\bar{D}_1(\phi, \phi'; \theta')$ is the uniform diffraction coefficient matrix for the junction of the two-part material coated PMC ground plane, which can be expressed as

$$\begin{aligned} \bar{D}_1(\phi, \phi'; \theta') \bar{F}_{0z} &\sim -\frac{e^{i\frac{\pi}{2}}}{\sqrt{2\pi K}} \\ &\cdot \left\{ \bar{F}_{1z}(\phi, \phi'; \theta') + \sum_{i=1}^5 \bar{r}_i \frac{1 - F(-2K\rho\gamma_i^2)}{2\gamma_i} \right\}; \end{aligned} \quad (34b)$$

in which

$$\gamma_i = \sin \left(\frac{w_i - \phi}{2} \right), \quad i = 1, 2, 3, 4, 5, \quad (34c)$$

$$\begin{aligned} w_1 &= \pi - \phi', \quad w_2 = w_{s_{b1}}^e, \quad w_3 = w_{s_{b2}}^e, \\ w_4 &= -\zeta_1^e, \quad w_5 = \pi + \zeta_2^e, \end{aligned} \quad (34d)$$

$$\bar{r}_1 = \bar{C}^{-1}(\pi - \phi') (\bar{A}_2^{(1)} - \bar{A}_1^{(1)}) \bar{C}(\pi + \phi') \bar{F}_{0z}, \quad (34e)$$

$$\bar{r}_2 = \bar{r}_{sw}(w_{s_{b1}}^e), \quad \bar{r}_3 = \bar{r}_{sw}(w_{s_{b2}}^e), \quad (34f)$$

$$\begin{aligned} \bar{r}_i &= \bar{C}(w_i) \bar{P}_i^o(w_i) \left[\frac{\bar{A}(w_i, \phi'; \theta')}{\cos w_i + \cos \phi'} + \bar{B}(w_i, \phi'; \theta') \right] \\ &\cdot \sin \phi' \bar{\Psi}(\phi') \bar{Z}(\nu^e, \zeta^e) \bar{C}'(\phi') \bar{F}_{0z}; \quad i = 4, 5 \end{aligned} \quad (34g)$$

where $\bar{P}_i^o(w_i)$, $i = 4, 5$, are the residues of $\sin w \bar{\Psi}(w)$ at w_i . The function $F(x)$ in (34b) is the well-known transition function [21] given by

$$F(x) = 2i\sqrt{x} e^{ix} \int_{\sqrt{x}}^{\infty} e^{-it^2} dt, \quad -\frac{3\pi}{2} < \arg(x) < \frac{\pi}{2}, \quad (34h)$$

where the branch cut for $F(x)$ in the complex x plane is the positive imaginary axis. Note that when the magnitude of x is large, $F(x)$ approaches 1. Therefore, as $K\rho \rightarrow \infty$, the only nonzero term left in the expression for \bar{D}_1 is the first term, which is referred to as the far-zone diffraction coefficient \bar{D}_{FZ} . It is important to note that the UTD solution obtained above satisfies the reciprocity property; in other words, \bar{D}_{FZ} satisfies the following condition:

$$\bar{D}_{FZ} = \begin{bmatrix} D_{11} & D_{12} \\ D_{21} & D_{22} \end{bmatrix}, \quad \begin{aligned} D_{11}(\phi, \phi'; \theta') &= D_{11}(\phi', \phi; \theta'), \\ D_{22}(\phi, \phi'; \theta') &= D_{22}(\phi', \phi; \theta'), \\ D_{12}(\phi, \phi'; \theta') &= D_{21}(\phi', \phi; \theta'). \end{aligned} \quad (35)$$

The derivation of the above symmetry property is discussed in Appendix II.

As stated earlier, \bar{f}_{1z} is only part of the solution for the canonical diffraction problem of a two-part material slab illustrated in Fig. 1. The remaining part of the solution is the field \bar{f}_{2z} , which is defined as

$$\bar{f}_{2z}(\rho, \phi, z) = \begin{bmatrix} E_z^o(\rho, \phi, z) \\ Z_0 H_z^e(\rho, \phi, z) \end{bmatrix}, \quad 0 < \phi < \pi. \quad (36a)$$

Note that \bar{f}_{2z} is the solution to the other half of the bisection problems (see Fig. 2), namely, the two-part material coated PEC ground plane. Also, \bar{f}_{2z} is readily obtained from the solution \bar{f}_{1z} if the concept of duality is employed. Thus, the total field, \bar{f}_{2z} , of the PEC bisection problem is given by

$$\bar{f}_{2z}(\rho, \phi, z) = \bar{f}_{1z}^i + \bar{f}_{2z}^r + \bar{f}_{2z}^{sw} + \bar{f}_{2z}^d, \quad 0 < \phi, \phi' < \pi, \quad (36b)$$

where the reflected field \bar{f}_{2z}^r , the surface wave field \bar{f}_{2z}^{sw} , and the diffracted field \bar{f}_{2z}^d , respectively, have the form of $\bar{L}_1 \bar{f}_{1z}^i$, $\bar{L}_1 \bar{f}_{1z}^{sw}$, and $\bar{L}_1 \bar{f}_{1z}^d$, except that the off-diagonal terms of all the matrices in (32), (33a), and (34a) change signs, the magnitudes E_{0z} and $Z_0 H_{0z}$ are interchanged, and the parameters $\epsilon_{r1,2}$ and $\mu_{r1,2}$ are interchanged; the matrix \bar{L}_1 is defined as follows:

$$\bar{L}_1 = \begin{bmatrix} 0 & 1 \\ 1 & 0 \end{bmatrix}. \quad (36c)$$

The solution (E_z, H_z) to the original problem shown in Fig. 1 is obtained by superposing the solutions to the two bisection problems, that is,

$$\begin{aligned} E_z(\rho, \phi, z) &= E_z^e(\rho, |\phi|, z) + \text{sgn}(\phi) E_z^o(\rho, |\phi|, z), \\ -\pi &< \phi < \pi, \end{aligned} \quad (37a)$$

$$\begin{aligned} H_z(\rho, \phi, z) &= H_z^e(\rho, |\phi|, z) + \text{sgn}(\phi) H_z^o(\rho, |\phi|, z), \\ -\pi &< \phi < \pi. \end{aligned} \quad (37b)$$

where $\text{sgn}(\phi) = 1$ if $\phi > 0$ and -1 if $\phi < 0$. If one defines

$$\bar{f}_z = \begin{bmatrix} E_z \\ Z_0 H_z \end{bmatrix}, \quad \bar{L}_2 = \begin{bmatrix} 1 & 0 \\ 0 & |\phi|/\phi \end{bmatrix}, \quad (38a)$$

(37) can be rewritten as

$$\tilde{f}_z(\rho, \phi, z) = \tilde{f}_z^i + \tilde{f}_z^r + \tilde{f}_z^s + \tilde{f}_z^{sw} + \tilde{f}_z^d, \quad (38b)$$

$$0 < |\phi|, \phi' < \pi,$$

where

$$\tilde{f}_z^i = \tilde{f}_{1z}^i \left(1 + \frac{|\phi|}{\phi}\right), \quad \tilde{f}_z^r = (\tilde{f}_{1z}^r + \tilde{f}_{2z}^r)U(\phi), \quad (38c)$$

$$\tilde{f}_z^s = \tilde{L}_2 [\tilde{f}_{1z}^s(-\phi) - \tilde{f}_{2z}^s(-\phi)]U(-\phi), \quad (38d)$$

$$\tilde{f}_z^{d,sw} = \tilde{L}_2 \left[\tilde{f}_{1z}^{d,sw}(|\phi|) + \frac{|\phi|}{\phi} \tilde{f}_{2z}^{d,sw}(|\phi|) \right]. \quad (38e)$$

V. NUMERICAL RESULTS

The UTD solutions developed in the previous section for the two-part planar material slab and the related geometries consist of simple functions, most of which are amenable to numerical computation. The only functions that require a simple numerical integration are $g_{\pm}(w, v)$. This simple integration can be quickly and efficiently computed with a Gaussian quadrature. In Fig. 3, the z component of the total field, which includes the scattered and the incident fields, for the two-part thin material slab is presented. It can be seen that the total field is continuous across the shadow boundaries of the incident, reflected, and surface wave fields. Furthermore, it is noted that a superposition of the two sets of GIBC, which were employed to replace the two bisection configurations in this study, is equivalent to a "jump" boundary condition being used to model the original two-part transparent slab. Hence, discontinuities occur at $\phi = 0^\circ$, 180° , and 360° for the results shown in Fig. 3.

To test the accuracy of the UTD solutions, the singly edge-diffracted fields in the far zone are computed for a thin material half-plane where the incident field is an obliquely incident plane wave ($\theta' = 45^\circ$) of two different polarizations (TM_z and TE_z) and ϕ' is fixed and equal to zero. The UTD solutions are compared with independent MM results as shown in Fig. 4, where the diffracted fields E_z^d and $Z_0 H_z^d$ are given as functions of the scattered angle ϕ . Note that the UTD solution for a material half-plane can be easily derived from the solution for the two-part slab geometry if one replaces either material medium 1 or 2 with free space. This can be done by letting the corresponding $\epsilon_r \rightarrow 1$ and $\mu_r \rightarrow 1$, or by letting the corresponding thickness $t \rightarrow 0$ in the solution obtained in the previous section. Note also that the MM solution for a single edge was obtained from a material strip of finite width by a time-domain isolation technique [22], which provides good results only when the field diffracted from the first edge of the strip can be fairly well isolated from the effect of the second edge; that is, when the scattered angle ϕ is not far away from 0° so that the difference between the path lengths for the field scattered from the first and the second edges is not small. Since the region near edge-on is the most critical, Fig. 4 provides a good indication of the validity of the UTD solution, and it is seen that the agreement between the UTD and MM results is very good.

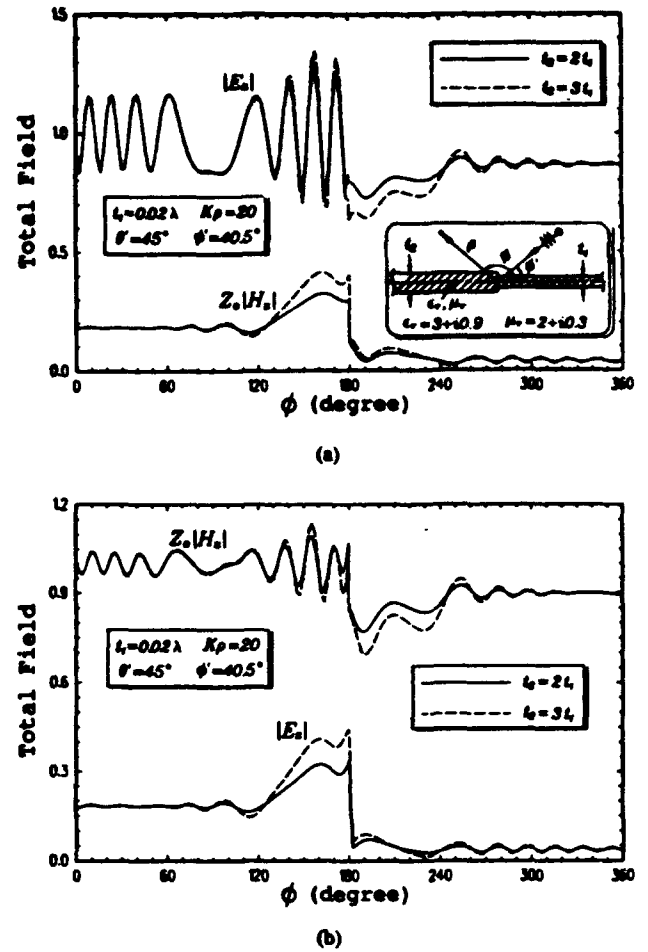


Fig. 3. Total field for a two-part planar material slab excited by an obliquely incident plane wave. (a) TM_z polarization: $E_{0z} = 1$, $Z_0 H_{0z} = 0$. (b) TE_z polarization: $E_{0z} = 0$, $Z_0 H_{0z} = 1$.

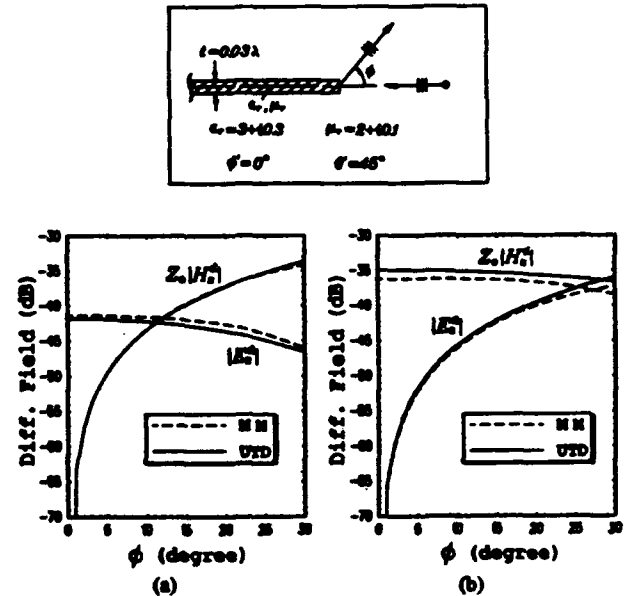


Fig. 4. UTD versus MM data for the far field diffracted by a material half-plane (oblique incidence). (a) TM_z polarization; (b) TE_z polarization.

In Fig. 5, the singly edge-diffracted fields in the far zone are computed for a thin material strip based on the newly

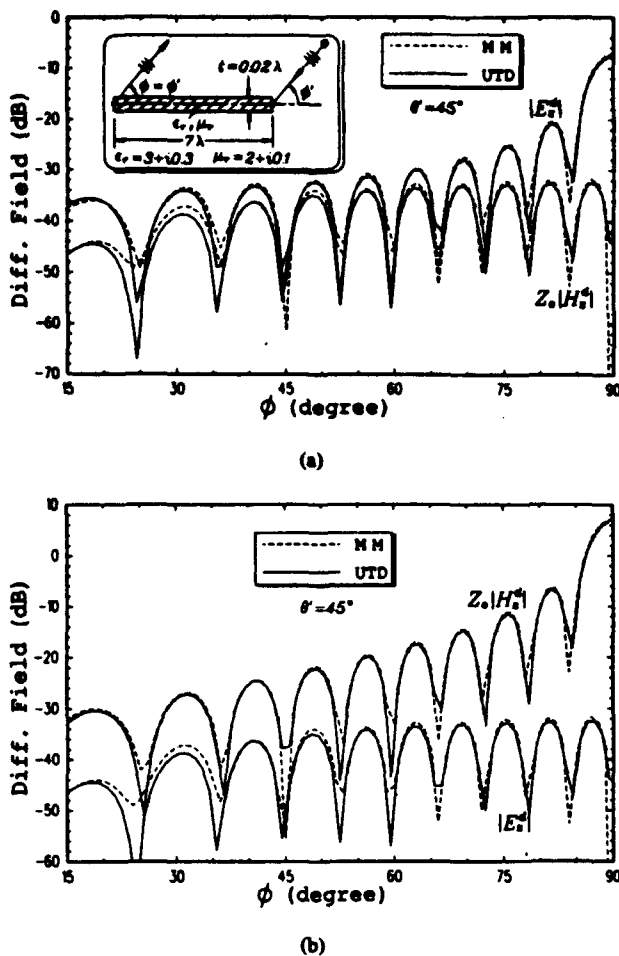


Fig. 5. UTD (without multiple interaction) versus MM data for the far field diffracted by a material strip with $\phi' = \phi$ (oblique incidence). (a) TM_z polarization: $E_{0z} = 1$, $Z_0 H_{0z} = 0$. (b) TE_z polarization: $E_{0z} = 0$, $Z_0 H_{0z} = 1$.

obtained UTD solution, where the strip width is 7λ and the scattered angle ϕ is equal to the incident angle ϕ' ; the incident field is an obliquely incident plane wave ($\theta' = 45^\circ$) of two different polarizations (TM_z and TE_z). The results computed from an independent MM solution for the material strip [18] are also included in Fig. 5 for comparison. It can be seen that the agreement between UTD and MM solutions is excellent for the observation aspect away from grazing. By including multiply diffracted fields for a finite strip as was done in [23], the results based on UTD can be made very accurate even in the region of grazing incidence or scattering.

VI. CONCLUSION

A uniform asymptotic solution to the problem of high-frequency diffraction by the planar junction of two thin material (dielectric/magnetic) half-planes has been developed in this paper. The incident field is assumed to be a plane wave of arbitrary polarization, obliquely incident to the axis or line of discontinuity in the otherwise planar two-dimensional material structure. The two-part transparent slab problem is not solved directly; instead, the solution is obtained by appropriately combining two solutions for the two related configurations involving PEC and PMC ground plane bisections of the original slab.

Actually, only the PMC bisection problem is solved using the Wiener-Hopf technique after the two-part grounded thin slab configuration is modeled by the GIBC of $0(t)$. By employing the duality principle, a solution to the PEC bisection problem is then obtained. Finally, a superposition of these solutions provides the result for the original problem. The final solutions are expressed in the high-frequency UTD forms, which involve relatively simple functions amenable to numerical calculations.

The application of GIBC or generalized resistive boundary conditions (GRBC's) of $0(t)$ yields second-order derivatives of the fields. This creates difficulties with magnetic dielectric materials because it gives rise to solutions which are neither unique nor reciprocal even after the edge condition has been applied. In this paper, the problem of uniqueness is solved by imposing a newly developed junction condition in addition to the boundary and radiation conditions as well as the usual edge condition. This junction condition is obtained by matching an approximate quasi-static solution with the corresponding Wiener-Hopf solution in their common domain of overlap near the edge (or junction). The solution obtained by this procedure yields a diffraction coefficient which automatically satisfies reciprocity; such a useful result obtained here is in contrast to the results in some papers found in the literature where the reciprocity condition has to be enforced explicitly. Note that the reciprocity property is not as readily apparent in the solution for the case of oblique incidence as it is for the case of normal incidence. Thus, the development of the reciprocity condition for the case of oblique incidence is provided in Appendix II.

The UTD solutions given in this paper are uniformly valid across the shadow boundaries of the incident (or transmitted), reflected, and surface wave fields. To verify the accuracy of the newly obtained UTD solutions, numerical results based on UTD are computed for some geometrical configurations and compared with corresponding results based on an independent MM solution. It is shown that the agreement between the two solutions is very good. Finally, it is noted that the solution to the two-part problem can also be applied to some special cases where either or both of the material half-planes in Fig. 1 reduce to free space, PEC, PMC, or resistive sheets. By including multiple interactions between the edges when their effects on the total scattering are significant, the UTD solutions obtained here can even be extended to treat inhomogeneous thin material strips with slowly varying electrical properties upon replacing them by sections of piecewise-constant material properties.

APPENDIX I

The functions $D_+^o(s)$ and $D_-^o(s)$, which are regular in the upper half s plane $\tau > \tau_-$ and the lower half s plane $\tau < \tau_+$, respectively, are given as follows:

$$D_{\pm}^o(s) = \pm \frac{i}{K(\sin \zeta_2^s - \sin \zeta_1^s)} \left\{ \frac{G_{\pm}(s, \zeta_2^s)}{G_{\pm}(s, \zeta_1^s)} \left[\frac{\tilde{A}_u^o}{s - K \cos \phi'} + \tilde{C}_u^o + C^{oo} \right] \mp \frac{G_+(K \cos \phi', \zeta_2^s)}{G_+(K \cos \phi', \zeta_1^s)} \frac{\tilde{A}_u^o}{s - K \cos \phi'} \right\}; \quad (39)$$

where

$$C^{ee} = \frac{\cos \theta'}{\sqrt{2\pi}} \left\{ \frac{[E_z^{ee}(0^+, 0) - E_z^{ee}(0^-, 0)]s}{K \sin \theta'} + \cot \theta' Z_0 [\sin \zeta_1^e H_z^{ee}(0^+, 0) - \sin \zeta_1^e H_z^{ee}(0^-, 0)] + Z_0 \left[\frac{H_y^{ee}(0^+, 0)}{1 + b_1^e \sin^2 \theta'} - \frac{H_y^{ee}(0^-, 0)}{1 + b_2^e \sin^2 \theta'} \right] \right\}, \quad (40a)$$

$$\tilde{C}_u^e = \frac{1}{\sqrt{2\pi} \sin \theta'} \left\{ - \left(\frac{\sin \zeta_2^e}{a_2^e} - \frac{\sin \zeta_1^e}{a_1^e} \right) \cos \theta' \cos \phi' E_x^{eu} \Big|_{y=0} + \left[\left(\frac{\sin \zeta_2^e}{a_2^e} - \frac{\sin \zeta_1^e}{a_1^e} \right) \frac{i \cos^2 \theta'}{K} \frac{\partial}{\partial y} + (\sin \zeta_2^e - \sin \zeta_1^e) \sin^2 \theta' \right] Z_0 H_z^{eu} \Big|_{y=0} \right\}, \quad (40b)$$

$$\tilde{A}_u^e = -\sqrt{\frac{2}{\pi}} \frac{K \sin \phi' (\sin \zeta_2^e - \sin \zeta_1^e)}{\sin \phi' + \sin \zeta_1^e} E_{0y}, \quad (40c)$$

and E_{0y} is the magnitude of the normal component of the incident field E_y^{ei} at the origin. Likewise, $D_{\pm}^e(s)$ are given by

$$D_{\pm}^e(s) = T_{\pm}(s) \left[\frac{\tilde{A}_u^e}{s - K \cos \phi'} + \tilde{C}_u^e + C^{ee} \right] \mp \frac{\tilde{A}_u^e}{s - K \cos \phi'} T_{\pm}(K \cos \phi'), \quad (41a)$$

$$T_+(s) = -\frac{1}{(a_2^e - a_1^e)(s^2 - s_e^2)} \cdot \left[a_2^e \frac{G_+(s, \nu_{a_2}^e) G_+(s, \nu_{b_2}^e)}{G_+(s, \nu_{a_1}^e) G_+(s, \nu_{b_1}^e)} + \alpha s + \delta \right], \quad (41b)$$

$$T_-(s) = \frac{1}{(a_2^e - a_1^e)(s^2 - s_e^2)} \cdot \left[a_1^e \frac{G_-(s, \nu_{a_1}^e) G_-(s, \nu_{b_1}^e)}{G_-(s, \nu_{a_2}^e) G_-(s, \nu_{b_2}^e)} + \alpha s + \delta \right], \quad (41c)$$

$$\alpha = \frac{1}{2s_e} \left[a_1^e \frac{G_+(s_e, \nu_{a_1}^e) G_+(s_e, \nu_{b_1}^e)}{G_+(s_e, \nu_{a_2}^e) G_+(s_e, \nu_{b_2}^e)} - a_2^e \frac{G_+(s_e, \nu_{a_2}^e) G_+(s_e, \nu_{b_2}^e)}{G_+(s_e, \nu_{a_1}^e) G_+(s_e, \nu_{b_1}^e)} \right], \quad (41d)$$

$$\delta = -\frac{1}{2} \left[a_1^e \frac{G_+(s_e, \nu_{a_1}^e) G_+(s_e, \nu_{b_1}^e)}{G_+(s_e, \nu_{a_2}^e) G_+(s_e, \nu_{b_2}^e)} + a_2^e \frac{G_+(s_e, \nu_{a_2}^e) G_+(s_e, \nu_{b_2}^e)}{G_+(s_e, \nu_{a_1}^e) G_+(s_e, \nu_{b_1}^e)} \right]; \quad (41e)$$

$$C^{ee} = \frac{-i}{a_1^e \sqrt{2\pi}} \left\{ Z_0 [a_2^e H_y^{ee}(0^+, 0) - a_1^e H_y^{ee}(0^-, 0)]s + a_1^e a_2^e \cot \theta' Z_0 [H_z^{ee}(0^+, 0) - H_z^{ee}(0^-, 0)]s + \frac{(s^2 - K^2 b_1^e \cos^2 \theta') a_2^e E_z^{ee}(0^+, 0) - (s^2 - K^2 b_2^e \cos^2 \theta') a_1^e E_z^{ee}(0^-, 0)}{K \sin \theta'} \right\}, \quad (42a)$$

$$s_e^2 = K^2 \left(1 + \frac{a_2^e b_1^e - a_1^e b_2^e}{a_2^e - a_1^e} \right), \quad \text{Im } s_e > 0, \quad (42b)$$

$$\tilde{C}_u^e = \frac{1}{\sqrt{2\pi} \sin \theta'} \left\{ \left[(a_2^e - a_1^e) \frac{\partial}{\partial y} + iK(b_2^e - b_1^e) \sin^2 \theta' \right] E_x^{eu} \Big|_{y=0} - iK \cos \theta' \cos \phi' (a_2^e - a_1^e) Z_0 H_z^{eu} \Big|_{y=0} \right\}. \quad (42c)$$

$$\tilde{A}_u^e = i\sqrt{\frac{2}{\pi}} \frac{\sin \phi' (a_2^e - a_1^e) (K^2 \cos^2 \phi' - s_e^2)}{\sin^2 \phi' + a_1^e \sin \phi' + b_1^e} Z_0 H_{0y}, \quad (42d)$$

and H_{0y} is the magnitude of the normal component of the incident field H_y^{ei} at the origin.

APPENDIX II

Let the entire upper half space $\{y > 0\}$ of the PMC bisection configuration depicted in Fig. 2 be enclosed by a surface S . The reciprocity theorem in the most general integral form for the entire region enclosed by S is given by

$$-\oint_S (\tilde{E}_a \times \tilde{H}_b - \tilde{E}_b \times \tilde{H}_a) \cdot \hat{n}' ds = \iiint_V (\tilde{E}_a \cdot \tilde{J}_b - \tilde{H}_a \cdot \tilde{M}_b - \tilde{E}_b \cdot \tilde{J}_a + \tilde{H}_b \cdot \tilde{M}_a) dv, \quad (43a)$$

where V is the volume of the entire region enclosed by S , \hat{n}' is the outer normal of S , \tilde{J}_a and \tilde{M}_a are, respectively, the electric and magnetic current densities of sources a and b ; \tilde{E}_a and \tilde{H}_a are, respectively, the total electric and magnetic fields radiated by sources a and b in the presence of the material coated PMC ground plane.

Let source a be a line source consisting of traveling line currents with $e^{-ikz \cos \theta'}$ dependence. As source a recedes to infinity (but is still captured inside S), the incident field radiated by source a becomes a plane wave field obliquely incident to the z axis with an angle θ' measured from the $+z$ axis. By the law of diffraction, the diffracted rays emanating from the edge (z axis) due to source a form the surface of a cone making the same cone angle with the edge as the incident ray. In other words, the angle formed between the diffracted rays and the $-z$ axis is θ' . Thus, to check the reciprocity property for the solution of the total field which includes the diffracted field, one would like the second source (i.e., source b) to be a line source with $e^{ikz \cos \theta'}$ dependence so that it excites an obliquely incident plane wave (as b recedes to infinity) in free space with an angle $\pi - \theta'$ measured from the $+z$ axis. It follows that

$$\begin{aligned} \iiint_V \tilde{J}_a dv &= \hat{z} I_a e^{\mp ikz \cos \theta'}, \\ \iiint_V \tilde{M}_a dv &= \hat{z} I_a^m e^{\mp ikz \cos \theta'}, \end{aligned} \quad (43b)$$

where $I_{a,b}$ and $I_{a,b}^m$ are the magnitudes of the corresponding electric and magnetic currents. Furthermore, since the bound-

any condition at the PMC plane ($y = 0$) together with the radiation condition (as $\rho \rightarrow \infty$) force the left-hand side of (43a) to vanish, the reciprocity condition reduces to

$$[E_{z_a}(\rho'_b)I_b - H_{z_a}(\rho'_b)I_b^m]e^{ikz \cos \theta'} \\ = [E_{z_b}(\rho'_a)I_a - H_{z_b}(\rho'_a)I_a^m]e^{-ikz \cos \theta'}, \quad (43c)$$

where ρ'_a and ρ'_b denote the the locations of sources a and b , respectively.

Since both sources a and b recede to infinity to produce plane wave incident fields, the evanescent surface wave fields vanish at the locations of the sources. Furthermore, it is well known that the geometrical optics fields satisfy the reciprocity condition. Therefore, it remains to be shown that the diffracted fields satisfy condition (43c). Applying (34a) (as $\rho \rightarrow \infty$) to (43c) yields, after some simplification, the following symmetry property:

$$\tilde{D}_{FZ} = \begin{bmatrix} D_{11} & D_{12} \\ D_{21} & D_{22} \end{bmatrix}, \\ D_{11}(\phi'_b, \phi'_a; \theta') = D_{11}(\phi'_a, \phi'_b; \pi - \theta'), \\ D_{22}(\phi'_b, \phi'_a; \theta') = D_{22}(\phi'_a, \phi'_b; \pi - \theta'), \\ D_{12}(\phi'_b, \phi'_a; \theta') = -D_{21}(\phi'_a, \phi'_b; \pi - \theta'); \quad (44)$$

where \tilde{D}_{FZ} is the far zone diffraction coefficient for the PMC bisection problem. Thus, to show that the UTD solution for the PMC bisection problem satisfies reciprocity, it is sufficient to verify that (44) holds for \tilde{D}_{FZ} . It can be shown from (34a) and (28b) that \tilde{D}_{FZ} indeed satisfies the condition in (44). Furthermore, since D_{11} and D_{22} are not changed when θ' is replaced by $\pi - \theta'$, whereas D_{12} and D_{21} change sign when θ' becomes $\pi - \theta'$, (44) can be rewritten as (35). Note that via the duality principle, it can also be shown that the solution for the PEC bisection problem satisfies the reciprocity condition.

REFERENCES

- [1] R.G. Rojas, H.C. Ly, and P.H. Pathak, "Electromagnetic plane wave diffraction by a planar junction of two thin dielectric/ferrite half planes," *Radio Sci.*, vol. 26, pp. 641-660, 1991.
- [2] L.A. Weinstein, *The Theory of Diffraction and the Factorization Method*. Boulder, CO: Golem Press, 1969.
- [3] R. Mittra and S.W. Lee, *Analytical Techniques in the Theory of Guided Waves*. New York: Macmillan, 1971.
- [4] B. Noble, *Methods Based on the Wiener-Hopf Technique*. New York: Pergamon Press, 1958.
- [5] F.G. Leppington, "Travelling waves in a dielectric slab with an abrupt change in thickness," *Proc. Roy. Soc. London*, vol. A386, pp. 443-460, 1983.
- [6] I. Anderson, "Plane wave diffraction by a thin dielectric half-plane," *IEEE Trans. Antennas Propagat.*, vol. 27, pp. 584-589, Sept. 1979.
- [7] R. G. Rojas and P. H. Pathak, "Diffraction of EM waves by a dielectric/ferrite half-plane and related configurations," *IEEE Trans. Antennas Propagat.*, vol. 37, pp. 751-763, June 1989.
- [8] R. G. Rojas, L. M. Chou, and P. H. Pathak, "Diffraction by a magnetic dielectric half-plane using generalized impedance/resistive boundary conditions," presented at 1988 URSI Radio Science Meeting, Syracuse Univ., Syracuse, NY.
- [9] A. Chakrabarti, "Diffraction by a dielectric half-plane," *IEEE Trans. Antennas Propagat.*, vol. 34, pp. 830-833, June 1986.
- [10] J. L. Volakis and T.B.A. Senior, "Diffraction by a thin dielectric half-plane," *IEEE Trans. Antennas Propagat.*, vol. 35, pp. 1483-1487, Dec. 1987.

- [11] J. M. L. Bernard, "Diffraction by a metallic wedge covered with dielectric material," *Wave Motion*, vol. 9, pp. 543-561, 1987.
- [12] T. B. A. Senior, "Diffraction by a generalized impedance half plane," *Radio Sci.*, vol. 26, pp. 163-167, 1991.
- [13] R. G. Rojas and L. M. Chou, "Diffraction by a partially coated electric conducting half plane," *Radio Sci.*, vol. 25, pp. 175-188, 1990.
- [14] R. G. Rojas, "Generalized impedance boundary conditions," *Electron. Lett.*, vol. 24, pp. 1093-1094, Aug. 1988.
- [15] R. G. Rojas and Z. Al-Hekail, "Generalized impedance/resistive boundary conditions for EM scattering problems," *Radio Sci.*, vol. 24, pp. 1-12, 1989.
- [16] A. Buyukaksoy, G. Uzgoren and A. Serbest, "Diffraction of an obliquely incident plane wave by the discontinuity of a two part thin dielectric plane," *Int. J. Eng. Sci.*, vol. 27, no. 6, pp. 701-710, 1989.
- [17] T. B. A. Senior, "Skew incidence on a dielectric half-plane," *Electromagnetics*, vol. 9, pp. 187-200, 1989.
- [18] R. G. Rojas, "Scattering by an inhomogeneous dielectric/ferrite cylinder of arbitrary cross-section shape-Oblique incidence case," *IEEE Trans. Antennas Propagat.*, vol. 36, pp. 238-245, 1988.
- [19] H. C. Ly, "A UTD analysis of EM diffraction by an abrupt discontinuity in thin planar material configurations," Ph.D. dissertation, Ohio State Univ., Dept. of E.E., winter 1992.
- [20] R. G. Rojas, "A Uniform GTD analysis of the EM diffraction by a thin dielectric/ferrite half-plane and related configurations," Ph.D. dissertation, Ohio State Univ., Dept. of E.E., winter 1985.
- [21] R. G. Kouyoumjian and P. H. Pathak, "A uniform geometrical theory of diffraction for an edge in a perfectly conducting surface," *Proc. IEEE*, vol. 62, pp. 1448-1461, Nov. 1974.
- [22] A. K. Dominek, L. Peters, Jr., and W. D. Burnside, "A time domain technique for mechanism extraction," *IEEE Trans. Antennas Propagat.*, vol. 35, pp. 305-312, Mar. 1987.
- [23] R. G. Rojas, H. C. Ly, P. H. Pathak, and R. Tiberio, "Electromagnetic plane wave diffraction by a three-part thin, planar dielectric/magnetic slab," *Radio Sci.*, vol. 26, pp. 1267-1280, 1991.



Hung Cam Ly (S'85) was born in Saigon, Vietnam, on March 16, 1959. He received the B.S. (summa cum laude), M.S., and Ph.D. degrees, all in electrical engineering, from Ohio State University, Columbus, in 1985, 1989, and 1992, respectively.

From October 1985 to March 1992 he was with the ElectroScience Laboratory at Ohio State as a Graduate Research Associate. His research interests include theoretical and computational electromagnetics, analysis of EM antenna and scattering problems, radar cross section studies, high-frequency

scattering from materials, and multiple scattering effects. Dr. Ly is a member of Tau Beta Pi and Eta Kappa Nu.

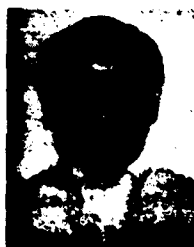


Roberto G. Rojas (S'80-M'85-SM'90) received the B.S.E.E. degree from New Mexico State University in 1979 and the M.S. and Ph.D. degrees in electrical engineering from Ohio State University in 1981 and 1985 respectively.

During the summer of 1979 he worked with Rockwell International in Albuquerque, NM. He has been with the ElectroScience Laboratory, Ohio State University, since 1979, first as a graduate student and then, starting in 1985, as a full-time researcher. His current research interests are in

electromagnetic scattering and modeling, high-frequency techniques, and numerical and analytical techniques for the analysis of MMIC.

Dr. Rojas was the winner of the 1988 R. W. P. King Prize Paper Award, the 1990 Browder J. Thompson Memorial Prize Award, both given by the IEEE, and the 1989 and 1993 Lumley Research Awards, given by the College of Engineering at Ohio State University. He has served as Chairman, Vice-Chairman, and Secretary/Treasurer of the Columbus, OH, chapter of the IEEE Antennas and Propagation Society and the IEEE Microwave Theory and Techniques Society. Dr. Rojas is a member of Sigma Xi and of U.S. Commission B of the International Union of Radio Science (URSI).



Prabhakar H. Pathak (M'76-SM'81-F'86) received the B.Sc. degree in physics from the University of Bombay, India, in 1962, the B.S. degree in electrical engineering from Louisiana State University, Baton Rouge, in 1965, and the M.S. and Ph.D. degrees from Ohio State University (OSU), Columbus, in 1970 and 1973, respectively.

From 1965 to 1966 he was an Instructor in the Department of Electrical Engineering at the University of Mississippi, Oxford. During the summer of 1966 he worked as an electronics engineer with the Boeing Company, Renton, WA. Since 1968 he has been with the OSU ElectroScience Laboratory. His research interests are in mathematical methods, electromagnetics, and uniform ray techniques. In 1983 he joined the faculty of the Department of Electrical Engineering at Ohio State, where he is currently a Professor. He has contributed to the development of the uniform geometrical theory of diffraction (UTD), which can be applied to analyze a variety of practical electromagnetics antenna and scattering problems. His work continues to be in the UTD and other high-frequency techniques, as well as in the analysis of guided waves, and microstrip and reflector antennas using high-frequency asymptotic techniques.

Dr. Pathak has presented invited lectures and several short courses on the UTD, both in the U.S. and abroad. He has also authored or coauthored chapters on ray methods for five books. He has served as Associate Editor for this journal for about five years. Currently, he is serving as an IEEE AP-S distinguished lecturer. Dr. Pathak is a member of Commission B of the International Scientific Radio Union (URSI) and Sigma Xi.

Scattering by Thin Wire Loaded with a Ferrite Ring

N. Wang and L. Peters, Jr.

Abstract—This communication presents a coupled integral equation formulation and the method of moments (MM) solution to the problem of scattering by a thin conducting wire of circular cross section with ferrite loading. It is proved that the ferrite loading can be used to reduce the radar cross section of long thin objects at their resonant frequency.

I. INTRODUCTION

It has long been recognized that ferrite beads can be used in lieu of inductive chokes to prevent unwanted energy from being coupled into power supplies. This same concept can be used to reduce the RCS of long thin objects at their resonant frequency. The purpose of this communication is to present a coupled integral equation formulation and the method of moments solution to the problem of scattering by thin conducting wire loaded with a ferrite ring. The reduction of RCS of long thin objects by ferrite loading is demonstrated in this communication by the numerical results.

II. ANALYSIS

Consider a thin conductor (wire) illuminated by an incoming plane wave. A ferrite ring with permeability μ_r is placed concentrically at the center of the wire. The geometry of the problem is shown

Manuscript received August 24, 1992; revised January 8, 1993. This work was supported by the Joint Services Electronics Program (N00014-89-J-1007).

The authors are with the ElectroScience Laboratory, Department of Electrical Engineering, Ohio State University, Columbus, OH 43212.

IEEE Log Number 9209213.

in Fig. 1. The thin wire has a radius a and a finite length l . The cross-sectional area of the ferrite ring is equal to πc^2 .

It is assumed that the wire is electrically thin such that only an axial current, I_z , is induced on the wire and I_z has no circumferential variation. It is also assumed that the area πc^2 is small enough that the induced magnetic field intensity, H_ϕ , inside the ferrite ring is uniform and circumferentially orientated. A coupled integral equation for the unknown axial current, I_z , and circumferential magnetic field intensity, H_ϕ , is formulated below.

Employing the well-established thin-wire theory developed by Richmond [1], the following equation along the axis of the thin wire is obtained:

$$E_z^i(I_z) + E_z^s(M_{eq}) = -E_z^i \quad (1)$$

Here $E_z^i(I_z)$ and $E_z^s(M_{eq})$ are the free-space fields generated by the induced electric current, I_z , and the equivalent magnetic current source, M_{eq} , respectively. E_z^i is the incident electric field and

$$\vec{M}_{eq} = \hat{\phi} j\omega\mu_0(\mu_r - 1)H_\phi \quad (2)$$

In the above equation, H_ϕ is the unknown constant magnetic field intensity inside the ferrite ring, and M_{eq} is confined by the ferrite material.

A second equation for I_z and H_ϕ can be obtained by noting that the total magnetic field intensity, H_ϕ , inside the ferrite ring is given by

$$H_\phi = H_\phi^i + H_\phi^s(I_z) + H_\phi^s(M_{eq}) \quad (3)$$

In this equation H_ϕ^i is the incident magnetic field. $H_\phi^s(I_z)$ and $H_\phi^s(M_{eq})$ are the free-space fields generated by I_z and M_{eq} respectively.

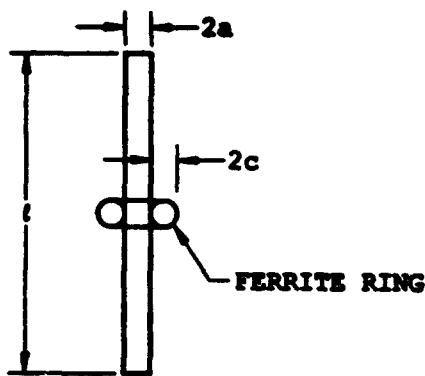


Fig. 1. A thin wire with ferrite ring.

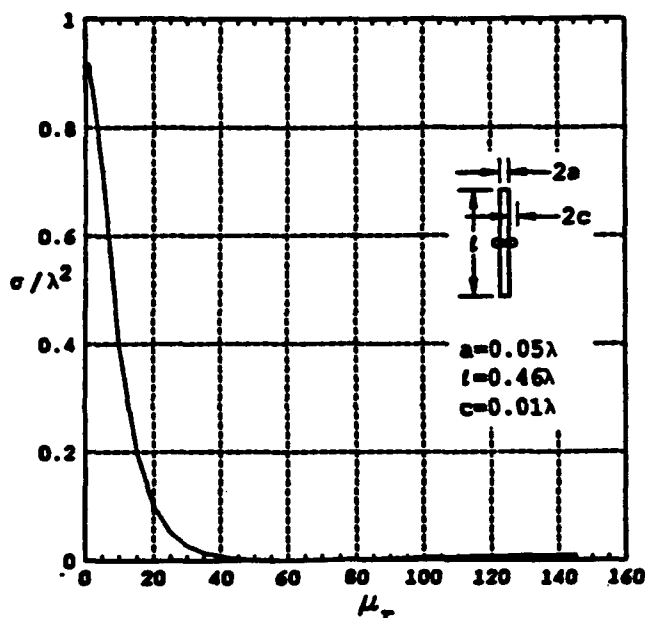


Fig. 2. RCS of a half-wavelength dipole with a ferrite bead placed as shown.

A solution to the coupled equations (1) and (3) using the methods of moments is outlined below.

The induced electric current, I_z , along the thin wire is expanded as

$$I_z(z) = \sum_{n=1}^N I_n F_n(z), \quad (4)$$

where I_n are unknown constants and $F_n(z)$ are the piecewise-sinusoidal expansion functions discussed by Richmond [1].

The induced magnetic field, H_ϕ , inside the ferrite ring is represented by a constant term:

$$H_\phi = I_{N+1} P(\phi), \quad (5)$$

where I_{N+1} is the unknown coefficient and $P(\phi)$ is constant pulse function with unit amplitude in the interval $0 \leq \phi \leq 2\pi$. Performing the Galerkin test on (1) and (3), one obtains the following equations:

$$-\int_m F_m(z) E_z^*(I_z) dz - \int_m F_m(z) E_z^*(M_{eq}) dz = \int_m F_m(z) E^i(z) dz \quad (6)$$

$$\int_0^{2\pi} P(\phi) [H_\phi - H_\phi^*(I_z) - H_\phi^*(M_{eq})] b d\phi = \int_0^{2\pi} P(\phi) H_\phi^i b d\phi. \quad (7)$$

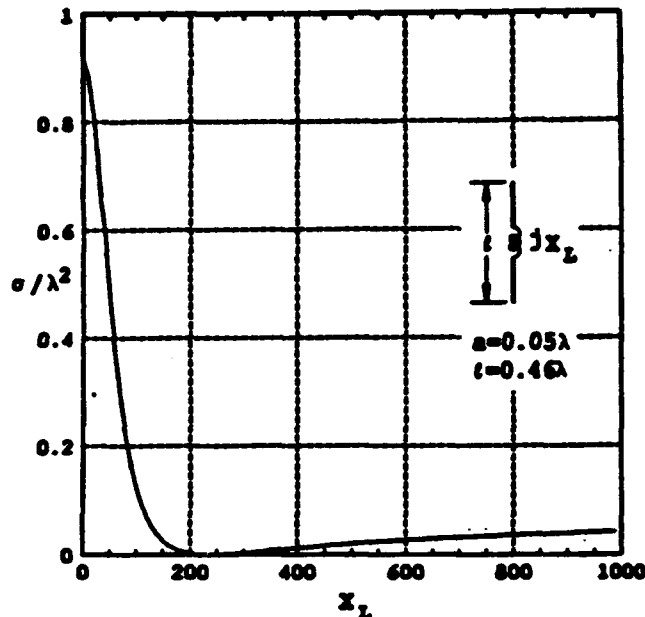


Fig. 3. RCS of an inductively loaded dipole.

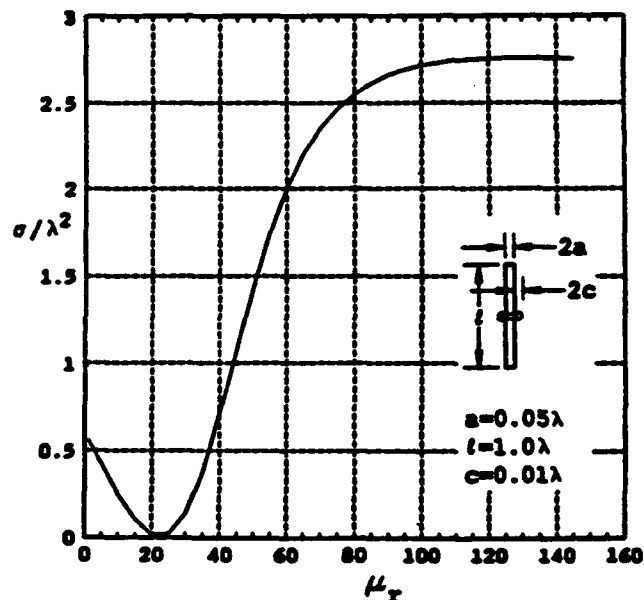


Fig. 4. RCS of a wavelength-long dipole loaded with a ferrite bead.

Substituting (4) and (5) into (6) and (7), the following set of $N+1$ equations can be obtained:

$$\sum_{n=1}^N I_n Z_{mn} + I_{N+1} Z_{m, N+1} = V_m, \quad m = 1, 2, \dots, N \quad (8a)$$

$$\sum_{n=1}^N I_n Z_{N+1, n} + I_{N+1} Z_{N+1, N+1} = V_{N+1}. \quad (8b)$$

Z_{mn} is the usual mutual impedance between two sinusoidal dipoles [1], and

$$Z_{m, N+1} = j\omega\mu_0(\mu_r - 1)\pi c^2 2\pi b H_\phi^m, \quad (9)$$

where $b = a + c$.

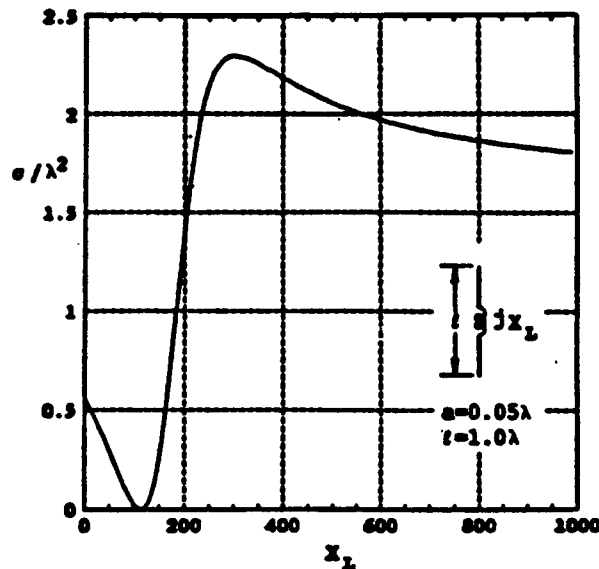


Fig. 5. RCS of a wavelength dipole with an inductive load.

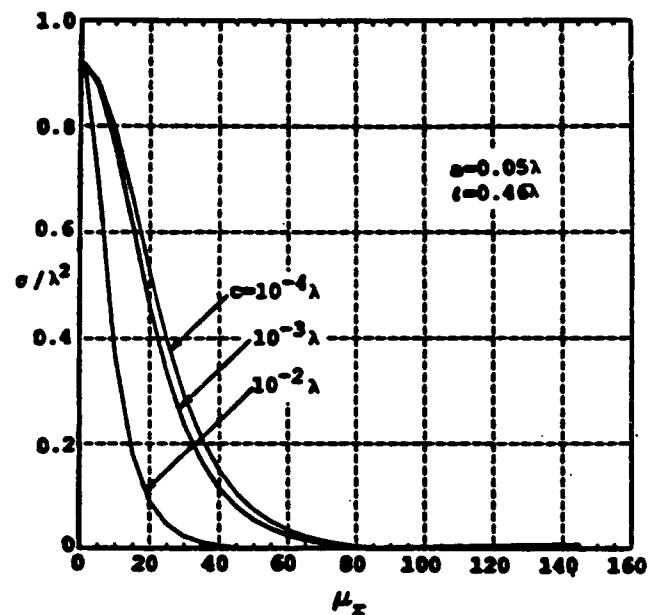


Fig. 7. RCS of bead-loaded dipole as a function of bead size (\$a = 0.05\lambda\$).

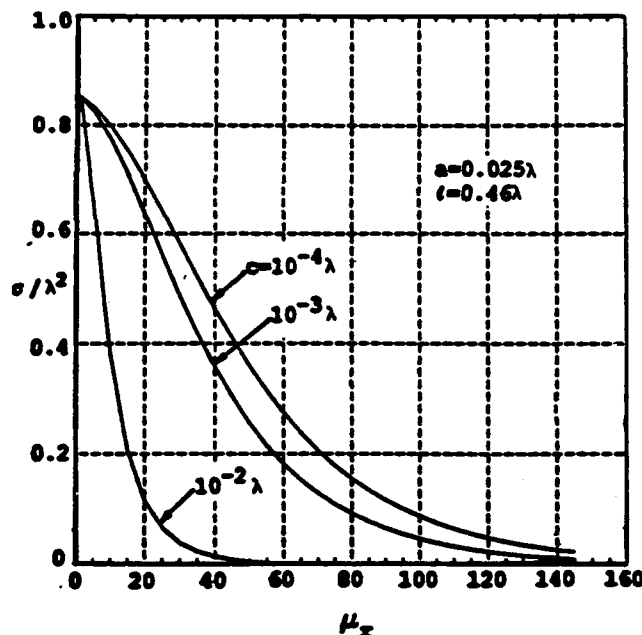


Fig. 6. RCS of ferrite-bead-loaded dipole as a function of bead size (\$a = 0.025\lambda\$).

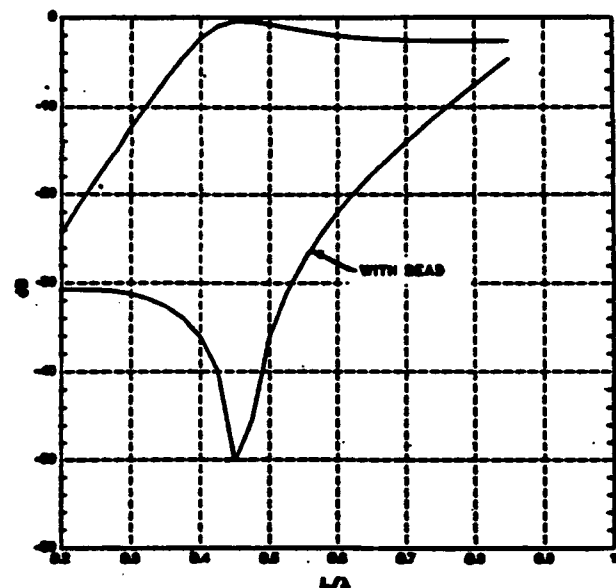


Fig. 8. Frequency dependence of RCS reduction from a rod with a ferrite bead with \$a = 0.05\lambda\$, \$c = 0.01\lambda\$, and \$\mu_r = 60\$.

H_ϕ^m is the magnetic field intensity arising from the electric current source $F_m(z)$, evaluated at the center of the ferrite ring. Note that the reciprocity theorem has been employed for the second term on the left-hand side of (8) to obtain the expression for $Z_{m,N+1}$. Expressions for $Z_{N+1,n}$ and $Z_{N+1,N+1}$ are given below:

$$Z_{N+1,n} = -2\pi b H_\phi^m \quad (10)$$

and

$$Z_{N+1,N+1} = 2\pi b [1 + \pi c^2 j\omega\mu_0(\mu_1 - 1)z_{00}/\eta_0^2], \quad (11)$$

where z_{00} is the zeroth-order generalized impedance for the circular electric wire loop [2], and η_0 is the intrinsic impedance of free space.

The matrix equation (8) can be readily solved for the unknowns I_n , and the far-zone scattered field can be easily obtained. Note that the

contribution to the scattered field from the ferrite ring is insignificant and is ignored in the calculation. In the next section numerical results for the scatter fields arising from ferrite-loaded thin wire will be presented.

III. NUMERICAL RESULTS AND DISCUSSIONS

In this section we present numerical results for the plane wave scattering by a straight piece of thin wire. The ferrite ring is placed at the center of the wire. The results are obtained for a normally incident plane wave with the incident electric field E^i parallel to the wire. Fig. 2 presents the broadside radar cross section (RCS) of a 0.46λ long thin wire as a function of the permeability, μ_r , for the ferrite ring. It can be seen that as μ_r increases the RCS of the

ferrite-ring-loaded thin wire is dramatically reduced. Corresponding results based on thin wire with a lumped load (jX_L) at the center are also obtained. The results for the inductive load are shown in Fig. 3. It is seen that the inductive loading has a similar effect of RCS reduction as that due to the ferrite ring. However, the ferrite bead is inserted on the wire whereas the inductive load must be inserted in series, making it necessary to cut the wire. Figs. 4 and 5 present the RCS curves for a one-wavelength-long thin wire. It is interesting to observe that as the μ_r or X_L is increased, the RCS of the λ -long dipole approaches that of two $\lambda/2$ -long dipoles.

This frequency dependence of ferrites may prove to be useful. It may be possible to design the material so that it is effective at the design frequency but not effective for frequencies much higher than the design frequency.

The effect due to the cross section area of the ferrite ring on the RCS of a thin wire is also investigated. The results for the case of a $0.025 \times 0.46\lambda$ wire are shown in Fig. 6. Note that, in Fig. 6, as the radar cross section area of the ferrite ring is decreased from a radius of $10^{-2}\lambda$ to $10^{-4}\lambda$ the effect of the ferrite-ring on the RCS of the loaded wire is gradually diminished. Fig. 7 gives the radar cross section when the radius of the wire is increased from 0.025λ

to 0.05λ . Note that the effectiveness of the bead has improved with this increase in radius (or for the fatter dipole).

It might be assumed that the RCS reduction introduced by the presence of the ferrite bead would be frequency dependent. As may be seen in Fig. 8, this is a broadband phenomenon and the RCS reduction is maintained for about a 4:1 bandwidth. It should also be possible to extend the bandwidth by use of multiple beads.

IV. SUMMARY AND DISCUSSION

This paper has presented a coupled integral equation and method of moments (MM) solution to the problem of scattering by a thin conducting wire of circular cross section with ferrite loading. It has been shown that the ferrite loading can be used to reduce the radar cross section of long thin objects at their resonant frequency.

REFERENCES

- [1] J. H. Richmond, "Radiation and scattering by thin-wire structures in the complex frequency domain," Tech. Rep. 2902-10, Ohio State University ElectroScience Laboratory, July 1973.
- [2] R. F. Harrington, *Field Computation by Moment Methods*. New York: Macmillan, 1968.

Analysis of diffraction by material discontinuities in thin material-coated planar surfaces based on Maliuzhinets method

H. C. Ly and R. G. Rojas

ElectroScience Laboratory, Department of Electrical Engineering, Ohio State University, Columbus, Ohio

(Received May 27, 1992; accepted September 30, 1992.)

The electromagnetic diffraction of a plane wave (transverse electric case) by a two-part material coated perfectly conducting ground plane and a material-coated perfectly conducting half plane is studied using the Maliuzhinets method. Each of the coatings is assumed to be electrically thin so that it can be replaced in the analysis by a generalized impedance boundary condition of $0(t)$, where t is the corresponding coating thickness. To solve each of the boundary value problems completely, one needs to impose an additional constraint which is determined here by matching an approximate quasi-static solution with the corresponding Maliuzhinets solution in the common region of overlap. This requires the asymptotic evaluation of the Maliuzhinets functions in various regions of the spectral domain. Furthermore, several constants that appear in the analysis are exactly related to the field and its derivatives evaluated at the edge or junction of the body under study. The backscattered and bistatic echo widths of a partially coated perfectly conducting half plane are computed with the solutions developed here (including multiple interaction) and compared with an independent moment method solution. The agreement between the two solutions is excellent.

1. INTRODUCTION

The generalized impedance boundary conditions (GIBCs), which involve field derivatives of higher order than the first, have frequently been used by many authors to model thin material slabs or coated metallic surfaces in electromagnetic (em) scattering problems. The application of GIBCs provides more accurate models for nonmetallic surfaces than the traditional Leontovich boundary conditions. However, difficulties arise when GIBCs are used because they yield solutions which are neither unique nor reciprocal even after the edge condition is applied. Note that there are special cases where solutions based on GIBCs can be found where no unknown constants remain and without the need to impose reciprocity. In several GIBC-based solutions involving magnetic dielectric materials found in the literature, the reciprocity condition is imposed explicitly in the analysis and any remaining unknown constants are set equal to zero [Rojas and Pathak, 1989; Rojas and Chou, 1990; Volakis and Senior, 1989]. Bernard [1987] considers a conducting wedge covered with magnetic dielectric material; however, his solution is not complete because

some terms in his solution remain unsolved. In his study of a coated half plane, Senior [1991] states that when the GIBCs are used, reciprocity should be explicitly imposed, and additional constraints are required to ensure uniqueness. Although his solution is still incomplete because it contains an unknown constant, it correctly predicts that the constant is related to the value of the field at the edge. In the study by Rojas *et al.* [1991a], an additional junction condition is developed for the first time for a thin magnetic dielectric material following a procedure introduced by Leppington [1983], who modeled the field near the junction by a quasi-static solution and then matched to the external Wiener-Hopf solution in the region of overlap to determine the additional constraint. As shown by Rojas *et al.* [1991a], the additional junction condition eliminates the need to explicitly impose reciprocity in the analysis, and all the unknown constants can be completely evaluated.

In this paper the Maliuzhinets method [Maliuzhinets, 1959] is employed to solve two canonical problems involving thin material-coated metallic surfaces which are modeled by GIBCs of $0(t)$ [Weinstein, 1969; Rojas and Al-hekail, 1989; Rojas, 1988], where t denotes the corresponding coating thickness. Specifically, the first problem is the em diffraction of a normally incident plane wave (transverse electric TE_z case) by the junction of a two-

Copyright 1993 by the American Geophysical Union.

Paper number 92RS02880.
0048-6604/93/92RS-02880\$06.00

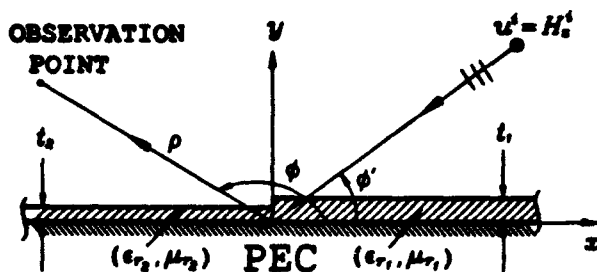


Fig. 1. Two-part material-coated PEC ground plane geometry with plane wave normal incidence.

part thin dielectric/magnetic coated perfect electric conducting (PEC) ground plane, whose geometry is depicted in Figure 1. Note that a similar problem has been solved by *Rojas et al.* [1991a] via the Wiener-Hopf technique along with an approximate quasi-static analysis. However, this two-part problem, which has not been analyzed by the Maliuzhinets method, is again considered here to demonstrate the analytical procedure and the application of the quasi-static approximation to obtain a unique solution based on the Maliuzhinets method. Note that the term uniqueness is used here to state the fact that the solution does not contain any unknown constants. The second problem considered here is the em diffraction of a normally incident plane wave (TE_z case) by a thin dielectric/magnetic coated PEC half plane illustrated in Figure 2, where the material coatings on the top face $\{x < 0, y = 0^+\}$ and the bottom face $\{x < 0, y = 0^-\}$ are different. For this half plane problem, the Maliuzhinets method seems to be a better and simpler approach than the Wiener-Hopf method because the latter requires matrix factorization which is much more complicated than the scalar factorization that one usually

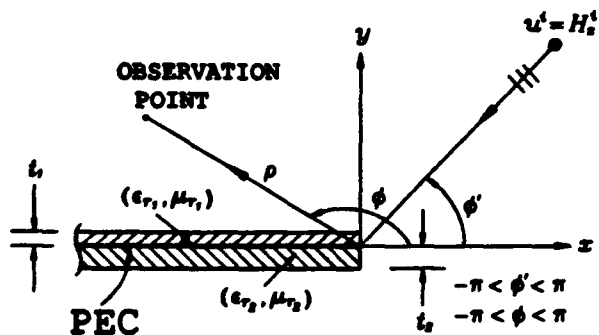


Fig. 2. Material-coated PEC half plane geometry with plane wave normal incidence.

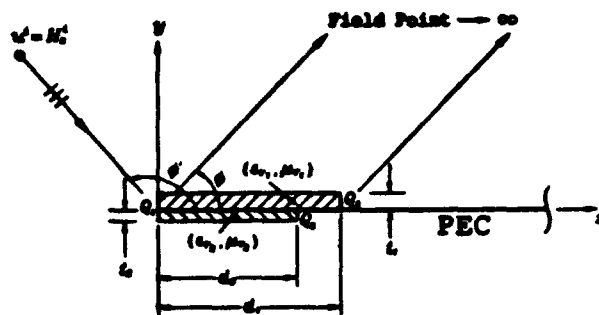


Fig. 3. Geometry pertaining to a partially coated PEC half plane.

encounters. Again, a quasi-static solution is developed and matched with the Maliuzhinets spectral function expanded in the common region of overlap to determine an additional condition, which in turn ensures uniqueness for the Maliuzhinets-based solution. As stated above, this last step requires the asymptotic evaluation of the Maliuzhinets functions in the common region of overlap. Furthermore, in contrast to some papers found in the literature based on the Maliuzhinets method, the analysis presented here gives the exact relationship between constants that appear in the analysis and the field and its derivatives evaluated at the junction or edge of the structure under study. This is a very important result because it gives a physical interpretation to the constants that appear in the analysis. Furthermore, it makes it possible to compare the junction condition obtained by the present method and the Wiener-Hopf technique [*Rojas et al.*, 1991a].

In section 2 the two-part problem depicted in Figure 1 is solved with the aid of the Maliuzhinets method after the GIBCs of $0(r)$ are employed to replace the grounded slab. It is shown that the present solution based on the Maliuzhinets approach is identical to the one based on the Wiener-Hopf technique presented by *Rojas et al.* [1991a]. It is also shown that the same junction condition obtained by *Rojas et al.* [1991a] to ensure uniqueness is again obtained here, though a different approach is used in this study. In section 3 a uniform (geometrical) theory of diffraction (UTD) solution is obtained for the coated half plane problem shown in Figure 2. To test the accuracy of the solutions obtained in this study, the scattering from a partially coated PEC half plane as shown in Figure 3 is calculated in section 4 using the solutions of

sections 2 and 3 (with multiple interaction included), and it is compared and shown to be in good agreement with an independent moment method (MM) solution [Newman, 1986]. Note that an $e^{-i\omega t}$ time dependence is assumed and suppressed throughout this paper.

2. TWO-PART GENERALIZED IMPEDANCE SURFACE

The two-part coated PEC plane shown in Figure 1 is equivalent to a two-part generalized impedance surface whose faces $\{x > 0, y = 0\}$ and $\{x < 0, y = 0\}$ satisfy the GIBC of $0(t)$. Let (ρ, ϕ, z) denote the cylindrical coordinates with ϕ measured from the $+x$ axis. Also, let $u(\rho, \phi) = H_z(\rho, \phi)$ be the scalar total field at an arbitrary field point (ρ, ϕ) in the upper half space $0 < \phi < \pi$. Then u satisfies the GIBC of $0(t)$ at the surfaces $\phi = 0$ and $\phi = \pi$ as follows:

$$\left[\frac{1}{k^2} \frac{\partial^2}{\partial \rho^2} + ia_{1/2} \frac{1}{k\rho} \frac{\partial}{\partial \phi} + (1 + b_{1/2}) \right] u(\rho, \phi) = 0, \quad \phi = \left\{ \begin{array}{l} 0 \\ \pi \end{array} \right. \quad (1a)$$

where

$$a_{1,2} = \sin \nu_{a,1,2} + \sin \nu_{b,1,2} = \frac{ie_{r,1,2}}{k(\epsilon_{r,1,2} - 1)t_{1,2}}, \quad (1b)$$

$$b_{1,2} = \sin \nu_{a,1,2} \sin \nu_{b,1,2} = \frac{\mu_{r,1,2} \epsilon_{r,1,2} - 1}{\epsilon_{r,1,2} - 1}, \quad (1c)$$

$$\sin \nu_{a,b,1,2} = \frac{a_{1,2}}{2} \mp \left[\left(\frac{a_{1,2}}{2} \right)^2 - b_{1,2} \right]^{1/2}. \quad (1d)$$

In addition to the boundary condition (1a), u must also satisfy the scalar two-dimensional Helmholtz equation and the radiation and edge conditions.

2.1. Formulation of Maliuzhinets spectral function

For a plane wave normally incident to the z axis at an angle ϕ' measured from the $+x$ -axis, the incident field u^i is given by

$$u^i(\rho, \phi) = \exp[-ik\rho \cos(\phi - \phi')], \quad 0 < \phi, \phi' < \pi; \quad (2)$$

in which the magnitude of the incident field at the origin is assumed to be unity. Following Maliuzhi-

nets approach, the total field u can be expressed in the form of Sommerfeld integral as follows:

$$u(\rho, \phi) = \frac{1}{2\pi i} \int_{\gamma} \exp(-ik\rho \cos \alpha) S\left(\alpha + \phi - \frac{\pi}{2}\right) d\alpha, \quad (3a)$$

where the spectral function S is the unknown to be solved, and γ is the so-called twofold Sommerfeld contour [Maliuzhinets, 1956]. Since the edge condition requires that u be bounded at $\rho = 0$, the asymptotic behavior of S as $|\text{Im } \alpha| \rightarrow \infty$ is given by

$$\lim_{|\text{Im } \alpha| \rightarrow \infty} S(\alpha) = \text{const} \quad (3b)$$

Furthermore, because of the radiation condition which requires that the scattered field $u - u^i$ be bounded in the region $|\phi - \pi/2| < \pi/2$ for $\rho \rightarrow \infty$, the function $S(\alpha)$ is regular in the strip $|\text{Re } \alpha| \leq \pi/2$ except that it has a first-order pole at $\alpha = \phi' - \pi/2$ in that strip to ensure the presence of the incident field given in (2).

Applying (3a) in (1a) yields the following integral equations:

$$\int_{\gamma} (\sin \alpha \pm \sin \nu_{a,n}) (\sin \alpha \pm \sin \nu_{b,n}) \cdot S\left(\alpha \pm \frac{\pi}{2}\right) \exp(-ik\rho \cos \alpha) d\alpha = 0. \quad (4a)$$

It follows from (3b) that the integrands in (4a) excluding the exponential term have the asymptotic behavior in the order $O(e^{2|\text{Im } \alpha|})$ as $|\text{Im } \alpha| \rightarrow \infty$. Thus according to Maliuzhinets [1958], (4a) is transformed into the following inhomogeneous functional difference equations for $S(\alpha)$:

$$\begin{aligned} \sin \alpha (A_{2/1} + A_{4/3} \cos \alpha) &= (\sin \alpha \pm \sin \nu_{a,n}) \\ &\cdot (\sin \alpha \pm \sin \nu_{b,n}) S\left(\alpha \pm \frac{\pi}{2}\right) - (\sin \alpha \mp \sin \nu_{a,n}) \\ &\cdot (\sin \alpha \mp \sin \nu_{b,n}) S\left(-\alpha \pm \frac{\pi}{2}\right), \end{aligned} \quad (4b)$$

where A_1, A_2, A_3 , and A_4 are constants. If all of these constants vanish, (4b) would become two homogeneous functional equations for $S(\alpha)$. Let $p(\alpha)$ be a solution for these homogeneous functional equations which is given by

$$p(\alpha) = \frac{\Psi(\alpha, \nu_{b_1})\Psi(-\alpha, \nu_{b_1})}{\Psi(\alpha, -\nu_{a_1})\Psi(-\alpha, -\nu_{a_1})}. \quad (5a)$$

Note that the functions $\Psi(\mp\alpha, -\nu_{a_{1,2}})$ are put in the denominator because $\text{Re } \nu_{a_{1,2}} < 0$ in contrast to $\text{Re } \nu_{b_{1,2}} > 0$ as seen from (1d) (a detailed discussion is given by Bernard [1987]). It can be shown that the function $\Psi(\alpha, \nu)$ can be expressed as

$$\Psi(\alpha, \nu) = \psi_{\pi/2}(\alpha + \pi - \nu)\psi_{\pi/2}(\alpha + \nu), \quad (5b)$$

where $\psi_{\pi/2}(\alpha)$ is a special case of the well-known Maliuzhinets function $\psi_\Phi(\alpha)$ for $\Phi = \pi/2$. Note that $\psi_\Phi(\alpha)$ is an even function of α , and its properties are summarized by Maliuzhinets [1959]. One of these properties is

$$\frac{\psi_\Phi(\alpha + 2\Phi)}{\psi_\Phi(\alpha - 2\Phi)} = \cotn \frac{1}{2} \left(\alpha + \frac{\pi}{2} \right). \quad (6a)$$

Applying (6a) with $\Phi = \pi/2$ to (5a), it is easily shown that $p(\alpha)$ indeed satisfies the homogeneous functional equations. It also follows from (6a) that

$$\begin{aligned} \frac{p(\alpha - \pi)}{p(\alpha + \pi)} &= (\cos \alpha + \sin \nu_{a_1})(\cos \alpha + \sin \nu_{b_1})(\cos \alpha \\ &\quad - \sin \nu_{a_1})(\cos \alpha - \sin \nu_{b_1}) / [(\cos \alpha - \sin \nu_{a_1})(\cos \alpha \\ &\quad - \sin \nu_{b_1})(\cos \alpha + \sin \nu_{a_1})(\cos \alpha + \sin \nu_{b_1})]. \end{aligned} \quad (6b)$$

Since the closest zeros and poles to the point $\alpha = 0$ of the Maliuzhinets function $\psi_{\pi/2}(\alpha)$ are, $\alpha = \pm 3\pi/2$ and $\alpha = \pm 5\pi/2$, respectively [Maliuzhinets, 1959], it follows from (5) that $p(\alpha)$ is free of poles and zeros in the strip $|\text{Re } \alpha| \leq \pi/2$. Thus the general solution that satisfies (4b) can be expressed as

$$S(\alpha) = p(\alpha)\tau(\alpha). \quad (7a)$$

Substituting (7a) into (4b), combining the two equations of (4b), and applying the identity (6b) yields

$$\tau(\alpha + \pi) - \tau(\alpha - \pi) = -q(\alpha), \quad (7b)$$

$$\begin{aligned} q(\alpha) &= -\frac{\cos \alpha}{p(\alpha - \pi)} [(A_2 - A_4 \sin \alpha)(\cos \alpha - \sin \nu_{a_1}) \\ &\quad \cdot (\cos \alpha - \sin \nu_{b_1}) + (A_1 + A_3 \sin \alpha) \\ &\quad \cdot (\cos \alpha - \sin \nu_{a_1})(\cos \alpha - \sin \nu_{b_1})] \\ &\quad \cdot [(\cos \alpha - \sin \nu_{a_1})(\cos \alpha - \sin \nu_{b_1}) \\ &\quad \cdot (\cos \alpha + \sin \nu_{a_1})(\cos \alpha + \sin \nu_{b_1})]^{-1}. \end{aligned} \quad (7c)$$

A particular solution of (7b) is given by

$$\tau_o(\alpha) = \frac{q(\alpha + \pi)}{1 - p(\alpha)p(\alpha + 2\pi)}. \quad (7d)$$

In other words, a particular solution for (4b) is $S_o(\alpha) = p(\alpha)\tau_o(\alpha)$ which must also satisfy the edge condition (3b); and this requires that

$$A_3 = A_4. \quad (8a)$$

$S_o(\alpha)$ can then be written explicitly as

$$\begin{aligned} S_o(\alpha) &= p(\alpha)\tau_o(\alpha) = [A_2(\cos^2 \alpha \\ &\quad + a_1 \cos \alpha + b_1) + A_1(\cos^2 \alpha + a_2 \cos \alpha \\ &\quad + b_2)] / [2(a_1 - a_2)(\sin^2 \alpha - \cos^2 \alpha_p)] \\ &\quad - \frac{A_3 \sin \alpha}{2(\sin^2 \alpha - \cos^2 \alpha_p)} \left(\cos \alpha + \frac{b_2 - b_1}{a_2 - a_1} \right), \end{aligned} \quad (8b)$$

$$\cos^2 \alpha_p = 1 + \frac{a_2 b_1 - a_1 b_2}{a_2 - a_1}. \quad (8c)$$

The most general solution for the homogeneous functional equations is given by $p(\alpha)\sigma(\alpha)$, where $\sigma(\alpha)$ satisfies the following difference equations:

$$\sigma\left(\alpha \pm \frac{\pi}{2}\right) = \sigma\left(-\alpha \pm \frac{\pi}{2}\right). \quad (9a)$$

Hence the most general expression for $S(\alpha)$ that satisfies (4b) is given by

$$S(\alpha) = S_o(\alpha) + p(\alpha)\sigma(\alpha). \quad (9b)$$

It is easy to verify that any function $f(\sin \alpha)$ can be a solution of (9a). Thus, to reproduce the incident field u^i given in (2), $\sigma(\alpha)$ may be of the form

$$\sigma_o(\alpha) = \frac{\sin \phi'}{p(\phi' - \pi/2)(\sin \alpha + \cos \phi')}. \quad (9c)$$

However, it is seen from (8b) that $S_o(\alpha)$ has two poles at $\alpha = \pm(\pi/2 - \alpha_p)$, which violate the condition that $S(\alpha)$ has only a simple pole at $\alpha = \phi' - \pi/2$ and is otherwise regular in the strip $|\text{Re } \alpha| \leq \pi/2$. Thus the second term $p(\alpha)\sigma(\alpha)$ of (9b) combined with $S_o(\alpha)$ must force the residues of $S(\alpha)$ to zero at $\alpha = \pm(\pi/2 - \alpha_p)$ by adjusting the constants A_1 , A_2 , and A_3 . Furthermore, $p(\alpha)$ has two non-physical poles at $\alpha = \pm(3\pi/2 + \nu_{a_{1,2}})$, which when ϕ is close to 0 or π , may be captured if the Sommerfeld contour γ is deformed into steepest descent paths. Since the residues of these poles introduce

nonphysical exponentially growing fields, they must be suppressed by setting the residues of $p(\alpha)\sigma(\alpha)$ to zero at $\alpha = \pm(3\pi/2 + \nu_{a_1})$. Consequently, one obtains the following expression for $\sigma(\alpha)$:

$$\sigma(\alpha) = \frac{1}{p(\phi' - \pi/2)(\sin^2 \alpha - \cos^2 \alpha_p)} \cdot \frac{(\sin \alpha + \cos \nu_{a_2})(\sin \alpha - \cos \nu_{a_1})}{(\cos \phi' - \cos \nu_{a_2})(\cos \phi' + \cos \nu_{a_1})} \cdot \left[\frac{\sin \phi'(\cos^2 \phi' - \cos^2 \alpha_p)}{\sin \alpha + \cos \phi'} + C \right] \quad (9d)$$

where the constant C is added so that (3b) holds. At this point, C as well as A_i ($i = 1, 2, 3$) are still unknown, and thus the total field u computed from $S(\alpha)$ is not unique unless these constants can be specified. Although A_i , $i = 1, 2, 3$ need not be known to obtain the solution of u for $\rho \neq 0$ because the function $S_\rho(\alpha)$ has neither residue nor steepest descent path (SDP) contributions to u when γ in (3a) is deformed into steepest descent paths, they are computed here because they are related to the field behavior at $\rho = 0$. The conditions discussed above which require the residues of $S(\alpha)$ be zero at $\alpha = \pm(\pi/2 - \alpha_p)$ can be used to obtain C in terms of A_i , but more information is needed before these constants are specified in terms of known parameters.

Before proceeding further, it is convenient to rewrite the expression of $S(\alpha)$. Note that the Maliuzhinets function $\psi_\Phi(\alpha)$ has the following property [Maliuzhinets, 1959]:

$$\psi_\Phi\left(\alpha + \frac{\pi}{2}\right)\psi_\Phi\left(\alpha - \frac{\pi}{2}\right) = \left[\psi_\Phi\left(\frac{\pi}{2}\right)\right]^2 \cos \frac{\pi\alpha}{4\Phi} \quad (10a)$$

It follows from (10a) (with $\Phi = \pi/2$) and (5b) that

$$\frac{\Psi(\phi' - \pi/2, -\nu_{a_2})\Psi(-\phi' + \pi/2, -\nu_{a_1})}{\Psi(\alpha, -\nu_{a_2})\Psi(-\alpha, -\nu_{a_1})} = \frac{\Psi(\alpha, -\pi - \nu_{a_2})\Psi(-\alpha, -\pi - \nu_{a_1})}{\Psi(\phi' - \pi/2, -\pi - \nu_{a_2})\Psi(-\phi' + \pi/2, -\pi - \nu_{a_1})} \cdot \frac{(\cos \phi' - \cos \nu_{a_2})(\cos \phi' + \cos \nu_{a_1})}{(\sin \alpha + \cos \nu_{a_2})(\sin \alpha - \cos \nu_{a_1})} \quad (10b)$$

Incorporating (10b), (9d), (8b), and (5a) into (9b) yields

$$S(\alpha) = \frac{1}{\sin^2 \alpha - \cos^2 \alpha_p} \left\{ \frac{A_3 \sin \alpha}{2} \left(\cos \alpha + \frac{b_2 - b_1}{a_2 - a_1} \right) + \frac{A_2(\cos^2 \alpha + a_1 \cos \alpha + b_1) + A_1(\cos^2 \alpha + a_2 \cos \alpha + b_2)}{2(a_1 - a_2)} + \frac{h(\alpha)}{h\left(\phi' - \frac{\pi}{2}\right)} \left[\frac{\sin \phi'(\cos^2 \phi' - \cos^2 \alpha_p)}{\sin \alpha + \cos \phi'} + C \right] \right\} \quad (11a)$$

$$h(\alpha) = h_2(\alpha)h_1(-\alpha), \quad h_{1/2}(\alpha) = \Psi(\alpha, \nu_{b_{1/2}})\Psi(\alpha, -\nu_{a_{1/2}}) \quad (11b)$$

To show that the constants A_1 , A_2 , and A_3 are related to the field u and its derivatives at the junction, a scheme similar to that of Maliuzhinets [1956] can be followed, namely, one may write

$$u(0, \phi) = \lim_{\rho \rightarrow 0} \frac{1}{2\pi i} \int_{\gamma_1} \left[S\left(\alpha + \phi - \frac{\pi}{2}\right) - S\left(-\alpha + \phi - \frac{\pi}{2}\right) \right] \exp(-ik\rho \cos \alpha) d\alpha, \quad (12a)$$

where γ_1 is the upper loop of the contour γ . Applying (11a) to (12a) and letting the horizontal part of γ_1 tend to infinity (that is, $\forall \alpha \in \gamma_1$, $\text{Im } \alpha \rightarrow \infty$), also noting that $S(i\infty) = -S(-i\infty)$ [Maliuzhinets, 1958], one obtains

$$u(0, \phi) = 2iS(i\infty) = -A_3, \quad (12b)$$

$$\frac{A_1 + A_2}{2(a_1 - a_2)} = \frac{C \left[\psi_{\pi/2}\left(\frac{\pi}{2}\right) \right]^2}{4h\left(\phi' - \frac{\pi}{2}\right)} \quad (12c)$$

Similarly,

$$\frac{\partial u}{\partial \rho} \Big|_{\rho=0} = \lim_{\rho \rightarrow 0} \frac{1}{2\pi i} \int_{\gamma_1} \left[S\left(\alpha + \phi - \frac{\pi}{2}\right) - S\left(-\alpha + \phi - \frac{\pi}{2}\right) \right] (-ik \cos \alpha) \exp(-ik\rho \cos \alpha) d\alpha. \quad (13a)$$

Letting the horizontal part of γ_1 tend to infinity and applying (4b) to (13a) with $\phi = 0$ and $\phi = \pi$, respectively, leads to

$$\left. \frac{\partial u}{\partial \rho} \right|_{\phi=0} = -ikA_1, \quad \left. \frac{\partial u}{\partial \rho} \right|_{\phi=\pi} = -ikA_2. \quad (13b)$$

2.2. Determination of the unique solution

As stated earlier, an approximate quasi-static solution can be used to obtain the additional information which is required for the determination of C in (11a) and A_i ($i = 1, 2, 3$). Since the geometry shown in Figure 1 is the same as the even configuration given by Rojas *et al.* [1991a], the quasi-static field obtained by Rojas *et al.* [1991a] can be applied here; namely,

$$u_q(\rho, \phi = \pi) \sim A_q - B_q \left[\rho + \frac{i}{k\pi} \left(\frac{1}{a_1} - \frac{1}{a_2} \right) \ln \rho \right], \quad t_{1/2} \ll \rho \ll k^{-1}. \quad (14a)$$

Note that the subscript q is used to denote a quasi-static field. The spectral function S_q corresponding to u_q can be obtained from the inversion of the Sommerfeld integral (3a) for $\text{Re}(-ik \cos \alpha) > 0$ [Maliuzhinets, 1958], which is given by

$$S_q\left(\alpha + \frac{\pi}{2}\right) = \frac{ik \sin \alpha}{2} \int_0^\infty u_q(\rho, \pi) \exp(ik\rho \cos \alpha) d\rho. \quad (14b)$$

Evaluating (14b) with u_q given in (14a) yields

$$S_q\left(\alpha + \frac{\pi}{2}\right) \sim \frac{\sin \alpha}{\cos \alpha} \left\{ A' - \frac{A_q}{2} + \frac{iB_q}{2k} \left[\frac{1}{\cos \alpha} - \frac{1}{\pi} \left(\frac{1}{a_1} - \frac{1}{a_2} \right) \ln(\cos \alpha) \right] \right\}, \quad 1 \ll |\cos \alpha| \ll (kt_{1/2})^{-1} \quad (14c)$$

where A' is a constant resulting from the transform of the term of $\ln \rho$. Noting that

$$\frac{\sin \alpha}{\cos \alpha} \sim \pm i, \quad \ln(\cos \alpha) \sim \mp i\alpha, \quad \text{Im } \alpha \geq 0, \quad \text{as } |\cos \alpha| \gg 1, \quad (14d)$$

(14c) can be rewritten as

$$S_q\left(\alpha + \frac{\pi}{2}\right) \sim \pm \left\{ iA' - \frac{iA_q}{2} - \frac{B_q}{2k} \left[\frac{1}{\cos \alpha} \pm \frac{i\alpha}{\pi} \left(\frac{1}{a_1} - \frac{1}{a_2} \right) \right] \right\}, \quad \text{Im } \alpha \geq 0, \quad 1 \ll |\cos \alpha| \ll (kt_{1/2})^{-1}. \quad (14e)$$

At this point, an additional condition is readily obtained if one matches (14e) with the asymptotic form of $S(\alpha + \pi/2)$, where $S(\alpha)$ is defined in (11a), within the region of overlap $1 \ll |\cos \alpha| \ll (kt_{1/2})^{-1}$. Applying (36) of the appendix to (11a) with α being replaced by $\alpha + \pi/2$, one obtains

$$S\left(\alpha + \frac{\pi}{2}\right) \sim \pm i \frac{A_3}{2} - \frac{A_2 + A_1}{2(a_1 - a_2)} \mp \frac{iC(a_1 a_2)^{1/2} \left[\psi_{\pi/2}\left(\frac{\pi}{2}\right) \right]^8}{4h\left(\phi' - \frac{\pi}{2}\right)} \left[\frac{1}{\cos \alpha} \pm \frac{i\alpha}{\pi} \left(\frac{1}{a_1} - \frac{1}{a_2} \right) \right] \mp i \frac{a_1 A_2 + a_2 A_1}{2(a_1 - a_2) \cos \alpha} + \dots, \quad \text{Im } \alpha \geq 0. \quad (15a)$$

Comparing (15a) and (14e), it is evident that they can only be matched to each other if the coefficient of the extra term of $(\cos \alpha)^{-1}$ vanishes; namely,

$$a_1 A_2 + a_2 A_1 = 0, \quad (15b)$$

or

$$\frac{1}{a_1} \left. \frac{\partial u}{\partial \rho} \right|_{\phi=0} + \frac{1}{a_2} \left. \frac{\partial u}{\partial \rho} \right|_{\phi=\pi} = 0. \quad (15c)$$

Note that (15c) is the same as the junction condition obtained by Rojas *et al.* [1991a]. Applying (15b) and (12c) to (11a), and setting the residues of $S(\alpha)$ to zero at $\alpha = \pm(\pi/2 - \alpha_p)$, one finally obtains the constants C , A_1 , A_2 , and A_3 as follows:

$$C = \sin \phi' [M(\alpha_p) - \cos \phi'], \quad A_{1/2} = \mp a_{1/2} \frac{C \left[\psi_{\pi/2}\left(\frac{\pi}{2}\right) \right]^8}{2h\left(\phi' - \frac{\pi}{2}\right)}, \quad (15d)$$

$$M(\alpha_p) = \cos \alpha_p \frac{h\left(\frac{\pi}{2} - \alpha_p\right) - h\left(\alpha_p - \frac{\pi}{2}\right)}{h\left(\frac{\pi}{2} - \alpha_p\right) + h\left(\alpha_p - \frac{\pi}{2}\right)}, \quad (15e)$$

$$A_3 = -a_1 a_2 \left[\psi_{\pi/2} \left(\frac{\pi}{2} \right) \right]^{16} / [4(a_2 - a_1)] \\ \cdot \sin \phi' [(a_2 - a_1) \sin \alpha_p + b_2 - b_1] \left\{ h\left(\phi' - \frac{\pi}{2}\right) \right. \\ \left. \cdot \left[h\left(\frac{\pi}{2} - \alpha_p\right) + h\left(\alpha_p - \frac{\pi}{2}\right) \right] \right\}. \quad (15f)$$

A unique solution for $u(\rho, \phi)$ can now be determined by evaluating the integral in (3a) with $S(\alpha)$ given in (11a) and C and A_i given in (15). Since the exponential function in (3a), that is, $\exp(-ik\rho \cos \alpha)$, possesses two isolated, simple saddle points at $\alpha = \pi$ and $\alpha = -\pi$ in the region $|\operatorname{Re} \alpha| \leq \pi$, the Sommerfeld integration contour γ can be deformed into two steepest descent paths $\operatorname{SDP}(\pm\pi)$ passing through these saddle points. Furthermore, the spectral function $S(\alpha + \phi - \pi/2)$ in (3a) is analytic everywhere except that it has several isolated simple poles. Therefore the total field $u(\rho, \phi)$ evaluated from (3a) consists of the integral contribution from the integration paths $\operatorname{SDP}(\pm\pi)$, which gives rise to the diffracted field u^d , and the residue contributions from the poles of $S(\alpha + \phi - \pi/2)$ if they are captured in the deformation of γ into $\operatorname{SDP}(\pm\pi)$. The residues from the real poles give rise to the incident field u^i and reflected field u^r , whereas the residues from the complex poles contribute to the surface wave field u^{sw} . In other words, the diffracted field u^d is given by

$$u^d(\rho, \phi) = \frac{1}{2\pi i} \left[\int_{\operatorname{SDP}(\pi)} S\left(\alpha + \phi - \frac{\pi}{2}\right) \right. \\ \cdot \exp(-ik\rho \cos \alpha) d\alpha + \int_{\operatorname{SDP}(-\pi)} S\left(\alpha + \phi - \frac{\pi}{2}\right) \\ \left. \cdot \exp(-ik\rho \cos \alpha) d\alpha \right]. \quad (16a)$$

By shifting the steepest descent paths $\operatorname{SDP}(\pi)$ and $\operatorname{SDP}(-\pi)$ to a new path $\operatorname{SDP}(\phi)$ with a saddle point at ϕ , where $0 \leq \phi \leq \pi$, (16a) can be rewritten as

$$u^d(\rho, \phi) = \frac{1}{2\pi i} \int_{\operatorname{SDP}(\phi)} \mathfrak{F}(\alpha, \phi') \\ \cdot \exp[ik\rho \cos(\alpha - \phi)] d\alpha, \quad (16b)$$

$$\mathfrak{F}(\alpha, \phi') = S\left(\alpha + \frac{\pi}{2}\right) - S\left(\alpha - \frac{3\pi}{2}\right) \\ = \frac{(a_1 - a_2) \left[\psi_{\pi/2} \left(\frac{\pi}{2} \right) \right]^{16} \sin \alpha \sin \phi'}{8h\left(\alpha - \frac{\pi}{2}\right)h\left(\phi' - \frac{\pi}{2}\right)} \\ \cdot \left[\frac{\cos \alpha \cos \phi' + \cos^2 \alpha_p}{\cos \alpha + \cos \phi'} - M(\alpha_p) \right]. \quad (16c)$$

Note that the identity (10a) has been used to obtain (16c). It is clearly seen from (16c) that the function $\mathfrak{F}(\alpha, \phi')$ is symmetric in α and ϕ' as required by the reciprocity property. Furthermore, it can be shown from the definition of the Maliuzhinets function $\psi_{\pi/2}(\alpha)$ [Maliuzhinets, 1959] that $\mathfrak{F}(\alpha, \phi')$ given in (16c) is exactly the same as the even symmetric spectral function based on the Wiener-Hopf technique obtained by Rojas *et al.* [1991a]. Likewise, it can also be shown that the reflected and surface wave fields obtained here are the same as the corresponding fields given by Rojas *et al.* [1991a].

3. GENERALIZED IMPEDANCE HALF PLANE

As indicated at the introduction, the half plane problem has also been considered by Volakis and Senior [1989] (based on Maliuzhinets method) for different coatings on both faces of the half plane and by Rojas and Chou [1990] (based on the Wiener-Hopf method) for equal coatings on both faces of the half plane. In these two solutions, the reciprocity condition is imposed in the analysis, and the remaining unknown constant is set equal to zero. In this section, the solution to the two-dimensional half plane problem, whose geometry is depicted in Figure 2, is obtained using the Maliuzhinets method combined with the quasi-static analysis, and it is rigorously shown that the remaining constant is not equal to zero, except for special cases. With the application of the GIBC of $Q(\epsilon)$, the material-coated half plane is equivalent to a generalized impedance half plane. Let $u(\rho, \phi) = H_z(\rho, \phi)$ be the total field at an arbitrary field point (ρ, ϕ) in the entire free

space $|\phi| < \pi$. The field $u(\rho, \phi)$ satisfies the scalar two-dimensional Helmholtz equation, the radiation condition, the edge condition, and the GIBC of $O(r)$ at the surfaces of the half plane $\phi = \pm\pi$ as follows:

$$\left[\frac{1}{k^2} \frac{\partial^2}{\partial \rho^2} \pm ia_{1/2} \frac{1}{k\rho} \frac{\partial}{\partial \phi} + (1 + b_{1/2}) \right] u(\rho, \phi) = 0, \quad (17)$$

$$\phi = \pm\pi,$$

where the parameters $a_{1/2} = \sin \nu_{a_{1/2}} + \sin \nu_{b_{1/2}}$ and $b_{1/2} = \sin \nu_{a_{1/2}} \sin \nu_{b_{1/2}}$ were defined in (1). As in the two-part problem discussed in the previous section, a quasi-static approximation for the total field in the neighborhood of the edge will be developed so that an additional condition is obtained to yield a unique solution for $u(\rho, \phi)$.

3.1. Formulation of the Maliuzhinets spectral function

For the half plane geometry excited by a normally incident plane wave as depicted in Figure 2, the GO (geometrical optics) incident field at a field point (ρ, ϕ) with an incident angle ϕ' measured from the $+x$ axis is given by

$$u^i(\rho, \phi) = \exp[-ik\rho \cos(\phi - \phi')] U(\phi - \phi' + \pi) - U(\phi - \phi' - \pi), \quad -\pi < \phi, \phi' < \pi, \quad (18)$$

where U is the unit step function. Note that the magnitude of the GO incident field at the edge is assumed to be unity. Note also that u^i exists only in the lit region, where $|\phi - \phi'| \leq \pi$. Following Maliuzhinets approach, u can be expressed as the Sommerfeld integral:

$$u(\rho, \phi) = \frac{1}{2\pi i} \int_{\gamma} \exp(-ik\rho \cos \alpha) S(\alpha + \phi) d\alpha, \quad (19a)$$

where γ is the twofold Sommerfeld contour. Because of the radiation condition, the spectral function $S(\alpha)$ is regular in the strip $|\operatorname{Re} \alpha| \leq \pi$ except that it has a first-order pole at $\alpha = \phi'$ to produce the incident field u^i . Furthermore, it follows from the edge condition that

$$\lim_{|\alpha| \rightarrow \pi} S(\alpha) = \text{const.} \quad (19b)$$

As in section 2, after applying the boundary condition in (17), (19a) becomes an integral equation which can be transformed into the inhomogeneous functional difference equations for $S(\alpha)$ as follows:

$$\begin{aligned} \sin \alpha (\bar{A}_{1/2} + \bar{A}_{3/4} \cos \alpha) &= (\sin \alpha \pm \sin \nu_{a_{1/2}})(\sin \alpha \\ &\pm \sin \nu_{b_{1/2}}) S(\alpha \pm \pi) - (\sin \alpha \mp \sin \nu_{a_{1/2}})(\sin \alpha \\ &\mp \sin \nu_{b_{1/2}}) S(-\alpha \pm \pi), \end{aligned} \quad (20)$$

where $\bar{A}_1, \bar{A}_2, \bar{A}_3$, and \bar{A}_4 are constants. The solution $S(\alpha)$ for (20) can be found following the same procedure given in the previous section. Thus the first step is to obtain a solution $\bar{p}(\alpha)$ for the homogeneous functional equations (equation (20) with the constants $\bar{A}_i, i = 1, 2, 3, 4$, set equal to zero); namely,

$$\bar{p}(\alpha) = \frac{\bar{\Psi}(\alpha, \nu_{b_1}) \bar{\Psi}(-\alpha, \nu_{b_2})}{\bar{\Psi}(\alpha, -\nu_{a_1}) \bar{\Psi}(-\alpha, -\nu_{a_2})}, \quad (21a)$$

$$\bar{\Psi}(\alpha, \nu) = \psi_{\pi} \left(\alpha + \frac{3\pi}{2} - \nu \right) \psi_{\pi} \left(\alpha + \frac{\pi}{2} + \nu \right). \quad (21b)$$

Note that $\psi_{\pi}(\alpha)$ is the well-known Maliuzhinets half plane function [Maliuzhinets, 1959]. It follows from the identity (6a) (with $\Phi = \pi$) that

$$\begin{aligned} \frac{\bar{p}(\alpha - 2\pi)}{\bar{p}(\alpha + 2\pi)} &= (\sin \alpha - \sin \nu_{a_1})(\sin \alpha - \sin \nu_{b_1})(\sin \alpha \\ &- \sin \nu_{a_2})(\sin \alpha - \sin \nu_{b_2}) / [(\sin \alpha + \sin \nu_{a_1}) \\ &\cdot (\sin \alpha + \sin \nu_{b_1})(\sin \alpha + \sin \nu_{a_2}) \\ &+ \sin \nu_{b_2}]). \end{aligned} \quad (21c)$$

Furthermore, since the closest zeros and poles to the point $\alpha = 0$ of the Maliuzhinets function $\psi_{\pi}(\alpha)$ are $\alpha = \pm 5\pi/2$ and $\alpha = \pm 7\pi/2$, respectively [Maliuzhinets, 1959], $\bar{p}(\alpha)$ is free of poles and zeros in the strip $|\operatorname{Re} \alpha| \leq \pi$. Thus the most general solution that satisfies (20) can be expressed as

$$S(\alpha) = S_o(\alpha) + \bar{p}(\alpha) \bar{q}(\alpha), \quad (22a)$$

where $S_o(\alpha)$ is a particular solution of (20) given by

$$\begin{aligned} S_o(\alpha) &= \bar{p}(\alpha) \bar{r}_o(\alpha) = [\bar{A}_1(\sin^2 \alpha - a_2 \sin \alpha + b_2) \\ &- \bar{A}_2(\sin^2 \alpha + a_1 \sin \alpha + b_1)] / [2(a_1 + a_2)(\sin^2 \alpha \\ &- \sin^2 \alpha_o)] \\ &+ \frac{\bar{A}_3 \cos \alpha}{2(\sin^2 \alpha - \sin^2 \alpha_o)} \left(\sin \alpha + \frac{b_1 - b_2}{a_1 + a_2} \right), \end{aligned} \quad (22b)$$

$$\sin^2 \alpha_o = -\frac{a_1 b_2 + a_2 b_1}{a_1 + a_2}. \quad (22c)$$

Note that $\bar{A}_3 = \bar{A}_4$ due to the edge condition (19b). The function $\bar{\sigma}(\alpha)$ satisfies the homogeneous difference equation

$$\bar{\sigma}(\alpha \pm \pi) - \bar{\sigma}(-\alpha \pm \pi) = 0. \quad (23a)$$

Hence $\bar{\sigma}(\alpha)$ is a function of $\sin \alpha/2$. Since the first term $\bar{S}_o(\alpha)$ in (22a) has four poles at $\alpha = \pm \alpha_o$ and $\pm(\pi - \alpha_o)$ in the strip $|\operatorname{Re} \alpha| \leq \pi$, which violate the condition that $\bar{S}(\alpha)$ is regular in the strip $|\operatorname{Re} \alpha| \leq \pi$ except at the simple pole $\alpha = \phi'$, the second term $\bar{p}(\alpha)\bar{\sigma}(\alpha)$ in (22a) must also have poles at $\alpha = \pm \alpha_o$ and $\pm(\pi - \alpha_o)$ so that the sum of these two terms yields zero residues at these unwanted poles by adjusting the constants \bar{A}_i , $i = 1, 2, 3$. Furthermore, $\bar{p}(\alpha)$ possesses two nonphysical poles at $\alpha = \pm(2\pi + \nu_{a_2})$, which may be captured and introduce exponentially growing fields if the integration contour γ is deformed into steepest descent paths. Thus taking into account the above conditions and noting that $\bar{\sigma}(\alpha)$ must have a form to reproduce the incident field \bar{u}^i given in (18), one obtains

$$\begin{aligned} \bar{\sigma}(\alpha) = & \frac{1}{\bar{p}(\phi')(\sin^2 \alpha - \sin^2 \alpha_o)} \\ & \cdot \frac{\left(\sin \frac{\alpha}{2} + \sin \frac{\nu_{a_1}}{2}\right) \left(\sin \frac{\alpha}{2} - \sin \frac{\nu_{a_2}}{2}\right)}{\left(\sin \frac{\phi'}{2} + \sin \frac{\nu_{a_1}}{2}\right) \left(\sin \frac{\phi'}{2} - \sin \frac{\nu_{a_2}}{2}\right)} \\ & \cdot \left[\frac{\frac{1}{2} \cos \frac{\phi'}{2} (\sin^2 \phi' - \sin^2 \alpha_o)}{\sin \frac{\alpha}{2} - \sin \frac{\phi'}{2}} \right. \\ & \left. + C_1 + C_2 \sin \frac{\alpha}{2} + C_3 \sin^2 \frac{\alpha}{2} \right]. \quad (23b) \end{aligned}$$

Note that the terms involving C_i , $i = 1, 2, 3$, are added so that (19b) is satisfied. Note also that $(\sin^2 \alpha - \sin^2 \alpha_o)$ is itself a function of $\sin \alpha/2$ because

$$\sin^2 \alpha - \sin^2 \alpha_o = -4 \left(\sin^2 \frac{\alpha}{2} - \sin^2 \frac{\alpha_o}{2} \right)$$

$$\cdot \left(\sin^2 \frac{\alpha}{2} - \cos^2 \frac{\alpha_o}{2} \right). \quad (23c)$$

It can be shown from (10a) (with $\Phi = \pi$) and (21b) that

$$\begin{aligned} & \frac{\bar{\Psi}(\phi', -\nu_{a_1}) \bar{\Psi}(-\phi', -\nu_{a_2})}{\bar{\Psi}(\alpha, -\nu_{a_1}) \bar{\Psi}(-\alpha, -\nu_{a_2})} \\ & = \frac{\bar{\Psi}(\alpha, -\pi - \nu_{a_1}) \bar{\Psi}(-\alpha, -\pi - \nu_{a_2})}{\bar{\Psi}(\phi', -\pi - \nu_{a_1}) \bar{\Psi}(-\phi', -\pi - \nu_{a_2})} \\ & = \frac{\left(\sin \frac{\phi'}{2} + \sin \frac{\nu_{a_1}}{2}\right) \left(\sin \frac{\phi'}{2} - \sin \frac{\nu_{a_2}}{2}\right)}{\left(\sin \frac{\alpha}{2} + \sin \frac{\nu_{a_1}}{2}\right) \left(\sin \frac{\alpha}{2} - \sin \frac{\nu_{a_2}}{2}\right)}. \quad (24a) \end{aligned}$$

Incorporating (24a), (23b), (22b), and (21a) into (22a) yields

$$\begin{aligned} \bar{S}(\alpha) = & \frac{1}{\sin^2 \alpha - \sin^2 \alpha_o} \left\{ \frac{\bar{A}_3 \cos \alpha}{2} \left(\sin \alpha + \frac{b_1 - b_2}{a_1 + a_2} \right) \right. \\ & + \frac{\bar{A}_1(\sin^2 \alpha - a_2 \sin \alpha + b_2) - \bar{A}_2(\sin^2 \alpha + a_1 \sin \alpha + b_1)}{2(a_1 + a_2)} \\ & + \frac{\bar{h}(\alpha)}{\bar{h}(\phi')} \left[\frac{\frac{1}{2} \cos \frac{\phi'}{2} (\sin^2 \phi' - \sin^2 \alpha_o)}{\sin \frac{\alpha}{2} - \sin \frac{\phi'}{2}} + C_1 + C_2 \sin \frac{\alpha}{2} \right. \\ & \left. \left. + C_3 \sin^2 \frac{\alpha}{2} \right] \right\}, \quad (24b) \end{aligned}$$

where

$$\begin{aligned} \bar{h}(\alpha) = & \bar{h}_1(\alpha) \bar{h}_2(-\alpha), \quad \bar{h}_{1/2}(\alpha) \\ = & \bar{\Psi}(\alpha, \nu_{b_n}) \bar{\Psi}(\alpha, -\pi - \nu_{a_n}). \quad (24c) \end{aligned}$$

As in section 2, it can be shown that \bar{A}_1 , \bar{A}_2 , and \bar{A}_3 are related to the field \bar{u} and its derivatives at the edge as follows:

$$\bar{u}(0, \phi) = 2i\bar{S}(i\infty) = \bar{A}_3, \quad (25a)$$

$$\frac{\bar{A}_1 - \bar{A}_2}{2(a_1 + a_2)} = -\frac{C_3 \left[\psi_\pi \left(\frac{\pi}{2} \right) \right]^8}{16\bar{h}(\phi')}, \quad (25b)$$

$$\frac{\partial u}{\partial \rho}(\rho, \phi = \pm \pi)|_{\rho=0} = -ik\bar{A}_{1/2}. \quad (25c)$$

3.2. Quasi-Static analysis

As in the two-part problem discussed in section 2, additional information is also required for the half plane problem before a unique solution for \bar{u} can be obtained. The new piece of information can be found by matching the result of the analysis above with the corresponding quasi-static solution which is approximated in the neighborhood of the edge of the coated half plane. Following the procedure given by *Rojas et al.* [1991a] and *Leppington* [1983], the quasi-static total field \bar{u}_q valid in the region $t_{1/2} \ll \rho \ll k^{-1}$ for the present half plane problem may be expressed as

$$\bar{u}_q \approx \bar{A}_q + \bar{B}_q \Phi, \quad (26a)$$

$$\Phi \sim x + \bar{Q} \ln \rho, \quad \rho/t_{1/2} \rightarrow \infty, \quad (26b)$$

where \bar{A}_q , \bar{B}_q , and \bar{Q} are constants. As in the quasi-static analysis by *Rojas et al.* [1991a], the matching constants \bar{A}_q and \bar{B}_q are of no concern here, and the key step is to determine \bar{Q} which can be accomplished by using the integral form of Laplace's equation, namely,

$$\oint_L \nabla \bar{u}_q \cdot \hat{n}' dl = \oint_L \frac{\partial \bar{u}_q}{\partial n'} dl = 0, \quad (26c)$$

where \hat{n}' is the outer normal of a closed contour L . Applying (26c) inside material 1 (coating on the top face of the PEC half plane) with the contour of integration L_1 as illustrated in Figure 4, one obtains

$$\bar{q}_1 - \bar{B}_q t_1 = 0, \quad \bar{q}_1 = \lim_{x_0/t_1 \rightarrow \infty} \int_{(0,0)}^{(-x_0, t_1)} \frac{\partial \bar{u}_q}{\partial n'} dl, \quad (26d)$$

where \bar{q}_1 is an integral along the free space-material 1 boundary, and the integral along the conducting half plane is exactly zero as a result of the boundary condition satisfied by \bar{u}_q on a PEC surface. Integrating (26c) along a similar contour inside material coating 2, where L_2 is depicted in Figure 4, yields

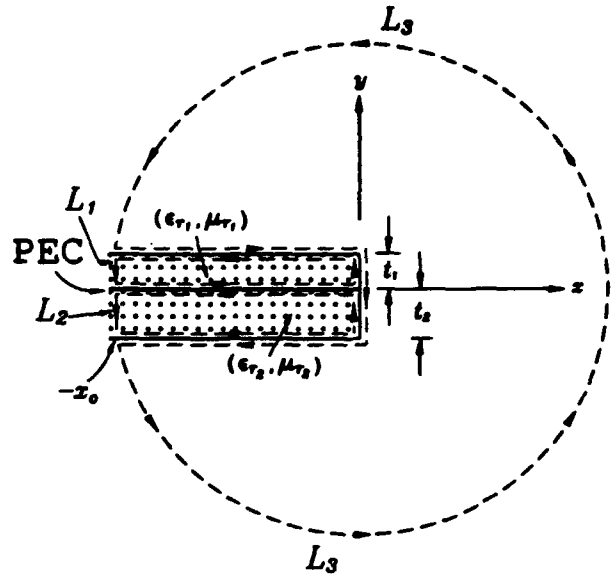


Fig. 4. Integration contours for the determination of \bar{Q} ($\rho/t_{1/2} \rightarrow \infty$).

$$\bar{q}_2 - \bar{B}_q t_2 = 0, \quad \bar{q}_2 = \lim_{x_0/t_2 \rightarrow \infty} \int_{(-x_0, -t_2)}^{(0,0)} \frac{\partial \bar{u}_q}{\partial n'} dl, \quad (26e)$$

where \bar{q}_2 is the integral along the free space-material 2 boundary. Likewise, integrating (26c) along the closed contour L_3 in free space and applying the boundary condition which requires that the tangential fields be continuous at the free space-material interfaces, one obtains (as $x_0/t_{1/2} \rightarrow \infty$)

$$-\frac{\bar{q}_2}{\epsilon_{r_2}} - \frac{\bar{q}_1}{\epsilon_{r_1}} + \bar{B}_q [2\pi\bar{Q} + (t_1 + t_2)] = 0. \quad (26f)$$

Incorporating (26d) and (26e) into (26f) yields a simple expression for \bar{Q} as

$$\bar{Q} = \frac{i}{2\pi k} \left(\frac{1}{a_1} + \frac{1}{a_2} \right), \quad (26g)$$

where a_1 and a_2 were defined in (1b). With \bar{Q} being determined, the asymptotic behavior of \bar{u}_q as $\rho/t_{1/2} \rightarrow \infty$ is specified, and no further analysis is required.

3.3. Determination of the unique solution

Following the same procedure used in section 2, the approximate expression for the spectral function $\bar{S}_q(\alpha \pm \pi)$ corresponding to \bar{u}_q is given by

$$S_q(\alpha \pm \pi) \sim \pm \left\{ i \left(\bar{A}' - \frac{\bar{A}_q}{2} \right) - \frac{\bar{B}_q}{2k} \left[\frac{1}{\cos \alpha} \mp \frac{ia}{2\pi} \left(\frac{1}{a_1} + \frac{1}{a_2} \right) \right] \right\}, \text{Im } \alpha \geq 0, 1 \ll |\cos \alpha| \ll (kt_{1/2})^{-1},$$

(27a)

where \bar{A}' is a constant resulting from the transform of the term $\ln \rho$. Applying (38) of the appendix to (24b) with α replaced by $\alpha + \pi$, one obtains the asymptotic form for $\bar{S}(\alpha + \pi)$ in the region $1 \ll |\cos \alpha| \ll (kt_{1/2})^{-1}$ as follows:

$$\bar{S}(\alpha + \pi) \sim \mp i \frac{\bar{A}_3}{2} + \frac{\bar{A}_1 - \bar{A}_2}{2(a_1 + a_2)} \pm \text{const } (a_1 a_2)^{1/4} \left[\frac{1}{\cos \alpha} \mp \frac{ia}{2\pi} \left(\frac{1}{a_1} + \frac{1}{a_2} \right) \right] \mp i \frac{a_1 \bar{A}_2 + a_2 \bar{A}_1}{2(a_1 + a_2) \cos \alpha} + \dots, \quad (27b)$$

Im $\alpha \geq 0$.

To match (27b) with (27a), it is necessary that the coefficient of the extra term of $(\cos \alpha)^{-1}$ be zero; that is,

$$a_1 \bar{A}_2 + a_2 \bar{A}_1 = 0, \text{ or } \frac{1}{a_1} \frac{\partial \bar{u}}{\partial \rho} \bigg|_{\rho=0} + \frac{1}{a_2} \frac{\partial \bar{u}}{\partial \rho} \bigg|_{\rho=-\pi} = 0. \quad (27c)$$

All the unknown constants in (24b) can now be completely specified from the conditions (27c) and (25b) together with the requirement that the residues of $\bar{S}(\alpha)$ be zero at the unwanted poles $\alpha = \pm \alpha_o$ and $\pm(\pi - \alpha_o)$ as discussed earlier. After some manipulation with the aid of the Maliuzhinets functions' properties given in (6a) and (10a), one obtains

$$C_1 = \sin \phi' \cos^2 \frac{\phi'}{2} - \cos \frac{\phi'}{2}$$

$$\frac{\bar{h}(\alpha_o) \bar{G}(\alpha_o) \sin^2 \frac{\alpha_o}{2} + \bar{h}(\pi - \alpha_o) \bar{G}(\pi - \alpha_o) \cos^2 \frac{\alpha_o}{2}}{\bar{h}(\alpha_o) \bar{H}(\alpha_o) + \bar{h}(\pi - \alpha_o) \bar{H}(\pi - \alpha_o)}, \quad (28a)$$

$$C_2 = \cos \frac{\phi'}{2} \left[\cos \phi' \right.$$

$$\left. + \cos \alpha_o \frac{\bar{h}(\alpha_o) \bar{H}(\alpha_o) - \bar{h}(\pi - \alpha_o) \bar{H}(\pi - \alpha_o)}{\bar{h}(\alpha_o) \bar{H}(\alpha_o) + \bar{h}(\pi - \alpha_o) \bar{H}(\pi - \alpha_o)} \right], \quad (28b)$$

$$C_3 = -\sin \phi'$$

$$+ \cos \frac{\phi'}{2} \frac{\bar{h}(\alpha_o) \bar{G}(\alpha_o) + \bar{h}(\pi - \alpha_o) \bar{G}(\pi - \alpha_o)}{\bar{h}(\alpha_o) \bar{H}(\alpha_o) + \bar{h}(\pi - \alpha_o) \bar{H}(\pi - \alpha_o)}, \quad (28c)$$

$$\bar{A}_{1/2} = \mp a_{1/2} \frac{C_3 \left[\psi_\pi \left(\frac{\pi}{2} \right) \right]^8}{8 \bar{h}(\phi')}, \quad (28d)$$

$$\bar{A}_3 = \frac{2(a_1 + a_2) \cos \frac{\phi'}{2}}{(a_1 + a_2) \sin \alpha_o + b_1 - b_2} \cdot \frac{\bar{h}(\alpha_o) \bar{h}(\pi - \alpha_o) \left[\bar{G}(\alpha_o) + 2 \bar{H}(\alpha_o) \cos \frac{\alpha_o}{2} \right]}{\bar{h}(\alpha_o) \bar{H}(\alpha_o) + \bar{h}(\pi - \alpha_o) \bar{H}(\pi - \alpha_o)}, \quad (28e)$$

where

$$\bar{H}(\alpha) = -\frac{1}{2^{1/2}} X_1 \cos \alpha + (1 + X_2) \cdot \sin \frac{\alpha}{2} + \frac{1}{2^{1/2}} (X_1 + X_3), \quad (29a)$$

$$\bar{G}(\alpha) = -\frac{1}{2} \cos^2 \alpha + \frac{1}{2^{1/2}} X_1 \cos \alpha \sin \frac{\alpha}{2} + 2^{1/2} (X_1 + X_3) \sin \frac{\alpha}{2} + 1 + X_2 + 2X_4; \quad (29b)$$

$$X_1 = \xi_{a_1} + \xi_{b_1} - \xi_{a_2} - \xi_{b_2}, \quad X_4 = \xi_{a_1} \xi_{b_1} \xi_{a_2} \xi_{b_2}, \quad (29c)$$

$$X_2 = \xi_{a_1} \xi_{b_1} + \xi_{a_2} \xi_{b_2} - (\xi_{a_1} + \xi_{b_1})(\xi_{a_2} + \xi_{b_2}), \quad (29d)$$

$$X_3 = \xi_{a_2} \xi_{b_2} (\xi_{a_1} + \xi_{b_1}) - \xi_{a_1} \xi_{b_1} (\xi_{a_2} + \xi_{b_2}), \quad (29e)$$

$$\xi_{a_{1,2}} = \cos \left(\frac{\pi}{4} + \frac{\pi + \nu_{a_{1,2}}}{2} \right), \quad \xi_{b_{1,2}} = \cos \left(\frac{\pi}{4} - \frac{\nu_{b_{1,2}}}{2} \right). \quad (29f)$$

With the constants C_i and \bar{A}_i determined above, a unique solution for the total field $\bar{u}(\rho, \phi)$ is completely specified by evaluating the Sommerfeld integral (19a).

3.4. Asymptotic analysis

By deforming the contour γ into two steepest descent paths $\text{SDP}(\pi)$ and $\text{SDP}(-\pi)$, the total field $\bar{u}(\rho, \phi)$ evaluated from the integral (19a) is given by

$$\bar{u}(\rho, \phi) = \bar{u}^i(\rho, \phi) + \bar{u}^r(\rho, \phi) + \bar{u}^{sw}(\rho, \phi) + \bar{u}^d(\rho, \phi), \quad -\pi < \phi, \phi' < \pi; \quad (30)$$

where \bar{u}^i and \bar{u}^r are the GO incident and reflected fields, respectively, contributed by the residues from the real poles of the integrand in (19a); \bar{u}^{sw} is the surface wave field contributed by the residues from the complex poles, and \bar{u}^d is the diffracted field which is the integral contribution from the integration paths $\text{SDP}(\pm\pi)$.

As can be seen from the expression (24b), there is a simple real pole from $\bar{S}(\alpha + \phi)$ at $\alpha = \phi' - \phi$ which is located within the strip $|\text{Re } \alpha| \leq \pi$ if $|\phi' - \phi| \leq \pi$. The residue contribution from this pole clearly produces the incident field \bar{u}^i defined in (18). In addition, $\bar{S}(\alpha + \phi)$ has two other real poles at $\alpha = \pm 2\pi - (\phi + \phi')$ which may also be captured in the deformation of the contour γ into $\text{SDP}(\pm\pi)$. The residue contribution from these two poles introduces the reflected field \bar{u}^r , which is given by

$$\bar{u}^r(\rho, \phi) = [R_1(\phi')U(\phi + \phi' - \pi) + R_2(-\phi') \cdot U(-\phi - \phi' - \pi)] \exp\{-ik\rho \cos(\phi + \phi')\}, \quad (31a)$$

where the reflection coefficients R_1 and R_2 are defined as

$$R_{1,2}(\phi') = -\frac{(\sin \phi' - \sin \nu_{a,1,2})(\sin \phi' - \sin \nu_{b,1,2})}{(\sin \phi' + \sin \nu_{a,1,2})(\sin \phi' + \sin \nu_{b,1,2})}. \quad (31b)$$

As stated earlier in the two-part problem, the steepest descent paths $\text{SDP}(\pm\pi)$ may be shifted to a new path $\text{SDP}(\phi)$ by changing variables, and the diffracted field \bar{u}^d is then given by

$$\bar{u}^d(\rho, \phi) = \frac{1}{2\pi i} \int_{\text{SDP}(\phi)} \bar{\mathcal{F}}(\alpha, \phi') \cdot \exp[ik\rho \cos(\alpha - \phi)] d\alpha, \quad (32a)$$

$$\bar{\mathcal{F}}(\alpha, \phi') = \bar{S}(\alpha + \pi) - \bar{S}(\alpha - \pi). \quad (32b)$$

Employing the identity (10a) together with some trigonometric relations in (32b), and after a tedious work of simplification, yields

$$\bar{\mathcal{F}}(\alpha, \phi') = \frac{\left[\psi_\pi\left(\frac{\pi}{2}\right)\right]^{16}}{16\bar{h}(\alpha)\bar{h}(\phi')} \cdot \cos \frac{\alpha}{2} \cos \frac{\phi'}{2} \left[\frac{\bar{F}(\alpha, \phi')}{\cos \alpha + \cos \phi'} + \bar{M}(\alpha_o) \right]; \quad (32c)$$

in which

$$\begin{aligned} \bar{F}(\alpha, \phi') &= 1 + X_2 + 2X_4 + \frac{1}{2} \cos \alpha \cos \phi' \\ &+ \frac{X_1}{2^{1/2}} \left(\cos \alpha \sin \frac{\phi'}{2} + \cos \phi' \sin \frac{\alpha}{2} \right) + 2(1 \\ &+ X_2) \sin \frac{\alpha}{2} \sin \frac{\phi'}{2} - \frac{2}{2^{1/2}} (X_1 + X_3) \left(\sin \frac{\alpha}{2} + \sin \frac{\phi'}{2} \right), \end{aligned} \quad (32d)$$

$$\bar{M}(\alpha_o) = -\frac{\bar{h}(\alpha_o)\bar{N}(\alpha_o) + \bar{h}(\pi - \alpha_o)\bar{N}(\pi - \alpha_o)}{\bar{h}(\alpha_o)\bar{H}(\alpha_o) + \bar{h}(\pi - \alpha_o)\bar{H}(\pi - \alpha_o)}, \quad (32e)$$

$$\begin{aligned} \bar{N}(\alpha) &= \frac{1}{8} (a_1 + a_2) \sin \frac{\alpha}{2} \cos \alpha + \frac{1}{2} \left(X_1 \sin \frac{\alpha}{2} \right. \\ &\left. - \frac{1}{2^{1/2}} \cos \alpha \right) (X_1 + X_3) + \frac{1}{2^{1/2}} X_1 (1 + X_2 + 2X_4), \end{aligned} \quad (32f)$$

where X_i , $i = 1, 2, 3, 4$, were defined in (29c)–(29f). The function $\bar{\mathcal{F}}(\alpha, \phi')$ exhibits the reciprocity property as shown by the symmetry in α and ϕ' . It is noted that (32c) has a similar form as the result developed by Senior [1991], except that (32c) is completely specified while Senior's solution still has an unknown constant to be determined by an additional constraint. Furthermore, in contrast to the analysis by Senior [1991], where the reciprocity condition is explicitly imposed in the analysis, the present analysis did not enforce reciprocity a priori, yet it yielded a unique solution which automatically satisfies reciprocity. Keeping only the leading term of order $(k\rho)^{-1/2}$, the asymptotic evaluation of (32a) recovers the high-frequency edge diffracted field, namely

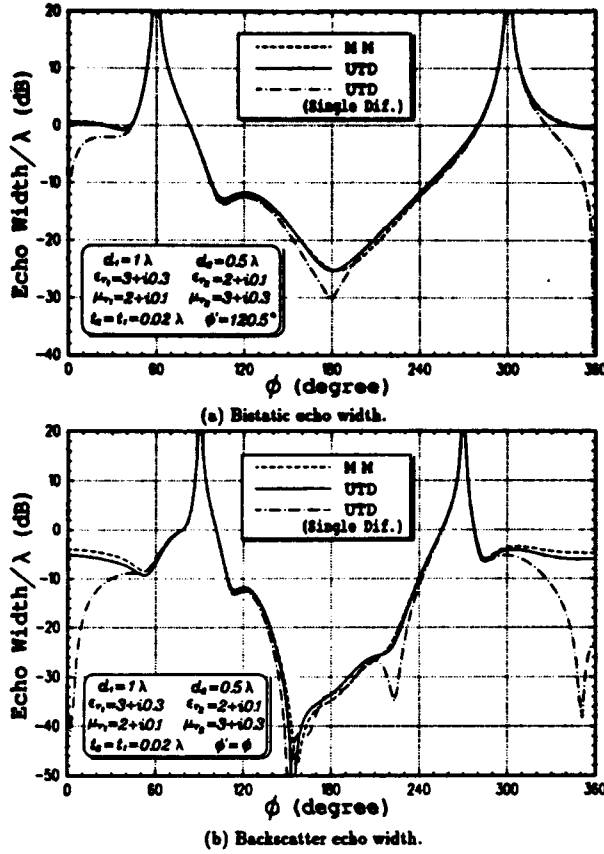


Fig. 5. UTD versus MM results for the geometry shown in Figure 3.

$$\bar{u}^d(\rho, \phi) \sim \frac{e^{ik\rho}}{\sqrt{\rho}} D(\phi, \phi'; \nu_{a_{12}}, \nu_{b_{12}}), \quad (33a)$$

$$-\pi < \phi, \phi' < \pi,$$

with the uniform diffraction coefficient D given by

$$D(\phi, \phi'; \nu_{a_{12}}, \nu_{b_{12}}) \sim \frac{e^{i\pi/4}}{\sqrt{2\pi k}} \left\{ \mathfrak{F}(\phi, \phi') + \sum_{i=1}^4 F_i \frac{1 - F(-2k\rho s_i^2)}{2s_i} \right\}; \quad (33b)$$

$$s_i = \sin \left(\frac{\bar{\alpha}_i - \phi}{2} \right), \quad i = 1, 2, 3, 4, \quad (33c)$$

$$\bar{\alpha}_1 = \pi - \phi', \quad \bar{\alpha}_2 = \pi + \phi', \quad \bar{\alpha}_3 = \pi + \nu_{b_1},$$

$$\bar{\alpha}_4 = -\pi - \nu_{b_1}, \quad F_2 = -1 \quad (33d)$$

$$F_1 = R_1(\phi'), \quad 0 \leq \phi' < \pi \quad (33e)$$

$$F_1 = R_2(-\phi'), \quad -\pi < \phi' < 0$$

$$F_{34} = \pm \frac{\left[\psi_\pi \left(\frac{\pi}{2} \right) \right]^{1/2} \Psi(\nu_{b_{12}}, \nu_{b_{12}}) \sec \frac{1}{2} \left(\frac{\pi}{2} + \nu_{b_{12}} \right)}{4\bar{h}(\phi')\bar{h}_{21}(-\pi - \nu_{b_{12}})\bar{\Psi}(\pi + \nu_{b_{12}}, -\pi - \nu_{b_{12}})} \cdot \cos \frac{\phi'}{2} \sin(\nu_{b_{12}}/2) \left[\frac{\bar{F}(\pm\{\pi + \nu_{b_{12}}\}, \phi')}{\cos \phi' - \cos \nu_{b_{12}}} + \bar{M}(\alpha_o) \right]. \quad (33f)$$

Note that F_i , $i = 1, 2, 3, 4$, are the residues of the function $\mathfrak{F}(\alpha, \phi')$ at the corresponding poles $\bar{\alpha}_i$, except when $-\pi < \phi' < 0$ the residue F_1 is evaluated at $\alpha = -\pi - \phi'$ instead of $\bar{\alpha}_1$. Also, the function $F(x)$ present in the residue terms of (33b) is the well-known transition function [Kouyoumjian and Pathak, 1974]. Finally, the surface wave field \bar{u}^{sw} is given by

$$\bar{u}^{sw}(\rho, \phi) = F_{sw_1} \exp[-ik\rho \cos(\nu_{b_1} - \phi)]U(\phi - \bar{\phi}_{s_1}) + F_{sw_2} \exp[-ik\rho \cos(\nu_{b_2} + \phi)]U(\bar{\phi}_{s_2} - \phi), \quad (34a)$$

$$\bar{\phi}_{s_{12}} = \pm \left\{ \pi + \operatorname{Re}(\nu_{b_{12}}) - \arccos \left[\frac{1}{\cosh(\operatorname{Im} \nu_{b_{12}})} \right] \right\}; \quad (34b)$$

and $F_{sw_1} = F_3$, $F_{sw_2} = -F_4$. Note that $F_{sw_{12}}$ are the residues of $\bar{S}(\alpha + \phi)$ at the surface wave poles $\alpha = \pm(2\pi + \nu_{b_{12}}) - \phi$.

4. NUMERICAL RESULTS

As stated earlier, the solution for the two-part problem developed in section 2 based on Maliuzhnet's method is identical to the known result given by Rojas *et al.* [1991a] based on the Wiener-Hopf technique. The accuracy of that solution has been verified [Rojas *et al.*, 1991a, b]. Thus it remains to illustrate the UTD solution developed in section 3 for the material-coated PEC half plane excited by a normally incident plane wave of TE_z polarization. Here a few far zone scatter patterns for the partially coated half plane geometry depicted in Figure 3 are presented and compared with a corresponding in-

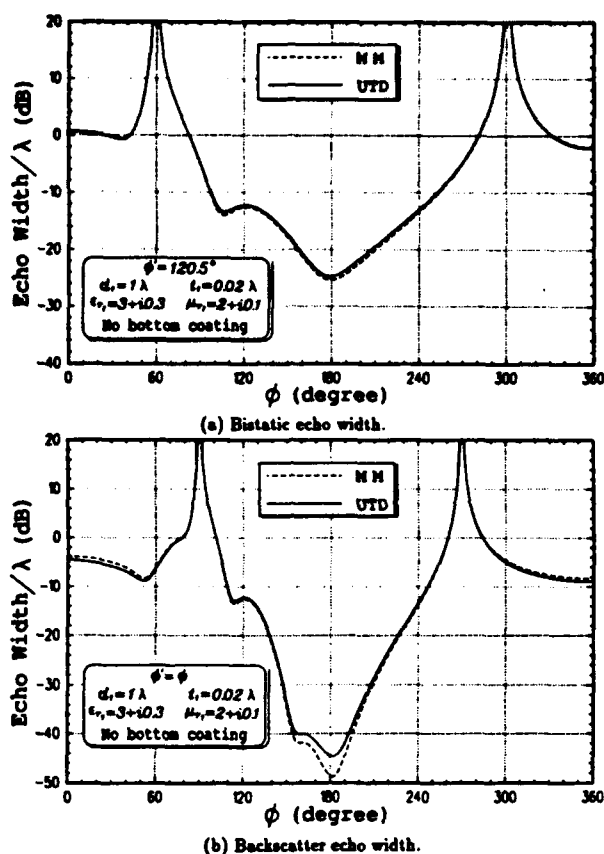


Fig. 6. UTD versus MM results for the geometry shown in Figure 3 without bottom coating.

dependent MM/Green's function solution given by Newman [1986]. The results based on UTD are computed with all multiply diffracted and surface wave field components up to third order included. Note that the procedure used to obtain these multiply diffracted and surface wave fields is based on the spectrally extended ray method developed by Tiberio and Kouyoumjian [1979, 1982, 1984], which has been applied to a resistive strip [Herman and Volakis, 1987], and it is described in detail by Rojas and Chou [1990] and Rojas *et al.* [1991b], where some multiple diffraction mechanisms not considered by previous authors are discussed. The expressions for the multiply diffracted fields of the partially coated half plane can be found in the work by Ly [1992]. It is shown in Figures 5 and 6 that the UTD solution agrees very well with the MM result for both bistatic and backscatter patterns. The results based only on single edge diffraction are also

included in Figure 5 to illustrate the importance of the multiply diffracted fields.

To further examine the usefulness of the UTD solution for small strip widths d_1 and d_2 , the UTD based bistatic and backscatter echo widths are compared with the MM in Figure 7 where $d_1 = d_2 = 0.1\lambda$ with other parameters keeping the initial values. It is evident from Figure 7 that for the chosen material parameters, the UTD results are very accurate even for such small strip widths by including up to third-order multiple diffraction. As mentioned earlier, the boundary conditions used to develop the UTD solution are valid only for thin coatings. Thus in Figure 8 the bistatic and backscatter echo widths are calculated for not very thin coatings; namely, $t_1 = t_2 = 0.05\lambda$ to show the limitation of the GIBCs of $O(t)$. Note that with the characteristics of the material used here, 0.05λ corresponds to $0.12\lambda_d$, where λ_d is the wavelength

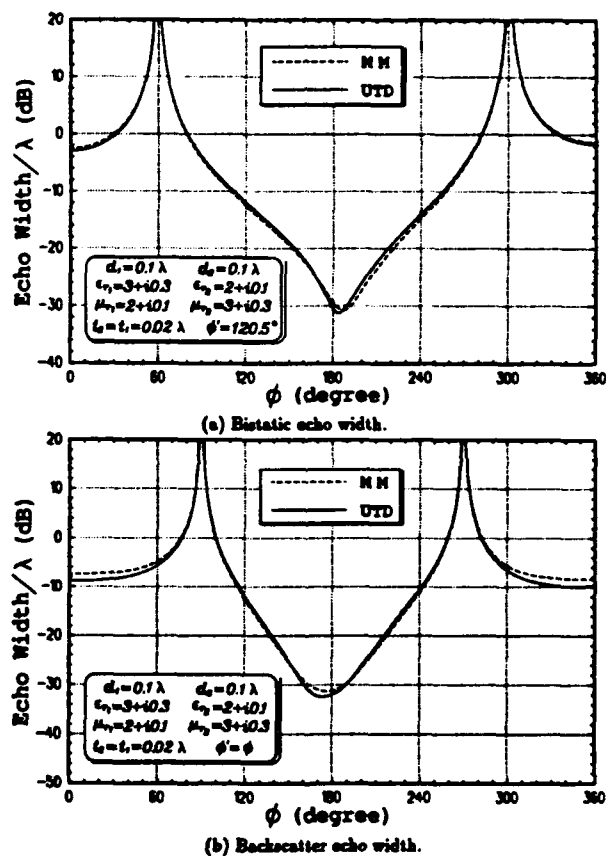


Fig. 7. UTD versus MM results for the geometry shown in Figure 3 with $d_1 = d_2 = 0.1\lambda$.

inside the material. Although the GIBCs of $\Omega(i)$ are not very accurate for these values of t_1 and t_2 , it seems that the agreement of the UTD solution with the MM data in Figure 8 is still reasonable.

5. CONCLUSIONS

The Maliuzhinets method is employed in this paper to analyze two diffraction problems involving thin material-coated metallic surfaces. Each of the electrically thin material coatings is modeled by a GIBC of $\Omega(i)$, where i denotes the thickness of the corresponding material layer. The application of GIBCs of $\Omega(i)$ (for magnetic dielectric materials) which involve second-order derivatives of the fields creates difficulties because it yields solutions which are neither unique nor reciprocal even after the edge condition has been applied. This difficulty is solved here by imposing a junction condition, some-

times referred to as a contact condition, in addition to the boundary and radiation conditions as well as the edge condition. The junction condition is developed by matching a quasi-static solution with the corresponding Maliuzhinets solution in their common region of overlap near the edge (or junction). The final solutions thus obtained do not contain any unknown constants and automatically satisfy the reciprocity condition.

It is noted that expressions for the constants A_i and \bar{A}_i ($i = 1, 2, 3$), which appear in sections 2 and 3, respectively, are developed here and are also expressed in terms of the field and its derivatives evaluated at the junction or edge of the scatterer. This is an important step because it gives a physical interpretation to these constants and allows the comparison of one of the junction conditions developed here to the one obtained by means of the Wiener-Hopf technique [Rojas *et al.*, 1991a].

Finally, the accuracy of the solutions developed here is assessed by considering the bistatic and backscattered echo width of a partially coated half plane. By including multiple interactions up to third order, the UTD solutions provide results which are in good agreement with corresponding moment method results.

APPENDIX

Approximate expressions valid in the region $1 \ll |\cos \alpha| \ll (kt_{1/2})^{-1}$ are obtained for the functions $h(\alpha + \pi/2)$ and $\bar{h}(\alpha + \pi)$ defined in (11b) and (24c), respectively. Since $a_{1/2}$, which is defined in (1b), is proportional to $(kt_{1/2})^{-1}$, the condition $|\cos \alpha| \ll |a_{1/2}|$ also implies $|\cos \alpha| \ll (kt_{1/2})^{-1}$.

Approximation for $h(\alpha + \pi/2) = h_2(\alpha + \pi/2)h_1(-\alpha - \pi/2)$

Since the Maliuzhinets function $\psi_{\pi/2}(\alpha)$ satisfies the identity (10a), it can be shown that

$$\begin{aligned} h_2\left(\alpha + \frac{\pi}{2}\right)h_2\left(-\alpha - \frac{\pi}{2}\right) &= \frac{1}{4} \left[\psi_{\pi/2}\left(\frac{\pi}{2}\right) \right]^8 \\ &\cdot (\sin^2 \alpha - a_2 \sin \alpha + b_2) \sim -\frac{1}{2} \left[\psi_{\pi/2}\left(\frac{\pi}{2}\right) \right]^8 \\ &\cdot a_2 \sin \frac{\alpha}{2} \cos \frac{\alpha}{2}, \quad |a_2| \rightarrow \infty. \end{aligned} \quad (35a)$$

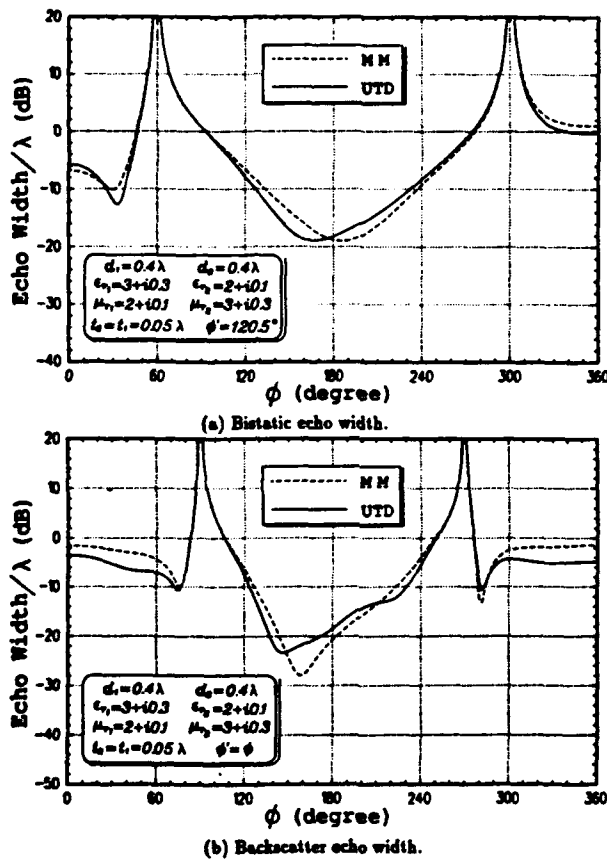


Fig. 8. UTD versus MM results for the geometry shown in Figure 3 with $t_1 = t_2 = 0.05\lambda$.

In the strip of interest where $|\operatorname{Re}(\alpha + \pi/2)| \leq \pi$, the function $h_2(\alpha + \pi/2)$ has a zero at $\alpha = \nu_{b_1} \rightarrow 0$ as $|a_2| \rightarrow \infty$. Likewise, $h_2(-\alpha - \pi/2)$ possesses a zero at $\alpha = -\pi - \nu_{b_1} \rightarrow -\pi$ as $|a_2| \rightarrow \infty$. Hence it follows from (35a) that

$$h_2\left[\pm\left(\alpha + \frac{\pi}{2}\right)\right] \sim \frac{i}{2^{1/2}} \left[\psi_{\pi/2}\left(\frac{\pi}{2}\right)\right]^4 a_2^{1/2} \begin{bmatrix} \sin \frac{\alpha}{2} \\ \cos \frac{\alpha}{2} \end{bmatrix}, \quad (35b)$$

$$|\cos \alpha| \ll |a_2|.$$

The approximation given above can be improved by adding a second term to (35b), namely,

$$h_2\left[\pm\left(\alpha + \frac{\pi}{2}\right)\right] \sim \frac{i}{2^{1/2}} \left[\psi_{\pi/2}\left(\frac{\pi}{2}\right)\right]^4 a_2^{1/2} \begin{bmatrix} \sin \frac{\alpha}{2} \\ \cos \frac{\alpha}{2} \end{bmatrix} \cdot [1 + H_2^\pm(\alpha)], \quad (35c)$$

where $[H_2^\pm(\alpha)] \ll 1$. Substituting (35c) into (35a) and neglecting the small product $H_2^+(\alpha)H_2^-(\alpha)$ leads to

$$H_2^+(\alpha) + H_2^-(\alpha) \sim \frac{\sin^2 \alpha + b_2}{a_2} \frac{1}{\sin \alpha}, \quad |\cos \alpha| \ll |a_2|. \quad (35d)$$

By decomposing the function $(1/\sin \alpha)$ as

$$\frac{1}{\sin \alpha} = \frac{-\alpha}{\pi \sin \alpha} + \frac{\pi + \alpha}{\pi \sin \alpha}, \quad (35e)$$

and noting that the approximation of $h_2(\alpha + \pi/2)$ must be regular in the strip $|\operatorname{Re}(\alpha + \pi/2)| \leq \pi$, one recognizes

$$H_2^+(\alpha) \sim \frac{(\pi + \alpha)(\sin^2 \alpha + b_2)}{\pi a_2 \sin \alpha} \rightarrow \frac{\alpha \sin \alpha}{\pi a_2}, \quad (35f)$$

$$1 \ll |\cos \alpha|.$$

Substituting (35f) into (35c) leads to

$$h_2\left(\alpha + \frac{\pi}{2}\right) \sim \frac{i}{2^{1/2}} \left[\psi_{\pi/2}\left(\frac{\pi}{2}\right)\right]^4 a_2^{1/2} \cdot \sin \frac{\alpha}{2} \left[1 - \frac{\alpha \sin \alpha}{\pi a_2}\right], \quad 1 \ll |\cos \alpha| \ll |a_2|. \quad (35g)$$

Similarly,

$$h_1\left(-\alpha - \frac{\pi}{2}\right) \sim \frac{i}{\sqrt{2}} \left[\psi_{\pi/2}\left(\frac{\pi}{2}\right)\right]^4 a_1^{1/2} \cdot \cos \frac{\alpha}{2} \left[1 + \frac{\alpha \sin \alpha}{\pi a_1}\right], \quad 1 \ll |\cos \alpha| \ll |a_1|. \quad (35h)$$

Multiplying (35h)–(35g) and retaining the first two terms yields

$$h\left(\alpha + \frac{\pi}{2}\right) \sim -\frac{\sin \alpha}{4} \left[\psi_{\pi/2}\left(\frac{\pi}{2}\right)\right]^8 \sqrt{a_1 a_2} \left[1 + \frac{\alpha \sin \alpha}{\pi} \left(\frac{1}{a_1} - \frac{1}{a_2}\right)\right], \quad 1 \ll |\cos \alpha| \ll (ka_{1/2})^{-1}. \quad (36)$$

Approximation for $\bar{h}(\alpha + \pi) = \bar{h}_1(\alpha + \pi)\bar{h}_2(-\alpha - \pi)$

The Maliuzhinets function $\psi_\pi(\alpha)$ has the following property [Maliuzhinets, 1959]:

$$\psi_\pi(\alpha + \pi)\psi_\pi(\alpha - \pi) = [\psi_\pi(\pi)]^2 \psi_{\pi/2}(\alpha). \quad (37a)$$

Hence it can be shown from (37a) that

$$\bar{h}_2(\alpha + \pi)\bar{h}_2(-\alpha - \pi) = [\psi_\pi(\pi)]^2 h_2\left(\alpha + \frac{\pi}{2}\right). \quad (37b)$$

Substituting into (37b) the approximation for $h_2(\alpha + \pi/2)$ given in (35c) and (35f) as $|a_2| \rightarrow \infty$, one obtains

$$\bar{h}_2(\alpha + \pi)\bar{h}_2(-\alpha - \pi) \sim \frac{i}{2^{1/2}} [\psi_\pi(\pi)]^8 \cdot \left[\psi_{\pi/2}\left(\frac{\pi}{2}\right)\right]^4 a_2^{1/2} \sin \frac{\alpha}{2} \cdot \left[1 - \frac{(\pi + \alpha)(\sin^2 \alpha + b_2)}{\pi a_2 \sin \alpha}\right], \quad |a_2| \rightarrow \infty. \quad (37c)$$

Thus, a two-term approximation for $\bar{h}_2(-\alpha - \pi)$ in the region $1 \ll |\cos \alpha| \ll |a_2|$ can be found following a similar procedure as discussed in the previous section, namely,

$$\bar{h}_2(-\alpha - \pi) \sim (-2)^{1/4} [\psi_\pi(\pi)]^4 \left[\psi_{\pi/2}\left(\frac{\pi}{2}\right)\right]^2 a_2^{1/4} \cdot \cos \frac{\alpha}{4} \left[1 - \frac{\alpha \sin \alpha}{2\pi a_2}\right]. \quad (37d)$$

Multiplying (37d) to a similar approximation of $\tilde{h}_1(\alpha + \pi)$ yields

$$\tilde{h}(\alpha + \pi) \sim \frac{i}{2^{1/2}} [\psi_\pi(\pi)]^8 \left[\psi_{\pi/2} \left(\frac{\pi}{2} \right) \right]^4 (a_1 a_2)^{1/4} \cdot \sin \frac{\alpha}{2} \left[1 - \frac{\alpha \sin \alpha}{2\pi} \left(\frac{1}{a_1} + \frac{1}{a_2} \right) \right], \quad (38)$$

$$1 \ll |\cos \alpha| \ll (k t_{1/2})^{-1}.$$

Acknowledgment. This work was supported in part by the Joint Services Electronics Program (contract N00014-89-J-1007) and by the Ohio State University Research Foundation.

REFERENCES

- Bernard, J. M. L., Diffraction by a metallic wedge covered with dielectric material, *Wave Motion*, 9, 543-561, 1987.
- Herman, M. I., and J. L. Volakis, High-frequency scattering by a resistive strip and extensions to conductive and impedance strips, *Radio Sci.*, 22, 335-349, 1987.
- Kouyoumjian, R. G., and P. H. Pathak, A uniform geometrical theory of diffraction for an edge in a perfectly conducting surface, *Proc. IEEE*, 62, 1448-1461, 1974.
- Leppington, F. G., Travelling waves in a dielectric slab with an abrupt change in thickness, *Proc. R. Soc. London*, A386, 443-460, 1983.
- Ly, H. C., A UTD analysis of em diffraction by an abrupt discontinuity in thin planar material configurations, Ph.D. dissertation, Dep. of Elec. Eng., Ohio State Univ., Columbus, 1992.
- Maliuzhinets, G. D., The radiation of sound by the vibrating boundaries of an arbitrary wedge, Part I, *Sov. Phys. Acoust.*, Engl. Transl. 1, 152-174, 1956.
- Maliuzhinets, G. D., Inversion formula for the Sommerfeld integral, *Sov. Phys. Dokl.*, Engl. Transl., 3, 52-56, 1958.
- Maliuzhinets, G. D., Excitation, reflection and emission of surface waves from a wedge with given face impedances, *Sov. Phys. Dokl.*, Engl. Transl., 3, 752-755, 1959.
- Newman, E. H., TM and TE scattering by a dielectric/ferrite cylinder in the presence of a half-plane, *IEEE Trans. Antennas Propag.*, AP-34, 804-813, 1986.
- Rojas, R. G., Generalized impedance boundary conditions, *Electron. Lett.*, 24, 1093-1094, 1988.
- Rojas, R. G., and Z. Al-hekail, Generalized impedance/resistive boundary conditions for em scattering problems, *Radio Sci.*, 24, 1-12, 1989.
- Rojas, R. G., and L. M. Chou, Diffraction by a partially coated electric conducting half plane, *Radio Sci.*, 25, 175-188, 1990.
- Rojas, R. G., and P. H. Pathak, Diffraction of em waves by a dielectric/ferrite half-plane and related configurations, *IEEE Trans. Antennas Propag.*, AP-37, 751-763, 1989.
- Rojas, R. G., H. C. Ly, and P. H. Pathak, Electromagnetic plane wave diffraction by a planar junction of two thin dielectric/ferrite half planes, *Radio Sci.*, 26, 641-660, 1991a.
- Rojas, R. G., H. C. Ly, P. H. Pathak, and R. Tiberio, Electromagnetic plane wave diffraction by a three-part thin, planar dielectric/magnetic slab, *Radio Sci.*, 26, 1267-1280, 1991b.
- Tiberio, R., and R. G. Kouyoumjian, A uniform GTD solution for the diffraction by strips illuminated at grazing incidence, *Radio Sci.*, 14, 933-941, 1979.
- Tiberio, R., and R. G. Kouyoumjian, An analysis of diffraction at edges illuminated by transition region fields, *Radio Sci.*, 17, 323-336, 1982.
- Tiberio, R., and R. G. Kouyoumjian, Calculation of the high-frequency diffraction by two nearby edges illuminated at grazing incidence, *IEEE Trans. Antennas Propag.*, AP-32, 1186-1196, 1984.
- Senior, T. B. A., Diffraction by a generalized impedance half plane, *Radio Sci.*, 26, 163-167, 1991.
- Volakis, J. L., and T. B. A. Senior, Application of a class of generalized boundary conditions to scattering by a metal backed dielectric half plane, *Proc. IEEE*, 77, 796-805, 1989.
- Weinstein, L. A., *The Theory of Diffraction and the Factorization Method*, Golem Press, Boulder, Colo., 1969.
- H. C. Ly and R. G. Rojas, ElectroScience Laboratory, Department of Electrical Engineering, Ohio State University, 1320 Kinnear Rd., Columbus, OH 43212.

Angle and Polarization Estimation in a Coherent Signal Environment

JIAN LI, Member, IEEE

R. T. COMPTON, Jr., Fellow, IEEE
The Ohio State University

It is shown how a uniform linear array of crossed dipoles may be used with the ESPRIT algorithm and spatial smoothing techniques to estimate the arrival directions and polarizations of incoming coherent plane waves. Some examples showing typical performance are presented.

Manuscript received January 30, 1991; revised June 10, 1992.

IEEE Log No. T-AES/29/3/08908.

This work was supported in part by the Joint Services Electronics Program under Contract N00014-89-J-1007 with The Ohio State University Research Foundation.

Authors' current addresses: J. Li, Dept. of Electrical Engineering, University of Kentucky, Lexington, KY 40506; R. T. Compton, Jr., Compton Research, Inc., 477 Poe Ave., Worthington, OH 43085-3036.

0018-9251/93/\$3.00 © 1993 IEEE

I. INTRODUCTION

The estimation of signal parameters via rotational invariance techniques (ESPRIT) algorithm of Roy, Paulraj and Kailath [1, 2] uses signal subspace methods to estimate the arrival angles of signals with an array. The ESPRIT algorithm has the distinct advantage over the multiple signal classification (MUSIC) algorithm [3] that it does not require a search over parameter space. When the MUSIC algorithm is used to estimate arrival angles, one must search over the set of all possible arrival angles to obtain the estimates. Although such a search is not difficult in one dimension, it quickly becomes prohibitive as the number of dimensions increases. Angle estimation problems involving electromagnetic signals often require a search over two spatial angles. Moreover, because electromagnetic signals usually arrive with unknown polarizations, two more search dimensions may be needed for each signal to estimate the signal polarizations. The ESPRIT algorithm avoids the problem of a search entirely and is thus preferable to the MUSIC algorithm.

In an earlier paper [4], the authors showed how the ESPRIT algorithm can be used with a linear array of cross-polarized dipoles to estimate signal polarizations and arrival angles in one angular dimension. Also, for problems where the signal polarization is not of interest, a related paper [5] shows how to incorporate unknown signal polarization in the ESPRIT algorithm so that signal arrival angles can be estimated in a way that works regardless of the signal polarizations.

In [4, 5], it was assumed that the incoming signals whose angles and polarizations are to be estimated are uncorrelated, or at most partially correlated. However, the performance of these methods degrades rapidly as the incident signals become highly correlated. They fail to work properly when the signals are coherent (i.e., perfectly correlated).

The purpose of this work is to show how the ESPRIT algorithm can be combined with spatial smoothing techniques [6-10] and used with a uniform linear array of crossed dipoles to estimate signal directions and polarizations for coherent signals. We present one method of spatial smoothing that can be used when it is necessary to estimate both the arrival angles and the polarizations of signals. We also present two additional methods that can be used when only the signal arrival angles are of interest, not the polarizations, but it is still necessary that the estimator work properly with arbitrarily polarized signals.

In Section II, we define the array that is used and the signal parameters. In Section III, we show how forward-only spatial smoothing [7, 8] can be combined with ESPRIT and used with a polarization-sensitive array to estimate both signal directions and polarizations for coherent signals. In Section IV, we describe an alternative procedure

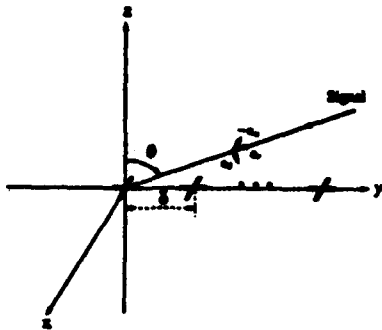


Fig. 1. Uniform linear array of crossed dipoles.

based on [5] that may be used with both forward-only (FO) and forward/backward [9, 10] spatial smoothing to estimate signal directions only. In Section V, we present some typical examples and compare the performance of the different techniques. Finally, Section VI contains our conclusions.

II. PROBLEM FORMULATION

Consider a $2L$ -element array consisting of L pairs of crossed dipoles, as shown in Fig. 1. The l th dipole pair, $l = 1, 2, \dots, L$, has its center on the y axis at $y = (l - 1)\delta$. The distance δ between two adjacent dipole pairs is a half wavelength. The signal from each dipole is processed separately. For the l th dipole pair, let $x_l(t)$ be the signal received on the x axis dipole and $y_l(t)$ the signal received on the y axis dipole.

Suppose K (with $K < L$) narrowband signals impinge on the array from angular directions $\{\theta_k, 0 \leq k \leq K\}$ in the yz plane, where θ denotes the standard polar angle in the yz plane, as shown in Fig. 1. It is assumed that each signal has an arbitrary elliptical electromagnetic polarization [11].

To specify signal polarization, we use the following definitions. An incoming transverse electromagnetic (TEM) wave propagating into the array has an electric field given by

$$\mathbf{E} = -E_x \mathbf{e}_x + E_\theta \mathbf{e}_\theta \quad (1)$$

where \mathbf{e}_x , \mathbf{e}_θ , and \mathbf{e}_r are unit vectors in the x , θ , and r directions, respectively, in Fig. 1. We consider the polarization ellipse produced by E_x and E_θ . Given this ellipse, we define α and β to be the ellipticity and the orientation angles, respectively (see [4]). We define β to be in the range $0 \leq \beta < \pi$, and α is always in the range $-\pi/4 \leq \alpha \leq \pi/4$. See Fig. 2.

For a given α and β , E_x and E_θ are given by (aside from a common phase factor) [4]

$$E_x = E \cos \gamma \quad (2)$$

$$E_\theta = E \sin \gamma e^{j\eta} \quad (3)$$

where γ describes the relative values of $|E_x|$ and $|E_\theta|$ and η is the phase by which the θ component leads the x component. γ is always in the range $0 \leq \gamma \leq \pi/2$, and η is in the range $-\pi \leq \eta < \pi$. Either pair of angles

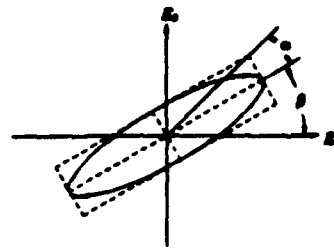


Fig. 2. Polarization ellipse.

(α, β) or (γ, η) uniquely define the polarization state of a wave. We can compute γ and η from α and β and α and β from γ and η [12, 4].

An arbitrary plane wave coming into the array is characterized by three angular parameters and an amplitude. The k th signal, $k = 1, 2, \dots, K$, is characterized by its arrival angle θ_k , its polarization ellipticity angle α_k and orientation angle β_k , and its amplitude E_k (i.e., E_k is the value of E in (2) and (3) for the k th signal). We say the k th signal is defined by $(\theta_k, \alpha_k, \beta_k, E_k)$.

We assume each dipole in the array is a short dipole, so the output voltages of the x and y axis dipoles are proportional to the x and y components, respectively, of the electric field. An incoming signal with components E_x and E_θ has x, y, z components:

$$\begin{aligned} \mathbf{E} &= -E_x \mathbf{e}_x + E_\theta \mathbf{e}_\theta \\ &= (-E_x) \mathbf{e}_x + (E_\theta \cos \theta) \mathbf{e}_y - (E_\theta \sin \theta) \mathbf{e}_z \quad (4) \\ &= E [(-\cos \gamma) \mathbf{e}_x + (\sin \gamma \cos \theta e^{j\eta}) \mathbf{e}_y \\ &\quad - (\sin \gamma \sin \theta e^{j\eta}) \mathbf{e}_z] \quad (5) \end{aligned}$$

where \mathbf{e}_x , \mathbf{e}_y , and \mathbf{e}_z are unit vectors in the x , y and z directions, respectively. We define the space phase factor

$$q = e^{j(2\pi\delta/\lambda)\sin\theta} \quad (6)$$

where λ is the wavelength of the signal. Including the time and space phase factors in (5), we find that an incoming signal characterized by $(\theta, \alpha, \beta, E)$ produces a signal vector in the crossed dipole pair centered at $y = (l - 1)\delta$ as follows:

$$\mathbf{z}_l = \begin{bmatrix} x_l(t) \\ y_l(t) \end{bmatrix} = \mathbf{u}(t) q^{l-1} \quad (7)$$

where

$$\mathbf{u} = \begin{bmatrix} -\cos \gamma \\ \sin \gamma \cos \theta e^{j\eta} \end{bmatrix} \quad (8)$$

and

$$s(t) = E e^{j(\omega t + \psi)} \quad (9)$$

with ω the frequency of the signal and ψ the carrier phase of the signal at the coordinate origin at $t = 0$.

We assume that K such signals, specified by θ_k , $k = 1, 2, \dots, K$, are incident on the array. In addition we assume a thermal noise voltage vector $\mathbf{n}_l(t)$ is

present on each signal vector $z_l(t)$. The $n_l(t)$ are assumed to be zero mean, complex Gaussian processes statistically independent of each other with covariance $\sigma^2 I$, where I denotes the identity matrix.

Under these assumptions, the total signal vector received by the crossed dipole pair centered at $y = (l-1)\delta$ is given by

$$z_l(t) = \sum_{k=1}^K u_k s_k(t) q_k^{l-1} + n_l(t), \quad l = 1, 2, \dots, L \quad (10)$$

where u_k and q_k are given by (8) and (6), respectively, with subscript k added to each angular quantity, and $s_k(t)$ is given by (9) with subscript k added to the amplitude and carrier phase.

The carrier phase angle ψ_1 is assumed to be a random variable uniformly distributed on $[0, 2\pi)$. The other ψ_k , for $k = 2, 3, \dots, K$, are also random variables but it is assumed that each of these differs from ψ_1 by a fixed amount. Thus, the ψ_k are all rigidly tied to one another, and the incident signals are coherent (i.e., perfectly correlated). In this case, each signal $s_k(t)$ can be written as a scaled replica of some signal $s_0(t)$ for which $E\{|s_0(t)|^2\} = 1$, i.e.,

$$s_k(t) = g_k s_0(t), \quad k = 1, 2, \dots, K \quad (11)$$

where g_1 is a real constant, and g_2, g_3, \dots, g_K are complex constants.

Let $z(t)$, $s(t)$, and $n(t)$ be column vectors containing the received signals, incident signals, and noise, respectively, i.e.,

$$\begin{aligned} z(t) &= \begin{bmatrix} z_1(t) \\ z_2(t) \\ \vdots \\ z_L(t) \end{bmatrix}, \\ s(t) &= \begin{bmatrix} s_1(t) \\ s_2(t) \\ \vdots \\ s_K(t) \end{bmatrix}, \\ n(t) &= \begin{bmatrix} n_1(t) \\ n_2(t) \\ \vdots \\ n_L(t) \end{bmatrix}. \end{aligned} \quad (12)$$

The received signal vector has the form

$$z(t) = A s(t) + n(t) \quad (13)$$

where A is a $2L \times K$ matrix

$$A = [a_1 \ a_2 \ \dots \ a_K] \quad (14)$$

with $2L \times 1$ columns

$$a_k = \begin{bmatrix} u_k \\ u_k q_k \\ \vdots \\ u_k q_k^{L-1} \end{bmatrix}. \quad (15)$$

The columns a_k are assumed linearly independent. They define a K -dimensional *signal subspace* in a $2L$ -dimensional space.

By assuming the columns in A are linearly independent, we are excluding from consideration degenerate cases, such as when a signal causes zero output on both the x and y axis dipoles at the same time.

We assume that the element signals are sampled at N distinct times t_n , $n = 1, 2, \dots, N$. The random noise vectors $n(t_n)$ at different sample times are assumed independent of each other. The problem of interest is to estimate the θ_k (and possibly the α_k, β_k) for $k = 1, 2, \dots, K$ from the measurements $z(t_n)$, $n = 1, 2, \dots, N$.

In Section III, we consider how to estimate all three parameters θ_k, α_k , and β_k from the $z(t_n)$. In Section IV we consider what can be done if we need to estimate only the θ_k .

III. ESTIMATING BOTH DIRECTION AND POLARIZATION FOR COHERENT SIGNALS

Consider the array covariance matrix of $z(t)$ which has the form

$$R = E\{z(t)z^H(t)\} = R_0 + \sigma^2 I \quad (16)$$

where

$$R_0 = A R_s A^H \quad (17)$$

with $(\cdot)^H$ denoting the complex conjugate transpose and $R_s = E\{s(t)s^H(t)\}$ representing the source covariance matrix.

In general, if the signals $s_1(t), \dots, s_K(t)$ are uncorrelated, R_s is diagonal. If the signals are partially correlated, R_s is nondiagonal but nonsingular. For the case considered here, the signals are completely correlated, so R_s is nondiagonal and singular.

As long as the $s_k(t)$ are not completely correlated, the eigenvectors of R_0 (or R) that correspond to the K largest eigenvalues of R_0 (or R) span the same signal subspace as the column vectors in A [3]. This fact is used in the original ESPRIT algorithm [1, 2] for estimating signal direction and in [4] for estimating both direction and polarization.

When the incident signals are coherent, however, using $E\{|s_0(t)|^2\} = 1$ and (11) yields

$$R_s = g g^H \quad (18)$$

where g is a $K \times 1$ column vector

$$g = [g_1 \ g_2 \ \dots \ g_K]^T \quad (19)$$

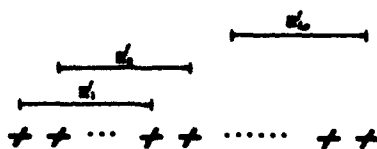


Fig. 3. Spatial smoothing scheme.

where $(\cdot)^T$ denotes the transpose. For this case, the matrix R_s is of rank 1 and the signal subspace based approach will not work. To use signal subspace methods with coherent signals, the signals must first be "decorrelated".

One method of overcoming the singularity of R_s for coherent signals is the FO spatial smoothing technique of Shan, Wax, and Kailath [7, 8]. The idea of this technique is to divide a total array of L elements into L_0 overlapping subarrays, as shown in Fig. 3. Each subarray then has $L_s = L - L_0 + 1$ elements and we assume that $L_s > K$. As shown in [7, 8], averaging the covariance matrices associated with the subarrays restores the rank of R_s and makes it possible to use signal subspace methods.

The FO method can be applied here. Let $\bar{z}_l^f(t)$ denote the column vector received from the l th subarray, i.e.,

$$\bar{z}_l^f(t) = [z_l^T(t) \quad z_{l+1}^T(t) \quad \dots \quad z_{l+L_s-1}^T(t)]^T, \quad 1 \leq l \leq L_0. \quad (20)$$

The covariance matrix of the l th subarray is [8]

$$\begin{aligned} R_l^f &= E\{\bar{z}_l^f(t)[\bar{z}_l^f(t)]^H\} \\ &= A\Phi_q^{l-1}R_s(\Phi_q^{l-1})^H A^H + \sigma^2 I \end{aligned} \quad (21)$$

where

$$\Phi_q = \text{diag}\{q_1, q_2, \dots, q_K\} \quad (22)$$

and where A is now the matrix in (14) and (15) with L replaced by L_s .

We define the FO spatially smoothed array covariance matrix R^f to be the average of the matrices R_l^f , i.e.,

$$R^f = \frac{1}{L_0} \sum_{l=1}^{L_0} R_l^f. \quad (23)$$

The matrix R^f can be written as

$$R^f = R_0^f + \sigma^2 I \quad (24)$$

where

$$R_0^f = A R_s^f A^H \quad (25)$$

with R_s^f denoting the FO spatially smoothed source covariance matrix

$$R_s^f = \frac{1}{L_0} \sum_{l=1}^{L_0} \Phi_q^{l-1} R_s (\Phi_q^{l-1})^H. \quad (26)$$

By replacing R_s with $g g^H$, (26) can be written

$$R_s^f = \frac{1}{L_0} C C^H \quad (27)$$

where

$$C = [g \quad \Phi_q g \quad \dots \quad \Phi_q^{L_0-1} g] = G \bar{A}_{L_0}^T \quad (28)$$

with

$$G = \text{diag}\{g_1, g_2, \dots, g_K\} \quad (29)$$

and

$$\bar{A}_{L_0} = \begin{bmatrix} 1 & 1 & \dots & 1 \\ q_1 & q_2 & \dots & q_K \\ \vdots & \vdots & \dots & \vdots \\ q_1^{L_0-1} & q_2^{L_0-1} & \dots & q_K^{L_0-1} \end{bmatrix}. \quad (30)$$

Note that as long as the signals arrive from *distinct* directions, the Vandermonde matrix \bar{A}_{L_0} is nonsingular. If in addition $L_0 > K$, then C is nonsingular so the rank of R_s^f is K .

A second potential method for overcoming the singularity of R_s for coherent signals is the forward/backward spatial smoothing technique of [9, 10]. The idea of this technique is to average the covariances matrices associated with both the subarrays shown in Fig. 3 and their complex conjugated backward subarrays. However, this method cannot be used in the present problem when we want to estimate α_k, β_k as well as θ_k . The reason is that the amplitudes of the elements of A given in (14) are not all unity, as can be seen from (8). However, if we want to estimate only the θ_k , but not the polarization, this technique can be used. We consider this case in the next section.

IV. ESTIMATING DIRECTION ONLY FOR COHERENT SIGNALS

In [5], the authors described a method for using the array of Fig. 1 to estimate signal directions only, but to do so in such a way that the estimator works properly regardless of signal polarization. This approach treated the x axis dipoles and the y axis dipoles as separate subarrays. The arithmetic average of the covariance matrices for the x and y axis dipoles was used as the total covariance matrix in the ESPRIT algorithm. We now show that, with coherent signals, this same approach can be used in combination with both the FO [7, 8] and forward/backward [9, 10] spatial smoothing techniques.

Let $x(t)$ denote the column vector received from the x axis dipoles, i.e.,

$$x(t) = [x_1(t) \quad x_2(t) \quad \dots \quad x_{L_s}(t)]^T \quad (31)$$

$x(t)$ is the subvector of $z(t)$ consisting of the odd-numbered elements of $z(t)$. The variables $x(t)$ can be written

$$x(t) = \bar{A}_{L_s} \Phi_x s(t) + n_x(t) \quad (32)$$

where \bar{A}_{L_s} is defined as in (30) with L_0 replaced by L_s , Φ_x is defined as

$$\Phi_x = \text{diag}\{-\cos \gamma_1, -\cos \gamma_2, \dots, -\cos \gamma_K\} \quad (33)$$

and $n_x(t)$ is a zero-mean complex Gaussian process with covariance $\sigma^2 I$. The matrix \bar{A}_{L_s} is the direction matrix for this approach. The angles of arrival are assumed to be distinct, so that the columns of \bar{A}_{L_s} define a K -dimensional signal subspace in an L_s -dimensional space. The covariance matrix of $x(t)$ is

$$\begin{aligned} R_x &= E\{x(t)x^H(t)\} \\ &= \bar{A}_{L_s} \Phi_x R_s \Phi_x^H \bar{A}_{L_s}^H + \sigma^2 I. \end{aligned} \quad (34)$$

Similarly, let $y(t)$ denote the column vector received from the y axis dipoles, i.e.,

$$y(t) = [y_1(t) \ y_2(t) \ \dots \ y_{L_s}(t)]^T \quad (35)$$

where $y(t)$ is the subvector of $z(t)$ consisting of the even-numbered elements of $z(t)$. The variables $y(t)$ can be written

$$y(t) = \bar{A}_{L_s} \Phi_y s(t) + n_y(t) \quad (36)$$

where

$$\begin{aligned} \Phi_y &= \text{diag}\{-\sin \gamma_1 \cos \theta_1 e^{j\eta_1}, -\sin \gamma_2 \cos \theta_2 e^{j\eta_2}, \dots, \\ &\quad -\sin \gamma_K \cos \theta_K e^{j\eta_K}\} \end{aligned} \quad (37)$$

and $n_y(t)$ is a zero-mean complex Gaussian process with covariance $\sigma^2 I$. The covariance matrix of $y(t)$ is

$$\begin{aligned} R_y &= E\{y(t)y^H(t)\} \\ &= \bar{A}_{L_s} \Phi_y R_s \Phi_y^H \bar{A}_{L_s}^H + \sigma^2 I. \end{aligned} \quad (38)$$

Consider \bar{R} , the average of R_x and R_y ,

$$\bar{R} = \frac{1}{2}(R_x + R_y). \quad (39)$$

\bar{R} can be written

$$\bar{R} = \bar{R}_0 + \sigma^2 I \quad (40)$$

where

$$\bar{R}_0 = \bar{A}_{L_s} \bar{R}_s \bar{A}_{L_s}^H \quad (41)$$

with \bar{R}_s defined as

$$\bar{R}_s = \frac{1}{2}(\Phi_x R_s \Phi_x^H + \Phi_y R_s \Phi_y^H) \quad (42)$$

$$= \frac{1}{2}[\Phi_x \mid \Phi_y] \begin{bmatrix} R_s & 0 \\ 0 & R_s \end{bmatrix} [\Phi_x^H \mid \Phi_y^H]. \quad (43)$$

As long as the incident signals are at most partially correlated, R_s is nonsingular. Since by assumption none of the incident signals produces zero output on both the x and y axis dipoles at the same time, $[\Phi_x \mid \Phi_y]$ is of rank K . Thus \bar{R}_s is nonsingular and the eigenvectors of \bar{R}_0 that correspond to the K largest eigenvalues of \bar{R}_0 span the same signal subspace as

the column vectors in \bar{A}_{L_s} . For this case, the ESPRIT algorithm can be applied to \bar{R} for direction estimation.

For coherent signals, however, (43) becomes

$$\bar{R}_s = \frac{1}{2}[\Phi_x \mid \Phi_y][\Phi_x \mid \Phi_y]^H \quad (44)$$

in which case the rank of \bar{R}_s is at most 2. Thus the coherent signals must first be "decorrelated" before the ESPRIT algorithm can be applied.

The first method of decorrelating the signals is the FO spatial smoothing technique of [7, 8]. We apply this method to the averaged covariance matrix \bar{R} in (39). In the curves below, we call this composite method the *alternative forward-only* (AFO) method.

In this method, the total array of L elements is divided into L_0 overlapping subarrays with $L_s = L - L_0 + 1$ elements in each subarray. Let $x_l^f(t)$ denote the column vector of the x axis dipole signals in the l th subarray,

$$\begin{aligned} x_l^f(t) &= [x_l(t) \ x_{l+1}(t) \ \dots \ x_{l+L_s-1}(t)]^T, \\ 1 \leq l \leq L_0 \end{aligned} \quad (45)$$

and let $y_l^f(t)$ denote the column vector of the y axis dipole signals in the l th subarray,

$$\begin{aligned} y_l^f(t) &= [y_l(t) \ y_{l+1}(t) \ \dots \ y_{l+L_s-1}(t)]^T, \\ 1 \leq l \leq L_0. \end{aligned} \quad (46)$$

Then let \bar{R}_l^f be the average of the covariance matrices of $x_l^f(t)$ and $y_l^f(t)$,

$$\bar{R}_l^f = \frac{1}{2}E\{x_l^f(t)[x_l^f(t)]^H + y_l^f(t)[y_l^f(t)]^H\}. \quad (47)$$

The AFO spatially smoothed covariance matrix \bar{R}^f is the average of \bar{R}_l^f :

$$\bar{R}^f = \frac{1}{L_0} \sum_{l=1}^{L_0} \bar{R}_l^f. \quad (48)$$

\bar{R}^f can be written

$$\bar{R}^f = \bar{R}_0^f + \sigma^2 I \quad (49)$$

where

$$\bar{R}_0^f = \bar{A}_{L_s} \bar{R}_s^f \bar{A}_{L_s}^H \quad (50)$$

with \bar{R}_s^f denoting the AFO spatially smoothed *source* covariance matrix

$$\begin{aligned} \bar{R}_s^f &= \frac{1}{2L_0} \sum_{l=1}^{L_0} [\Phi_x \Phi_q^{l-1} R_s (\Phi_q^{l-1})^H \Phi_x^H \\ &\quad + \Phi_y \Phi_q^{l-1} R_s (\Phi_q^{l-1})^H \Phi_y^H]. \end{aligned} \quad (51)$$

By using (26)–(27), \bar{R}_s^f can be written

$$\begin{aligned} \bar{R}_s^f &= \frac{1}{2L_0} [\Phi_x C C^H \Phi_x^H + \Phi_y C C^H \Phi_y^H] \\ &= \frac{1}{2L_0} C_1 C_1^H \end{aligned} \quad (52)$$

where (see (28))

$$\begin{aligned} C_1 &= [\Phi_x C | \Phi_y C] \\ &= [\Phi_x G \bar{A}_{L_0}^T | \Phi_y G \bar{A}_{L_0}^T] \\ &= G[\Phi_x \bar{A}_{L_0}^T | \Phi_y \bar{A}_{L_0}^T]. \end{aligned} \quad (53)$$

The last equality holds because G , Φ_x , and Φ_y are diagonal matrices.

The minimum number of subarrays L_0 required to make \bar{R}_s^f nonsingular is between $K/2$ and K depending on the signal scenario. On the one hand, suppose all incident signals are linearly polarized so there is no output on the y axis dipoles. Since by assumption none of the signals produces zero output on both the x and y axis dipoles at the same time, the diagonal elements of Φ_x are then nonzero. For \bar{R}_s^f to be nonsingular in this case, we must have $L_0 \geq K$. On the other hand, assume K is even and suppose $K/2$ signals produce zero outputs on the x axis dipoles and the other $K/2$ signals produce zero outputs on the y axis dipoles. In this case we must have $L_0 \geq K/2$ for \bar{R}_s^f to be nonsingular.

The second method for decorrelating the signals is the forward/backward spatial smoothing technique of [9, 10]. In the curves below, we label this method, when used with the averaged covariance matrix \bar{R} in (39), the *alternative forward/backward* (AFB) method.

The AFB spatially smoothed array covariance matrix $\bar{R}^{f/b}$ is defined as [9, 10]

$$\bar{R}^{f/b} = \frac{1}{2}[\bar{R}^f + J(\bar{R}^f)^* J] \quad (54)$$

where \bar{R}^f is defined in (48), superscript $*$ denotes complex conjugate, and J is the exchange matrix

$$J = \begin{bmatrix} 0 & \dots & 0 & 1 \\ 0 & \dots & 1 & 0 \\ \vdots & & \vdots & \vdots \\ 1 & \dots & 0 & 0 \end{bmatrix}. \quad (55)$$

From (49), we have

$$J(\bar{R}^f)^* J = J(\bar{R}_0^f + \sigma^2 I)^* J = J(\bar{R}_0^f)^* J + \sigma^2 I. \quad (56)$$

Then using the relation

$$\bar{A}_{L_0}^T J = \Phi_q^{(L_0-1)} \bar{A}_{L_0}^H \quad (57)$$

we have from (50)

$$\begin{aligned} J(\bar{R}^f)^* J &= J(\bar{A}_{L_0} \bar{R}_s^f \bar{A}_{L_0}^H)^* J \\ &= \bar{A}_{L_0} \Phi_q^{-(L_0-1)} (\bar{R}_s^f)^* [\Phi_q^{(L_0-1)}]^H \bar{A}_{L_0}^H. \end{aligned} \quad (58)$$

Therefore $\bar{R}^{f/b}$ can be written as

$$\bar{R}^{f/b} = \bar{R}_0^{f/b} + \sigma^2 I \quad (59)$$

where

$$\bar{R}_0^{f/b} = \bar{A}_{L_0} \bar{R}_s^{f/b} \bar{A}_{L_0}^H \quad (60)$$

and $\bar{R}_s^{f/b}$ denotes the AFB spatially smoothed source covariance matrix

$$\bar{R}_s^{f/b} = \frac{1}{2}[\bar{R}_s^f + \Phi_q^{-(L_0-1)} (\bar{R}_s^f)^* [\Phi_q^{(L_0-1)}]^H]. \quad (61)$$

Furthermore, from (52) we have

$$\begin{aligned} \bar{R}_s^{f/b} &= \frac{1}{4L_0} [C_1 C_1^H + \Phi_q^{-(L_0-1)} C_1^T C_1^T [\Phi_q^{(L_0-1)}]^H] \\ &= \frac{1}{4L_0} [C_1 C_1^H + \Phi_q^{-(L_0-1)} C_1^T J J^H C_1^T [\Phi_q^{(L_0-1)}]^H] \\ &= \frac{1}{4L_0} C_2 C_2^H \end{aligned} \quad (62)$$

where we have used $J J^H = I$ and defined

$$C_2 = [C_1 | \Phi_q^{-(L_0-1)} C_1^T J]. \quad (63)$$

Next, using (53), we have

$$\begin{aligned} C_2 &= [G \Phi_x \bar{A}_{L_0}^T | G \Phi_y \bar{A}_{L_0}^T | \Phi_q^{-(L_0-1)} \\ &\quad \times G^* \Phi_x^* \bar{A}_{L_0}^H J | \Phi_q^{-(L_0-1)} G^* \Phi_y^* \bar{A}_{L_0}^H J] \\ &= [G \Phi_x \bar{A}_{L_0}^T | G \Phi_y \bar{A}_{L_0}^T | G^* \Phi_x^* \Phi_q^{-(L_0-1)} \\ &\quad \times \bar{A}_{L_0}^T | G^* \Phi_y^* \Phi_q^{-(L_0-1)} \bar{A}_{L_0}^T] \end{aligned} \quad (64)$$

where we have used (57) with L_s replaced by L_0 and $L = L_s + L_0 - 1$. C_2 may then be written as

$$\begin{aligned} C_2 &= G[\Phi_x \bar{A}_{L_0}^T | \Phi_y \bar{A}_{L_0}^T | \Phi_q^{-(L_0-1)} G^* G^{-1} \\ &\quad \times \Phi_q^{-(L_0-1)} \bar{A}_{L_0}^T | \Phi_q^{-(L_0-1)} G^* G^{-1} \Phi_q^{-(L_0-1)} \bar{A}_{L_0}^T] \\ &= G[\Phi_x \bar{A}_{L_0}^T | \Phi_y \bar{A}_{L_0}^T | \Phi_q^* H \bar{A}_{L_0}^T | \Phi_q^* H \bar{A}_{L_0}^T] \end{aligned} \quad (65)$$

where H is the diagonal matrix

$$H = G^* G^{-1} \Phi_q^{-(L_0-1)} \quad (66)$$

$$= \text{diag}\{h_1, h_2, \dots, h_K\} \quad (67)$$

with

$$h_k = \frac{g_k^* q_k^{-(L_0-1)}}{g_k}, \quad k = 1, 2, \dots, K. \quad (68)$$

For $\bar{R}_s^{f/b}$ to be nonsingular, the minimum number of subarrays L_0 required is between $K/4$ and K , depending on the signal scenario. Each of the submatrices $\Phi_x \bar{A}_{L_0}^T$, $\Phi_y \bar{A}_{L_0}^T$, $\Phi_q^* H \bar{A}_{L_0}^T$, and $\Phi_q^* H \bar{A}_{L_0}^T$, is a $K \times L_0$ matrix. To make C_2 have rank K , there must be K independent column vectors somewhere in the set of these four submatrices. For most combinations of signals, C_2 will be full rank if $L_0 = K/4$, i.e., so there are $K/4$ columns in each of the submatrices in (65). Usually these $K/4$ columns in each submatrix will be linearly independent of each other, so C_2 will

have rank K . However, for certain specific choices of signal parameters, some of these columns will be linearly dependent, in which case L_0 will need to be larger than $K/4$. Choosing $L_0 = K$, however, is always sufficient to make C_2 full rank, because then each of the four submatrices in (65) has rank K , regardless of the signal parameters.

V. SIMULATION RESULTS

We now show several examples illustrating the use of these techniques with coherent signals. The results below were obtained by using fifty Monte Carlo trials. The array consisted of $L = 10$ pairs of crossed dipoles. All incident signals were assumed to have the same unit amplitude E_k . The signal-to-noise ratio (SNR) shown in the figures is defined as $-10\log_{10}\sigma^2$ dB. A finite number of data samples N was taken at each dipole output. The subarray covariance matrices were estimated from the available data samples, as described in [4] and [5]. The spatially smoothed covariance matrices were obtained from the subarray covariance matrix estimates.

We first show an example that illustrates how the results for spatial smoothing with coherent signals compare with those using the method in [5] with partially correlated signals and no spatial smoothing. We consider an example with 7 coherent signals. The SNR for each signal is 20 dB and the number of data samples is $N = 200$. The number of incident signals is assumed known in the estimator. The direction of arrival estimates are computed by using the AFB technique. Two subarrays ($L_0 = 2$) of 9 elements ($L_s = 9$) are used. Fig. 4 shows the direction estimates obtained with each of the 50 independent trials plotted on a unit circle at those angles from the center of the circle. The 50 estimates of the angles are superimposed on the same plot, so the spread in angles can be seen. Fig. 4(a) shows the results when the signals arrive from equally spaced angles every 20° between -55° and 65° . The corresponding ellipticity angles are also equally spaced between -45° and 45° and the orientation angles are zero. Fig. 4(b) shows the results for a smaller separation between signals, every 11.5° between -29.5° and 39.5° and for the same polarizations. As may be seen, the estimation accuracy is poor when the signals are spaced every 11.5° . The reason is that when the angles are closer the direction matrix \bar{A}_L is becoming ill-conditioned. This example illustrates the resolution limits for this technique as the 7 arrival angles approach one another.

Next, for comparison, Fig. 5 shows the corresponding results when 7 partially correlated signals are incident and the technique of [5] is used, i.e., there is no spatial smoothing. The other parameters of the signals are the same as for Fig. 4. In this case, an array of 9 elements is used, to make the results comparable to those in Fig. 4. Fig. 5(a)

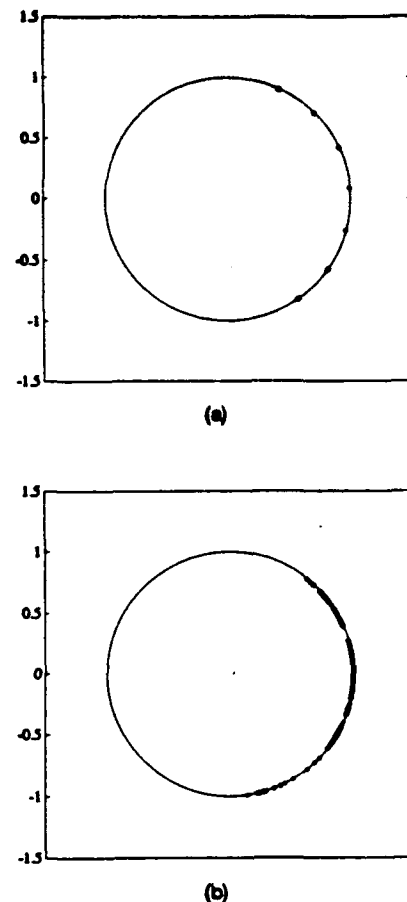
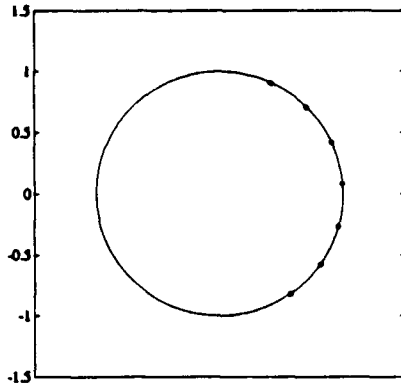


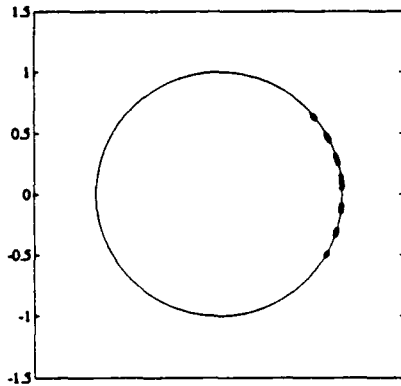
Fig. 4. Direction estimates of 7 coherent signals obtained with AFB method with $L = 10$, SNR = 20 dB, $N = 200$, $L_0 = 2$, orientation angles zero, ellipticity angles equally spaced between -45° and 45° . (a) Signals arrive from equally spaced angles every 20° between -55° and 65° . (b) Signals arrive from equally spaced angles every 11.5° between -29.5° and 39.5° .

shows the results when the signals are evenly spaced from -55° to 65° , and Fig. 5(b) shows them when they are spaced from -29.5° to 39.5° . Note that the results in Figs. 4(a) and 5(a) are similar, but with the signals more closely spaced, the results in Fig. 5(b) are much better than those in Fig. 4(b).

This example illustrates that the resolution of the AFB technique for coherent arrivals is poorer than what can be achieved with partially correlated signals. This drop in performance occurs because the full rank spatially smoothed matrix $\bar{R}_s^{f/b}$ for coherent sources is different from the full rank source covariance matrix R_s for noncoherent sources. The numerical condition of R_s for noncoherent sources is determined by how strongly the sources are correlated, but not by the arrival directions. The numerical condition of $\bar{R}_s^{f/b}$, on the other hand, is determined by how closely the arrival angles are spaced, as can be seen from (62) and (65). Note that $\bar{R}_s^{f/b}$ depends on \bar{A}_{L_s} , which is a function of the arrival angles. As the arrival angles become more closely-spaced, the columns of \bar{A}_{L_s}



(a)



(b)

Fig. 5. Direction estimates of 7 noncoherent signals obtained with the method in [5] with $L = 10$, $\text{SNR} = 20$ dB, $N = 200$, orientation angles zero, ellipticity angles equally spaced between -45° and 45° . (a) Signals arrive from equally spaced angles every 20° between -55° and 65° . (b) Signals arrive from equally spaced angles every 11.5° between -29.5° and 39.5° .

become more nearly linearly dependent, and $\bar{\mathbf{R}}_s^{f/b}$ becomes more ill conditioned. Moreover, as the coherent arrivals become more closely spaced, $\bar{\mathbf{R}}_0^{f/b}$ in (60) becomes more ill-conditioned because both $\bar{\mathbf{A}}_L$ and $\bar{\mathbf{R}}_s^{f/b}$ become ill-conditioned. For partially correlated signals, the ill-conditioning is less serious because only $\bar{\mathbf{A}}_L$ in $\bar{\mathbf{R}}_0$ of (17) becomes ill-conditioned. The more ill-conditioned $\bar{\mathbf{R}}_0^{f/b}$ or $\bar{\mathbf{R}}_0$, the more sensitive the matrix is to noise perturbation [13]. (These comments apply to the FO and AFO spatial smoothing techniques as well.)

We next show the error performance of these spatial smoothing techniques with coherent signals. For the next three examples, we use $N = 31$ data samples.

First, we consider a case where three identical signals arrive from 20° , 25° , and 30° . The corresponding ellipticity angles are 45° , 40° , and 35° , respectively, and the orientation angles are zero. For this case, the signal directions are closely spaced and the signal polarizations are similar. Fig. 6(a) shows the direction estimate error variances (in dB with respect

to degrees squared) for the first signal and for the FO, AFO, and AFB approaches as functions of the SNR when $L_0 = 3$. Fig. 6(b) shows the variance of the polarization estimates for the FO approach for the first signal. These curves were obtained by assuming that the number of incident signals is known. The variance of the polarization estimates in Fig. 6(b) is defined as the mean-squared value of the angular distance ζ on the Poincaré sphere between \mathbf{M} and $\hat{\mathbf{M}}$, the points representing the actual and estimated polarizations (γ, η) and $(\hat{\gamma}, \hat{\eta})$, respectively, as described in [4], where

$$\cos \zeta = \cos 2\gamma \cos 2\hat{\gamma} + \sin 2\gamma \sin 2\hat{\gamma} \cos(\eta - \hat{\eta}) \quad (69)$$

with ζ in the range $0 \leq \zeta \leq \pi$.

When the number of incident signals is unknown, we also used the minimum description length (MDL) criterion [14, 15] with the spatially smoothed covariance matrix to estimate the number of incident signals. Fig. 6(c) shows the probability that the correct number was obtained as a function of the SNR for each of the three methods.

Next, we consider an example where three identical signals arrive from $(25 - \Delta\theta)^\circ$, 25° , and $(25 + \Delta\theta)^\circ$, so $\Delta\theta$ is the angle separation between two adjacent angles. The corresponding ellipticity angles are 45° , 40° , and 35° , respectively, and the orientation angles are zero. The SNR per signal is 20 dB. Fig. 7 shows the error variances and the probability of estimating the number of signals correctly for the FO, AFO, and AFB approaches as a function of $\Delta\theta$ when $L_0 = 3$.

Finally, we consider an example where three identical signals arrive from 13° , 25° , and 37° . The corresponding ellipticity angles are 45° , $(45 - \Delta\alpha)^\circ$, and $(45 - 2\Delta\alpha)^\circ$ and the orientation angles are zero, so $\Delta\alpha$ is the polarization separation between adjacent signals. The SNR per signal is again 20 dB. Fig. 8 shows the performance of the FO, AFO, and AFB approaches as a function of $\Delta\alpha$ when $L_0 = 3$.

Figs. 6, 7, and 8 show that the AFO approach yields better performance in estimating both the signal directions and the number of incident signals than the FO approach. Note that the signal subspace dimension in the FO approach is twice as much as the dimension in the AFO approach, but the number of averaging subarrays is half as much. Thus these figures show that better results may be obtained by trading the signal subspace dimension for a larger number of averaging subarrays.

From Figs. 6, 7 and 8, we note also that using the AFB approach yields much better performance in estimating both the signal directions and the number of incident signals than the FO approaches do. The reason for this may be seen by comparing the AFO and AFB approaches. Using the forward/backward approach results in two extra submatrices in \mathbf{C}_2 , as may be seen by comparing (65) with (53). The extra

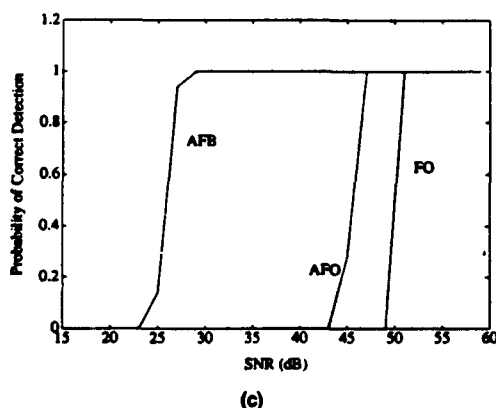
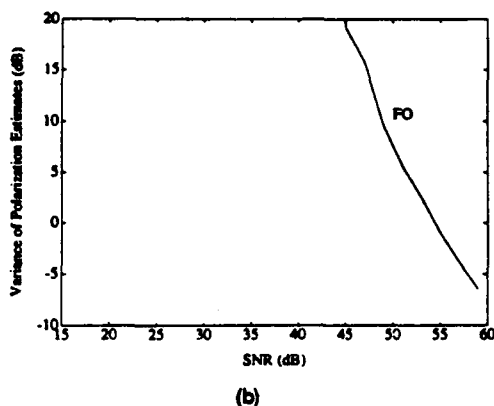
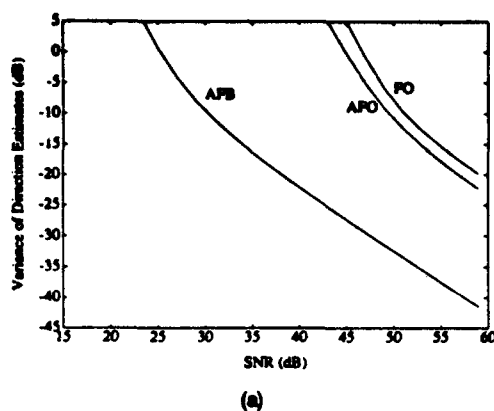


Fig. 6. Performance of FO, AFO, AFB methods versus SNR for 3 identical signals arriving from 20° , 25° , and 30° with $L = 10$, $N = 31$, $L_0 = 3$, orientation angles zero, ellipticity angles 45° , 40° , and 35° , respectively. (a) Variance of direction estimates. (b) Variance of polarization estimates. (c) Probability of correct detection.

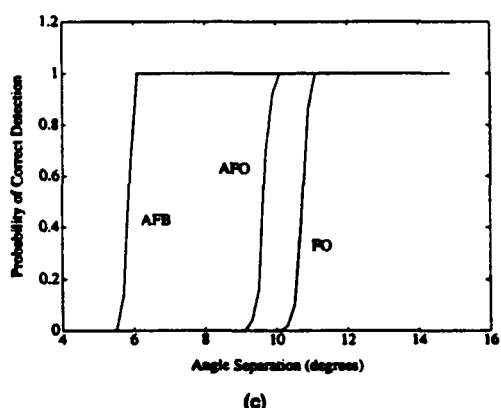
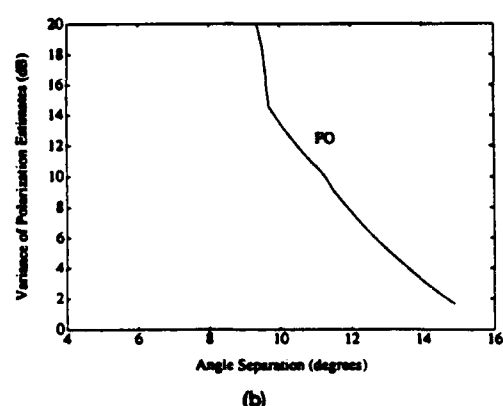
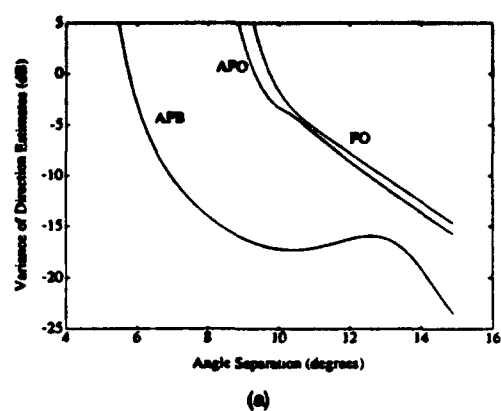


Fig. 7. Performance of FO, AFO, AFB methods versus $\Delta\theta$ for 3 identical signals arriving from $(25 - \Delta\theta)^\circ$, 25° , and $(25 + \Delta\theta)^\circ$ with $L = 10$, $N = 31$, SNR = 20 dB, $L_0 = 3$, orientation angles zero, ellipticity angles 45° , 40° , and 35° , respectively. (a) Variance of direction estimates. (b) Variance of polarization estimates. (c) Probability of correct detection.

submatrices reduce the ill-conditioning of $\bar{\mathbf{R}}_s^{f/b}$ when the signal directions are closely spaced.

VI. CONCLUSIONS

We have described how a uniform linear array of crossed dipoles may be used with the ESPRIT algorithm and spatial smoothing to estimate the directions and polarizations of arbitrarily polarized

coherent signals. We have shown that the FO spatial smoothing approach may be used to estimate both signal directions and polarizations. The forward/backward spatial smoothing approach may be used to estimate signal directions only. Both smoothing approaches may be used to estimate the number of incident signals. Some examples showing typical results were presented. It is found that spatial smoothing yields poorer resolution for coherent

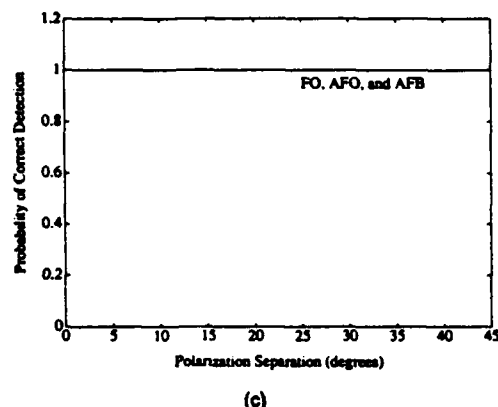
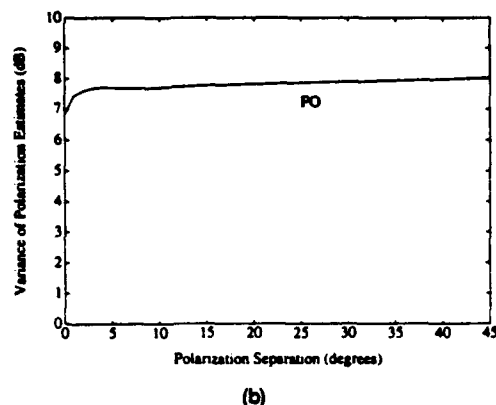
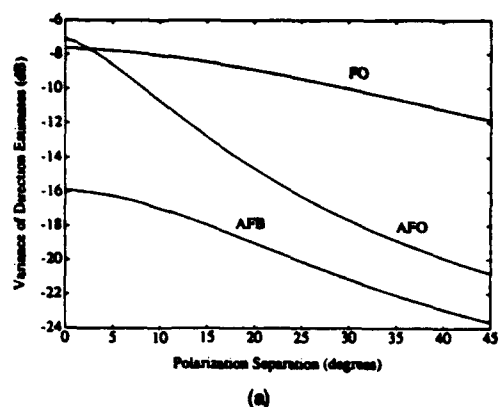


Fig. 8. Performance of FO, AFO, AFB methods versus $\Delta\alpha$ for 3 identical signals arriving from 13° , 25° , and 37° with $L = 10$, $N = 31$, $\text{SNR} = 20$ dB, $L_0 = 3$, orientation angles zero, ellipticity angles 45° , $(45 - \Delta\alpha)^\circ$, and $(45 - 2\Delta\alpha)^\circ$, respectively.
(a) Variance of direction estimates. (b) Variance of polarization estimates. (c) Probability of correct detection.

signals than would be obtained with uncorrelated or partially correlated signals, but of course without spatial smoothing ESPRIT cannot be used at all with coherent sources. The results also show that the forward/backward spatial smoothing approach yields much better performance in estimating both the signal directions and the number of incident signals than the FO approaches do.

REFERENCES

- [1] Roy, R., Paulraj, A., and Kailath, T. (1986) ESPRIT—A subspace rotation approach to estimation of parameters of cisoids in noise. *IEEE Transactions on Acoustics, Speech and Signal Processing*, ASSP-34 (Oct. 1986), 1340–1342.
- [2] Roy, R., and Kailath, T. (1989) ESPRIT—Estimation of signal parameters via rotational invariance techniques. *IEEE Transactions on Acoustics, Speech and Signal Processing*, ASSP-37 (July 1989), 984–995.
- [3] Schmidt, R. O. (1986) Multiple emitter location and signal parameter estimation. *IEEE Transactions on Antennas and Propagation*, AP-34 (Mar. 1986), 276–280.
- [4] Li, J., and Compton, Jr., R. T. (1991) Angle and polarization estimation using ESPRIT with a polarization sensitive array. *IEEE Transactions on Antennas and Propagation*, 39 (Sept. 1991), 1376–1383.
- [5] Li, J., and Compton, Jr., R. T. (1991) Angle estimation using a polarization sensitive array. *IEEE Transactions on Antennas and Propagation*, 39 (Sept. 1991), 1539–1542.
- [6] Evans, J. E., Johnson, J. R., and Sun, D. F. (1982) Applications of advanced signal processing techniques to angle of arrival estimation in ATC navigation and surveillance systems. MIT Lincoln Lab., Technical Report, Lexington, MA, Nov. 1982.
- [7] Shan, T., and Kailath, T. (1986) Adaptive beamforming for coherent signals and interference. *IEEE Transactions on Acoustics, Speech and Signal Processing*, ASSP-33, (June 1986), 527–536.
- [8] Shan, T., Wax, M., and Kailath, T. (1985) On spatial smoothing for direction-of-arrival estimation of coherent signals. *IEEE Transactions on Acoustics, Speech and Signal Processing*, ASSP-33 (Aug. 1985), 806–811.
- [9] Williams, R. T., Prasad, S., Mahalanabis, A. K., and Sibul, L. H. (1988) An improved spatial smoothing technique for bearing estimation in a multipath environment. *IEEE Transactions on Acoustics, Speech and Signal Processing*, ASSP-36 (Apr. 1988), 425–432.
- [10] Pillai, S. U., and Kwon, B. H. (1989) Forward/backward spatial smoothing techniques for coherent signal identification. *IEEE Transactions on Acoustics, Speech and Signal Processing*, ASSP-37 (Jan. 1989), 8–15.
- [11] Balanis, C. A. (1982) *Antenna Theory—Analysis and Design*. New York: Harper & Row Publishers, Inc., 1982.
- [12] Dechamps, G. A. (1951) Geometrical representation of the polarization of a plane electromagnetic wave. *Proceedings of the IRE*, 39 (May 1951), 540–544.
- [13] Stewart, G. W. (1973) *Introduction to Matrix Computations*. New York: Academic Press, 1973.
- [14] Wax, M., and Kailath, T. (1985) Detection of signals by information theoretic criteria. *IEEE Transactions on Acoustics, Speech and Signal Processing*, ASSP-33 (Apr. 1985), 387–392.
- [15] Shan, T., Paulraj, A., and Kailath, T. (1987) On smoothed rank profile tests in eigenstructure methods for direction-of-arrival estimation. *IEEE Transactions on Acoustics, Speech and Signal Processing*, ASSP-35 (Oct. 1987), 1377–1385.



Jian Li (S'87—M'91) was born on April 17, 1965. She received the M.Sc. and Ph.D. degrees in electrical engineering from The Ohio State University, Columbus, in 1987 and 1991, respectively.

From April 1991 to June 1991, she was an Adjunct Assistant Professor with the Department of Electrical Engineering, The Ohio State University, Columbus. Since July 1991, she has been an Assistant Professor with the Department of Electrical Engineering, University of Kentucky, Lexington. Her current research interests include sensor array signal processing, spectral estimation, and communications.

Dr. Li is a member of Sigma Xi and Phi Kappa Phi.



R. T. Compton, Jr. (F'84) was born in St. Louis, MO, in 1935. He received the S.B. degree from Massachusetts Institute of Technology, Cambridge, in 1958, and the M.Sc. and Ph.D. degrees from The Ohio State University, Columbus, in 1961 and 1964, all in electrical engineering.

Dr. Compton was an Assistant Professor of Engineering at Case Institute of Technology, Cleveland, OH, from 1965 to 1967, and an NSF Postdoctoral Fellow at the Technische Hochschule, Munich, Germany, from 1967 to 1968. From 1968 to 1991, he was with The Ohio State University as an Associate Professor and then as Professor of Electrical Engineering. Since 1992, he has been working as a Consultant under the name Compton Research, Inc.

Dr. Compton is a member of Sigma Xi and Pi Mu Epsilon. In 1983 he received the M. Barry Carlton Award for best paper from the IEEE Aerospace and Electronic Systems Society.

A proof of the Woodward-Lawson sampling method for a finite linear array

Gary A. Somers

The Ohio State University ElectroScience Laboratory, Department of Electrical Engineering, Columbus, Ohio

(Received October 21, 1991; revised February 25, 1993; accepted February 25, 1993.)

An extension of the continuous aperture Woodward-Lawson sampling theorem has been developed for a finite linear array of equidistant identical elements with arbitrary excitations. It is shown that by sampling the array factor at a finite number of specified points in the far field, the exact array factor over all space can be efficiently reconstructed in closed form. The specified sample points lie in real space and hence are measurable provided that the interelement spacing is greater than approximately one half of a wavelength. This paper provides insight as to why the length parameter used in the sampling formulas for discrete arrays is larger than the physical span of the lattice points in contrast with the continuous aperture case where the length parameter is precisely the physical aperture length.

1. INTRODUCTION

In a pair of classic papers, *Woodward and Lawson* [1948] and *Woodward* [1946], a very popular technique was developed for synthesizing finite continuous aperture excitations given a finite number of (far field) samples. The Woodward-Lawson technique implements an aperture excitation that is formed by summing a finite number of uniform amplitude linear phase distributions. *Woodward and Lawson* [1948] hinted at extending this technique to linear arrays of discrete elements. Their expressions for the continuous aperture case contain a parameter which corresponds to the length of the continuous aperture. This length parameter was incorrectly assumed to be the physical length of the discrete array in *Balanis* [1982], while *Stutzman and Thiele* [1981] used the correct length which extends past the physical array lattice points by one half of the interelement spacing on both ends of the array.

In this paper the extension of the Woodward-Lawson sampling method for finite linear arrays is formally proven using a technique that highlights the reasons for the length disparity between the continuous aperture and the discrete aperture cases. The far fields of a linear array are determined exactly by sampling the far field at a minimal number of predetermined locations. This method efficiently reconstructs the far field in closed form

without the need to solve simultaneous equations. A practical constraint of this technique is that the interelement spacing must be greater than or equal to one half of a wavelength for the sampled field points to lie in real space (at a real angle θ) if there are an even number of elements or the interelement spacing must be greater than a distance slightly smaller than a half of a wavelength if there are an odd number of elements. This restriction is significant and excludes an empirical application of this theory to some practical arrays. This practical constraint does not imply that any approximations have been made with regard to the sampling analysis; it is exact. An $\exp j\omega t$ time dependence is assumed and suppressed throughout this paper.

2. ANALYTICAL FORMULATION

We are considering a linear array of $M + 1$ equally spaced elements that reside on the array lattice shown in Figure 1. It is assumed that the element pattern of each element is known and that it is the same for all elements which is equivalent to the typical assumption that the far fields of the linear array can be expressed as follows:

$$E(r) = EP(\theta, \phi) AF(\theta) \frac{\exp -jkr}{4\pi r} \quad (1)$$

where $E(r)$ is the electric far field, $EP(\theta, \phi)$ is the element pattern, and $AF(\theta)$ is the array factor which can be expressed by the well-known relationship

Copyright 1993 by the American Geophysical Union.

Paper number 93RS00591.
0048-6604/93/93RS-00591\$08.00

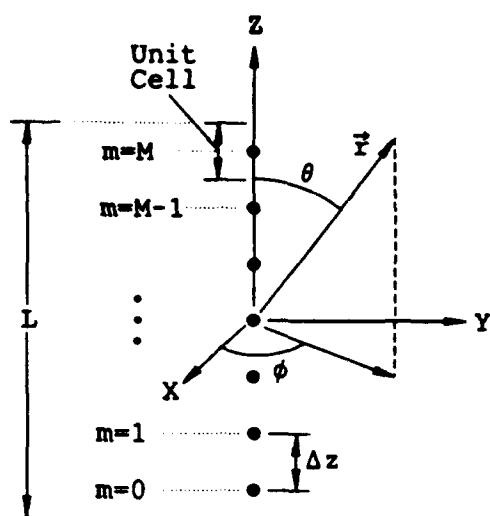


Fig. 1. Array lattice configuration.

$$AF(\theta) = \sum_{m=0}^M C_m \exp \left[-jk \hat{r} \cdot \hat{z} \left(m - \frac{M}{2} \right) \Delta z \right]$$

$$= \sum_{m=0}^M C_m \exp \left[-jk \cos(\theta) \left(m - \frac{M}{2} \right) \Delta z \right]. \quad (2)$$

C_m is the complex amplitude of the m th element, M is the index corresponding to the $M + 1$ th element, \hat{z} is the unit vector along the array axis, and Δz is the interelement spacing. The objective of this work is to efficiently determine $AF(\theta)$ from a finite minimal number of sampled far-field values, $AF(\theta_n)$, in which θ_n is specified.

2.1. Sampling theory development

Equation (2) shows that the array factor is space limited by $z = \pm(M \Delta z/2)$ and that C_m are Fourier series coefficients of $AF(\theta)$ [Bucci and France-

schetti, 1987]. It is noted that C_m is defined in configuration space, whereas $AF(\theta)$ is defined in $\cos(\theta)$ space. This allows Shannon's sampling theorem [Peebles, 1976] to be applied in $\cos(\theta)$ space resulting in the following representation for $AF(\theta)$:

$$AF(\theta) = \sum_{n=-\infty}^{\infty} AF(\theta_n) \frac{\sin \left(\frac{kL \cos(\theta)}{2} - n\pi \right)}{\frac{kL \cos(\theta)}{2} - n\pi}, \quad (3)$$

where

$$\theta_n = \cos^{-1} \left(\frac{n\lambda}{L} \right), \quad (4)$$

and L is the length parameter of the array which must be determined. Shannon's sampling theorem dictates that the field must be sampled in $\cos(\theta)$ space at intervals equal to or less than $\lambda/(\text{length of array})$, which is the Nyquist rate. An exception to this rule occurs if there are delta function excitations at the endpoints of the interval in the band-limited domain (configuration space) [Peebles, 1976], which is the case here since the array is composed of a collection of point sources. The sampling theorem is obtained by repeating the finite (physical) band of elements in configuration space so that the array is periodic (and infinite) (see Figure 2). The far-field pattern in $\cos \theta$ space is low-pass filtered to allow only the original spatial bandwidth (i.e., the physical length L_p) to contribute to the array factor $AF(\theta)$. The length parameter L dictates the distance between the repeating finite bands of elements. If the length parameter equals the physical length of the array, then the first and last elements of the adjacent arrays are coincident, and information is lost. This is the onset of aliasing. The concept of the unit cell was introduced to define the

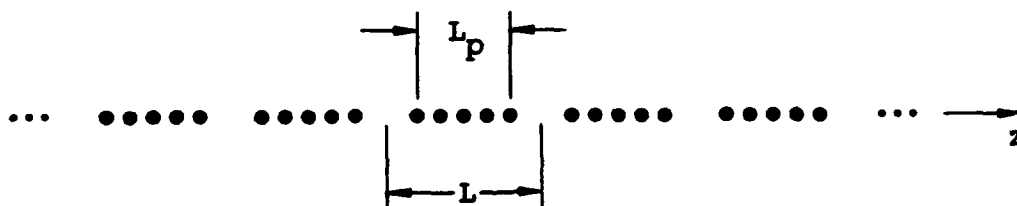


Fig. 2. Example of a five-element array in configuration space after the original array has been repeated. The physical length is given by L_p , and the length parameter is given by L .

length parameter L so that the delta function excitations are no longer at the edges of the band; thus the Nyquist rate can be used without introducing aliasing problems. Each unit cell is defined to consist of a line segment of length Δz which has the radiating element at its center. The unit cell ensures that a source-free region surrounds each array element which serves to artificially extend the array endpoints by half a unit cell (or $\Delta z/2$) beyond the physical dimensions of the array. In other words, if the array is considered to be longer on both the top and the bottom (in this case by $\Delta z/2$, half the unit cell), then the radiating elements do not lie on either of the endpoints of the array, and, consequently, the Nyquist rate can be applied. L is defined to be the total distance spanned by all of the unit cells as shown in Figure 1.

Equation (4) shows that the field is sampled at λ/L intervals in $\cos(\theta)$ space. Geometrically, it is seen that

$$L = (M + 1)\Delta z \quad (5)$$

or

$$\frac{\lambda}{\Delta z} = (M + 1) \frac{\lambda}{L} \quad (6)$$

By examining (2), it is clear that $AF(\theta)$ is periodic in $\cos(\theta)$ space with periodicity $\lambda/\Delta z$ which along with (6), implies the following recursion relationship:

$$AF(\theta_{n+M+1}) = AF(\theta_n) (-1)^M \quad (7)$$

This equation is a consequence of sampling at the Nyquist rate and defining the array boundaries to be extended past its physical boundary by $\Delta z/2$ on both ends of the array. Recognizing the identity in (7), (3) can be expressed as

$$AF(\theta) = \sum_{m=q}^{q+M} AF(\theta_m) \sum_{n=-\infty}^{\infty} \frac{(-1)^{nM} \sin\left(\frac{kL \cos(\theta)}{2} - (m + n(M+1))\pi\right)}{\frac{kL \cos(\theta)}{2} - (m + n(M+1))\pi} \quad (8)$$

or

$$AF(\theta) = \sin\left(\frac{kL \cos(\theta)}{2}\right) \sum_{m=q}^{q+M} AF(\theta_m) \sum_{n=-\infty}^{\infty} \frac{(-1)^{m+nM+n(M+1)}}{\frac{kL \cos(\theta)}{2} - (m + n(M+1))\pi} \quad (9)$$

Equation (9) shows that $AF(\theta)$ is determined by $M + 1$ complex samples and since the array has $M + 1$ complex excitations, we can conclude that this representation of $AF(\theta)$ uses a minimal number of samples. This is true because the number of degrees of freedom in the array, $2(M + 1)$, equals the number of independent field quantities sampled. The integer quantity q in the indices of the first summation determines the interval of m in which θ_m is sampled. The minimum practical interelement spacing is dictated by the condition that all the sampling angles must be real:

$$\frac{|m|_{\max} \lambda}{L} = \frac{|m|_{\max} \lambda}{(M + 1)\Delta z} \leq 1 \quad (10)$$

which is seen by examining (4). Since the value of q is arbitrary, we will choose q such that $|m|_{\max}$ remains as small as possible, thereby allowing the smallest possible interelement spacing Δz to be used. The sampling theorem remains valid for all interelement spacing and consequently for real and complex sampled angles. However, from a practical standpoint, it is not possible to physically measure a field value at a complex angle. For $|m|_{\max}$ to be minimal a good choice of q is

$$q = \begin{cases} -M/2; & M \text{ even,} \\ (1-M)/2; & M \text{ odd.} \end{cases} \quad (11)$$

with this choice of q , $|m|_{\max}$ is given by

$$|m|_{\max} = \begin{cases} M/2; & M \text{ even,} \\ (M+1)/2; & M \text{ odd.} \end{cases} \quad (12)$$

By substituting the above expression for $|m|_{\max}$ into (10), the lower bound of the interelement spacing

can be determined under the constraint that the sampled field points lie in real space:

$$\begin{aligned} \frac{\Delta z}{\lambda} &\geq \frac{M}{2(M+1)}; & M \text{ even,} \\ \frac{\Delta z}{\lambda} &\geq \frac{1}{2}; & M \text{ odd.} \end{aligned} \quad (13)$$

Equation (9) can be expressed as

$$AF(\theta) = \sin\left(\frac{kL \cos(\theta)}{2}\right) \sum_{m=q}^{q+M} AF(\theta_m) F(\theta; m, M; kL), \quad (14)$$

where $F(\theta; m, M; kL)$ is given by

$$F(\theta; m, M; kL) = \sum_{n=-\infty}^{\infty} \frac{(-1)^{m+n}}{\frac{kL \cos(\theta)}{2} - (m+n(M+1))\pi}. \quad (15)$$

Letting

$$w = \frac{1}{M+1} \left[\frac{kL \cos(\theta)}{2} - m\pi \right], \quad (16)$$

$F(\theta; m, M; kL)$ can be expressed as

$$F(\theta; m, M; kL) = \frac{(-1)^m}{M+1} \left(\sum_{n=-\infty}^{\infty} \frac{(-1)^n}{w - n\pi} \right). \quad (17)$$

Performing the following algebraic manipulation yields

$$F(\theta; m, M; kL) = \frac{(-1)^m}{M+1} \cdot \left(\sum_{n=-\infty}^{-1} \frac{(-1)^n}{w - n\pi} + \frac{1}{w} + \sum_{n=1}^{\infty} \frac{(-1)^n}{w - n\pi} \right) \quad (18)$$

$$F(\theta; m, M; kL) = \frac{(-1)^m}{M+1} \cdot \left(\frac{1}{w} + \sum_{n=1}^{\infty} \frac{(-1)^n}{w + n\pi} + \sum_{n=1}^{\infty} \frac{(-1)^n}{w - n\pi} \right) \quad (19)$$

$$F(\theta; m, M; kL) = \frac{(-1)^m}{M+1} \left(\frac{1}{w} + 2w \sum_{n=1}^{\infty} \frac{(-1)^n}{w^2 - n^2\pi^2} \right) \quad (20)$$

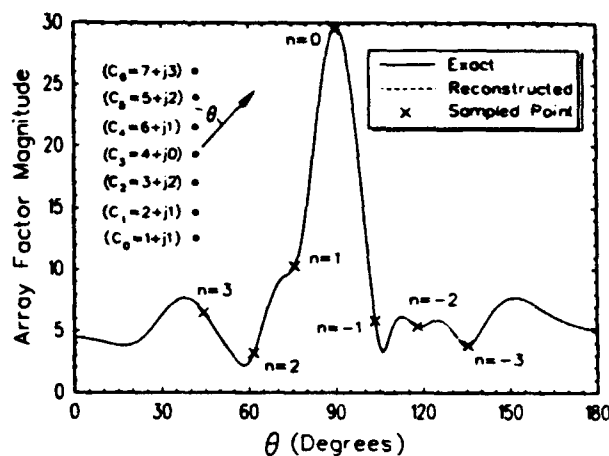


Fig. 3. Comparison of generated and reconstructed array factor data.

$$F(\theta; m, M; kL) = \frac{(-1)^m}{M+1} \csc(w) \quad (21)$$

Where the following identity was used [Abramowitz and Stegun, 1964],

$$\csc(z) = \frac{1}{z} + 2z \sum_{n=1}^{\infty} \frac{(-1)^n}{z^2 - n^2\pi^2}. \quad (22)$$

The array factor can be expressed in terms of the sampled values by substituting (21) into (14):

$$AF(\theta) = \frac{\sin\left(\frac{kL \cos(\theta)}{2}\right)}{M+1} \sum_{m=q}^{q+M} AF(\theta_m) (-1)^m \csc(w). \quad (23)$$

or

$$AF(\theta) = \sum_{m=q}^{q+M} AF(\theta_m) \frac{\sin\left(\frac{kL \cos(\theta)}{2} - m\pi\right)}{(M+1) \sin\left[\frac{1}{M+1} \left(\frac{kL \cos(\theta)}{2} - m\pi\right)\right]} \quad (24)$$

which is the Woodward-Lawson sampling theorem extended to handle the array case. Figure 3 shows a comparison between the "exact" data which is generated by substituting an interelement spacing of

$\Delta z = 0.6\lambda$, $M = 6$ (which indicates a seven-element array) and an assumed set of complex element excitations, C_m , into (2). The reconstructed data (dashed line) which are a result of substituting the sampled field points (which are indicated by crosses) into (24). Note that the two curves overlay and are indistinguishable.

To deal with the synthesis problem, one can determine the complex current excitations required to produce the array factor under the condition that the array factor is specified at the $M + 1$ sample angles θ_n , $n = 0, \dots, M$ [Stutzman and Thiele, 1982]:

$$I_m = \frac{1}{M+1} \sum_{n=0}^M AF(\theta_n) e^{-j2\pi n z_m/L} \quad (25)$$

or

$$I_m = \frac{1}{M+1} \sum_{n=0}^M AF(\theta_n) e^{-jk z_m \cos \theta_n}, \quad (26)$$

where I_m and z_m are the current and the position of the m th element, respectively, and L is the length parameter defined previously.

2.2. Limiting case: single element ($M = 0$)

The antenna sampling theorem is valid for an array of arbitrary size. In this section we shall confirm its validity by verifying the limiting case of a single element. If we apply (24) with $M = 0$ and use $q = 0$ as suggested by (11), then the array factor can be expressed as

$$AF(\theta) = AF(\theta_0) \quad (27)$$

where, by applying (4),

$$\theta_0 = \cos^{-1}(0) = \pi/2. \quad (28)$$

Equation (27) indicates that the array factor is isotropic which is what one would expect from a single element. Note that the sampling angle of $\pi/2$ is arbitrary since the orientation (array axis) of the "array" can be considered to be in any direction and the angle of $\pi/2$ is referenced to the array axis.

3. CONCLUSION

In this paper the Woodward-Lawson sampling method has been extended to deal with the case of

the far field of a finite array that has uniformly spaced identical elements with arbitrary excitation. Since there exists a Fourier series relationship between the array element domain and cosine space, and the array is spatially bounded, Shannon's sampling theorem was applied in cosine space. The length parameter of the array was defined so that the reconstructed array factor possesses recursive properties and avoids aliasing problems. The infinite number of sampling points and the array factor are periodic in cosine space which permits a simplification by which only a finite minimal number of sampled points are required to exactly reproduce the array factor. This proof provides insight as to why the length parameter of the array is larger than the physical span of the lattice points in contrast with the continuous aperture case in which the length parameter corresponds to the physical length of the aperture.

Acknowledgments. The author wishes to thank P. H. Pathak of The Ohio State University for his careful review of this paper and his comments. The author is also grateful to the reviewers for their valuable detailed suggestions. This work was supported in part by an Ohio Aerospace Institute/NASA Space Grant Doctoral Fellowship and in part by the Joint Services Electronics Program under contract N00014-89-J-1007.

REFERENCES

- Abramowitz, M., and I. A. Stegun, *Handbook of Mathematical Functions With Formulas, Graphs, and Mathematical Tables*, p. 75, NBS Appl. Math. Ser., 55, National Bureau of Standards, Gaithersburg, Md., 1964.
- Balanis, C. A., *Antenna Theory Analysis and Design*, pp. 676-678, Harper Collins, New York, 1982.
- Bucci, O. M., and G. Franceschetti, On the Spatial Bandwidth of Scattered Fields, *IEEE Trans. Antennas Propag.*, AP-35(12), 1445-1455, 1987.
- Peebles, P. Z., *Communication System Principles*, pp. 288-291, Addison-Wesley, Reading, Mass., 1976.
- Stutzman, W. L., and G. A. Thiele, *Antenna Theory and Design*, p. 534, John Wiley, New York, 1981.
- Woodward, P. M., A method for calculating the field over a plane aperture required to produce a given polar diagram, *J. IEE*, 93, Part IIIA, 1554-1558, 1946.
- Woodward, P. M., and J. D. Lawson, The theoretical precision with which an arbitrary radiation-pattern may be obtained from a source of finite extent, *J. IEE*, 95, Part II, 363-370, 1948.

G. A. Somers, The Ohio State University ElectroScience Laboratory, 1320 Kinnear Road, Columbus, OH 43212.

Maximum Likelihood Angle Estimation for Signals with Known Waveforms

Jian Li, *Member, IEEE*, and R. T. Compton, Jr., *Fellow, IEEE*

Abstract—We consider maximum likelihood estimation of the arrival angles of narrow-band plane waves when one or all signals have known waveforms. We present computationally efficient and rapidly converging algorithms that iteratively maximize the likelihood functions. We also obtain Cramer-Rao bounds for these estimators. Finally, we describe the conditions under which incorporating knowledge of one or all of the signal waveforms in the estimators improves the accuracy of the angle estimates.

I. INTRODUCTION

ALGORITHMS are needed for estimating the arrival angles of signals incident on an array of sensors when one or all signals have known waveforms but unknown gains or phases. For example, one such application occurs in some packet radio systems currently under study (for example, see [1]–[3]), in which each packet contains a known pseudonoise (PN) code [4] acquisition preamble. In these systems, an antenna array is used to estimate the packet arrival angles and then to separate colliding packets arriving from different angles. In unslotted packet radio systems, each packet arrives at the antenna array at an arbitrary time. For these systems, the preamble is used to distinguish the newly arrived packet from other packets that arrive earlier or later. The newly arrived packet is the signal of interest and is the desired signal. Because of the acquisition code, the desired packet waveform is known, but not its exact amplitude or phase. Other packets that arrive around the same time are considered interfering signals. In unslotted packet radio systems, the waveforms of the interfering signals are best modeled as unknown. In slotted packet radio systems, however, all the incident signals have known waveforms. This difference is due to the timing of the packets. In slotted systems, all packets start at essentially the same time, at the beginning of a time slot. With the packets aligned in time, the presence of the known preambles means that each packet waveform

is known (except for an unknown amplitude or phase). In either case, when only the desired signal waveform is known or when all the signal waveforms are known, these waveforms may be incorporated into the process of obtaining the direction estimates of the packets.

Few existing angle estimation techniques make any use of the signal waveforms. Recent techniques such as those due to Böhme [5], Bresler and Macovski [6], Ziskind and Wax [7], Schmidt [8] and Roy Kailath [9] are examples of what are called conditional and unconditional angle estimators by Stoica and Nehorai [10]. In these estimators, the incident signals are assumed to be either unknown deterministic signals or Gaussian random processes with unknown correlations. The estimate maximize (EM) algorithm presented by Feder and Weinstein [11] is an exception. The EM algorithm is a method of splitting the search for the maximum likelihood (ML) estimate into a set of parallel searches. The case of signals with known waveforms is considered in [11] but is not explored fully. Miller and Fuhrmann [12] also described a generalized EM algorithm that is intended primarily for the case of unknown signal waveforms. They also briefly consider signals with known waveforms and unknown gains, but they do not explore this case fully, either.

In this paper, we consider the angle estimation problem for multiple signals with known waveforms and for a desired signal with known waveform in the presence of interfering signals. We describe computationally efficient ML algorithms that avoid the need for a multidimensional search, as is required to maximize the likelihood function directly when multiple signals are present. For multiple signals with known waveforms, we present two iterative algorithms for computing the angle estimates. One approach is based on the alternating maximization (AM) approach of Ziskind and Wax [7] and the other is based on the EM approach of Feder and Weinstein [11]. Our approaches differ from the AM approach and the EM algorithm, however, in that we consider a uniform linear array of sensors and we obtain the angle estimates by finding polynomial roots rather than by searching over parameter space. For a signal with known waveform in the presence of interfering signals, we propose an iterative algorithm that combines the merits of the iterative quadratic ML (IQML) approach of Bresler and Macovski [13], [6] and the AM approach [7]. It transforms the multidimensional search problem into an iterative one-dimensional search problem. We compare the performance of these ML es-

Manuscript received January 29, 1991; revised October 20, 1992. The associate editor coordinating the review of this paper and approving it for publication was Prof. S. Unnikrishna Pillai. This work was supported in part by the Joint Services Electronics Program under Contract N00014-89-J-1007 with the Ohio State University Research Foundation.

J. Li was with the Department of Electrical Engineering, Ohio State University, Columbus, OH 43210. She is now with the Department of Electrical Engineering, University of Florida, Gainesville, FL 32611.

R. T. Compton, Jr., was with the ElectroScience Laboratory, Department of Electrical Engineering, Ohio State University, Columbus, OH 43212. He is now with Compton Research, Inc., Worthington, OH 43085. IEEE Log Number 9210126.

timators with each other and with that of a suboptimal estimator that first estimates the angles without using the signal waveforms or the desired signal waveform (the IQML estimator [6]) and then determines which angle estimate corresponds to which waveform or extracts the desired signal angle. We also present Cramer-Rao (CR) bounds for these estimators and compare the performance of the estimators to their CR bounds.

The paper is organized as follows. In Section II, we formulate the problem. In Section III, we describe angle estimators for multiple signals with known waveforms and derive CR bounds for the estimators. In Section IV, we describe angle estimators for a desired signal with known waveform in the presence of interfering signals. We also derive CR bounds for the estimators. In Section V, we show numerical results and examine the performance of the estimators. Finally, Section VI contains our conclusions.

II. PROBLEM FORMULATION

Consider a uniform linear array with M isotropic sensors. The distance between two adjacent sensors is assumed to be a half wavelength at the signal frequency. Suppose K narrow-band plane waves with known waveforms impinge on the array from distinct angles θ_k , $k = 1, \dots, K$, relative to the array normal. (By narrow band, we mean that signals received on different sensors differ only by a phase factor.) The number of incident signals K is assumed known. (If the number of signals is unknown, it may be estimated as described, for example, in [14].) Suppose that the signal from θ_k has form

$$s_k(t) = \alpha_k p_k(t) \quad (1)$$

where $p_k(t)$ denotes the waveform and α_k the gain.

For multiple signals with known waveforms, $p_1(t)$, $p_2(t)$, \dots , $p_K(t)$ are known waveforms that may be correlated (or even perfectly correlated) with each other. To simplify the problem, we shall assume that when two waveforms $p_k(t)$ are perfectly correlated, they are actually identical. In other words, we exclude from consideration the case where two $p_k(t)$ differ only by a phase factor. Such a phase difference between two $p_k(t)$ can be incorporated into the definitions of the gains α_k , so there is no loss of generality with this assumption.

For a signal with known waveform in the presence of interfering signals, the signal from θ_1 is the desired signal and $p_1(t)$ is known. The rest of the signals are interfering signals and $s_2(t)$, \dots , $s_K(t)$ are unknown. The desired signal is assumed to be uncorrelated or almost uncorrelated with the interfering signals, i.e., $E\{s_1^*(t)s_k(t)\}$, $k = 2, 3, \dots, K$, is zero or almost zero, where $(\cdot)^*$ denotes the complex conjugate. Thus the desired signal waveform can be used to distinguish it from the interfering signals. However, the interfering signals may be correlated (or even perfectly correlated) with each other.

With K signals incident, the total signal $x_m(t)$ received at the m th sensor is the sum of the K signals plus an additive noise component,

divitive noise component,

$$x_m(t) = \sum_{k=1}^K \alpha_k p_k(t) e^{-j\pi m \sin \theta_k} + n_m(t) \quad (2)$$

where $n_m(t)$ is a zero-mean Gaussian noise process with variance σ^2 . The $n_m(t)$ are independent of each other and the incident signals.

Let $x(t)$, $s(t)$, $P(t)$, α , and $n(t)$ be

$$x(t) = [x_1(t) \ x_2(t) \ \dots \ x_M(t)]^T \quad (3)$$

$$s(t) = [s_1(t) \ s_2(t) \ \dots \ s_K(t)]^T \quad (4)$$

$$P(t) = \text{diag} \{ p_1(t), p_2(t), \dots, p_K(t) \} \quad (5)$$

$$\alpha = [\alpha_1 \ \alpha_2 \ \dots \ \alpha_K]^T \quad (6)$$

$$n(t) = [n_1(t) \ n_2(t) \ \dots \ n_M(t)]^T \quad (7)$$

where $(\cdot)^T$ denotes the transpose. The received signal vector has the form

$$x(t) = A(\theta)s(t) + n(t) = A(\theta)P(t)\alpha + n(t) \quad (8)$$

where $A(\theta)$ (with $\theta = [\theta_1 \ \theta_2 \ \dots \ \theta_K]^T$) is the direction matrix, whose columns are the direction vectors of the incident signals

$$A(\theta) = [a(\theta_1) \ a(\theta_2) \ \dots \ a(\theta_K)] \quad (9)$$

with

$$a(\theta_k) = [1 \ \phi_k \ \dots \ \phi_k^{M-1}]^T \quad (10)$$

and

$$\phi_k = e^{-j\pi \sin \theta_k}. \quad (11)$$

The array output is sampled at N distinct times t_n , $n = 1, 2, \dots, N$. The random noise vectors $n(t_n)$ at different sample times are assumed independent of each other. The problem of interest for multiple signals with known waveforms is to determine the angles θ_k , $k = 1, 2, \dots, K$, from the measurements $x(t_n)$, $n = 1, 2, \dots, N$. The problem of interest for a signal with known waveform in the presence of interfering signals is to determine the desired angle θ_1 . In the following sections, we describe three approaches based on ML estimation that may be used to solve these problems.

III. MAXIMUM LIKELIHOOD ANGLE ESTIMATION FOR MULTIPLE SIGNALS WITH KNOWN WAVEFORMS

We first consider estimators for multiple signals with known waveforms and derive CR bounds for these estimators.

A. Angle Estimation Algorithms

One way of estimating the signal angles is to start with the IQML algorithm of Bresler and Macovski [6], a maximum likelihood method originally discussed by Kumareshan *et al.* [13]. This method does not incorporate the signal waveforms and does not tell us which angle estimate corresponds to which known signal waveform.

However, we can augment the IQML algorithm by estimating the received signal waveforms and then correlating them with the known waveforms to determine which waveform corresponds to each angle. We consider that approach in part 1 below.

Then, in part 2, we present two algorithms that do incorporate the signal waveforms. Both of these methods are based on maximum likelihood estimation. The two methods involve two different iterative procedures for computing the ML estimates.

1) *The IQML Algorithm with Signal Correlation:* One method for estimating the signal angles, which we shall call Method A, is based on the IQML algorithm [6], [15]. In this method, the first step is to use the IQML algorithm to estimate signal angles without taking advantage of the known signal waveforms. The IQML algorithm iteratively computes the maximum likelihood angle estimates and converges quickly. However, this algorithm, like many others, may converge to a local extremum instead of a global one. Yet the first step of the IQML algorithm is equivalent to a linear prediction approach [16] with the linear prediction order equal to the number of incident signals. For sufficiently high signal-to-noise ratio (SNR), the angle estimates obtained with this first step are sufficiently accurate that the convergence to a global extremum is guaranteed.

After obtaining the angle estimates $\bar{\theta}_1, \dots, \bar{\theta}_K$ from the IQML algorithm, we next use the known signal waveforms to determine which waveform corresponds to which angle in the set $\{\bar{\theta}_1, \dots, \bar{\theta}_K\}$. To do this, we first estimate the waveform of each incident signal and then correlate these waveform estimates with the known waveforms. The estimated waveforms of the incident signals are obtained from $\bar{\theta}_k, k = 1, 2, \dots, K$, as follows [8]:

$$s(t_n) = [A^H(\bar{\theta})A(\bar{\theta})]^{-1}A^H(\bar{\theta})x(t_n), \quad n = 1, 2, \dots, N \quad (12)$$

where $(\cdot)^H$ denotes the complex conjugate transpose,

$$A(\bar{\theta}) = [a(\bar{\theta}_1) \ a(\bar{\theta}_2) \ \dots \ a(\bar{\theta}_K)] \quad (13)$$

and

$$s(t_n) = [s_1(t_n) \ s_2(t_n) \ \dots \ s_K(t_n)]^T. \quad (14)$$

Next, we correlate each waveform in $s(t)$ against all of the known waveforms $p_k(t)$. Let $\hat{q}_{k,k'}$ be the square of the magnitude of the cross correlation between each signal estimate $s_{k'}(t)$ and the k th waveform $p_k(t)$ normalized with respect to the average power of $p_k(t)$,

$$\hat{q}_{k,k'} = \frac{\left| \sum_{n=1}^N p_k^*(t_n) s_{k'}(t_n) \right|^2}{\sum_{n=1}^N |p_k(t_n)|^2}, \quad 1 \leq k, k' \leq K. \quad (15)$$

To determine which $p_k(t)$ corresponds to a given $\bar{\theta}_{k'}$, for each $s_{k'}(t)$, we choose the $p_k(t)$ for which $\hat{q}_{k,k'}$ is maximum.

The angle estimates obtained in this way are suboptimal, because the waveforms are not utilized in forming the estimates. Nevertheless, this is one method of determining the arrival angle for each signal waveform.

2) *Maximum Likelihood Algorithms that Incorporate the Known Signal Waveforms:* Now we present two ML algorithms that incorporate the known signal waveforms in the estimation. When all signal waveforms are known, maximizing the likelihood function is equivalent to minimizing q , where [15]

$$q = \frac{1}{N} \sum_{n=1}^N [x(t_n) - A(\theta)P(t_n)\alpha]^H [x(t_n) - A(\theta)P(t_n)\alpha]. \quad (16)$$

The minimization of q is done over θ if α is known or over $\{\alpha, \theta\}$ if α is unknown.

To minimize q in (16) directly would involve either 1) a K -dimensional search if α is known, 2) a $3K$ -dimensional search if α is unknown and complex, or 3) a $2K$ -dimensional search if α is unknown and real, or if $\alpha_k = e^{j\beta_k}, k = 1, 2, \dots, K$, with β_k unknown and real. We describe below two iterative approaches that may be used instead to avoid the multidimensional search. These approaches are based on the alternating maximization (AM) approach to Ziskind and Wax [7] and the estimate maximize (EM) approach of Feder and Weinstein [11].

These two approaches are given in a) and b) below. Both methods involve iteration on both α and θ . To begin either algorithm, it is necessary to have initial estimates for α and θ . The initial estimate for θ may be obtained by using the angle estimates resulting from Method A above or from other computationally efficient techniques such as MUSIC, ESPRIT, or others [8], [9], [16]. We let

$$\theta^{(0)} = [\theta_1^{(0)} \ \theta_2^{(0)} \ \dots \ \theta_K^{(0)}]^T$$

be the initial set of angle estimates obtained with one of these methods. The initial estimate

$$\alpha^{(0)} = [\alpha_1^{(0)} \ \alpha_2^{(0)} \ \dots \ \alpha_K^{(0)}]^T$$

for α is obtained as follows [15]. Of course, if α is known, we simply set

$$\alpha^{(0)} = \alpha. \quad (17)$$

But if α is unknown, a least squares method is used to determine $\alpha^{(0)}$. Let

$$\gamma = \left[\sum_{n=1}^N P^H(t_n) A^H(\theta^{(0)}) A(\theta^{(0)}) P(t_n) \right]^{-1} \cdot \left[\sum_{n=1}^N P^H(t_n) A^H(\theta^{(0)}) x(t_n) \right]. \quad (18)$$

Then, if α is unknown and complex, we choose

$$\alpha^{(0)} = \gamma. \quad (19)$$

If α is unknown and real, we let

$$\alpha^{(0)} = \text{Re}(\gamma). \quad (20)$$

Of, if $\alpha_k = e^{j\beta_k}$ for each k , with β_k unknown and real, we choose

$$\alpha_k^{(0)} = e^{j\beta_k^{(0)}} \quad (21)$$

where $\beta^{(0)} = [\beta_1^{(0)} \ \beta_2^{(0)} \ \cdots \ \beta_K^{(0)}]^T$ is

$$\beta^{(0)} = \arg(\gamma). \quad (22)$$

Now we present the two methods that iteratively compute the maximum likelihood angle estimates.

a) A maximum likelihood method based on alternating maximization: The first approach, which we call Method B.1, is based on the AM algorithm [7]. At each iteration, a minimization is performed first with respect to θ_1 , then with respect to α_1 , then with respect to θ_2 , then with respect to α_2 , and so forth. At the k th step of the $(i+1)$ st iteration, for $k = 1, 2, \dots, K$, we fix

$$\theta_1^{(i+1)}, \alpha_1^{(i+1)}, \dots, \theta_{k-1}^{(i+1)}, \alpha_{k-1}^{(i+1)}, \theta_{k+1}^{(i)}, \dots, \theta_K^{(i)}, \alpha_K^{(i)}$$

We compute $\theta_k^{(i+1)}$ by fixing $\alpha_k^{(i)}$ and compute $\alpha_k^{(i+1)}$ by fixing $\theta_k^{(i+1)}$. The $\theta_k^{(i+1)}$ and $\alpha_k^{(i+1)}$ are updated from $x_k^{(i+1)}(t_n)$ whose m th element is

$$x_m(t_n) = \sum_{k=1}^{K-1} \alpha_k^{(i+1)} p_k(t_n) e^{-j(m-1)\pi \sin \theta_k^{(i+1)}} - \sum_{k=k+1}^K \alpha_k^{(i)} p_k(t_n) e^{-j(m-1)\pi \sin \theta_k^{(i)}}$$

by solving for the zeros of a polynomial of order $2(M-1)$. The updating procedure is described in the Appendix.

Method B.1 consists of the following steps:

- 1) Initialize: Let $i = 0$ and obtain $\theta^{(0)}$ using the IQML algorithm (or some other algorithm).
- 2) Compute $\alpha^{(0)}$ from (17), (19), (20), or (21).
- 3) For $k = 1, 2, \dots, K$, obtain $\theta_k^{(i+1)}$ and $\alpha_k^{(i+1)}$ from $x_k^{(i+1)}(t_n)$.
- 4) Check convergence: If

$$\max_k |\theta_k^{(i+1)} - \theta_k^{(i)}| < \epsilon_1$$

let $\hat{\theta} = \theta^{(i)}$; otherwise, let $i = i + 1$ and go to (3). (ϵ_1 is a suitable convergence constant. $\hat{\theta}$ is the final estimate of θ .)

This method is bound to converge to at least a local minimum of q [7]. Since q is minimized at every step, the value of q will never increase. However, it is possible that the algorithm may converge to a local minimum instead of the global minimum. Nevertheless, in the examples we have tried, it has always converged to the proper result in a small number of iterations. This result occurs because the initial angle estimates obtained with the IQML algorithm have been sufficiently accurate that the global convergence has been guaranteed.

b) A maximum likelihood method based on the estimate maximize algorithm: The second approach, Method

B.2, is based on the EM algorithm [11] and works as follows. At each iteration, the observed signals $x(t)$ are decomposed into their signal components plus noise [11], and the angle estimates are updated individually from these separate components.

As the first step in the $(i+1)$ st iteration, we decompose the observed signals into their signal components plus noise. The purpose of this decomposition is to decouple the complicated multidimensional minimization of q in (16) into K separate minimizations. For $k = 1, 2, \dots, K$, we let

$$\bar{x}_k^{(i+1)}(t_n) = a(\theta_k^{(i)}) \alpha_k^{(i)} p_k(t_n) + \frac{1}{K} \left[x(t_n) - \sum_{k=1}^K a(\theta_k^{(i)}) \alpha_k^{(i)} p_k(t_n) \right]. \quad (23)$$

Note that the first term of the right side of (23) is the k th signal component and the second term the noise component. For the second step of the $(i+1)$ st iteration, we calculate $\alpha_k^{(i+1)}$ and $\theta_k^{(i+1)}$ from $\bar{x}_k^{(i+1)}(t_n)$ by solving for the zeros of a polynomial of order $2(M-1)$. The updating of $\alpha_k^{(i+1)}$ and $\theta_k^{(i+1)}$ is described in the Appendix.

Method B.2 consists of the following steps:

- 1) Initialize: Let $i = 0$ and obtain $\theta^{(0)}$ using the IQML algorithm (or some other algorithm).
- 2) Compute $\alpha^{(0)}$ from (17), (19), (20), or (21).
- 3) For $k = 1, 2, \dots, K$, obtain $\alpha_k^{(i+1)}$ and $\theta_k^{(i+1)}$ from $\bar{x}_k^{(i+1)}(t_n)$.
- 4) Check convergence: If

$$\max_k |\theta_k^{(i+1)} - \theta_k^{(i)}| < \epsilon_2$$

let $\hat{\theta} = \theta^{(i)}$; otherwise, let $i = i + 1$ and go to (3). (ϵ_2 is a suitable convergence constant. $\hat{\theta}$ is the final estimate of θ .)

This method always converges at least to a local minimum of q [11]. But as usual there is no guarantee that it will converge to the global minimum. Nevertheless, in our examples, it has always converged to the proper result in a small number of iterations. The reason is again that the IQML algorithm has provided good initial angle estimates.

Methods B.1 and B.2 both minimize q in (16) iteratively. Within each iteration, however, Method B.2 computes $\alpha_k^{(i+1)}$ and $\theta_k^{(i+1)}$ in parallel while Method B.1 computes them serially.

B. Cramer-Rao Bounds

Using the results in [17], we may obtain the Cramer-Rao bounds (CRB's) of any unbiased estimator of θ for both cases of known and unknown signal waveforms.

1) Unknown Signal Waveforms: If all signal waveforms are unknown, it has been shown in [17] that the mean-square error (MSE) of any unbiased estimate of θ

$= [\theta_1 \ \theta_2 \ \cdots \ \theta_K]^T$ is bounded below by the CRB,

$$\text{CRB}(\theta) = \frac{\sigma^2}{2} \left\{ \sum_{n=1}^N \text{Re}[S^H(t_n) D^H(\theta) P_{A^\perp(\theta)} D(\theta) S(t_n)] \right\}^{-1} \quad (24)$$

where

$$P_{A^\perp(\theta)} = [I - A(\theta)(A^H(\theta)A(\theta))^{-1}A^H(\theta)] \quad (25)$$

$$S(t_n) = \text{diag}\{s_1(t_n), s_2(t_n), \dots, s_K(t_n)\} \quad (26)$$

$$D(\theta) = [d(\theta_1) \ d(\theta_2) \ \cdots \ d(\theta_K)] \quad (27)$$

with

$$d(\theta_k) = [0 \ -j\pi \cos(\theta_k)\phi_k \ \cdots \ -j(M-1)\pi \cos(\theta_k)\phi_k^{M-1}]^T. \quad (28)$$

2) Known Signal Waveforms: We present below the CRB's for the four cases of known α , unknown real α , unknown complex α , and $\alpha_k = e^{j\theta_k}$, $k = 1, 2, \dots, K$, with β_k unknown and real. These CRB's have been obtained by modifying the results in [17] under the assumption that the signal waveforms are known. The Fisher information matrix for the general case where α is unknown and complex may be found first. By deleting the column(s) and row(s) of this Fisher information matrix corresponding to the amplitude or phase of α , the Fisher information matrices for other assumptions of α may be found. Detailed derivations of the results below may be found in [15].

For α known, it can be shown that the MSE of any unbiased estimate of θ is bounded below by the CRB

$$\text{CRB}(\theta) = \frac{\sigma^2}{2} \{\Gamma\}^{-1} \quad (29)$$

where

$$\Gamma = \text{Re} \left[\sum_{n=1}^N S^H(t_n) D^H(\theta) D(\theta) S(t_n) \right]. \quad (30)$$

For α unknown and complex, the MSE of any unbiased estimate of θ is bounded below by the CRB

$$\text{CRB}(\theta) = \frac{\sigma^2}{2} \{\Gamma - \text{Re}(\Delta^T \Lambda^{-1} \Delta)\}^{-1} \quad (31)$$

where

$$\Delta = \sum_{n=1}^N S^H(t_n) A^H(\theta) D(\theta) S(t_n) \quad (32)$$

$$\Lambda = \sum_{n=1}^N S^H(t_n) A^H(\theta) A(\theta) S(t_n). \quad (33)$$

For α unknown and real, the MSE of any unbiased estimate of θ is bounded below by the CRB

$$\text{CRB}(\theta) = \frac{\sigma^2}{2} \{\Gamma - \text{Re}(\Delta)^T [\text{Re}(\Lambda)]^{-1} \text{Re}(\Delta)\}^{-1}. \quad (34)$$

For $\alpha_k = e^{j\theta_k}$, $k = 1, 2, \dots, K$, with β_k unknown and real, the MSE of any unbiased estimate of θ is bounded below by the CRB

$$\text{CRB}(\theta) = \frac{\sigma^2}{2} \{\Gamma - \text{Im}(\Delta)^T [\text{Re}(\Lambda)]^{-1} \text{Im}(\Delta)\}^{-1}. \quad (35)$$

Comparing the bounds in (24), (29), (31), (34), and (35), we note that the ratio between any two of the bounds is independent of the variance of the additive noise or the signal-to-noise ratio (SNR). Also, the bounds in (29), (31), (34), and (35) will not change as long as $S(t)$ or $s_k(t) = \alpha_k p_k(t)$ is fixed no matter how we define α_k and $p_k(t)$. When $S(t)$ is fixed, the SNR of each incident signal $s_k(t)$ is fixed.

It can be shown easily that the bounds in (24) and (31) are the same when the number of samples is $N = 1$, as one would expect. (For $N = 1$, not knowing the value of complex α is the same as not knowing the only data sample of the signals.)

For $N > 1$ and uncorrelated signals, i.e.,

$$\sum_{n=1}^N s_{k_1}^*(t_n) s_{k_2}(t_n) = 0, \quad k_1, k_2 = 1, 2, \dots, K, k_1 \neq k_2 \quad (36)$$

we can show that the $\text{CRB}(\theta)$ is a diagonal matrix when the signal waveforms are known. For α known and α unknown and real,

$$\text{CRB}(\theta) = \frac{3\sigma^2}{N(M-1)M(2M-1)\pi^2} \cdot \text{diag} \left\{ \frac{1}{P_1 \cos^2 \theta_1}, \dots, \frac{1}{P_K \cos^2 \theta_K} \right\} \quad (37)$$

where P_k is the average power of the k th incident signal, i.e.,

$$P_k = \frac{1}{N} \sum_{n=1}^N |s_k(t_n)|^2. \quad (38)$$

For α unknown and complex and $\alpha_k = e^{j\theta_k}$, $k = 1, 2, \dots, K$, with β_k unknown and real,

$$\text{CRB}(\theta) = \frac{6\sigma^2}{N(M^2-1)M\pi^2} \cdot \text{diag} \left\{ \frac{1}{P_1 \cos^2 \theta_1}, \dots, \frac{1}{P_K \cos^2 \theta_K} \right\}. \quad (39)$$

Note that for this case of uncorrelated known waveforms, the CR bound of an angle estimate is independent of the presence of all other incident signals, no matter how closely spaced these other signals are. Note also that the CR bounds for the cases of known and unknown phases of the incident signals $s_k(t)$ differ by a factor $2(2M-1)/(M+1)$, as seen from (37) and (39). For large M ,

$2(2M - 1)/(M + 1)$ is about 6 dB. This 6 dB improvement when α is known or unknown real is consistent with the CR bounds obtained for the frequency estimate of a single sinusoid in Gaussian noise derived in [18]. This improvement occurs because signal arrival angles depend on the phase differences of the signals received at different sensors and knowing the phases of the signal waveforms helps improve the angle estimates. Note also that the k th diagonal element of the right side of (39) is the same as the CR bound for the case of a single signal with unknown waveform arriving from θ_k [17]. This result shows that for the case of a single incident signal, the CR bounds are the same for the case of unknown waveform and for the case of known waveform with α unknown and complex or $\alpha = e^{j\beta}$, with β unknown and real. Finally, we note that as for the case of unknown signal waveforms, the CR bounds for all of the known waveform cases are inversely proportional to the number of data samples N .

For coherent signals, we can show that the CR bounds are also inversely proportional to N . For this case, the CR bounds go to infinity as the angle separation between two signals goes to zero. It can also be shown that the CR bound for the case of known coherent signal waveforms with α unknown and complex is the same as the CR-bound for unknown coherent signal waveforms, i.e., (31) and (24) are the same for coherent signals.

IV. MAXIMUM LIKELIHOOD ANGLE ESTIMATION FOR A SIGNAL WITH KNOWN WAVEFORM IN THE PRESENCE OF INTERFERING SIGNALS

We next consider estimators for a desired signal with known waveform in the presence of interfering signals and derive CR bounds for these estimators.

A. Angle Estimation Algorithms

The desired angle estimate may be obtained by augmenting the IQML algorithm and by using the known desired signal waveform to determine which angle corresponds to the desired signal. The angle estimate may also be obtained by a maximum likelihood estimator that properly incorporates the known desired signal waveform in the estimation process.

1) *The IQML Algorithm with Signal Correlation:* The approach we consider below is similar to Method A and is called Method C. In this approach, we first obtain the angle estimates $\hat{\theta}_1, \dots, \hat{\theta}_K$ from the IQML algorithm and compute $s_k(t)$, $k = 1, 2, \dots, K$, as in Section III-A1. Next let \hat{q}_k be the square of the magnitude of the cross correlation between each $s_k(t)$ and the desired signal waveform $p_1(t)$ normalized by the power of $s_k(t)$

$$\hat{q}_k = \frac{\left| \sum_{n=1}^N p_1^*(t_n) s_k(t_n) \right|^2}{\sum_{n=1}^N |s_k(t_n)|^2}, \quad k = 1, 2, \dots, K. \quad (40)$$

Since the desired signal is assumed uncorrelated or almost uncorrelated with the interfering signals, the estimate of the desired signal angle, $\hat{\theta}_1$, is the element in the set $\{\hat{\theta}_1, \hat{\theta}_2, \dots, \hat{\theta}_K\}$ that corresponds to the maximum $\{q_1, q_2, \dots, q_K\}$. (The rest of the angles in the set $\{\hat{\theta}_1, \hat{\theta}_2, \dots, \hat{\theta}_K\}$ are the interfering signal angles.)

2) *A Maximum Likelihood Algorithm that Incorporates the Known Waveform:* Now we present an ML algorithm that incorporates the known desired signal waveform from the beginning. We shall refer to this method as Method D. It is easy to show that in order to include the known signal waveform in the estimation process, we should minimize the quantity [15]

$$q = \frac{1}{N} \sum_{n=1}^N x_I^H(t_n) P_{A^\perp(\theta)} x_I(t_n) = \text{tr} \{P_{A^\perp(\theta)}, R_I\} \quad (41)$$

where $\theta_I = [\theta_2 \ \theta_3 \ \dots \ \theta_K]^T$,

$$x_I(t_n) = x(t_n) - a(\theta_1) \alpha_1 p_1(t_n) \quad (42)$$

$$P_{A^\perp(\theta_I)} = I - A(\theta_I) [A^H(\theta_I) A(\theta_I)]^{-1} A^H(\theta_I) \quad (43)$$

and

$$R_I(\theta_I) = \frac{1}{N} \sum_{n=1}^N x_I(t_n) x_I^H(t_n). \quad (44)$$

The algorithm we propose for minimizing q is again an iterative approach similar to the alternating maximization approach of Ziskind and Wax [7]. At each iteration, a minimization is performed first with respect to α_1 (if α_1 is unknown), then with respect to θ_I , and finally with respect to θ_1 [15].

As the first step in the $(i + 1)$ st iteration, we fix $\theta_I^{(i)}$ and $\theta_1^{(i)}$. If α_1 is known, we simply set

$$\alpha_1^{(i+1)} = \alpha_1. \quad (45)$$

However, if α_1 is unknown, we minimize q with respect to $\alpha_1^{(i+1)}$. By substituting (42) in (41) and setting derivatives with respect to the appropriate variables to zero, it is easy to show that if α_1 is unknown and real,

$$\alpha_1^{(i+1)} = \text{Re} \left\{ \frac{a^H(\theta_1^{(i)}) P_{A^\perp(\theta_I^{(i)})} \sum_{n=1}^N p_1^*(t_n) x(t_n)}{a^H(\theta_1^{(i)}) P_{A^\perp(\theta_I^{(i)})} a(\theta_1^{(i)}) \sum_{n=1}^N |p_1(t_n)|^2} \right\}. \quad (46)$$

If α_1 is unknown and complex,

$$\alpha_1^{(i+1)} = \frac{a^H(\theta_1^{(i)}) P_{A^\perp(\theta_I^{(i)})} \sum_{n=1}^N p_1^*(t_n) x(t_n)}{a^H(\theta_1^{(i)}) P_{A^\perp(\theta_I^{(i)})} a(\theta_1^{(i)}) \sum_{n=1}^N |p_1(t_n)|^2} \quad (47)$$

and if $\alpha_1 = e^{j\beta_1}$ with β_1 unknown and real,

$$\alpha_1^{(i+1)} = e^{j\beta_1^{(i+1)}} \quad (48)$$

where

$$\beta_1^{(i+1)} = \arg \left\{ a^H(\theta_1^{(i)}) P_{A^\perp(\theta_1^{(i)})} \sum_{n=1}^N p_1^*(t_n) x(t_n) \right\}. \quad (49)$$

For the second step in the $(i+1)$ st iteration, we solve for $\theta_1^{(i+1)}$ by fixing $\alpha_1^{(i+1)}$ and $\theta_1^{(i)}$. For this step, we minimize q by applying the IQML algorithm to $x_j^{(i+1)}(t_n)$, where

$$x_j^{(i+1)}(t_n) = x(t_n) - a(\theta_1^{(i)}) \alpha_1^{(i+1)} p_1(t_n). \quad (50)$$

In this case, the initial polynomial for the IQML algorithm is chosen so that its zeros are $e^{-j\pi \sin \theta_k^{(i)}}$, $k = 1, 2, \dots, K$.

For the last step of the $(i+1)$ st iteration, we fix $\alpha_1^{(i+1)}$ and $\theta_1^{(i+1)}$ and then find $\theta_1^{(i+1)}$. $\theta_1^{(i+1)}$ is the value of θ_1 that minimizes

$$q^{(i+1)}(\theta_1) = \text{tr} \{ P_{A^\perp(\theta_1^{(i+1)})} R_j^{(i+1)}(\theta_1) \}. \quad (51)$$

The required solution for $\theta_1^{(i+1)}$ is obtained with a one-dimensional search. We limit the search domain to $(\theta_1^{(i)} - \gamma, \theta_1^{(i)} + \gamma)$, where γ is chosen according to our confidence in $\theta_1^{(i)}$.

To summarize, the ML algorithm that utilizes the known desired signal waveform consists of the following steps:

1) Initialize: Let $i = 0$ and obtain θ_1^0 and θ_1^0 using the IQML algorithm, as described in Method A.

2) Update $\alpha_1^{(i+1)}$ from (45) if α_1 is known, (46) if α_1 is unknown and real, (47) if α_1 is unknown and complex, or (48) if $\alpha_1 = e^{j\beta_1}$ and β_1 is unknown and real.

3) Compute $x_j^{(i+1)}(t_n)$ using (50).

4) Compute $\theta_1^{(i+1)}$ by applying the IQML algorithm to $x_j^{(i+1)}(t_n)$.

5) Find $\theta_1^{(i+1)}$ that minimizes $q^{(i+1)}(\theta_1)$ in (51).

6) Check convergence: if $|\theta_1^{(i+1)} - \theta_1^{(i)}| < \epsilon_3$, let $\hat{\theta}_1 = \theta_1^{(i)}$, otherwise, let $i = i + 1$ and go to (2). (ϵ_3 is a suitable small constant. $\hat{\theta}_1$ is the final estimate of θ_1 .)

This algorithm is again bound to converge to a local minimum [7]. However, as usual, there is no guarantee that it will converge to the global minimum. Nevertheless, in the examples we have tried, it always converges to the proper result in a small number of iterations due to good initial angle estimates obtained with the IQML algorithm. In general, the number of iterations required drops as the angle between the desired and the interfering signals becomes larger. In our simulation examples, fewer than 10 iterations were needed. The number of iterations required by the IQML algorithm in Step 4 was fewer than 5.

B. Cramer-Rao Bounds

Using the results in [17], we may obtain Cramer-Rao bounds (CRB's) for any unbiased estimator of θ_1 for the case of known desired signal waveform [15].

If α_1 is known, it can be shown that the MSE of any unbiased estimate of θ is bounded below by the CRB,

$$\text{CRB}(\theta) = \frac{\sigma^2}{2} \left\{ \sum_{n=1}^N \bar{\Gamma}(t_n) \right\}^{-1} \quad (52)$$

where

$$\bar{\Gamma}(t_n) = \text{Re} [S^H(t_n) D^H(\theta) P_{A^\perp(\theta)} D(\theta) S(t_n)]. \quad (53)$$

If α_1 is unknown and complex, the MSE of any unbiased estimate of θ is bounded below by

$$\text{CRB}(\theta) = \frac{\sigma^2}{2} \left\{ \sum_{n=1}^N \bar{\Gamma}(t_n) - \frac{\text{Re} \left(\left[\sum_{n=1}^N f(t_n) \right] \left[\sum_{n=1}^N f^H(t_n) \right] \right)}{\sum_{n=1}^N \eta(t_n)} \right\}^{-1} \quad (54)$$

where

$$f(t_n) = S^H(t_n) D^H(\theta) P_{A^\perp(\theta)} a(\theta_1) s_1(t_n) \quad (55)$$

and

$$\eta(t_n) = |s_1(t_n)|^2 a^H(\theta_1) P_{A^\perp(\theta)} a(\theta_1). \quad (56)$$

If α_1 is unknown and real, the MSE of any unbiased estimate of θ is bounded below by

$$\text{CRB}(\theta) = \frac{\sigma^2}{2} \left\{ \sum_{n=1}^N \bar{\Gamma}(t_n) - \frac{\text{Re} \left[\sum_{n=1}^N f(t_n) \right] \text{Re}^T \left[\sum_{n=1}^N f(t_n) \right]}{\sum_{n=1}^N \eta(t_n)} \right\}^{-1}. \quad (57)$$

Finally, if $\alpha_1 = e^{j\theta_1}$ with β_1 unknown and real, the MSE of any unbiased estimate of θ is bounded below by

$$\text{CRB}(\theta) = \frac{\sigma^2}{2} \left\{ \sum_{n=1}^N \bar{\Gamma}(t_n) - \frac{\text{Im} \left[\sum_{n=1}^N f(t_n) \right] \text{Im}^T \left[\sum_{n=1}^N f(t_n) \right]}{\sum_{n=1}^N \eta(t_n)} \right\}^{-1} \quad (58)$$

Comparing the bounds in (24), (52), (57), (54), and (58), we note again that the ratio between any two of the bounds is independent of the variance of the additive noise or the signal-to-noise ratio. Also, the bounds in (52), (57), (54), and (58) are independent of α_1 as long as $s_1(t)$ is fixed so that the SNR of the desired signal is fixed.

It again can be shown that the bounds in (24) and (54) are the same when $N = 1$, as one would expect. For $N > 1$, we can show that the CR bounds for all cases of the known desired waveform are inversely proportional to the number of data samples N .

Also, by using $P_{[A_1 A_2]^T} = P_{A_1^T} + P_{A_2^T} - I$, where $A_3 = P_{A_1^T} A_2$, it can be shown from (54) and (24) that the CR bounds for the desired angle estimate are the same for the cases of known and unknown desired signal waveform when α_1 is unknown and complex.

Finally, it can be shown from (52) and (58) that for the cases of a single interfering signal with α_1 known or with $\alpha_1 = e^{j\theta_1}$ but β_1 unknown and real, the CR bounds for the desired angle estimate will remain finite even as the direction of the interfering signal approaches that of the desired signal. However, as the directions of two or more interfering signals approach the direction of the desired signal, the CR bounds for the desired angle estimate will go to infinity for all assumptions of α_1 .

V. TYPICAL RESULTS

In this section, we show typical performance changes that result when all known signal waveforms or the known desired signal waveform are incorporated. The examples illustrate the conditions under which incorporating knowledge of the known signal waveforms in the ML estimator can improve the accuracy of the angle estimates or the desired angle estimates. For the curves below, each incident signal is a BPSK (binary phase-shift keyed) signal modulated by one period of a 31-b pseudonoise (PN) sequence [4]. The incident signals $s_k(t)$, $k = 1, 2$, have unit power at each sensor and are sampled at a rate of one sample per bit. For the case of unknown complex α , we assumed $\alpha = [2e^{j\pi/4} \ 2e^{-j\pi/3}]^T$. For the case of unknown real α , we assumed $\alpha = [2 \ 2]^T$. For the case of $\alpha_k = e^{j\theta_k}$ with unknown real β_k , we assumed $\beta = [\pi/4 \ -\pi/3]^T$. Note that the gains α are set at the given values for the simulations and the waveforms $p_k(t)$ changed accordingly, and the incident signals $s_k(t)$ are assumed the same for different values of α . The SNR at each sensor output, defined as $-10 \log_{10} \sigma^2$ dB, is assumed to be 20 dB. The number of data samples is assumed $N =$

31 and the number of sensors is assumed $M = 10$. Thus the Rayleigh angle resolution limit for the array is $2/(M - 1)$ rad or 12.73° .

We first consider the case of multiple signals with known waveforms. For the curves below, it is assumed that two signals arrive from $\theta_1 = 30^\circ$ and $\theta_2 = (30 - \Delta\theta)^\circ$, so $\Delta\theta$ is the angle separation between the signals. For the first series of curves, the two known signal waveforms are from two different PN sequences with low cross-correlation. Thus the incident signals are almost uncorrelated (or noncoherent). Fig. 1 shows the CR bounds for the root-mean-square errors (RMSE's) of $\hat{\theta}_1$, i.e., the square root of the MSE's of $\hat{\theta}_1$, as a function of $\Delta\theta$. (The curves for the other angle estimates are similar.) Fig. 1 shows that incorporating the known signal waveforms significantly improves the CR bounds for $\hat{\theta}_1$, especially for small $\Delta\theta$. For this case of known waveforms, the CR bounds for $\hat{\theta}_1$ depend little on $\Delta\theta$, as discussed in Section III-B. Fig. 1(a) shows that for large $\Delta\theta$, where the incident signals have little effect on each other, the improvement due to incorporating the known signal waveforms is about 6 dB when α is known or unknown and real. However, Fig. 1(b) shows that little improvement is obtained for large $\Delta\theta$ when α is unknown and complex or when $\alpha_k = e^{j\theta_k}$, $k = 1, 2$, with the β_k unknown and real. These results are again consistent with the discussion in Section III-B.

Fig. 1 also shows the performance results, i.e., the RMSE's, for Methods A, B.1, and B.2 obtained by using 50 Monte Carlo simulations with independent trials. The convergence constants used in the iterative algorithms were chosen to be $\epsilon_1 = \epsilon_2 = 0.005^\circ$. We note that the ML estimates from Methods B.1 and B.2 are very close to the best unbiased estimates one can get. (Because of the limited number of Monte Carlo simulations, the RMSE curves may occasionally fall below the CRB's.) Note also that comparing the performance of Method A with that of Methods B.1 and B.2 is similar to comparing the CR bounds for $\hat{\theta}_1$.

Fig. 2 shows the average number of iterations needed to obtain convergence in Methods B.1 and B.2. Note that Method B.1 requires fewer iterations than Method B.2 when α is known or unknown and real. For small $\Delta\theta$ and α known or unknown and real, Method B.2 is not as attractive as Method B.1 since the number of iterations required by Method B.1 is less than half as much as required by Method B.2. On the other hand, Method B.2

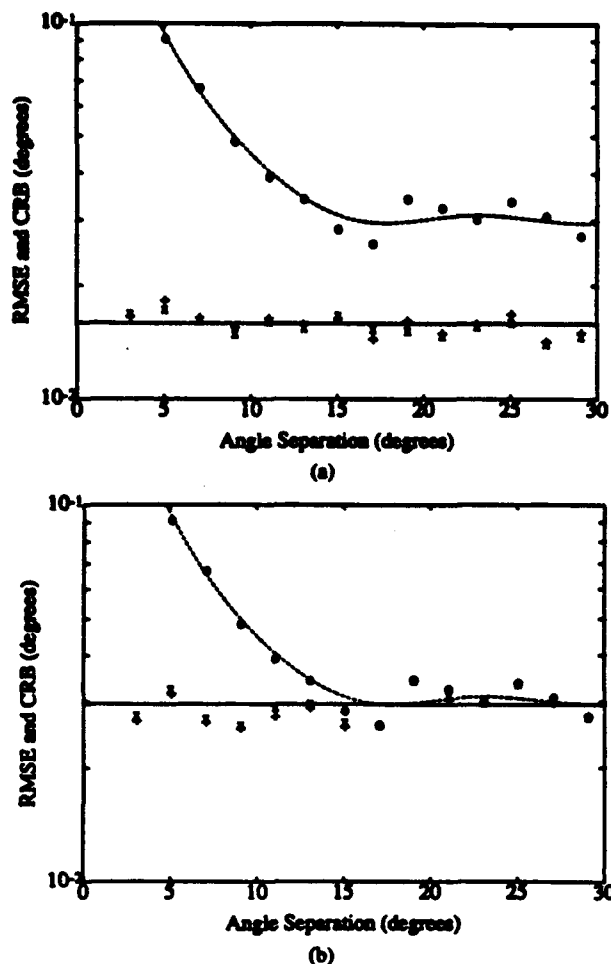


Fig. 1. Root-mean-square errors and the corresponding CR bounds of $\hat{\theta}$, versus $\Delta\theta$ for multiple noncoherent signals with known waveforms. Solid curve: known signal waveforms; dashed curve: unknown signal waveforms. Symbol o: Method A; symbol x: Method B.1; symbol +: Method B.2. For known signal waveforms, we assume (a) α known or α unknown real, and (b) α unknown complex or $\alpha_k = e^{j\beta_k}$, $k = 1, 2$, with β_k unknown real.

requires fewer iterations than Method B.1 when α is unknown and complex or when $\alpha_k = e^{j\beta_k}$, $k = 1, 2$, with β_k unknown and real, especially for small $\Delta\theta$. For the latter two types of α , Method B.2 is more attractive since it can be used to compute angle estimates in parallel during each iteration.

For the second series of curves, the two known signal waveforms are from two identical PN sequences, so the incident signals are coherent (perfectly correlated). Except for the signal coherence, all parameters used below are the same as above. The case of α unknown and complex will not be shown below since as shown in Section III-B that for this case, the CR bounds are the same for known and unknown waveforms.

Fig. 3 shows that the CR bounds for the RMSE's of $\hat{\theta}_1$ for coherent signals with known waveforms are functions of $\Delta\theta$. This result occurs because since the known waveforms are identical for this case, they cannot be used to distinguish the incident signals. Figs. 3(a) and (b) show again that for large $\Delta\theta$, where the incident signals have

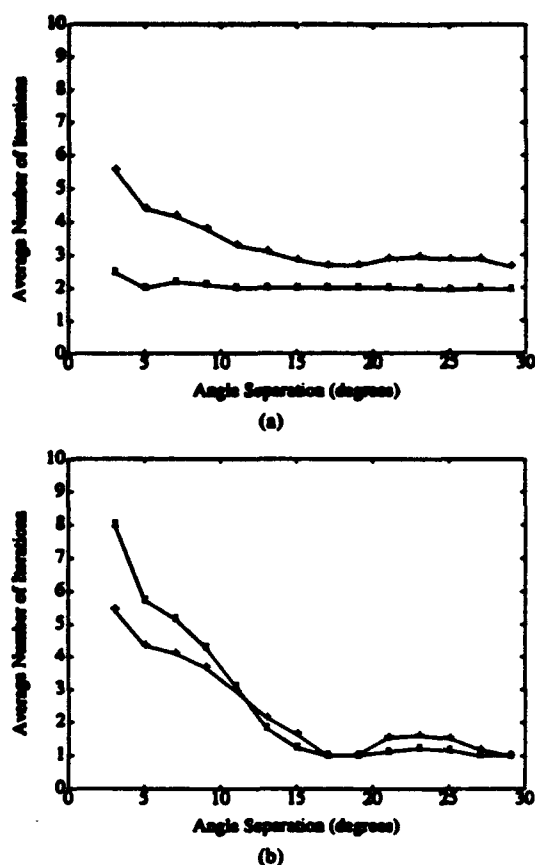
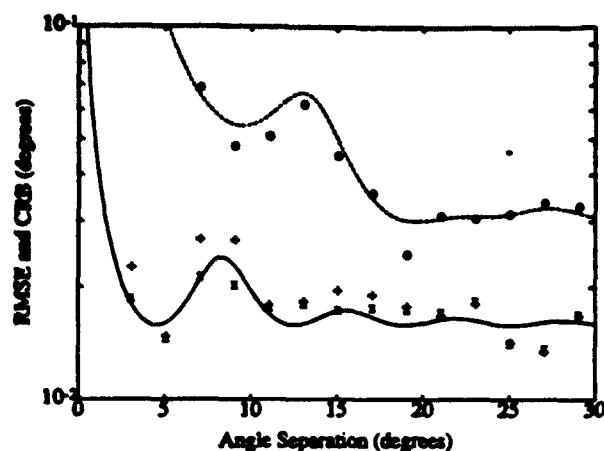


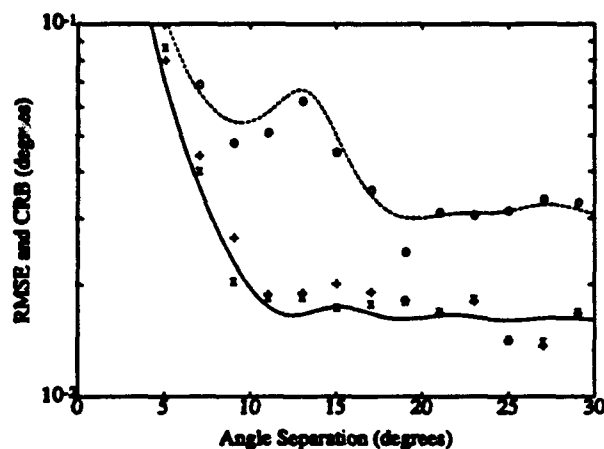
Fig. 2. The number of iterations versus $\Delta\theta$ for multiple noncoherent signals with known waveforms. Solid curve with symbol x: Method B.1; solid curve with symbol +: Method B.2. For Methods B.1 and B.2, we assume (a) α known or α unknown real, and (b) α unknown complex or $\alpha_k = e^{j\beta_k}$, $k = 1, 2$, with β_k unknown real.

little effect on each other, the improvement due to incorporating the known signal waveforms is about 6 dB when α is known or unknown and real. However, Fig. 3(c) shows that little improvement is obtained for large $\Delta\theta$ when $\alpha_k = e^{j\beta_k}$, $k = 1, 2$, with the β_k unknown and real. Fig. 3 also shows that for small $\Delta\theta$, the lowest CR bound is achieved when α is known. Fig. 3(b) and (c) show that for small $\Delta\theta$ with coherent known waveforms, the CR bound for $\alpha_k = e^{j\beta_k}$ with β_k unknown and real may be lower than the one for α unknown and real. This result shows that the knowledge of the amplitudes of the incident signals $s_k(t)$ may be used to better distinguish closely spaced coherent incident signals. Fig. 3 also shows the performance results for Methods A, B.1, and B.2. Note that the ML estimates from Methods B.1 and B.2 are very close to the best unbiased estimates one can get. Our simulations show that the average number of iterations needed for both Methods B.1 and B.2 and for all cases of α is no more than 6. Our simulations also show that the average number of iterations required by Methods B.1 or B.2 is almost the same for the case of coherent signals. For this case, therefore, Method B.2 is more attractive since it can be used to compute angle estimates in parallel during each iteration.

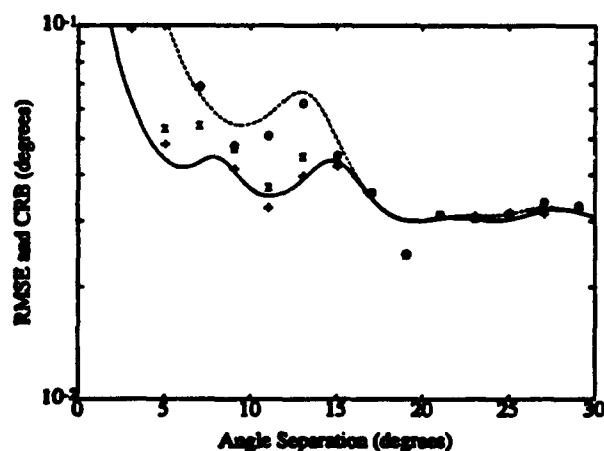
We next consider the case of a signal with known wave-



(a)



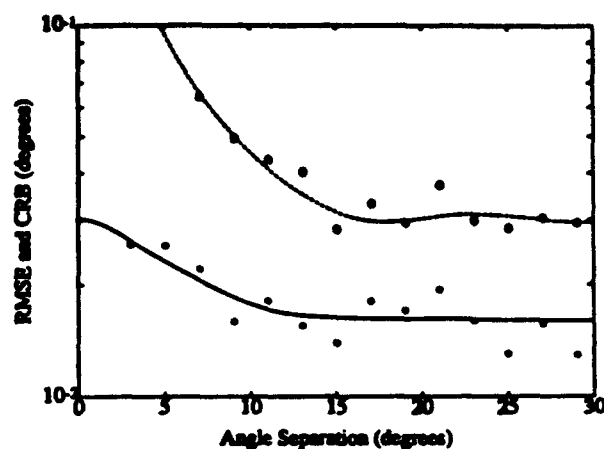
(b)



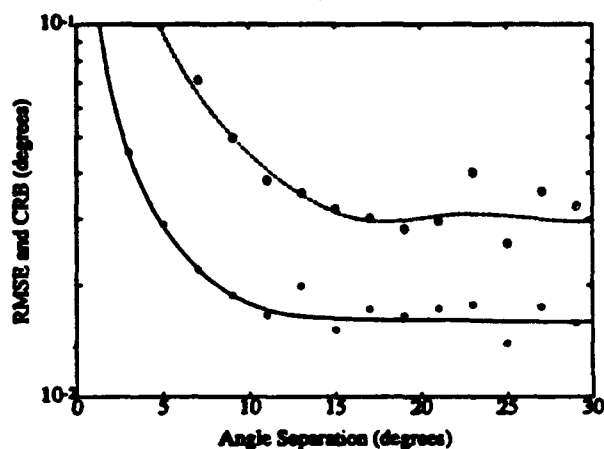
(c)

Fig. 3. Root-mean-square errors and the corresponding CR bounds of $\hat{\theta}_1$ versus $\Delta\theta$ for multiple coherent signals with known waveforms. Solid curve: known signal waveforms; dashed curve: unknown signal waveforms. Symbol o: Method A; symbol x: Method B.1; symbol +: Method B.2. For known signal waveforms, we assume (a) α_1 known, (b) α_1 unknown real, and (c) $\alpha_1 = e^{j\theta_1}$, $k = 1, 2$, with β_1 unknown real.

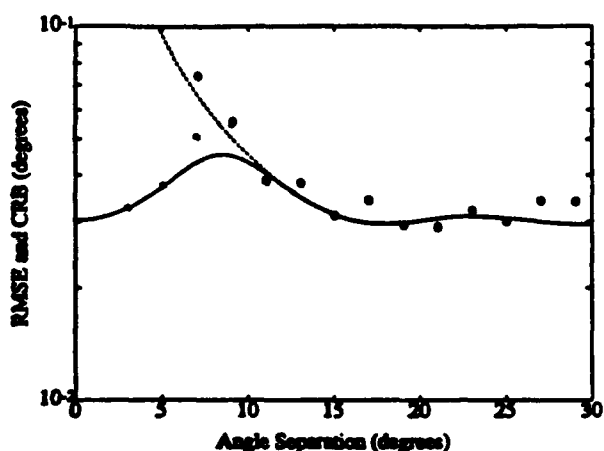
form in the presence of interfering signals that are almost uncorrelated with the desired signal. Since the CR bounds are the same for unknown desired signal waveform and for known desired signal waveform with α_1 unknown and complex, as discussed in Section IV-B, we will not show curves for this case of α_1 unknown and complex. In Fig.



(a)



(b)



(c)

Fig. 4. Root-mean-square errors and the corresponding CR bounds of the desired $\hat{\theta}_1$ versus $\Delta\theta$ for the desired signal with known waveform in the presence of a single interfering signal. Solid curve: known desired signal waveform; dashed curve: unknown desired signal waveform. Symbol o: Method C; symbol +: Method D. For known desired signal waveform, we assume (a) α_1 known, (b) α_1 unknown real, and (c) $\alpha_1 = e^{j\theta_1}$ with β_1 unknown real.

4, it is assumed that the desired signal arrives from $\theta_1 = 30^\circ$ and the single interfering signal arrives from $\theta_2 = (30 - \Delta\theta)^\circ$, so $\Delta\theta$ is the angle separation between the desired and interfering signals. Fig. 4 shows the RMSE's obtained with Methods C and D and the corresponding CR

bounds for the desired angle estimate $\hat{\theta}_1$ as a function of $\Delta\theta$. The convergence constant used in Method D was chosen to be $\epsilon_3 = 0.005^\circ$. Note that the ML estimates obtained from Methods C and D are very close to the best unbiased estimates one can get. Figs. 4(a) and (c) show that the CR bounds for the desired $\hat{\theta}_1$ remain finite for α_1 known and $\alpha_1 = e^{j\beta_1}$ with β_1 unknown and real even as $\Delta\theta$ approaches zero, as discussed in Section IV-B. This result shows that closely spaced desired and interfering signals can be distinguished by knowing the desired signal $s_1(t)$ or knowing the waveform and amplitude of $s_1(t)$. For small $\Delta\theta$, Fig. 4 shows that the smallest CR bound is achieved when α_1 is known. Figs. 4(b) and (c) show that for small $\Delta\theta$, the CR bound for $\alpha_1 = e^{j\beta_1}$ with β_1 unknown and real may be lower than the one for α_1 unknown and real. Figs. 4(a) and (b) shows again that for large $\Delta\theta$, where the interfering signal has little effect on the desired signal, the improvement due to incorporating the known desired signal waveform is about 6 dB when α_1 is known or unknown and real. Fig. 4(c) shows that little improvement is obtained for large $\Delta\theta$ when $\alpha_1 = e^{j\beta_1}$ with the β_1 unknown and real.

We also considered an example where the desired signal arrives from $\theta_1 = 30^\circ$ and two interfering signals arrive from $\theta_2 = (30 - \Delta\theta)^\circ$ and $\theta_3 = (30 - 2\Delta\theta)^\circ$, so $\Delta\theta$ is the angle separation between the signals. Moreover, the interfering signals are assumed coherent. Our numerical results show that when the directions of the two interfering signals approach the direction of the desired signal, i.e., $\Delta\theta$ approaches zero, the CR bounds for all assumptions of α_1 go to infinity, as discussed in Section IV-B.

VI. CONCLUSIONS

We have presented maximum likelihood algorithms that incorporate knowledge of multiple known signal waveforms with known or unknown gains or a known desired signal waveform with a known or unknown gain into the process of estimating the signal angles with uniform linear arrays. These algorithms avoid the complexity of a multidimensional search. For the case of multiple signals with known waveforms, we presented two algorithms that compute the ML estimates iteratively and converge in a few iterations. For the case of a desired signal in the presence of interfering signals, we presented an algorithm that transforms the multidimensional search problems into an iterative one-dimensional search problem. For comparison, we have also used the IQML algorithm augmented to determine which signal waveform corresponds to which estimated angle or to extract the desired signal angle. Curves were presented that compare the performance of the ML estimators with each other and also with the IQML algorithms. Both the actual performance and the Cramer-Rao bounds were shown under several assumptions for the signal gains or the desired signal gain. These curves show the conditions under which incorporating the multiple known signal waveforms or the known desired signal waveforms in the estimators improves the angle estimates.

APPENDIX

In this Appendix, we consider the case of one incident signal with known waveform $p(t)$. For this case, both α and θ are scalars. The maximum likelihood (ML) estimates of α (if α is unknown) and θ are found by minimizing the quantity (see (16))

$$q = \frac{1}{N} \sum_{n=1}^N [x(t_n) - a(\theta)p(t_n)\alpha]^H [x(t_n) - a(\theta)p(t_n)\alpha]. \quad (59)$$

Dropping all terms not involving α and θ , we get

$$q = \sum_{m=1}^M [-\alpha^* e^{j(m-1)\pi \sin \theta_1} y_m - \alpha e^{-j(m-1)\pi \sin \theta_1} y_m^*] + |\alpha|^2 Q \quad (60)$$

where we have defined

$$y_m = \frac{1}{N} \sum_{n=1}^N x_m(t_n) p^*(t_n) \quad (61)$$

and

$$Q = \frac{1}{N} \sum_{n=1}^N |p(t_n)|^2. \quad (62)$$

A. Unknown θ

The value of θ that minimizes q is found by setting the derivative of (60) with respect to θ to zero. Setting $dq/d\theta$ to zero yields

$$\alpha \sum_{m=1}^M (m-1) y_m^* z^{m-1} - \alpha^* \sum_{m=1}^M (m-1) y_m z^{-(m-1)} = 0 \quad (63)$$

where

$$z = e^{-j\pi \sin \theta}. \quad (64)$$

To obtain the appropriate solution to (60), we must take into account the assumed form of α . For the simplest case, when α is known, we obtain the ML estimate of θ by finding the zeros of (63) and then using (64).

When α is unknown and complex, setting $dq/(d \operatorname{Re}(\alpha))$ and $dq/(d \operatorname{Im}(\alpha))$ to zero and solving for the resulting α gives

$$\alpha = \frac{1}{MQ} \sum_{m=1}^M y_m z^{-(m-1)}. \quad (65)$$

Substituting (65) into (63) for α and canceling unnecessary terms yields

$$\sum_{m_1=1}^M \sum_{m_2=1}^M (m_1 - m_2) y_{m_1}^* y_{m_2} z^{m_1 - m_2} = 0. \quad (66)$$

In this case the ML estimates for θ and α are found by solving for the zeros of (66) and then using (64) and (65) to get α and θ .

When α is unknown and real, the α in (63) can be canceled. Thus for this case we have

$$\sum_{m=1}^M (m-1)y_m^* z^{m-1} - \sum_{m=1}^M (m-1)y_m z^{-(m-1)} = 0. \quad (67)$$

Setting $dq/d\alpha$ to zero and solving for the resulting α gives

$$\alpha = \text{Re} \left\{ \frac{1}{MQ} \sum_{m=1}^M y_m z^{-(m-1)} \right\}. \quad (68)$$

The zeros of (67) along with (64) and (68) then give the ML estimates of α and θ .

Finally, when $\alpha = e^{j\beta}$ with β unknown and real, (63) can be rewritten as

$$e^{j2\beta} \sum_{m=1}^M (m-1)y_m^* z^{m-1} - \sum_{m=1}^M (m-1)y_m z^{-(m-1)} = 0. \quad (69)$$

Setting $dq/d\beta$ to zero and solving for the resulting $e^{j2\beta}$ gives

$$e^{j2\beta} = \frac{\sum_{m=1}^M y_m z^{-(m-1)}}{\sum_{m=1}^M y_m^* z^{m-1}}. \quad (70)$$

The resulting α is therefore

$$\alpha = \exp \left\{ j \arg \left[\sum_{m=1}^M y_m z^{-(m-1)} \right] \right\}. \quad (71)$$

Substituting (70) into (69) for $e^{j2\beta}$ and canceling unnecessary terms yields the same equation as (66). From the zeros of (66), we obtain the ML estimates of α and θ from (64) and (71).

B. Known θ

For the case where θ is known and α is unknown, α may be estimated from (65), (68), or (71) when α is unknown and complex, unknown and real, or $\alpha = e^{j\beta}$ with β unknown and real, respectively. In these equations, the z is computed with (64) by using the known θ .

ACKNOWLEDGMENT

The authors gratefully acknowledge the helpful comments from the reviewers. The authors especially appreciate one of the reviewers for his insightful comments on the CR bounds.

REFERENCES

- [1] J. Ward and R. T. Compton, Jr., "Improving the performance of a slotted ALOHA packet radio network with an adaptive array," *IEEE Trans. Commun.*, vol. 40, pp. 292-300, Feb. 1992.
- [2] J. Ward and R. T. Compton, Jr., "High throughput slotted ALOHA packet radio networks with adaptive arrays," *IEEE Trans. Commun.*, to be published.
- [3] J. Ward and R. T. Compton, Jr., "High throughput unslotted ALOHA packet radio networks with adaptive arrays," *IEEE Trans. Commun.*, submitted for publication.
- [4] S. W. Golomb, *Shift Register Sequences*. San Francisco, CA: Holden-Day, 1967.
- [5] J. F. Böhme, "Estimation of source parameters by maximum likelihood and nonlinear regression," in *Proc. ICASSP 84*, 1984, pp. 7.3.1-7.3.4.
- [6] Y. Bresler and A. Macovski, "Exact maximum likelihood parameter estimation of superimposed exponential signals in noise," *IEEE Trans. Acoust., Speech, Signal Processing*, vol. ASSP-34, pp. 1081-1089, Oct. 1986.
- [7] I. Ziskind and M. Wax, "Maximum likelihood localization of multiple sources by alternating projection," *IEEE Trans. Acoust., Speech, Signal Processing*, vol. ASSP-36, pp. 1553-1560, Oct. 1988.
- [8] R. O. Schmidt, "Multiple emitter location and signal parameter estimation," *IEEE Trans. Antennas Propag.*, vol. AP-34, pp. 276-280, Mar. 1986.
- [9] R. Roy and T. Kailath, "ESPRIT—Estimation of signal parameters via rotational invariance techniques," *IEEE Trans. Acoust., Speech, Signal Processing*, vol. 37, pp. 984-995, July 1989.
- [10] P. Stoica and A. Nehorai, "Performance study of conditional and unconditional direction-of-arrival estimation," *IEEE Trans. Acoust., Speech, Signal Processing*, vol. 38, pp. 1783-1795, Oct. 1990.
- [11] M. Feder and E. Weinstein, "Parameter estimation of superimposed signals using the EM algorithm," *IEEE Trans. Acoust., Speech, Signal Processing*, vol. 36, pp. 477-489, Apr. 1988.
- [12] M. I. Miller and D. R. Fuhrmann, "Maximum-likelihood narrow-band direction finding and the EM algorithm," *IEEE Trans. Acoust., Speech, Signal Processing*, vol. 38, pp. 1560-1577, Sept. 1990.
- [13] R. Kumaresan, L. L. Scharf, and A. K. Shaw, "An algorithm for pole-zero modeling and spectral analysis," *IEEE Trans. Acoust., Speech, Signal Processing*, vol. ASSP-34, pp. 637-640, June 1986.
- [14] M. Wax and T. Kailath, "Detection of signals by information theoretic criteria," *IEEE Trans. Acoust., Speech, Signal Processing*, vol. ASSP-33, pp. 387-392, Apr. 1985.
- [15] J. Li, "Array signal processing for polarized signals and signals with known waveforms," Ph.D. dissertation, Ohio State University, Columbus, OH, Mar. 1991.
- [16] S. U. Pillai, *Array Signal Processing*. New York: Springer-Verlag, 1989.
- [17] P. Stoica and A. Nehorai, "MUSIC, maximum likelihood, and Cramer-Rao bound," *IEEE Trans. Acoust., Speech, Signal Processing*, vol. 37, pp. 720-741, May 1989.
- [18] D. Rife and R. Boorstyn, "Single-tone parameter estimation from discrete-time observations," *IEEE Trans. Inform. Theory*, vol. IT-20, pp. 591-598, Sept. 1974.



Jian Li (S'88-M'90) was born on April 17, 1965. She received the M.Sc. and Ph.D. degrees in electrical engineering from Ohio State University, Columbus, in 1987 and 1991, respectively.

From April 1991 to June 1991, she was an Adjunct Assistant Professor with the Department of Electrical Engineering, Ohio State University, Columbus. From July 1991 to June 1993, she was with the Department of Electrical Engineering, University of Kentucky, Lexington. Since August 1993, she has been an Assistant Professor with the

Department of Electrical Engineering, University of Florida, Gainesville. Her current research interests include sensor array signal processing, radar detection and estimation theory, image segmentation, and communications.

Dr. Li is a member of Sigma Xi and Phi Kappa Phi.



R. T. Compton, Jr., (S'58-M'59-SM'82-F'84) was born in St. Louis, MO, in 1935. He received the S.B. degree from the Massachusetts Institute of Technology in 1958 and the M.Sc. and Ph.D. degrees from Ohio State University in 1961 and 1964, respectively, all in electrical engineering.

From 1958 to 1962, he was with DECO Electronics, Inc., Leesburg, VA, and Battelle Memorial Institute, Columbus, OH. From 1962 to 1965, he worked at the Antenna Laboratory (now the ElectroScience Laboratory), Ohio State University, Columbus, OH, and in 1964-1965, he was an Assistant Professor of Electrical Engineering at Ohio State University. From 1965 to 1967, he

was an Assistant Professor of Engineering at Case Institute of Technology, Cleveland, OH. He spent the year 1967-1968 as a National Science Foundation Postdoctoral Fellow at the Technische Universität, Munich, Germany. In 1968 he returned to the Department of Electrical Engineering, Ohio State University, where he was Associate Professor (1968-1980), Professor (1980-1991), and a member of the ElectroScience Laboratory. Since 1992, he has been working as a private consultant under the name Compton Research, Inc. He is the author of *Adaptive Antennas: Concepts and Performance*, (Prentice-Hall, Inc., 1988), and has published over 50 refereed IEEE papers.

Dr. Compton is a member of Sigma Xi and Pi Mu Epsilon. In 1983 he received the M. Barry Carlton Award from the IEEE Aerospace and Electronic Systems Society for best paper of the year.

EM Diffraction by a Resistive Strip Attached to an Impedance Wedge

R. G. Rojas and M. Otero

The ElectroScience Laboratory
Department of Electrical Engineering
The Ohio State University
Columbus, OH 43212, USA

Abstract—The high frequency electromagnetic diffraction by a finite length resistive strip attached to a wedge with equal impedance faces is presented. The problem considered is two dimensional where the incident field is a plane wave polarized TM or TE to the axis of the wedge. Since the scatterer has two points of diffraction, the original problem can be first broken up into two simpler canonical problems which, due to the symmetry of the scatterer, can be obtained by a proper combination of special cases of the well known Maliuzhinets impedance wedge solution. A uniform asymptotic solution of these two canonical problems is developed which is continuous across the various shadow boundaries. This analysis also takes into account interactions between the two points of diffraction and points of reflection up to third order where spectral techniques are used to obtain the fields which are multiply diffracted and reflected as well as transmitted across the resistive strip. Incorporating these higher order interactions enhances the accuracy of the solution. Several numerical results are presented including comparisons with an independent moment method solution.

I. INTRODUCTION

For many applications, it is desirable to reduce or modify the electromagnetic scattering characteristics of a wedge shaped object. If the surface of the scatterer is conducting, it may be coated with radar absorbing materials to reduce its scattering. Such thinly coated conducting surfaces can often be approximated in the analysis by a Leontovich (impedance) boundary condition on the wedge faces. Although coating the surface will reduce the specular component of the scattered field, it may have little effect on the field which is diffracted from the wedge tip. Attaching resistive cards to the edges of scatterers is a well known technique for reducing scattering and was very successfully applied to reduce the echo width of a semi-infinite perfect electric conductor (PEC) half plane [1-2]. It seemed appropriate to extend the use of resistive cards for reducing the scattering from the wedge tip. Therefore, the configuration chosen in this paper [3] is a wedge with impedance faces with a resistive card attached to the wedge tip (Fig. 1).

To analyze this configuration, the method used is the Uniform Geometrical Theory of Diffraction (UTD). This is a high frequency technique which is useful if the size of the scatterer is on the order of a wavelength or larger, as opposed to a numerical technique, such as the method of moments, which is primarily useful at

low frequencies. Compared to numerical techniques, UTD provides better physical insight into the scattering mechanisms of the object. It also allows us to reduce the original configuration into a number of simpler configurations. Therefore, the solution can be obtained by a superposition of solutions to more fundamental, canonical problems. Keeping in mind that in the high frequency regime, the scatterer depicted in Fig. 1 has two points of diffraction, i.e., Q_1 and Q_2 , the two fundamental problems to be solved are the scattering from a semi-infinite (half plane) resistive sheet with Q_1 at its edge, and a semi-infinite resistive sheet attached to an impedance wedge at Q_2 . Note, as shown here, the solution for the former can be obtained from a special case of the latter.

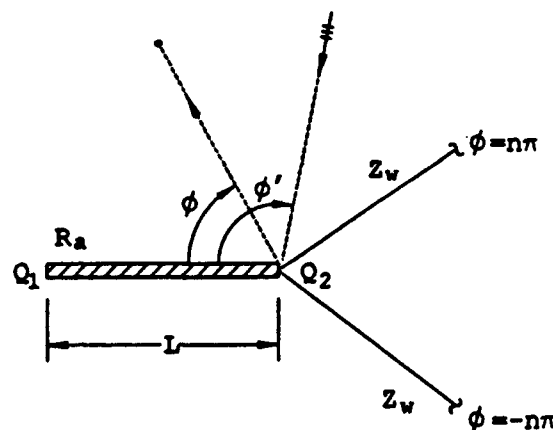


Figure 1. Resistive strip attached to a wedge with impedance faces.

It is worth pointing out that the original goal was to obtain a solution for the wedge in Fig. 1 with different impedance values. However, it turns out that the problem of diffraction by the junction of a resistive half plane and impedance wedge with different impedance values on its faces yields a second order functional difference equation for which, to the best knowledge of the present authors, no solution has been found. Thus, the next logical step was to assume that the faces of the wedge have equal impedance values. However, due to the symmetry of the scatterer, it will be shown here that it is not necessary to do a complete analysis of the mixed boundary value problem for the junction problem. Instead, the solution for the resistive half plane to impedance wedge (with equal impedances on both faces) junction can be obtained by an appropriate combination of special cases of the well known Maliuzhinets solution to a wedge with different impedances [4]. Once the canonical solution to the junction problem has been solved, that solution can then be used as a building block to construct the solution to the more complex geometry of Fig. 1. A special case of the resistive half plane to impedance wedge junction is the planar junction of a resistive half plane to an impedance (equal impedances on both faces) half plane which corresponds to $n = 1$ in Fig. 1. This latter geometry is analyzed by Uzgören et al. [16] by means of the Wiener-

Hopf technique which is suitable for planar geometries. It can be shown that the solution obtained here, which is based on the Maliuzhinets method, reduces to the simpler case considered in [16]. Furthermore, note that in the geometry depicted in Fig. 1 the resistive strip is of finite length, whereas, in [16] only a resistive half plane is considered.

Since there are two points of diffraction, namely Q_1 and Q_2 in Fig. 1, multiple diffraction mechanisms between these points will be included in this analysis. This is handled by a spectrally extended ray technique. Note that in this analysis, the interaction of the fields that diffract from the resistive edge and the fields reflected from the wedge faces are also taken into account.

This paper is organized as follows. In Section II, the method of analysis and the solution for the two canonical geometries, i.e., resistive half plane-wedge junction and resistive half plane by itself, will be discussed. In Section III, the multiply diffracted fields will be analyzed by means of a spectrally extended ray technique. In Section IV, numerical results will be presented and a brief discussion on the physical interpretation of the results will be given. Finally, in Section V, some concluding remarks will be given. Throughout this report, it is assumed that the fields have an $e^{-i\omega t}$ time dependence.

II. METHOD OF ANALYSIS

As pointed out in the previous section, the original problem depicted in Fig. 1 can be solved by first solving two canonical problems. The first fundamental problem to be solved is the diffraction from a semi-infinite resistive sheet attached to an impedance wedge for a plane wave incident field (see Fig. 1 with $L \rightarrow \infty$). This is a two-dimensional scalar problem since the incident field has no z -dependence and can either be TM_z or TE_z . Using cylindrical coordinates, the wedge axis is coincident with the z -axis, the resistive sheet is in the xz -plane, and the angles ϕ and ϕ' are measured positive from the resistive sheet. The angle between the resistive sheet and the wedge face is $n\pi$. Note that $-\pi \leq \phi \leq \pi$, whereas, without loss of generality, it is assumed that $0 \leq \phi' \leq n\pi$. The wedge faces are impenetrable with a surface impedance Z_w , whereas the resistive sheet is a penetrable surface with a surface resistance R_a . For purposes of analysis, a somewhat more general problem depicted in Fig. 2(a) will be considered in this section. The scatterer of Fig. 1 can be recovered by letting R_c go to infinity. The analysis of this problem can be further simplified by using an even and odd mode analysis. The equivalent problems obtained in Fig. 2(b) are derived taking into account that the resistive boundary condition states that the tangential electric field is continuous across a resistive sheet; whereas, the discontinuity of the tangential magnetic field is proportional to the tangential electric field, i.e.,

$$\begin{aligned}\hat{n} \times (\vec{E}^+ - \vec{E}^-) &= 0 \\ \hat{n} \times \hat{n} \times \vec{E} &= -R_a \hat{n} \times (\vec{H}^+ - \vec{H}^-)\end{aligned}\quad (1)$$

where the subscripts (+) and (-) denote the top and bottom faces of the resistive sheet, respectively. Also, \hat{n} is a unit vector normal to the surface of the resistive sheet directed from the (-) side to the (+) side, and \vec{E} and \vec{H} are the electric

and magnetic fields, respectively. Figure 2 shows how the original problem is decomposed into a superposition of the even excitation and odd excitation cases. The even excitation case is then equivalent to mounting the resistive sheet over a PEC ground plane for the TE_z case or a perfect magnetic conductor (PMC) for the TM_z case. The odd excitation case is equivalent to the even one except that the PEC and PMC ground planes are interchanged. The canonical problem now to be solved is the scattering from a wedge with different impedance faces, where the solution is valid in the region $0 \leq \phi, \phi' \leq n\pi$. The superposition of the even and odd cases results in a solution to the original problem where the resulting scattered field is valid everywhere in the region $-n\pi \leq \phi \leq n\pi$. Note that the even and odd mode analysis shows that the second order functional difference equation alluded to in section I for a wedge with different impedance faces must reduce, for the configuration shown in Fig. 1, to two uncoupled first order functional difference equations similar to those obtained by Maliuzhinets [4].

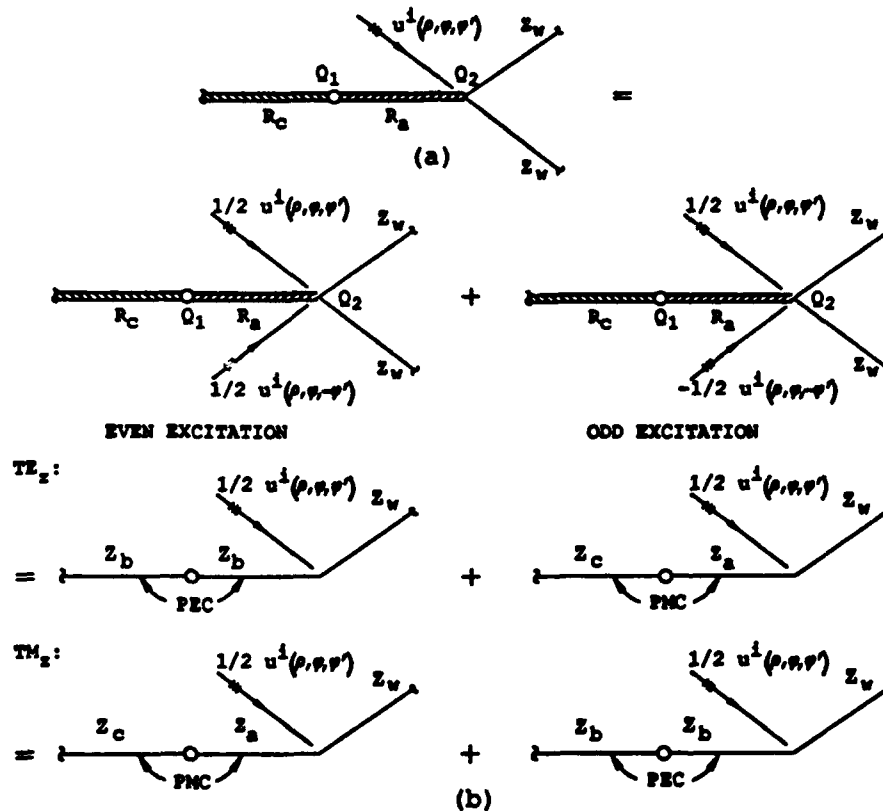


Figure 2. Even and odd mode analysis. (a) Original configuration. (b) Equivalent configuration where $Z_a = 2R_a$, $Z_b = 0$ and $Z_c = 2R_c$.

Now the solution to the problem of the scattering from a wedge with impedance faces Z_a and Z_w , where ϕ is measured from wedge face Z_a and ranges in values from $\phi = 0$ to $\phi = n\pi$ at the impedance face Z_w , will be briefly reviewed. The faces of the wedge satisfy the impedance or Leontovich boundary condition, given by

$$\begin{aligned} \vec{E} - \hat{\phi}(\hat{\phi} \cdot \vec{E}) &= \pm \hat{\phi} \times \vec{H} Z_i \\ \vec{H} - \hat{\phi}(\hat{\phi} \cdot \vec{H}) &= \mp \hat{\phi} \times \vec{E} Y_i \quad ; \quad \phi = \begin{cases} 0 \\ n\pi \end{cases} \end{aligned} \quad (2)$$

where $\hat{\phi}$ is the unit vector normal to the impedance faces i ($i = a$ for $\phi = 0$, $i = w$ for $\phi = n\pi$), $Y_i = 1/Z_i$. As stated above, when the fields have no z -dependence, it can be shown that the problem can be reduced to two scalar problems, namely, $TM_z, E_z \neq 0, H_z = 0$ and $TE_z, E_z = 0, H_z \neq 0$. Thus, let us define the scalar function U as follows

$$U = \begin{cases} E_z & \text{for } TM_z \\ H_z & \text{for } TE_z \end{cases} \quad (3)$$

The technique used to solve the resulting scalar problem is that which was developed by Maliuzhinets [4]. This method consists of expressing the total field as a spectrum of plane waves which can be written as an integral over a spectral function

$$U(\rho, \phi) = \frac{U_0}{2\pi i} \int_{\gamma} \tilde{U}(\alpha + \frac{n\pi}{2} - \phi, \nu^{e,h}) e^{-ik\rho \cos \alpha} d\alpha \quad (4)$$

where ρ is the distance from the tip of the wedge to the point of observation and it is assumed that the incident field is given by

$$U^{inc}(\rho, \phi) = U_0 e^{-ik\rho \cos(\phi - \phi')} \quad (5)$$

The spectral function \tilde{U} in (4) can be written as follows:

$$\tilde{U}(\alpha, \nu^{e,h}) = \frac{\Psi(\alpha, \nu_a^{e,h}, \nu_w^{e,h})}{\Psi(\frac{n\pi}{2} - \phi', \nu_a^{e,h}, \nu_w^{e,h})} \sigma(\alpha) \quad (6)$$

$$\sigma(\alpha) = \frac{\sin(\frac{\phi'}{n})/n}{\sin(\frac{\alpha}{n}) - \cos(\frac{\phi'}{n})} \quad (7)$$

The function $\Psi(\alpha, \nu_a^{e,h}, \nu_w^{e,h})$ can be written in terms of the well known Maliuzhinets function $\psi_n(\alpha)$ [4] and is given by

$$\begin{aligned} \Psi(\alpha, \nu_a^{e,h}, \nu_w^{e,h}) &= \psi_n\left(\alpha + \frac{n\pi}{2} + \nu_a^{e,h} - \frac{\pi}{2}\right) \psi_n\left(\alpha + \frac{n\pi}{2} - \nu_a^{e,h} + \frac{\pi}{2}\right) \\ &\quad \cdot \psi_n\left(\alpha - \frac{n\pi}{2} + \nu_w^{e,h} - \frac{\pi}{2}\right) \psi_n\left(\alpha - \frac{n\pi}{2} - \nu_w^{e,h} + \frac{\pi}{2}\right) \end{aligned} \quad (8)$$

where

$$\sin \nu_{a,w} = \begin{cases} \eta_0/Z_{a,w} & \text{for } TM_z, \nu = \nu^e \\ Z_{a,w}/\eta_0 & \text{for } TE_z, \nu = \nu^h \end{cases} \quad (9)$$

and η_0 is the free-space intrinsic impedance. The integration path in (4) is along the twofold Sommerfeld contour γ shown in Fig. 2 of [6]. This means that the

scattered field from an interior impedance wedge in the form of a spectral integral is available for further analysis.

II.A Junction of Impedance Wedge and Resistive Half Plane

The next step is to combine the even and odd solutions as depicted in Fig. 2 to obtain the fields for the wedge-resistive half plane junction Q_2 shown in Fig. 1 with $L \rightarrow \infty$. Keeping in mind that the origin of the coordinate system is Q_2 and the angles ϕ and ϕ' are measured from the face of the R_a resistive strip, the total field can be written as follows ($-\pi \leq \phi \leq \pi$, $0 \leq \phi' \leq \pi$)

$$U(\rho, \phi) = \frac{U^{\text{inc}}(Q_2)}{2\pi i} \int_{\gamma} \frac{1}{2} \left[\tilde{U}^v(\alpha + \frac{n\pi}{2} - |\phi|, \nu^e, h) + \text{sgn}(\phi) \tilde{U}^o(\alpha + \frac{n\pi}{2} - |\phi|, \nu^e, h) \right] e^{-ik\rho \cos \alpha} d\alpha \quad (10)$$

where $\text{sgn}(x)$ is the sign function defined as follows

$$\text{sgn}(x) = \begin{cases} -1 & \text{for } x < 0 \\ 1 & \text{for } x > 0 \end{cases} \quad (11)$$

The spectral functions $\tilde{U}^{v,o}(\alpha, \nu)$ are given by ($Z_a = 2R_a$)

$$\begin{aligned} \text{TE}_z: \quad \tilde{U}^o(\alpha, \nu^h) &= \frac{\Psi(\alpha, \nu_a^h, \nu_w^h)}{\Psi(\frac{n\pi}{2} - \phi', \nu_a^h, \nu_w^h)} \sigma(\alpha) \\ \tilde{U}^v(\alpha, \nu^h) &= -\frac{\sin(\frac{\alpha}{2n} - \frac{\pi}{4}) \psi_n(\alpha - \frac{n\pi}{2} + \nu_w^h - \frac{\pi}{2}) \psi_n(\alpha - \frac{n\pi}{2} - \nu_w^h + \frac{\pi}{2}) \sigma(\alpha)}{\sin(\frac{\phi'}{2n}) \psi_n(\nu_w^h - \frac{\pi}{2} - \phi') \psi_n(-\nu_w^h + \frac{\pi}{2} - \phi')} \\ \text{TM}_z: \quad \tilde{U}^v(\alpha, \nu^e) &= \tilde{U}^o(\alpha, \nu^h) \\ \tilde{U}^o(\alpha, \nu^e) &= \frac{\psi_n(\alpha - \frac{n\pi}{2} + \nu_w^e - \frac{\pi}{2}) \psi_n(\alpha - \frac{n\pi}{2} - \nu_w^e + \frac{\pi}{2}) \sigma(\alpha)}{\psi_n(\nu_w^e - \frac{\pi}{2} - \phi') \psi_n(-\nu_w^e + \frac{\pi}{2} - \phi')} \end{aligned} \quad (12)$$

Note that in (12) the expression for $\tilde{U}^v(\alpha, \nu^e)$ for the TM_z case is obtained from the previous expression for $\tilde{U}^o(\alpha, \nu^h)$ for the TE_z case with ν^h replaced by ν^e .

Although (10) cannot be evaluated in closed form, having this integral in the form of a spectrum of plane waves is particularly useful for evaluating multiply diffracted fields as will be seen later. An alternative and more useful representation of this integral can also be obtained (shown in the next section) by deforming the original contour γ into two steepest descent contours.

II.B. Asymptotic evaluation of Diffracted Field

The integral in (10) is now evaluated asymptotically by deforming the Sommerfeld contour as shown in Fig. 4 of [6].

Contributions from integrating along the SDP gives the diffracted field, $U^d(\rho, \phi)$, while the residues from encircling the G.O. and S.W. poles give rise to the G.O. and surface wave fields, $U^{\text{G.O.}}(\rho, \phi)$ and $U^{\text{S.W.}}(\rho, \phi)$, respectively. The total field can then be expressed as

$$U(\rho, \phi) = U^{\text{G.O.}}(\rho, \phi) + U^{\text{S.W.}}(\rho, \phi) + U^d(\rho, \phi) \quad (13)$$

To somewhat simplify the analysis that follows, it is assumed that $\frac{1}{2} \leq n \leq 1$ in the rest of this paper. Note that in most practical applications $\frac{1}{2} \leq n$.

Thus, the G.O. field is given by

for $0 \leq \phi \leq n\pi$:

$$\begin{aligned}
 U^{G.O.}(\rho, \phi) = & U^{inc}(\rho, \phi) + \frac{1}{2} [\Gamma(\phi', \nu_a^{e,h}) \mp 1] U_0 e^{-ik\rho \cos(\phi+\phi')} S(\pi - \phi - \phi') \\
 & + \Gamma(n\pi - \phi', \nu_w^{e,h}) U_0 e^{-ik\rho \cos(\phi+\phi'-2n\pi)} S(\phi + \phi' - [2n-1]\pi) \\
 & + \frac{1}{2} \Gamma(n\pi + \phi', \nu_w^{e,h}) U_0 [\Gamma(\phi', \nu_a^{e,h}) \mp 1] e^{-ik\rho \cos(\phi-\phi'-2n\pi)} \\
 & \cdot S(\phi - \phi' - [2n-1]\pi) S(-\phi + \phi' + n\pi) + \frac{1}{2} \Gamma(n\pi - \phi', \nu_w^{e,h}) \\
 & \cdot U_0 [\Gamma(2n\pi - \phi', \nu_a^{e,h}) \mp 1] e^{-ik\rho \cos(\phi-\phi'+2n\pi)} S(\phi - \phi' + n\pi) \\
 & \cdot S(-\phi + \phi' - [2n-1]\pi) ; \quad \left\{ \begin{array}{l} TM_z \\ TE_z \end{array} \right\} \quad (14)
 \end{aligned}$$

for $-n\pi \leq \phi \leq 0$:

$$\begin{aligned}
 U^{G.O.}(\rho, \phi) = & \frac{1}{2} [1 \pm \Gamma(\phi', \nu_a^{e,h})] U_0 e^{-ik\rho \cos(-\phi+\phi')} S(\pi + \phi - \phi') \\
 & + \frac{1}{2} \Gamma(n\pi + \phi', \nu_w^{e,h}) [1 \pm \Gamma(\phi', \nu_a^{e,h})] U_0 e^{-ik\rho \cos(-\phi-\phi'-2n\pi)} \\
 & \cdot S(-\phi - \phi' - [2n-1]\pi) S(\pi[1-n] - \phi') \\
 & + \frac{1}{2} \Gamma(n\pi - \phi', \nu_w^{e,h}) [1 \pm \Gamma(\phi', \nu_a^{e,h})] U_0 e^{-ik\rho \cos(-\phi-\phi'-2n\pi)} \\
 & \cdot S(\phi + \phi' - [2n-1]\pi) S(\phi' - [2n-1]\pi) ; \quad \left\{ \begin{array}{l} TM_z \\ TE_z \end{array} \right\} \quad (15)
 \end{aligned}$$

where $S(x)$ is the unit step function defined as follows

$$S(x) = \begin{cases} 0 & \text{for } x < 0 \\ 1 & \text{for } x \geq 0 \end{cases} \quad (16)$$

and $\Gamma(\phi', \nu)$ is the Fresnel reflection coefficient, namely

$$\Gamma(\phi', \nu) = \frac{\sin \phi' - \sin \nu}{\sin \phi' + \sin \nu} \quad (17)$$

It is noted that the expressions in (14) and (15) would include additional multiple reflected terms for values of n less than $\frac{1}{2}$.

A surface wave pole arises from the singularity in the function $\Psi(\alpha + \frac{n\pi}{2} - \phi, \nu_a, \nu_w)$ which occurs in the spectral function given in (12). If this pole is captured by the contour, it corresponds to a surface wave propagating along the face of the wedge which is given by

TM_z:

$$U^{S.W.}(\rho, \phi) = \frac{U^{inc}(Q_2)}{2} \cdot [r_{sw}^v(\phi', \nu_w^e) + \text{sgn}(\phi)r_{sw}^o(\phi', \nu_w^e)] e^{-ik\rho \cos \alpha_{sw}^e S(|\phi| - \phi_{sw}^e)}$$

TE_z:

$$U^{S.W.}(\rho, \phi) = \frac{U^{inc}(Q_2)}{2} \cdot [r_{sw}^v(\phi', \nu_w^h) + \text{sgn}(\phi)r_{sw}^o(\phi', \nu_w^h)] e^{-ik\rho \cos \alpha_{sw}^h S(|\phi| - \phi_{sw}^h)} \quad (18)$$

where $\nu_w = \nu_{wR} + i\nu_{wI}$, $\alpha_{sw}^h = -\nu_w^h - \pi + |\phi| - n\pi$, $\phi_{sw}^h = n\pi + \nu_{wR}^h + \text{sgn}(\nu_{wI}^h) \arccos\left(\frac{1}{\cosh \nu_{wI}^h}\right)$ and r_{sw} is the residue for the corresponding spectral function given in (12) evaluated at $\alpha = \alpha_{sw}$ with Z_w as the impedance of the wedge face, namely

$$r_{sw}^{v,o}(\phi', \nu_w^{e,h}) = \lim_{\alpha \rightarrow \alpha_{sw}} (\alpha - \alpha_{sw}) \tilde{U}^{v,o}\left(\alpha + \frac{n\pi}{2} - |\phi|, \nu_w^{e,h}\right) \quad (19)$$

To simplify the evaluation of the diffracted field, the two SDP contours shown in Fig. 4 of [6] are shifted so as to combine them into a single SDP contour in the ω plane where the saddle point is at $\omega = |\phi|$. The diffracted field can then be written as

$$U^d(\rho, \phi) = \frac{U^{inc}(Q_2)}{2\pi i} \int_{SDP(|\phi|)} \frac{1}{2} [B_2^v(\omega, \phi') + \text{sgn}(\phi)B_2^o(\omega, \phi')] e^{ik\rho \cos(\omega - |\phi|)} d\omega \quad (20)$$

where the contour $SDP(|\phi|)$ is from $[\phi - \pi/2 + i\infty]$ to $[\phi + \pi/2 - i\infty]$. The spectral functions $B_2^{v,o}(\omega, \phi')$ can be written in terms of the Maliuzhinets functions and a summation involving cotangent functions [5]

TM_z:

$$B_2^v(\omega, \phi') = \frac{\psi_n^8(\frac{\pi}{2})}{8n\Psi(\frac{n\pi}{2} - \phi', \nu_a^e, \nu_w^e)\Psi(\frac{n\pi}{2} - \omega, \nu_a^e, \nu_w^e)} \cdot \sum_{i=1}^2 \sum_{j=1}^2 \epsilon_i \epsilon_j A(\epsilon_i \omega, \epsilon_j \phi', \nu_a^e, \nu_w^e) \cot\left(\frac{\pi - \epsilon_i \omega + \epsilon_j \phi'}{2n}\right)$$

$$B_2^o(\omega, \phi') = \lim_{Z_a \rightarrow 0} B_2^v(\omega, \phi')$$

TE_z:

$$B_2^o(\omega, \phi', \nu_{a,w}^h) = B_2^v(\omega, \phi', \nu_{a,w}^e)$$

$$B_2^v(\omega, \phi') = \lim_{Z_a \rightarrow 0} B_2^o(\omega, \phi') \quad (21)$$

where

$$\epsilon_i = \begin{cases} 1 & \text{for } i = 1 \\ -1 & \text{for } i = 2 \end{cases} \quad (22)$$

and

$$\begin{aligned}
 A(\omega, \phi', \nu_a, \nu_w) &= C_1(\nu_a, \nu_w) - C_2(\nu_a, \nu_w) [\sin(\phi'/n) - \sin(\omega/n)] \\
 &\quad + \sin(\phi'/n) \sin(\omega/n) \\
 C_1(\nu_a, \nu_w) &= \cos\left(\frac{\pi - 2\nu_a}{2n}\right) \cos\left(\frac{\pi - 2\nu_w}{2n}\right) - \cos^2\left(\frac{\pi}{2n}\right) \\
 C_2(\nu_a, \nu_w) &= \frac{\cos\left(\frac{\pi - 2\nu_a}{2n}\right) - \cos\left(\frac{\pi - 2\nu_w}{2n}\right)}{2 \sin\left(\frac{\pi}{2n}\right)} \quad (23)
 \end{aligned}$$

Note that in (21) the expression for $B_2^o(\omega, \phi', \nu_{a,w}^h)$ for the TE_z case is obtained from the previous expression for $B_2^v(\omega, \phi', \nu_{a,w}^e)$ for the TM_z case with $\nu_{a,w}^e$ replaced by $\nu_{a,w}^h$. The limit in (21) should be taken taking into account that $\psi_n(\alpha) = O\{\exp\left|\frac{Im(\alpha)}{4n}\right|\}$ as $|Im\alpha| \rightarrow \infty$. The integral given in (20) can now be evaluated asymptotically using the Van der Waerden method [7]. The function $B_2(\omega, \phi')$ is an analytic function except for some real and complex simple poles. The real poles arise from the cotangent functions which correspond to the G.O. poles and are located at $\omega_1 = \pi - \phi'$, $\omega_2 = -\pi + \phi'$, $\omega_3 = -\phi' + (2n-1)\pi$, $\omega_4 = -\omega_3$ and $\omega_5 = -\phi' - (2n-1)\pi$. The complex pole which is closest to the saddle point comes from the function $\Psi\left(\frac{n\pi}{2} - \omega, \nu_a, \nu_w\right)$ and occurs at $\omega_6 = -\nu_w - n\pi - \pi$. This pole corresponds to a surface wave traveling away from the edge along the wedge face.

The asymptotic evaluation of (20) yields ($|\phi| \leq n\pi$; $0 \leq \phi' \leq n\pi$) for large $k\rho$

$$\begin{aligned}
 U^d(\rho, \phi) &\sim U^{inc}(Q_2) \frac{e^{ik\rho}}{\sqrt{\rho}} \left\{ D(\phi, \phi') \right. \\
 &\quad \left. + \frac{1}{2i\sqrt{k\pi}} \sum_{l=1}^M \frac{r_l}{s_l} \left[1 - \mathcal{F}(ik\rho s_l^2) \right] \right\} \quad (24)
 \end{aligned}$$

where the diffraction coefficient is given by

$$D(\phi, \phi') = -\frac{e^{i\pi/4}}{\sqrt{2\pi k}} \left(\frac{1}{2} B_2^v(|\phi|, \phi') + \text{sgn}(\phi) \frac{1}{2} B_2^o(|\phi|, \phi') \right) \quad (25)$$

The residues, r_l , are determined by

$$r_l = \lim_{\omega \rightarrow \omega_l} (\omega - \omega_l) \left(\frac{1}{2} B_2^v(\omega, \phi') + \text{sgn}(\phi) \frac{1}{2} B_2^o(\omega, \phi') \right) \quad (26)$$

and

$$s_l = \sqrt{2} e^{i\pi/4} \sin\left(\frac{\omega_l + |\phi|}{2}\right) \quad (27)$$

where ω_l is a pole and $\mathcal{F}(x)$ is the well known transition function given by

$$\mathcal{F}(x) = 2i\sqrt{x} e^{iz} \int_{\sqrt{x}}^{\infty} e^{-t^2} dt \quad ; \quad -3\pi/2 < \arg(x) < \pi/2 \quad (28)$$

II.D Results for Resistive Sheet to Wedge Junction

Now the bistatic scattering from the PEC wedge, resistive sheet configuration shown in Fig. 3 with $n = 0.75$ and $\rho = 2\lambda$ will be examined. For this case the incident field is TM_z , and the incidence angle is 120° . For this incidence angle, there are four shadow boundaries and they are located at $\phi = -60^\circ, -30^\circ, 30^\circ$, and 60° . A plot of the total field, as well as the G.O. and diffracted fields, is shown in Fig. 4(a). Here it is clearly seen how the diffracted field compensates for the discontinuities that occur in the G.O. field at the shadow boundaries which results in a continuous total field.

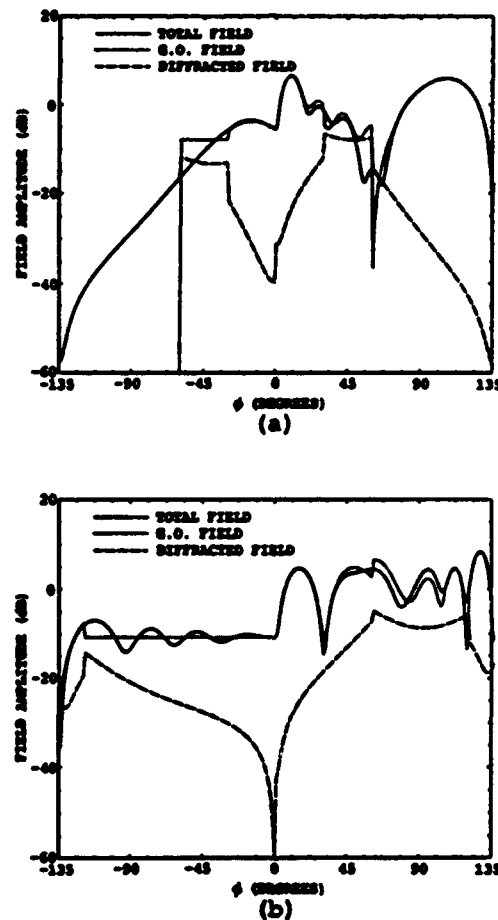


Figure 4. Bistatic scattering for an incident TM_z field for the configuration of Fig. 2 where $R_a = 150 \Omega$, $n = 0.75$ and $\rho = 2\lambda$. (a) $\phi' = 120^\circ$. (b) $\phi' = 30^\circ$.

Next, the same configuration but for an incidence angle of 30° will be examined. In this case there are three shadow boundaries and the incident field penetrates the resistive sheet and reflects from the lower wedge face resulting in a shadow boundary at $\phi = -120^\circ$ (see Fig. 3(c)). The corresponding field plot is shown in Fig. 4(b) for the diffracted, G.O., and total fields. As in the previous case, the diffracted field compensates the G.O. field at the shadow boundaries including the one at $\phi = -120^\circ$, indicating that the solution is valid in the region $\phi < 0$.

II.E Two-part Resistive Half Plane Problem

The second canonical problem to be solved is the diffraction from the point Q_1 in Fig. 1 with $L \rightarrow \infty$, i.e., the half plane problem. However, the more general problem of scattering from the planar junction at Q_1 between two semi-infinite resistive strips as shown in Fig. 2(a) with $L \rightarrow \infty$ (where L is the length of the resistive strip R_a), will be considered first. The solution for the resistive half plane by itself with its edge at Q_1 , can be obtained by letting the value of R_c go to infinity. This two-part problem was obtained previously by H. C. Ly [8] and Rojas, et al. [9,10]. However, for determining multiple diffraction between a resistive card junction and the impedance wedge junction, it is more convenient to have the spectral solution for the resistive card junction in terms of the solution of the impedance wedge junction. Another reason for considering this problem is to show that it can also be obtained by a proper combination of the well known Maliuzhinets wedge solution. To accomplish this, the even and odd mode analysis shown in Fig. 2 is used. The solution can now be obtained from the superposition of the even and odd mode solutions for an impedance wedge with an interior wedge angle of π ($n = 1$). It is worth noting that since $Z_b = 0$ for the TM_z odd case and the TE_z even case (see Fig. 2(b)), there is a diffracted field contribution only for the TM_z even case and for the TE_z odd case. The other two cases only contribute G.O. fields. Simplifying the spectral function defined in (21) with $n = 1$, the following spectral function for the two-part resistive geometry of Fig. 2(a) is obtained, where the resistive strip R_a is assumed to be infinitely long,

$$B_{TM,TE}(\omega, \phi'_1) = B_1^{v,o}(\omega, \phi'_1) \\ = - \frac{\psi_1^8(\frac{\pi}{2})(\sin \nu_a^{e,h} - \sin \nu_c^{e,h}) \sin \omega \sin \phi'_1}{\Psi(\frac{\pi}{2} - \phi'_1, \nu_a^{e,h}, \nu_c^{e,h}) \Psi(\frac{\pi}{2} - \omega, \nu_a^{e,h}, \nu_c^{e,h}) (\cos \omega + \cos \phi'_1)} \quad (29)$$

where the origin of the coordinate system is Q_1 and the angles ϕ_1 and ϕ'_1 are measured from the face of the R_a resistive strip. The total field can then be written as follows

$$U^{TM,TE}(\rho_1, \phi_1) = \delta \frac{U^{inc}(Q_1)}{2\pi i} \int_{SDP(|\phi_1|)} \frac{1}{2} B_1^{v,o}(\omega, \phi'_1) e^{ik\rho_1 \cos(\omega - |\phi_1|)} d\omega \\ + U_{TM,TE}^{G.O.}(\rho_1, \phi_1) \quad (30)$$

The geometrical optics field is given by

$$\begin{aligned}
 U_{TM,TE}^{G.O.}(\rho_1, \phi_1) = & U^{inc}(\rho_1, \phi_1) S(\phi_1) + \frac{\delta}{2} U^{inc}(Q_1) \\
 & \cdot \{ [\Gamma(\phi'_1, \nu_c^{s,A}) - \text{sgn}(\phi_1)\zeta] S(\pi - |\phi_1| - \phi'_1) \\
 & + [\Gamma(\phi'_1, \nu_c^{s,A}) - \text{sgn}(\phi_1)\zeta] S(|\phi_1| + \phi'_1 - \pi) \} \\
 & \cdot e^{-ik\rho_1 \cos(|\phi_1| + \phi'_1)}
 \end{aligned} \quad (31)$$

where ρ_1 is the distance from Q_1 to the point of observation and

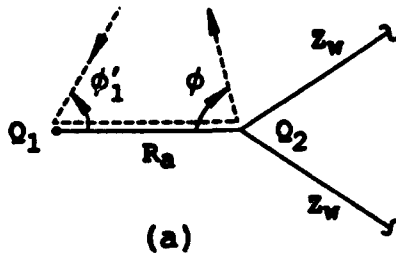
$$\delta = \begin{cases} -1 & \text{TE}_z \text{ case with } \phi_1 < 0 \\ 1 & \text{otherwise} \end{cases} ; \quad \zeta = \begin{cases} 1 & \text{for TM}_z \\ -1 & \text{for TE}_z \end{cases} \quad (32)$$

This spectral function can now be used in conjunction with the spectral function obtained in (21) to obtain the multiple diffraction coefficients.

III. MULTIPLE DIFFRACTION

Once the limit $R_c \rightarrow \infty$ is taken in (29) and (30), the two single diffraction coefficients for Q_1 and Q_2 in Fig. 1 are obtained. In addition to these single diffraction terms, there is also multiple diffraction that can occur between Q_1 and Q_2 . For this analysis, the double and triple diffraction terms which are shown in Fig. 5 are being considered.

DOUBLE DIFFRACTION



TRIPLE DIFFRACTION

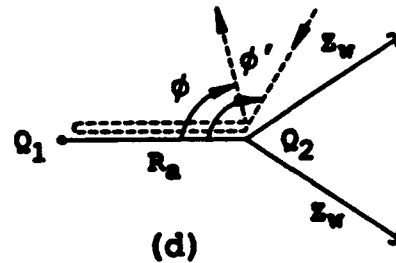
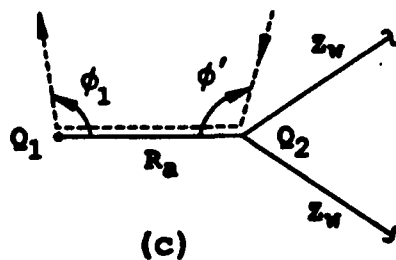
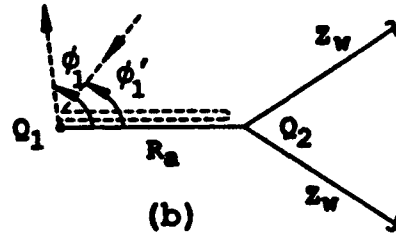


Figure 5. Multiple diffraction between wedge tip Q_2 and resistive strip edge Q_1 .

Since the field which is diffracted from the first diffraction point is in general not ray optical at the second point of diffraction, the multiple diffraction coefficient cannot be obtained by successive application of the single diffraction coefficient. Instead, the spectrally extended ray technique developed by Tiberio and Kouyoumjian [11,12,13] is used. In this method, the field which is diffracted from the first diffraction point is expanded into a spectrum of plane waves and each plane wave component is multiplied by the diffraction coefficient of the second point of diffraction. The spectral integral is then evaluated asymptotically which yields the correct multiple diffraction coefficient.

III.A Evaluation of Doubly Diffracted Field

The configuration which is used to solve for the doubly diffracted field is shown in Figs. 5(a),(c). For a field incident on Q_1 with incidence angle ϕ'_1 , its scattered field can be represented by a spectrum of plane waves with complex scattering angle ω . Next, this scattered spectral component is considered to be incident on Q_2 with incidence angle $-\omega$ and scatters with an angle of ϕ . The far-zone doubly diffracted field can now be written as a spectral integral with the SDP passing through the origin, namely

$$U_{12}^d(\phi, \phi'_1) = -\frac{\delta U^{\text{inc}}(Q_1) e^{i\pi/4} f(\rho)}{8\pi i \sqrt{2\pi k}} \int_{SDP(0)} B_1^{v,o}(\omega, \phi'_1) B_2^{v,o}(|\phi|, -\omega) e^{ikL \cos(\omega)} d\omega \quad (33)$$

where $f(y) = \exp(iky)/\sqrt{y}$. The contour $SDP(0)$ is from $[-\frac{\pi}{2} + i\infty]$ to $[\frac{\pi}{2} - i\infty]$ and the superscripts "v" and "o" correspond to the TM_z and TE_z cases, respectively. The integral given by (33) is now evaluated asymptotically by first mapping into the u -plane, where $u = \sqrt{2} \exp(i\pi/4) \sin(\omega/2)$ and then using the modified Pauli-Clemmow method. The resulting doubly diffracted field can be written as follows

$$U_{12}^d(\phi, \phi'_1) \sim U^{\text{inc}}(Q_1) D_{12}(\phi, \phi'_1) f(\rho) f(L) \quad (34)$$

where the double diffraction coefficient is given by

$$\begin{aligned} D_{12}^{\text{TM}}(\phi, \phi'_1) = & \left[-\delta i \psi_1^4\left(\frac{\pi}{2}\right) \psi_n^8\left(\frac{\pi}{2}\right) u_\xi^2 \sin(\phi'_1/2)(1 + \cos \nu_s^e) \right] \\ & \cdot \left[16\pi k n^2 \psi_1(-\phi'_1 + \frac{\pi}{2} + \nu_s^e) \psi_1(-\phi'_1 + \frac{3\pi}{2} - \nu_s^e) \right. \\ & \cdot \left. \psi_1^2\left(\frac{\pi}{2} + \nu_s^e\right) \Psi\left(\frac{n\pi}{2}, \nu_s^e, \nu_w^e\right) \right]^{-1} \\ & \cdot \frac{1}{\Psi\left(\frac{n\pi}{2} - |\phi|, \nu_s^e, \nu_w^e\right)} \sum_{j=1}^2 \epsilon_j \left(\prod_{m=1}^M (-u_{k_m}^2) \sum_{n=1}^N Y_{p_n} [1 - \mathcal{F}(ikLu_{p_n}^2)] \right) \\ & \cdot G_j(|\phi|) \end{aligned}$$

$$D_{12}^{\text{TE}}(\phi, \phi'_1) = \frac{-\delta \psi_1^4(\frac{\pi}{2}) \psi_n^8(\frac{\pi}{2}) u_5^2 \sin \phi'_1}{16\pi k n^2 \psi_1(-\phi'_1 + \frac{\pi}{2} + \nu_a^A) \psi_1(-\phi'_1 + \frac{\pi}{2} - \nu_a^A) \psi_1^2(\frac{\pi}{2} + \nu_a^A)} \cdot \frac{1}{\Psi(\frac{n\pi}{2} - |\phi|, \nu_a^A, \nu_w^A) \Psi(\frac{n\pi}{2}, \nu_a^A, \nu_w^A) \tan(\nu_a^A/2)} \cdot \sum_{j=1}^2 \epsilon_j \left(\prod_{m=1}^M (-u_{km}^2) \sum_{n=1}^N Y_{pn} [1 - \mathcal{F}(ikLu_{pn}^2)] \right) G_j(|\phi|) \quad (35)$$

where

$$G_j(|\phi|) = 2 \left[C_2(\nu_a, \nu_w) + \sin\left(\frac{\epsilon_j |\phi|}{n}\right) \right] \cot\left(\frac{\pi + \epsilon_j |\phi|}{2n}\right) + A(\epsilon_j |\phi|, 0, \nu_a, \nu_w) \csc^2\left(\frac{\pi + \epsilon_j |\phi|}{2n}\right) \quad (36)$$

and

$$Y_{pn} = (u_{pn}^2 - u_5^2) \left[\prod_{m=1, m \neq n}^N (u_{pn}^2 - u_{pm}^2) \right]^{-1} \quad (37)$$

The poles in the u -plane are then tabulated accordingly;

$$\begin{aligned} u_1 &= \sqrt{2}e^{i\pi/4} \sin(|\phi| - \pi)/2 \\ u_2 &= \sqrt{2}e^{i\pi/4} \sin([(2n-1)\pi - |\phi|]/2) \\ u_3 &= \sqrt{2}e^{i\pi/4} \sin([(2n-1)\pi + |\phi|]/2) \\ u_4 &= \sqrt{2}e^{i\pi/4} \sin([\phi'_1 - \pi]/2) \\ u_5 &= \sqrt{2}e^{i\pi/4} \sin([- \nu_a]/2) \\ u_6 &= \sqrt{2}e^{i\pi/4} \sin([(4n-1)\pi - |\phi|]/2) \end{aligned} \quad (38)$$

The indices used in the summation and product terms of (35) are defined in Table 1 for $\beta = |\phi|$. Using reciprocity, the doubly diffracted field $U_{21}^d(\phi_1, \phi')$ from Q_2 to Q_1 is given in (34) with Q_1 , ρ and $D_{12}(\phi, \phi'_1)$ replaced by Q_2 , ρ_1 and $D_{21}(\phi_1, \phi')$, respectively, where

$$D_{21}(\phi_1, \phi') = D_{12}(\phi, \phi'_1) \quad (39)$$

j	β	M	k_m ($m = 1, M$)	N	p_n ($n = 1, N$)
1	$\beta < 2\pi(2n-1)$	1	2	3	2, 4, 5
1	$\beta \geq 2\pi(2n-1)$	2	2, 6	4	2, 4, 5, 6
2	$\beta < 2\pi(1-n)$	2	1, 3	4	1, 3, 4, 5
2	$\beta \geq 2\pi(1-n)$	1	1	3	1, 4, 5

Table 1. Indices used to identify corresponding poles in the u -plane.

III.B Triple Diffraction

Here, the far-zone fields which are triply diffracted from Q_1 and from Q_2 (see Fig. 5(b),(d)) are determined. The spectral representation for the field diffracted from Q_1 is given by

$$U_{121}^d(\phi_1, \phi'_1) = \delta \frac{U^{\text{inc}}(Q_1)}{4\pi i} f(L) f(\rho_1) \int_{SDP(0)} B_1^{v,o}(|\phi_1|, -\omega) D_{12}^{\text{TM,TE}}(\omega, \phi'_1) \cdot e^{ikL \cos \omega} d\omega \quad (40)$$

where $D_{12}^{\text{TM,TE}}(\omega, \phi'_1)$ is the double diffraction coefficient for the field incident on Q_1 with incidence angle ϕ'_1 and diffracted from Q_2 with a complex scattering angle ω , and $B_1^{v,o}(|\phi_1|, -\omega)$ is the spectral function for the field incident on Q_1 with incidence angle $-\omega$ and diffracted with angle ϕ_1 (B_1^v for TM_z and B_1^o for TE_z). Likewise, one gets the following for the field triply diffracted from Q_2

$$U_{212}^d(\phi, \phi') = \delta \frac{U^{\text{inc}}(Q_2)}{4\pi i} f(L) f(\rho) \int_{SDP(0)} B_2^{v,o}(|\phi|, -\omega) D_{21}^{\text{TM,TE}}(\omega, \phi') \cdot e^{ikL \cos \omega} d\omega \quad (41)$$

The asymptotic evaluation of (40) and (41) are conducted in the same manner as for the double diffraction case. For the evaluation of the diffraction coefficient from point Q_1 , the poles arise from the single diffraction term from Q_1 , given by the term $B_1^{v,o}(|\phi_1|, -\omega)$ in (40). The resulting triply diffracted field from Q_1 is

$$U_{121}^d(\phi_1, \phi'_1) \sim U^{\text{inc}}(Q_1) D_{121}(\phi_1, \phi'_1) f(\rho_1) f^2(L) \quad (42)$$

where

$$\begin{aligned} D_{121}^{\text{TM}}(\phi_1, \phi'_1) = & -\frac{\delta \sqrt{2} e^{i\pi/4} \psi_1^8(\frac{\pi}{2}) \psi_n^8(\frac{\pi}{2}) u_s^4 \cos^2(n\pi) \sin(\phi'_1/2) \sin(|\phi_1|/2)}{8n^3(\pi k)^{3/2} \psi_1^4(\frac{\pi}{2} + \nu_s^e) \Psi^2(\frac{n\pi}{2}, \nu_s^e, \nu_w^e) \psi_1(-|\phi_1| + \frac{\pi}{2} + \nu_s^e)} \\ & \cdot \frac{(1 + \cos \nu_s^e)^2 \Delta^D(\phi'_1) \Delta^T(|\phi_1|)}{\psi_1(-|\phi_1| + \frac{3\pi}{2} - \nu_s^e) \psi_1(-\phi'_1 + \frac{\pi}{2} + \nu_s^e) \psi_1(-\phi'_1 + \frac{3\pi}{2} - \nu_s^e)} \\ & \cdot \left[-C_1(\nu_s^e, \nu_w^e) \csc^2\left(\frac{\pi}{2n}\right) \cot\left(\frac{\pi}{2n}\right) + 2 \cot\left(\frac{\pi}{2n}\right) \right. \\ & \quad \left. - 2C_2(\nu_s^e, \nu_w^e) \csc^2\left(\frac{\pi}{2n}\right) \right] \\ D_{121}^{\text{TE}}(\phi_1, \phi'_1) = & \frac{\delta \sqrt{2} e^{i\pi/4} \psi_1^8(\frac{\pi}{2}) \psi_n^8(\frac{\pi}{2}) u_s^4 \cot^2(\nu_s^e/2)}{8n^3(\pi k)^{3/2} \psi_1(-\phi'_1 + \frac{\pi}{2} + \nu_s^e) \psi_1(-\phi'_1 + \frac{3\pi}{2} - \nu_s^e) \psi_1^4(\frac{\pi}{2} + \nu_s^e)} \\ & \cdot \frac{\sin \phi'_1 \sin |\phi_1| \cos^2(n\pi) \Delta^D(\phi'_1) \Delta^T(|\phi_1|)}{\psi_1(-|\phi_1| + \frac{\pi}{2} + \nu_s^e) \psi_1(-|\phi_1| + \frac{3\pi}{2} - \nu_s^e) \Psi^2(\frac{n\pi}{2}, \nu_s^e, \nu_w^e)} \end{aligned}$$

$$\begin{aligned} & \left[2 \cot \left(\frac{\pi}{2n} \right) - 2C_2(\nu_s^A, \nu_w^A) \csc^2 \left(\frac{\pi}{2n} \right) \right. \\ & \left. - C_1(\nu_s^A, \nu_w^A) \csc^2 \left(\frac{\pi}{2n} \right) \cot \left(\frac{\pi}{2n} \right) \right] \end{aligned} \quad (43)$$

The term u_5 is defined in (38). The function $\Delta^D(\phi'_1)$ is associated with the double diffraction term while $\Delta^T(|\phi_1|)$ is associated with the triple diffraction term. These functions are defined as follows;

$$\begin{aligned} \Delta^D(\phi'_1) &= \sum_{n=1}^3 Y_n^D [1 - \mathcal{F}(ikLu_n^{D^2})] \\ Y_n^D &= (u_n^{D^2} - u_3^{D^2}) \left[\prod_{m=1, m \neq n}^3 (u_n^{D^2} - u_m^{D^2}) \right]^{-1} \\ \Delta^T(|\phi_1|) &= \sum_{n=1}^2 Y_n^T [1 - \mathcal{F}(ikLu_n^{T^2})] \\ Y_n^T &= (u_n^{T^2} - u_2^{T^2}) \left[\prod_{m=1, m \neq n}^2 (u_n^{T^2} - u_m^{T^2}) \right]^{-1} \end{aligned} \quad (44)$$

For the function $\Delta^D(\phi'_1)$, there are three poles in the u -plane which came from the evaluation of the double diffraction term $D_{12}^{v,o}(\omega, \phi'_1)$ in (40) and they are given by

$$\begin{aligned} u_1^D &= \sqrt{2}e^{i\pi/4} \sin([\phi'_1 - \pi]/2) \\ u_2^D &= \sqrt{2}e^{i\pi/4} \sin([2n - 1]\pi/2) \\ u_3^D &= \sqrt{2}e^{i\pi/4} \sin([-\nu_a]/2) \end{aligned} \quad (45)$$

For the term $\Delta^T(|\phi_1|)$, the two poles from $B_1^{v,o}(|\phi_1|, -\omega)$ are being included, namely

$$\begin{aligned} u_1^T &= \sqrt{2}e^{i\pi/4} \sin([|\phi_1| - \pi]/2) \\ u_2^T &= \sqrt{2}e^{i\pi/4} \sin([-\nu_a]/2) \end{aligned} \quad (46)$$

The evaluation of the field triply diffracted from junction Q_2 is slightly more complicated because the poles arise from the term $B_2^{v,o}(|\phi|, -\omega)$ in (41), which is the single diffraction from the wedge-resistive strip junction. This term has more poles than the single diffraction term from point Q_1 . Thus, the triply diffracted field $U_{212}^d(\phi, \phi')$ from Q_2 is given by (42) with Q_1 , ρ_1 and $D_{121}(\phi_1, \phi'_1)$, replaced by Q_2 , ρ and $D_{212}(\phi, \phi')$, respectively, where

$$\begin{aligned}
D_{212}^{TM}(\phi, \phi') &= \frac{-\delta\sqrt{2}e^{i\pi/4}\psi_1^4(\frac{\pi}{2})\psi_n^{16}(\frac{\pi}{2})u_5^4}{512n^4(\pi k)^{3/2}\Psi(\frac{n\pi}{2}-\phi', \nu_s^e, \nu_w^e)\Psi(\frac{n\pi}{2}-|\phi|, \nu_s^e, \nu_w^e)} \\
&\quad \cdot \frac{(1+\cos\nu_s^e)\cot(\nu_s^e/2)}{\psi_1^4(\nu_s^e+\frac{\pi}{2})\Psi^2(\frac{n\pi}{2}, \nu_s^e, \nu_w^e)} \sum_{j=1}^2 \epsilon_j \Lambda_j^D(\phi') \sum_{j=1}^2 \epsilon_j \Lambda_j^T(|\phi|) \\
D_{212}^{TE}(\phi, \phi') &= \frac{\delta i\sqrt{2}e^{i\pi/4}\psi_1^4(\frac{\pi}{2})\psi_n^{16}(\frac{\pi}{2})u_5^4}{256n^4(\pi k)^{3/2}\Psi(\frac{n\pi}{2}-\phi', \nu_s^h, \nu_w^h)\Psi(\frac{n\pi}{2}-|\phi|, \nu_s^h, \nu_w^h)\tan^2(\nu_s^h/2)} \\
&\quad \cdot \frac{1}{\psi_1^4(\nu_s^h+\frac{\pi}{2})\Psi^2(\frac{n\pi}{2}, \nu_s^h, \nu_w^h)} \sum_{j=1}^2 \epsilon_j \Lambda_j^D(\phi') \sum_{j=1}^2 \epsilon_j \Lambda_j^T(|\phi|) \quad (47)
\end{aligned}$$

Again, the term u_5 is defined in (38). The function $\Lambda_j^D(\phi')$ is associated with the double diffraction term while $\Lambda_j^T(|\phi|)$ is associated with the triple diffraction term. These functions are defined as follows:

$$\begin{aligned}
\Lambda_j^\alpha(\beta) &= \left(\prod_{m=1}^M (-u_{k_m}^{\alpha^2}) \sum_{n=1}^N Y_{p_n}^\alpha [1 - \mathcal{F}(ikLu_{p_n}^{\alpha^2})] \right) G_j(\beta) \\
Y_{p_n}^\alpha &= (u_{p_n}^{\alpha^2} - u_5^{\alpha^2}) \left[\prod_{m=1, m \neq n}^N (u_{p_n}^{\alpha^2} - u_{p_m}^{\alpha^2}) \right]^{-1} \quad (48)
\end{aligned}$$

where $\alpha = D$ and $\beta = \phi'$ for the double diffraction term, $\alpha = T$ and $\beta = |\phi|$ for the triple diffraction term, and $G_j(\beta)$ is defined in (36). The poles for the double diffraction term $\Lambda_j^D(\phi')$ are

$$\begin{aligned}
u_1^D &= \sqrt{2}e^{i\pi/4} \sin([\phi' - \pi]/2) \\
u_2^D &= \sqrt{2}e^{i\pi/4} \sin([(2n-1)\pi - \phi']/2) \\
u_3^D &= \sqrt{2}e^{i\pi/4} \sin([(2n-1)\pi + \phi']/2) \\
u_4^D &= -\sqrt{2}e^{i\pi/4} \\
u_5^D &= \sqrt{2}e^{i\pi/4} \sin([- \nu_a]/2) \\
u_6^D &= \sqrt{2}e^{i\pi/4} \sin([(4n-1)\pi - \phi']/2) \quad (49)
\end{aligned}$$

The indices used in the summation and product for the term $\Lambda_j^D(\phi')$ are defined in Table 1 for $\beta = \phi'$. Similarly, the poles for the triple diffraction term $\Lambda_j^T(|\phi|)$

are

$$\begin{aligned}
 u_1^T &= \sqrt{2}e^{i\pi/4} \sin(|\phi| - \pi)/2) \\
 u_2^T &= \sqrt{2}e^{i\pi/4} \sin([(2n-1)\pi - |\phi|]/2) \\
 u_3^T &= \sqrt{2}e^{i\pi/4} \sin([(2n-1)\pi + |\phi|]/2) \\
 u_5^T &= \sqrt{2}e^{i\pi/4} \sin([- \nu_a]/2) \\
 u_6^T &= \sqrt{2}e^{i\pi/4} \sin([(4n-1)\pi - |\phi|]/2)
 \end{aligned} \tag{50}$$

The indices used in the summation and product for the term $\Lambda_j^T(|\phi|)$ are defined in Table 2.

j	$ \phi $	M	k_m ($m = 1, M$)	N	p_n ($n = 1, N$)
1	$ \phi < 2\pi(2n-1)$	1	2	2	2, 5
1	$ \phi \geq 2\pi(2n-1)$	2	2, 6	3	2, 5, 6
2	$ \phi < 2\pi(1-n)$	2	1, 3	3	1, 3, 5
2	$ \phi \geq 2\pi(1-n)$	1	1	2	1, 5

Table 2. Indices used to identify corresponding poles in the u -plane for the term $\Lambda_j^T(|\phi|)$.

III.C Reflection from Wedge Faces

In addition to the multiple diffraction between the resistive half plane edge Q_1 and the resistive card-wedge junction Q_2 , the fields can also reflect from the wedge faces. The incident ray can first reflect from the wedge face and then diffract from the resistive half plane edge Q_1 and vice versa. Figure 6 shows the various diffraction and reflection mechanisms that were included in this analysis.

The field which is singly diffracted from Q_1 can then reflect from the wedge face and vice versa (Fig. 6(a)). The incident field can also reflect from the wedge face first then diffract from Q_1 then reflect again (Fig. 6(b)). Finally, the field can doubly diffract from Q_2 to Q_1 and then reflect (Fig. 6(c)) and vice versa. The reflected field is obtained by multiplying the field by the appropriate Fresnel reflection coefficient when it reflects from the wedge face. The Fresnel reflection coefficient, $\Gamma(\phi^i, \nu)$, is defined in (17) where ϕ^i is the angle between the ray and the wedge face and $\sin \nu$ is defined in (9). Reflections from the wedge face introduce shadow boundaries into the scattered field. The total field at these shadow boundaries is then compensated for by the appropriate multiple diffraction term.

III.D Double Diffraction Compensation for Shadow Boundary of Single Diffraction Term

For the configuration shown in Fig. 7, where the faces of the wedge are PECs, it is assumed that $n = .6$, $R_a = 100\Omega$, and $L = 1\lambda$. It is of interest to examine the backscattered case for a TM_z field which is singly diffracted from Q_1 and reflected from the wedge face as well as the field which is reflected from the wedge

face and diffracted from Q_1 . This field has a shadow boundary at $\phi_1 = 144^\circ$ as shown in Fig. 8. Also shown in Fig. 8 is the field which is doubly diffracted from Q_1 to Q_2 and from Q_2 to Q_1 . The doubly diffracted field exhibits a slope discontinuity at the shadow boundary which is due to the G.O. pole $\omega = -(2n-1)\pi + |\phi|$ (where $\phi = \pi - \phi_1$) crossing the saddle point when $\phi = (2n-1)\pi$. This slope discontinuity in the diffracted field compensates the diffracted-reflected and the reflected-diffracted fields at the shadow boundary resulting in a total field which is uniform across the shadow boundary.

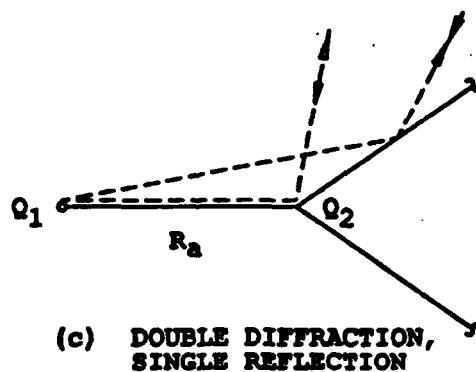
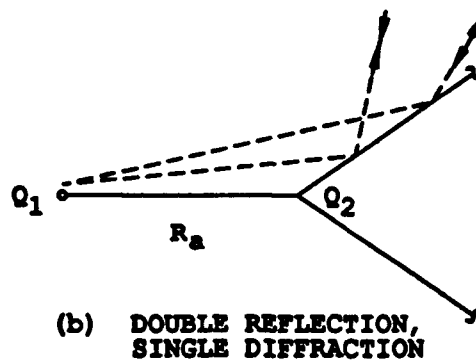
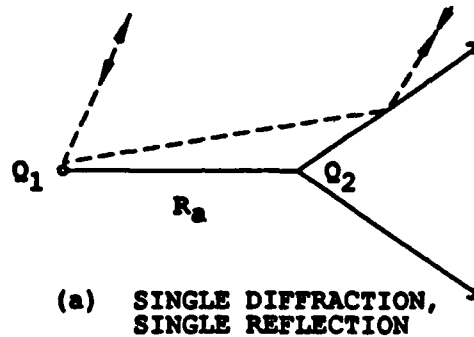


Figure 6. Diffracted-reflected and reflected-diffracted fields.

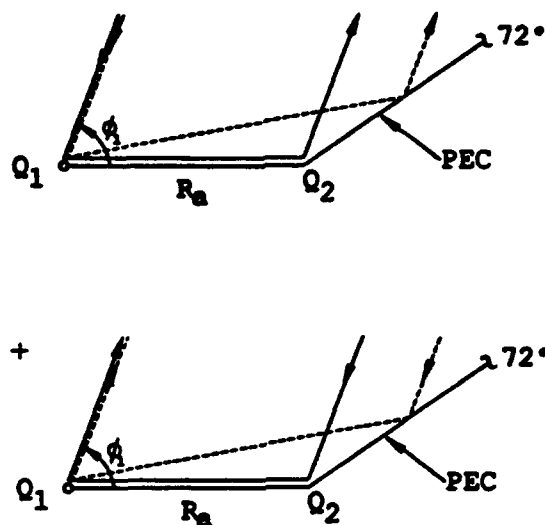


Figure 7. Backscatter ray paths for singly diffracted field reflecting from wedge face, reflected field diffracted from edge Q_1 , and double diffracted field.

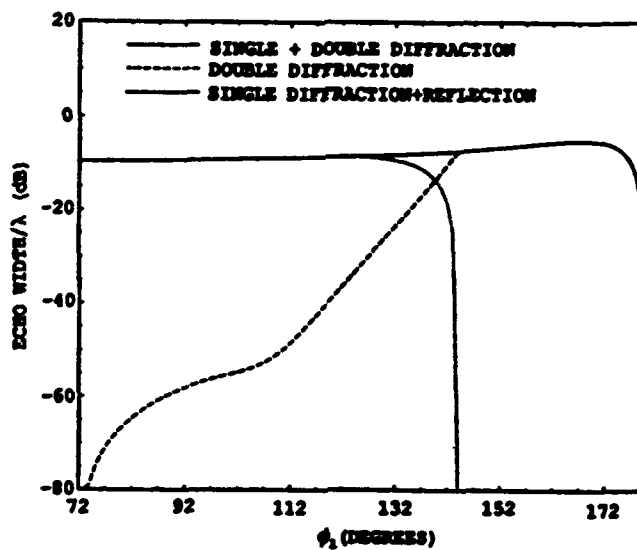


Figure 8. TM_z backscatter singly and doubly diffracted fields corresponding to the configuration shown in Fig. 7 with $R_a = 100\lambda$ and $L = 1\lambda$.

III.E Triple Diffraction Compensation for Shadow Boundary of Double Diffraction Term

Considering the same configuration from the previous example, the bistatic case shown in Fig. 9 will now be examined. Here a field with incidence angle $\phi'_1 = 100^\circ$ is considered which is doubly diffracted from Q_2 to Q_1 and then reflected from the wedge face with a shadow boundary at $\phi_1 = 144^\circ$. Also included in the analysis is the field which is incident at $\phi'_1 = 100^\circ$ and triply diffracted from Q_2 . A plot of both of these components as well as the total field is shown in Fig. 9. As was the case in the previous example, the slope discontinuity in the triply diffracted field compensates the doubly diffracted-reflected field at the shadow boundary.

III.F Surface Wave Fields

As noted in Section II, the faces of the wedge can support surface wave fields, whereas, the resistive strip cannot because R_a is real while Z_w can be complex. The surface wave fields are excited by the fields incident on the resistive strip-wedge junction (Q_2) and travel along both faces of the wedge. In (18), the surface wave fields excited by the incident field of (5) are given. However, additional surface waves are excited by the multiple diffracted fields incident at Q_2 . Therefore, the total surface wave field is the superposition of all these surface wave components. Since the far-zone fields are of interest in this paper, the surface wave fields are not important, except on the faces of the wedge ($\phi = \pm n\pi$) for the lossless case (Z_w purely imaginary). Thus, they are neglected in the present analysis.

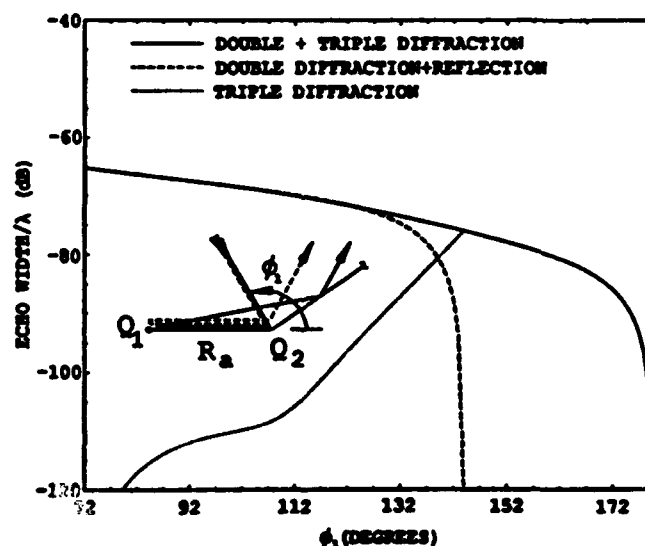


Figure 9. TM_z bistatic doubly diffracted-reflected and triply diffracted fields with $\phi' = 100^\circ$, $R_a = 100\Omega$ and $L = 1\lambda$.

IV. RESULTS

To verify the solutions developed in the previous sections, a comparison was made with a moment method solution [15]. Since this moment method solution is for a resistive card attached to a semi-infinite PEC half plane, only the limiting case of the present UTD solution for a wedge angle $n = 1$ can be checked. The configuration that was used is shown in Fig. 1, for which the incident field is TM_z or TE_z , $n = 1$, $Z_w = 0$ and where the backscattered field is being considered. For the TM_z case, $R_a = 500\Omega$, and for the TE_z case, $R_a = \eta_0^2/(4 \times 500)\Omega$. Since the scattered field is a function of $\sin \nu$ of (9), consider the values of $\sin \nu$ in the three regions of the configuration: free-space (air), resistive card (R_a), and PEC half plane (PEC). For the TM_z case, the values for $\sin \nu^e$ are 0 (air), $\eta_0/1000$ (R_a), and ∞ (PEC), while for the TE_z case, the values for $\sin \nu^h$ are ∞ (air), $\eta_0/1000$ (R_a), and 0 (PEC). Therefore the TM_z and TE_z cases are mirror images of each other. The results are given in Fig. 10, and they show excellent agreement between the TM_z moment method and UTD solutions. As expected, the TE_z UTD solution is a mirror image (with respect to 90°) of the TM_z solution.

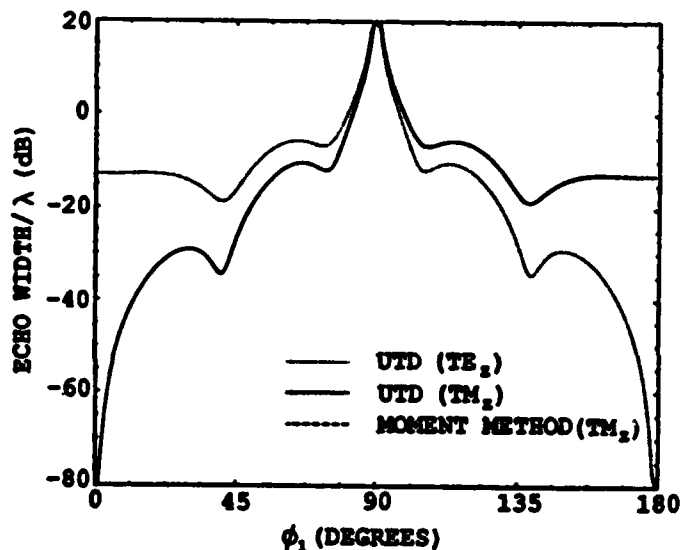


Figure 10. TM_z ($R_a = 500\Omega$), and TE_z ($R_a = 70.94\Omega$) backscatter echo width for UTD vs. moment method solution for the configuration shown in Fig. 1 with $n = 1$, $Z_w = 0$, and $L = 1\lambda$.

An efficient method for numerically computing the Maliuzhinets functions defined in (8) was obtained from the following relation developed by Bernard [14] in which the function is expressed as a product of Gamma functions over a finite number of terms with a remainder that can be expressed as an integral

$$\psi_n(\alpha) = \prod_{l=0}^N \left\{ \frac{\Gamma^2\left(\frac{1}{2} + \frac{1}{2}[l + \frac{1}{2}]/n\right)}{\Gamma\left(\frac{1}{2} + \frac{1}{2}[\alpha/\pi + (l + \frac{1}{2})]/n\right) \Gamma\left(\frac{1}{2} + \frac{1}{2}[-\alpha/\pi + (l + \frac{1}{2})]/n\right)} \right\}^{(-1)^l} \cdot \exp\left(\int_0^\infty \frac{(-1)^{N+1} e^{-\nu(N+1)\pi} (1 - \cosh(\alpha\nu))}{2\nu \cosh(\nu\frac{\pi}{2}) \sinh(\nu n\pi)} d\nu\right) \quad (51)$$

Since the integral is rapidly convergent due to the exponential term in the integrand, the upper limit can be truncated at a reasonable finite value allowing for efficient numerical evaluation of the integral. Three terms were used in the product of the Gamma functions and the limits of integration were from 0 to 1. The integration was carried out using an 8-point Gaussian integration routine.

The first case that is considered is the backscattered echo width for a PEC wedge with a one wavelength long resistive strip. The configuration is shown in Fig. 1 with a TM_z incident field, $Z_w = 0$ and $n = 0.8$. The results are shown in Fig. 11 for a case with no resistive strip and then for three different resistance values. Incorporating the resistive strip to the wedge introduces a specular component to the scattered field which is indicated by the increased echo width around $\phi_1 = 90^\circ$. For backscattered angles close to endfire, i.e., for ϕ_1 close to 180° , the effect of the strip is to reduce the echo width of the wedge. The same configuration is also examined for a TE_z incident field (Fig. 12). For this case, a PEC wedge with a one wavelength resistive strip of resistance $R_a = 100\Omega$ is compared to a PEC wedge alone. The resistive card has little effect at endfire which is expected since the electric field is normal to the resistive sheet at this point. However, as in the TM_z case, there is a strong reflected field at $\phi_1 = 90^\circ$.

For the next case, the same geometry as in Figs. 11 and 12 is considered for a TM_z incident field but the resistance value is held constant at $R_a = 100\Omega$ while the length of the strip is varied (Fig. 13). As expected, increasing the length of the strip increases the specular component around $\phi_1 = 90^\circ$ but also decreases the echo width near endfire.

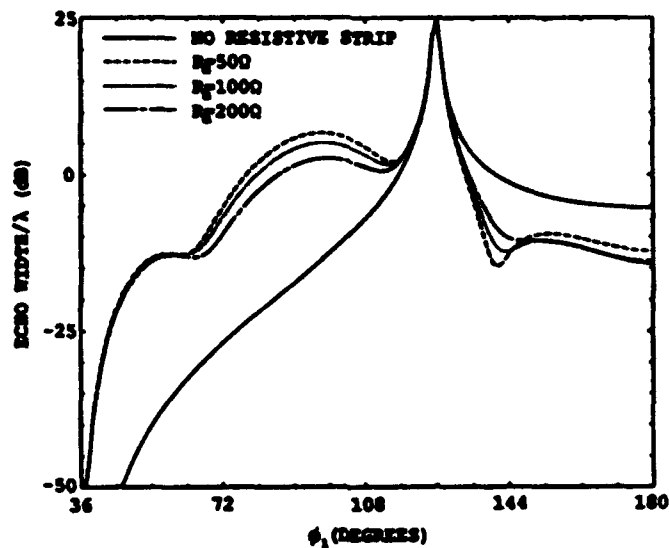


Figure 11. TM₂ backscatter echo width for the configuration shown in Fig. 1 with various values of R_a , $L = 1\lambda$, $Z_w = 0$, and $n = 0.8$.

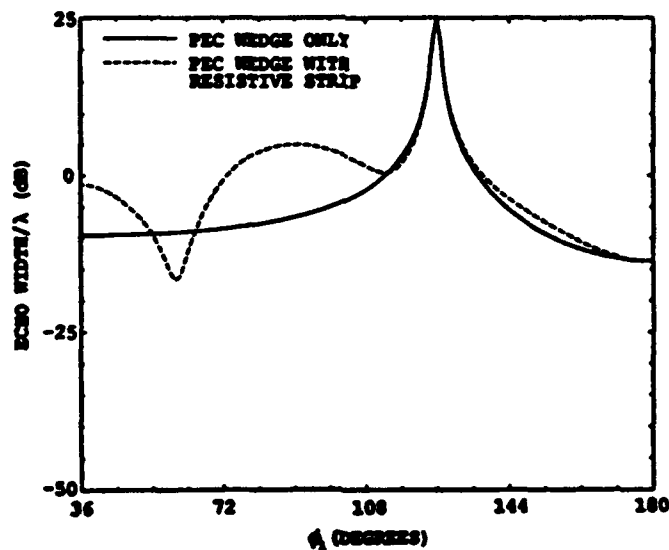


Figure 12. TE₂ backscatter echo width for the configuration shown in Fig. 1 with $R_a = 1000\Omega$, $L = 1\lambda$, $Z_w = 0$, and $n = 0.8$.

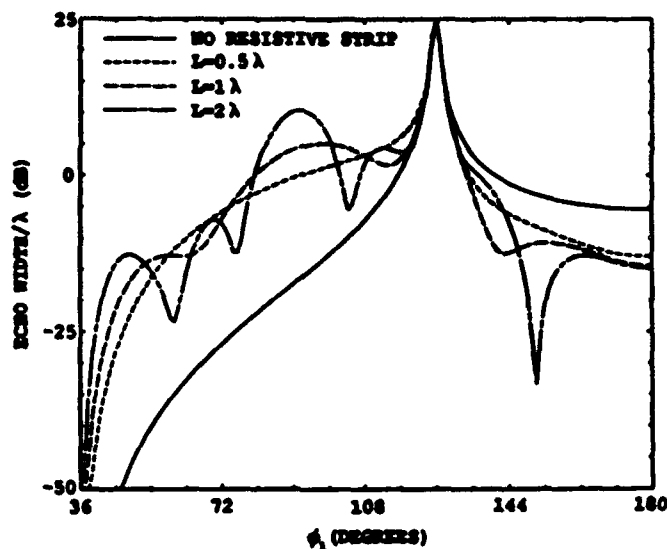


Figure 13. TM_2 backscatter echo width for the configuration shown in Fig. 1 with various values of L , $R_s = 100\Omega$, $Z_w = 0$, and $n = 0.8$.

Another case to be considered is the effect of adding an impedance surface to the wedge faces. The incident field is TM_z , $n = .8$, and the surface impedance is $Z_w = 37.7 - i188.5\Omega$. The backscattered echo width is shown in Fig. 14. Compared to the PEC wedge, the impedance wedge has a reduced echo width near endfire by about 4 dB. Incorporating a one wavelength resistive strip of $R_s = 100\Omega$ to the impedance wedge further reduces the echo width by approximately 9 dB. A bistatic TM_z case is shown in Fig. 15(a) where incident field is near endfire at $\phi'_1 = 179.5^\circ$. Incorporating the impedance surface and the resistive strip reduces the echo width throughout the range of observation angles $-180^\circ < \phi_1 < -36^\circ$ and $36^\circ < \phi_1 < 180^\circ$. Note that in the angular region enclosed by the wedge, i.e., $-36^\circ < \phi_1 < 36^\circ$, the field is exactly zero as expected. The same case is also examined for TE_z polarization (see Fig. 15(b)). The effect of adding the surface impedance is to cause the field to vanish along the wedge faces, however, it has almost no effect in the regions $-180^\circ < \phi_1 < -36^\circ$ and $36^\circ < \phi_1 < 180^\circ$. These results also show that the addition of a resistive card has almost no effect for the TE_z case. Finally, Fig. 16 shows the TM_z backscattered echo width for an impedance wedge with a resistive card attached to its tip (Fig. 1) for two different wedge angles. As expected, the backscattered field near $\phi_1 = 180^\circ$ is decreased by decreasing the interior wedge angle (increasing n).

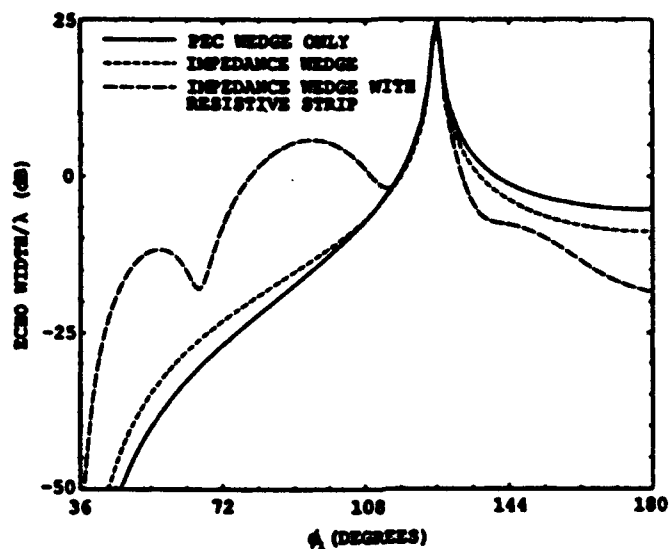
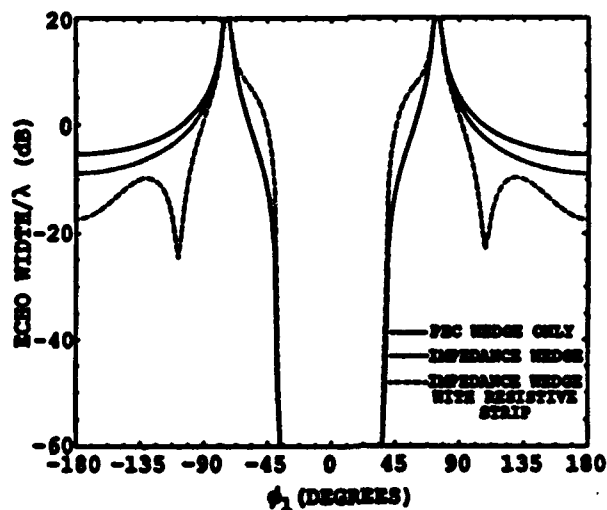


Figure 14. TM_z backscatter echo width for the configuration shown in Fig. 1 comparing the effect of adding an impedance surface to the wedge faces and then a resistive strip. $R_a = 100\Omega$, $L = 1\lambda$, $n = 0.8$, and $Z_w = 37.7 - i188.5\Omega$.



(a)

Figure 15. Bistatic echo width for the configuration shown in Fig. 1 comparing the effect of adding an impedance surface to the wedge faces and then a resistive strip where $R_a = 100\Omega$, $L = 1\lambda$, $n = 0.8$, $Z_w = 37.7 - i188.5\Omega$, and $\phi'_1 = 179.5^\circ$, (a) TM_z .

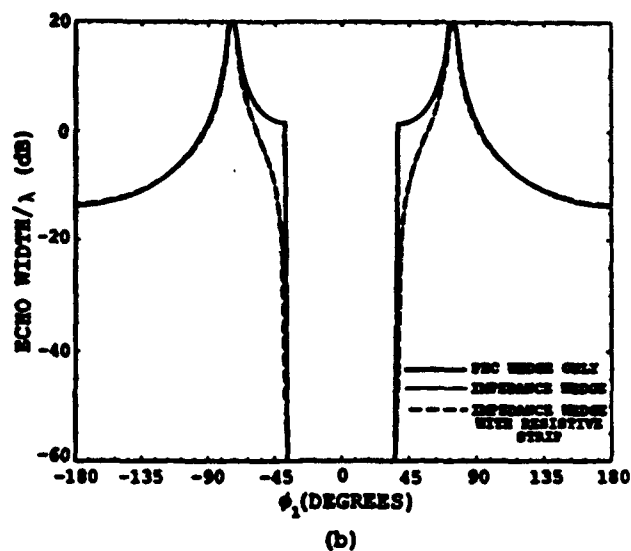


Figure 15. Bistatic echo width for the configuration shown in Fig. 1 comparing the effect of adding an impedance surface to the wedge faces and then a resistive strip where $R_a = 100\Omega$, $L = 1\lambda$, $n = 0.8$, $Z_w = 37.7 - i188.5\Omega$, and $\phi'_1 = 179.5^\circ$ (b) TE_z .

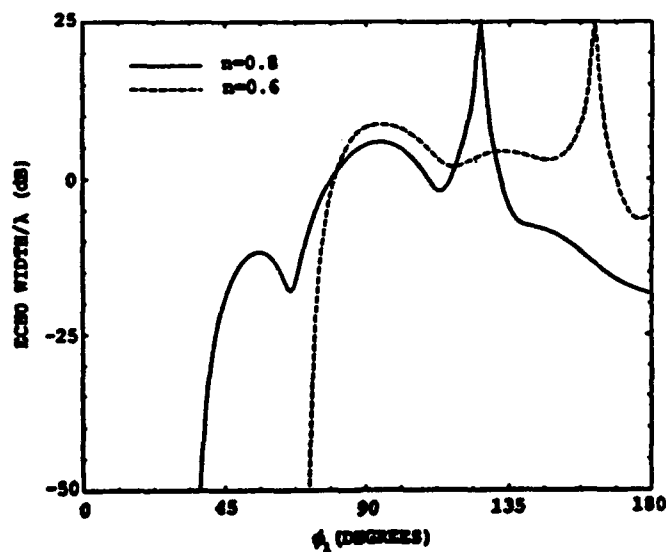


Figure 16. TM_z backscatter echo width for the configuration shown in Fig. 1 for two wedge angles with $R_a = 100\Omega$, $L = 1\lambda$, and $Z_w = 37.7 - i188.5\Omega$.

V. CONCLUSION

A uniform asymptotic solution for the scattering from an impedance wedge (with equal impedances on both faces) attached to a resistive strip was presented. Using an even and odd mode analysis allowed the solution of this problem to be obtained from the solution of the much simpler configuration of an impedance wedge with different impedance faces. The incident field is a plane wave either TM_z or TE_z and the asymptotic evaluation for the scattered field is valid across the shadow boundaries. Since there are two points of diffraction, multiple diffraction between these points up to third order was included in this analysis. Also included in the analysis were reflections from the wedge faces of the diffracted fields as well as fields that are first reflected and then diffracted which introduced shadow boundaries in the scattered field. Careful accounting of the G.O. poles when determining the multiple diffraction terms compensated for the presence of these shadow boundaries.

One of the potential applications for the solutions developed here is that they can be used as design tools for reducing the echo width of wedge shaped structures.

VI. ACKNOWLEDGEMENTS

This work was supported in part by The Ohio State University ElectroScience Laboratory Compact Range Consortium, the Joint Services Electronics Program (Contract N00014-89-J-1007) and by The Ohio State University Research Foundation.

The Editor thanks M. Idemen, J.-M. L. Bernard, and G. Pelosi for reviewing the paper.

REFERENCES

1. Rojas, R. G., and M. F. Otero, "Synthesis of the frequency response of an inhomogeneous resistive strip," Technical Report 721929-21, Ohio State Univ. ElectroScience Lab., Aug. 1990.
2. Rojas, R. G., and M. F. Otero, "Synthesis of the frequency response of an inhomogeneous resistive strip," 1991 IEEE-APS International Symposium, The University of Western Ontario, London, Canada, June 24-28.
3. Rojas, R. G., and M. F. Otero, "Diffraction by a resistive strip attached to an impedance wedge," 1991 URSI Radio Science meeting, The University of Western Ontario, London, Canada, June 24-28.
4. Maliuzhinets, G. D., "Excitation, reflection and emission of surface waves from a wedge with given face impedances," *Sov. Phys. Dokl.*, Vol. 3, 752-755, 1959.
5. Tiberio, R., G. Pelosi, G. Manara and P. H. Pathak, "High-frequency scattering from a wedge with impedance faces illuminated by a line source, Part I: Diffraction," *IEEE Trans. Antennas Propagat.*, Vol. AP-37, No. 2, 212-218, Feb. 1989.
6. Rojas, R. G., "Electromagnetic diffraction of an obliquely incident plane wave field by a wedge with impedance faces," *IEEE Trans. Antennas Propagat.*, Vol. AP-36, No. 7, 956-970, July 1988.
7. Rojas, R. G., "Comparison between two asymptotic methods," *IEEE Trans. Antennas Propagat.*, Vol. AP-35, No. 12, 1489-1492, Dec. 1987.

8. Ly, H. C., "A UTD analysis of the diffraction by planar two- and three-part configurations consisting of thin dielectric/ferrite materials," M.S. Thesis, The Ohio State University, Department of Electrical Engineering, Winter 1989.
9. Rojas, R. G., H. C. Ly and P. H. Pathak, "Electromagnetic plane wave diffraction by a planar junction of two thin dielectric/ferrite half planes," *Radio Science*, Vol. 26, 641-660, May-June 1991.
10. Senior, T. B. A., "Skew incidence on a material junction," *Radio Science*, Vol. 26, 305-311, March-April 1991.
11. Tiberio, R., and R. G. Kouyoumjian, "A uniform GTD solution for the diffraction by strips illuminated at grazing incidence," *Radio Science*, Vol. 14, 933-941, 1979.
12. Tiberio, R., and R. G. Kouyoumjian, "An analysis of diffraction at edges illuminated by transition region fields," *Radio Science*, Vol. 17, 323-336, 1982.
13. Tiberio, R., and R. G. Kouyoumjian, "Calculation of the high-frequency diffraction by two nearby edges illuminated at grazing incidence," *IEEE Trans. Antennas Propagat.*, Vol. AP-32, 1186-1196, Nov. 1984.
14. Bernard, J. M. L., "Diffraction by a metallic wedge covered with Dielectric Material," *Wave Motion*, Vol. 9, 543-561, 1987.
15. Newman, E., "TM and TE scattering by a dielectric/ferrite cylinder in the presence of a half plane," *IEEE Trans. Antennas Propagat.*, Vol. AP-34, No. 6, 804-813, Jun. 1986.
16. Uzgören, G., A. Büyükkaksoy, A. H. Serbest, "Diffraction coefficient related to a discontinuity formed by impedance and resistive halfplanes," *Proc. IEE*, Vol. 136, Pt. H, No. 1, 19-23, Feb. 1989.

Roberto G. Rojas received the B.S.E.E. degree from New Mexico State University, in 1979, and the M.Sc. and Ph.D. degrees in electrical engineering from The Ohio State University, in 1981 and 1985, respectively. Since 1979 he has been with The Ohio State University ElectroScience Laboratory, where he currently holds the position of Senior Research Associate. His current research interests are in electromagnetic scattering and modeling, high frequency techniques, numerical and analytical techniques for the analysis of MMIC. Dr. Rojas has won the 1988 R.W.P. King Prize Paper Award, the 1990 Browder J. Thompson Memorial Prize Award, both given by IEEE, and the 1989 Research Award, given by the College of Engineering at The Ohio State University. He is a Senior member of IEEE and a member of URSI Commission B.

Michael F. Otero was born in New York City, N.Y. on August 31, 1962. He received a B.S.E.E. degree from the Polytechnic Institute of New York in 1984. From 1984 to 1989 he worked as an antenna engineer at the Raytheon Co. in Tewksbury, Mass. During his employment at Raytheon, he received a M.S.E.E. from the University of Massachusetts at Amherst in 1986. He is currently working as a Graduate Research Associate at the Ohio State University ElectroScience Laboratory where he is enrolled as a Ph.D. student. His present research interests are in numerical and high-frequency asymptotic techniques.